LARGE EDDY SIMULATION OF FLOW AROUND A FINITE SQUARE CYLINDER

A Thesis Submitted to

the College of Graduate Studies and Research

in Partial Fulfillment of the Requirements

for the Degree of Doctor of Philosophy

in the Department of Mechanical Engineering

University of Saskatchewan

Saskatoon, Saskatchewan

by

Maryam Einian

Permission to Use

In presenting this thesis in partial fulfillment of the requirements for a Postgraduate degree from the University of Saskatchewan, I agree that the Libraries of this University may make it freely available for inspection. I further agree that permission for copying of this thesis in any manner, in whole or in part, for scholarly purposes may be granted by the professors who supervised my thesis work or, in their absence, by the Head of the Department or the Dean of the College in which my thesis work was done. It is understood that any copying or publication or use of this thesis or parts thereof for financial gain shall not be allowed without my written permission. It is also understood that due recognition shall be given to me and to the University of Saskatchewan in any scholarly use which may be made of any material in my thesis.

Requests for permission to copy or to make other use of material in this thesis in whole or part should be addressed to:

Head of the Department of Mechanical Engineering

University of Saskatchewan

Saskatoon, Saskatchewan, Canada

S7N 5A9

Abstract

The main objective of this research is to develop, document and study numerically the flow around finite-height square cylinders mounted on a ground plane, particularly in the near-wake region, under various geometrical conditions. Both the time-averaged and instantaneous flow fields are studied. This thesis consists of three main parts: a comprehensive study of flow over an aspect ratio AR = 5 square cylinder, the effect of sub-grid scale (SGS) models on the numerical simulation and the effect of aspect ratio on the flow structure.

The first part of the thesis presents the time-averaged and instantaneous flow fields for flow over a wall-mounted finite-height square cylinder of aspect ratio of AR = 5 at a Reynolds number of Re = 500. The time-averaged flow field results are shown to be in good agreement with experiments. Comparison of the time-averaged results with the velocity field for a square cylinder immersed in a thicker boundary layer, suggests that the boundary layer thickness especially affects the upwash flow (Wang et al., 2009). The instantaneous velocity fields provide an in-depth view of the unsteady nature of the flow field. For the flow over a square cylinder of AR = 5, the instantaneous velocity fields are symmetric near the free end. However, antisymmetric patterns observed downstream may be an indication of the presence of periodic von-Karman type vortices.

Since the wake regions are characterized by large-scale unsteady motions, turbulent flow over bluff bodies is well suited to large eddy simulation in which the large energy-containing scales of motion, which are responsible for most of the momentum transport, are resolved whereas the small-scale turbulent fluctuations are modeled. In the second part of the thesis, the performance

of the three SGS models, the Smagorinsky model (SM), dynamic Smagorinsky model (DSM) and dynamic non-linear model (DNM) are studied for two grid sets of lower and higher resolution. The results indicated that in case of the DSM insufficient grid resolution leads to erroneous predictions, whereas the DNM is a major improvement as the predictions are similar on both the coarse and fine grids.

In the third and final part of the thesis, the effect of aspect ratio on the flow over a wall-mounted finite-height square cylinder is numerically investigated. The wake of a finite square cylinder is studied for three aspect ratios of AR = 3, 5 and 7. The time-averaged vorticity was shown to vary with aspect ratio, e.g. as the aspect ratio increases, the vortex structures in a horizontal plane at mid-height became shorter and rounder in shape. The flow field of the finite cylinder is known to be strongly affected by the aspect ratio (Adaramola et al., 2006). For cylinders with relatively small aspect ratios, the two ends affect the flow patterns and significantly alter the flow structure.

Acknowledgments

First and foremost I would like to express my gratitude to my supervisors, Professor Donald. J. Bergstrom and Professor David Sumner, for their support, guidance, understanding, and patience. I appreciate their vast knowledge and skill in many areas and their generous help and advice. Their guidance helped me throughout the time of research and writing of this thesis. I could not have imagined having better advisors and mentors for my Ph.D. study.

Special thanks go to the members of my committee, Professors James D. Bugg, Carey J. Simonson, and Raymond J. Spiteri, for the assistance they provided at all levels of the research project. I would like to thank Dr. Philip LePoudre for his assistance with the parallel programming.

I am grateful to the Department of Mechanical Engineering for providing me a comfortable research environment. I would also like to thank Mr. David Deutscher for his assistance with the laboratory demonstration. Finally, I would like to thank the department secretary, Mrs. Kelley Neale, who helped me throughout my Ph.D. program.

Table of Contents

List of Tables

List of Figures

Nomenclature

English Symbols

a_P, a_E, a_W,	coefficient for the pressure correction equation
A	cross-sectional area of the control volume
A_i	cross-sectional area of the control volume perpendicular to the i-th dimension
AR	aspect ratio: H/D
$AR_{critical}$	critical aspect ratio
b'	source term for the pressure correction equation
C_D	drag coefficient: $D/½\rho_\infty U_\infty^2 A$
C_N	coefficient for the dynamic nonlinear SGS stress model
Cp	pressure coefficient: $(p-p_\infty)/½\rho_\infty U_\infty^2$
Cp_b	base pressure coefficient: Cp at $\theta = 180°$
C_S	coefficient of the Smagorinsky model
C_W	coefficient for the dynamic nonlinear SGS stress model
d	constant
D	side length for a square cylinder or diameter of a circular cylinder
E	power
f	a function of space; vortex shedding frequency, relaxation factor
f_μ	damping function of Smagorinsky model
G_i	combination of the diffusion terms of the Navier-Stokes equations
$G^{(k)}$	coefficients, functions of irreducible tensorial invariants
$G(x,y)$	filter kernel function
h, H	height of the cylinder

H_i	convection terms of the Navier-Stokes equations
i	index: $i = 1, 2, \ldots$; or imaginary unit
$\mathrm{I}_{(d)}$	identity matrix ($d = 1 \sim 6$)
j	index: $j = 1, 2, \ldots$
l_z	spanwise extent of the domain
L	dimension of the physical domain
L_{ij}	Leonard stress: $T_{ij} - \tilde{\tau}_{ij}$
M_{ij}	differential tensorial function: $\alpha_{ij} - \tilde{\beta}_{ij}$
N_{ij}	differential tensorial function: $\varsigma_{ij} - \tilde{\eta}_{ij}$
p	pressure
p_∞	free stream pressure
p'	corrected pressure
Q	Second invariant
Pe	Peclet number: $u_i \Delta x / \nu$
Re	Reynolds number: $\rho_\infty U_\infty D / \mu_\infty$
S	matrix: $[\,\overline{S}_{ij}\,]$
S_{ij}	strain rate tensor
St	Strouhal number: fD/U_∞
t	time
Δt	time step
T_{ij}	test-grid level SGS stress
$\mathrm{T}^{(\mathrm{i})}$	independent symmetric tensorial elements related to the products of S and Ω (i = $1 \sim 11$)
U	local flux velocity

U_∞	free stream velocity
u^*	intermediate velocity component
u_i	the i-th velocity component
u_i'	SGS velocity component: $u_i' = u_i - \overline{u}_i$
u_τ	shear velocity: $(\tau_w/\rho)^{1/2}$
$\langle u_1' u_2' \rangle$	Reynolds shear stress
ΔV	volume of the control volume
W_{ij}	differential tensorial function: $\lambda_{ij} - \tilde{\gamma}_{ij}$
x, y, z	3-D Cartesian coordinates
x_i, x'_i	coordinates (i = 1, 2, 3)
Δx_i	grid size in the x direction
Δx_{ie}	averaged grid size in the x direction and the next neighbor
y^+	dimensionless wall distance: $u_\tau y/\nu$

Greek Symbols

α	angle of attack
α_{ij}	tensor: $2\tilde{\overline{\Delta}}^2 \left\lvert \tilde{\overline{S}} \right\rvert \tilde{\overline{S}}_{ij}$
β_{ij}	tensor: $2\overline{\Delta}^2 \left\lvert \overline{S} \right\rvert \overline{S}_{ij}$
γ_{ij}	tensor: $4\overline{\Delta}^2 \left(\overline{S}_{ik}\overline{\Omega}_{kj} - \overline{\Omega}_{ik}\overline{S}_{kj} \right)$
Γ	diffusion coefficient
δ	boundary layer thickness on the ground plane at the location of the cylinder
δ_{ij}	Kronecker delta = 1 if $i = j$, otherwise = 0
Δ	mesh or filter size

η_{ij} tensor: $4\overline{\Delta}^2\left(\overline{S}_{ik}\overline{S}_{kj}-\frac{1}{3}\overline{S}_{mn}\overline{S}_{nm}\delta_{ij}\right)$

λ_{ij} tensor: $4\tilde{\overline{\Delta}}^2\left(\tilde{\overline{S}}_{ik}\tilde{\overline{\Omega}}_{kj}-\tilde{\overline{\Omega}}_{ik}\tilde{\overline{S}}_{kj}\right)$

μ dynamic viscosity

μ_∞ free stream dynamic viscosity

ν kinematic viscosity

ν_∞ free stream kinematic viscosity

ν_{sgs} subgrid-scale viscosity

ν_T eddy viscosity

ξ_{ij} tensor: $4\tilde{\overline{\Delta}}^2\left(\tilde{\overline{S}}_{ik}\tilde{\overline{S}}_{kj}-\frac{1}{3}\tilde{\overline{S}}_{mn}\tilde{\overline{S}}_{nm}\delta_{ij}\right)$

ρ fluid density

ρ_∞ free stream density

τ shear stress

τ_{ij} grid level SGS stress

$\overline{\tau}_{ij}$ viscous stress tensor: $\overline{\tau}_{ij} = <u_i' u_j'>$

τ_w shear stress at the wall

ω vorticity

Ω flow domain

Ω_{ij} the vorticity tensor: ½ ($u_{i,j}$ - $u_{j,i}$)

Subscripts and Superscripts

$(\,)_1$ streamwise component

$(\,)_2$ spanwise component

$(\,)_3$	wall-normal component
$(\,)_b$	component at the back face of the control volume
$(\,)_B$	component at the back neighbor node
$(\,)_e$	component at the east face of the control volume
$(\,)_E$	component at the east neighbor node
$(\,)_f$	component at the front face of the control volume
$(\,)_F$	component at the front neighbor node
$(\,)_{ij}$	tensor: $i, j = 1, 2, 3$
$(\,)_i$	vector component: $i = 1, 2, 3$
$(\,)_{,i}$	spatial derivative: $\partial(\,)/\partial x_i$
$(\,)_{i,j}$	spatial derivative: $\partial(\,)_i/\partial x_j$
$(\,)^n$	result at the n-th time step
$(\,)_n$	component at the north face of the control volume
$(\,)_N$	component at the north neighbor node
$(\,)_p$	component at the center of the control volume
$(\,)_P$	component at the central node
$(\,)_s$	component at the south face of the control volume
$(\,)_S$	component at the south neighbor node
$(\,)_w$	component at the west face of the control volume
$(\,)_W$	component at the west neighbor node
$\overline{(\quad)}$	grid level filter; or resolved quantity
$(\,)^*$	intermediate result between two time steps

Abbreviations

ADI	Alternative Direction Implicit
CFD	Computational Fluid Dynamics
CFL	Courant–Friedrichs–Lewy condition: $u\Delta t/\Delta x$
DNS	Direct Numerical Simulation
DSM	Dynamic Smagorinsky Model
EVM	Eddy Viscosity Model
FVM	Finite-Volume Method
LES	Large Eddy Simulation
DNM	Non-Linear Dynamic Model
PIV	Particle Image Velocimetry
POD	Proper Orthogonal Decomposition Technique
QUICK	Quadratic Upwind Interpolation for Convective Kinematics
RANS	Reynolds Averaged Navier-Stokes method
SGS	Subgrid-scale
SM	Smagorinsky Model
TDMA	Tri-Diagonal Matrix Algorithm

Chapter 1

Introduction

1.1. Flow over Bluff Bodies

Bluff bodies can be found in many engineering applications, such as bridges, tall buildings and towers, maritime vessels, road and rail based vehicles and in various aeronautical applications. Many high-rise buildings can be described as a wall-mounted finite-height cylinder with a free end (Figure 1.1).

Figure 1.1: Downtown Edmonton from the air (Wikipedia.org)

A bluff body has a non-streamlined geometry that produces significant resistance when immersed in a moving fluid. Separation occurs over a large section of a bluff body, which produces a high pressure drag force and a large wake region.

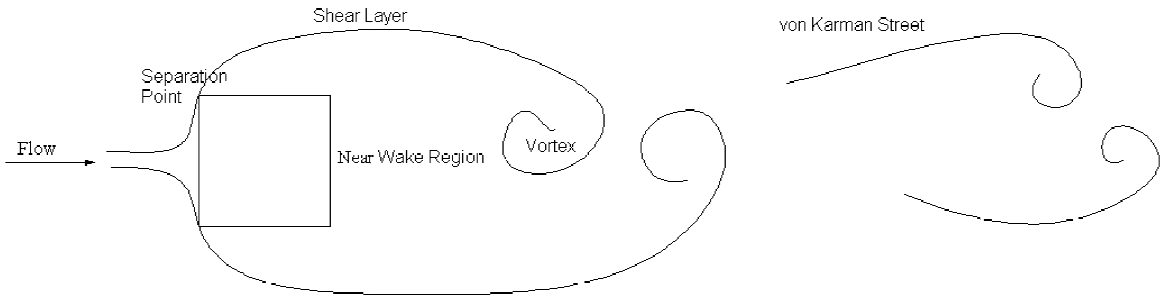

Figure 1.2: Sketch of the flow structure around an infinite square cylinder, $50 < Re < 2\times10^5$.

As shown in Figure 1.2, bluff body wakes involve complicated phenomena, including the interactions of three shear flows in the same problem: a boundary layer, a separating free shear layer, and a wake. Here, the Reynolds number is defined as $Re = \rho U_\infty D/\mu$, where ρ, μ, D and U_∞ are the fluid density, dynamic viscosity, cylinder diameter or side length or side width, and free stream velocity, respectively. The wake of a bluff body is often characterized by periodic, alternate vortex shedding, and the formation of a von Karman vortex street.

The inter-relationship between the mean drag coefficient, base pressure, and vortex shedding, and the size (width, streamwise extent of the mean recirculation zone) of the near-wake region is complex and needs improved physical insight, for three-dimensional bluff bodies and surface-mounted finite-height bluff bodies. This improved physical understanding will assist engineers in preventing flow-induced vibrations and reducing wind loading.

1.2. The Challenge of the Computational Fluid Dynamics Methods

CFD is a promising tool that allows physical insight to be gained into the flow around bluff body flows. In computational fluid dynamics (CFD) numerical methods and algorithms are used to solve and analyze problems that involve fluid flows. Due to the rapid advancement of computers in recent years, CFD has become one of the most significant research techniques in the study of

turbulent flows. By providing the instantaneous velocity and pressure fields CFD has made accessible data that were never previously measurable.

Considering the numerical simulation of flow around bluff bodies, there are three different methods: Reynolds Averaged Navier-Stokes method (RANS), Large Eddy Simulation (LES), and Direct Numerical Simulation (DNS). DNS solves all the time and length scales and requires grid and computational resources that are not readily available. In order to overcome the DNS limitation, turbulence models are used. The RANS turbulence models generally produce too much eddy viscosity and over-damp the unsteady motion of the fluid. This problem is expected in the construction of the RANS turbulence models because of the assumption that all scales of the unsteady motion of the fluid are captured and modeled by the turbulence model. Spatially filtered turbulence models such as LES can provide improved results for simulating unsteady flows.

1.3. Motivation

For a finite circular or square cylinder mounted on a ground plane (Figure 1.3), the flow over the free end and the flow around the junction of the cylinder and the ground plane change the vortex structure in the wake dramatically compared to a two-dimensional or "infinite" cylinder (Adaramola et al., 2006).

Figure 1.3 shows a schematic diagram of the cylinder mounted on a ground plane and immersed in a thin laminar boundary layer with thickness δ. The angle of attack is set to $\alpha = 0°$. x and y show the location of the probe behind the prism. Similar to the hot-wire measurements three probes were picked to store the velocity and pressure variation throughout the simulation.

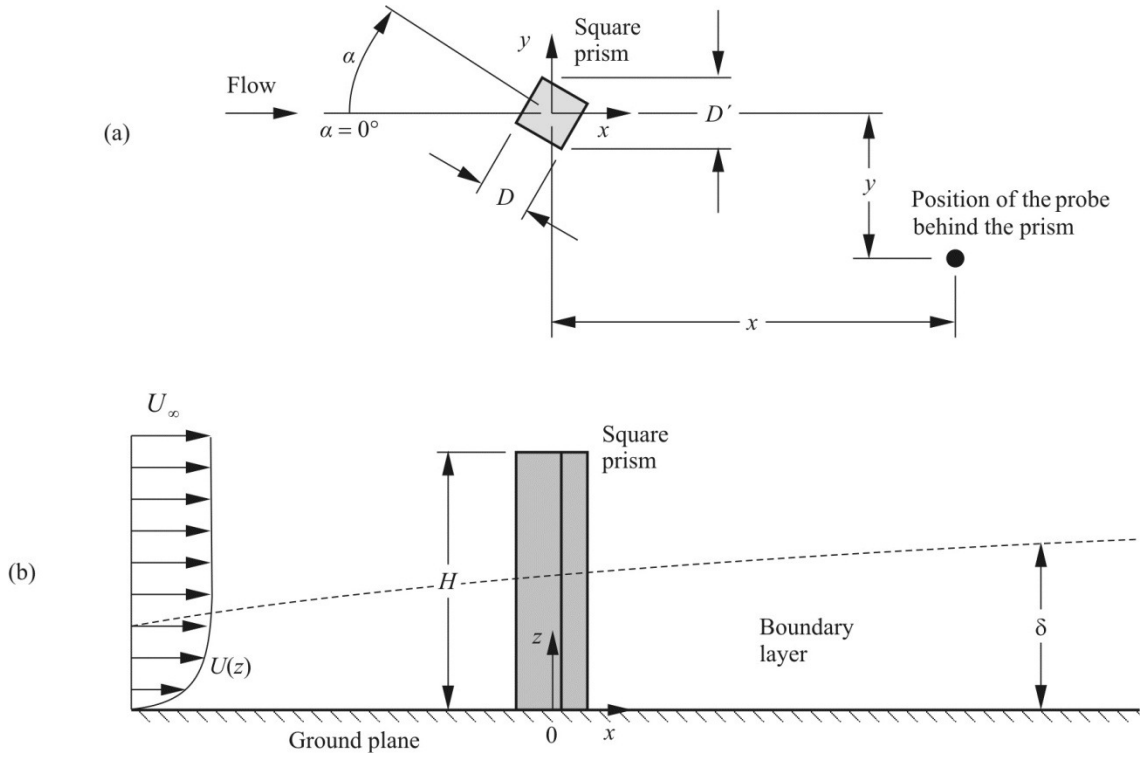

Figure 1.3: The schematics of a flow over a surface-mounted square cylinder.

The free end of a finite-height cylinder is the main source of the three-dimensionality of the flow. The free end changes the vortex formation region, vortex-shedding pattern and the surface pressure distribution (Park and Lee, 2000). The free end creates a pair of streamwise tip vortices, which induces a downwash flow along the upper wake centreline.

In the wake region behind the wall-mounted cylinder, besides the tip vortices, a pair of weaker vortices is also observed close to the ground plane, known as the base vortices. The base vortex pair is responsible for a weak upwash flow field.

The flow field of the finite cylinder is highly affected by the aspect ratio (Adaramola et al., 2006). For cylinders with relatively small aspect ratios, the two ends affect the flow patterns directly and interact with each other at the same time. For these cylinders, the end effects will drastically alter the flow structure. For flows around cylinders with low aspect ratios, the tip

vortices are dominant, and symmetric arch-type vortex structures are observed. On the other hand, for a very long cylinder, it can be expected that the flow pattern in the middle of the cylinder should resemble the structure of an "infinite" or two-dimensional cylinder. For higher aspect ratios, an antisymmetric von-Karman vortex shedding behavior is present.

Besides the aspect ratio of the cylinder, the boundary layer thickness on the ground plane affects the creation of the base vortices. Where a thicker boundary layer is present, the base vortices are stronger and the upwash flow is more pronounced (Wang et al., 2006).

For modeling unsteady fluid flow behavior, such as that encountered in the flow around a cylinder, a more viable method compared to other numerical methods is large eddy simulation (LES) in which the large energy-containing scales of motion, which are responsible for most of the momentum transport, are solved for, whereas the small-scale turbulent fluctuations are modeled (Wikstrom et al., 2004). In other words, in LES the effects of the large scales are directly computed and only the small sub-grid scales (SGS) are modeled. Since small scales tend to be more isotropic than the large ones, it should be possible to parameterize them, using simpler and more universal models than standard Reynolds stress models (Germano et al., 1991).

Tutar and Hold (2001) used both RANS and LES models in a subcritical flow regime to simulate the transitional flow around a two-dimensional stationary circular cylinder. In the first set of simulations, they implemented the enhanced two-equation turbulence models based on the eddy viscosity. In the second set of simulations, they carried out the flow simulation using LES, which was based on a standard sub-grid scale model with a near-wall approach. They compared both methods' results with each other and with experimental data in order to determine the relative performance of these turbulence models and to find the best model for the flow of

interest. They showed that the LES method, leads to a much more realistic picture for the vortex shedding flow in this transitional flow regime.

For finite circular cylinders, the flow is sensitive to the Reynolds number. However, in cases like a square cylinder, where the geometry exhibits sharp corners, the separation points are fixed and the solution is less sensitive to modelling in the near-wall region (Frohlich et al., 1998).

1.4. Objectives and Scope

The main objective of this research is to develop, document and study numerically the flow around finite-height square cylinders mounted on a ground plane, particularly in the near-wake region, under various geometrical conditions. Both the time-averaged and instantaneous flow fields will be studied. The secondary objective of the research is to study the effect of various sub-grid scale (SGS) models.

In the present study a methodology to perform LES around a wall-mounted square cylinder, using the fractional-step method on a non-uniform Cartesian grid, is summarized. To have a more powerful code, a multi-grid approach is introduced. It is shown that for a wall-mounted cylinder, due to the difficulty in applying numerical simulations for thin boundary layers at high Reynolds numbers, the most extensive large eddy simulations were carried out for a relatively low Reynolds number. For modeling the flow, the fluid motion should be decomposed by filtering into a large-scale component that will be computed exactly and a small sub-grid scale component which will be modeled. Regarding the large-scale components, the problem was studied from different aspects. Compared with other methods like SIMPLE, the fractional-step method is more appropriate in the case of unsteady flows. Choosing between collocated or

staggered grid is ambiguous. Both methods have their own advantages and disadvantages, though it seems that using the collocated arrangement better supports the multi-grid procedures. However, from the energy conservation point of view, the finite-volume method is the more logical choice. For modeling the SGS, the Smagorinsky, Dynamic Smagorinsky and non-linear Smagorinsky models are studied, and based on the results, the Dynamic Non-linear model is more accurate.

1.5. The Expected Contributions

This study is one of few studies to perform an LES simulation of the flow around a surface-mounted finite square cylinder. This study provides new physical insight into the complex, three-dimensional, turbulent, and unsteady near-wake flow structures, including both the time-averaged representation and instantaneous behavior. It should be noted that this type of information is very difficult to obtain with conventional experimental techniques. The only technique that could be used would be Tomographic PIV, which is very new and probably does not have the temporal resolution.

In this research, the time-averaged flow field over a wall-mounted finite-height square cylinder was numerically investigated for an aspect ratio of AR = 5 at a Reynolds number of Re = 500, and it was shown that the results were in a good agreement with experiments. However, the main advantage of numerical simulations over most experimental studies is that the former typically gives more detailed information on the flow field in space and time. Often the actual dynamics of the flow can be better resolved and understood by considering the instantaneous behavior of the flow rather than only the time-averaged results. The instantaneous flow field is

studied systematically through the three-dimensional 2nd invariant iso-surfaces over a vortex shedding-cycle, which is considered to be a significant contribution of this thesis. The numerical simulation suggested similar structures to those obtained by the phase average measurements of Bourgeois et al, (2011).

The current study also offers insight into the effects of different subgrid-scale models for LES simulations of the flows over bluff bodies. The effect of the subgrid-scale models was studied by comparing the solutions of three SGS models for a square cylinder with AR = 5 at Re = 500. Three different SGS models (SM, DSM and DNM) were implemented on two different grid levels. Previously, both the SM and DSM models have been employed in the numerical simulation of the flows over bluff bodies. The flow field around a bluff body includes various types of flow features such as separation, free shear layers and vortex shedding, which makes it difficult to pre-select one specific value of C_S as required by a SM. Even though the DSM has significant advantages over the SM, the DSM still has several aspects that require improvement. One of these shortcomings is large fluctuations in the value of C_S which can make computations unstable which is particularly serious in the 3-D computation of bluff body aerodynamics (Murakami et al., 1999). The DNM proposed by Wang and Bergstrom (2005) exhibits significant flexibility and local stability without the need for volume or plane averaging to avoid excessive backscatter of SGS turbulence kinetic energy. Also both time-averaged and instantaneous results indicate that the DNM is less dependent on the grid resolution than the DSM. In addition, it appears to result in a finer-scale vortex structure than the DSM, which warrants further investigation. The investigation of this may be considered as the second contribution of this thesis.

As was mentioned before, the flow field and vortex structure of the finite cylinder is highly affected by the aspect ratio. Although the general effects of AR are well-established in the literature, this work provides more insight into the two main types of wake structure encountered for cylinders greater than and less than the critical aspect ratio. Therefore, as a third contribution, the effect of the aspect ratio on the flow over a wall-mounted finite-height square cylinder was numerically investigated for three aspect ratios of AR = 3, 5 and 7 at Re = 500.

1.6. Outline of the Thesis

Chapter 2 presents the experimental and numerical studies reported in the literature. In this chapter the effects of the free end, aspect ratio and the boundary layer thickness on the vortex structure under various physical and geometrical conditions is reviewed. Besides the experimental results, the results of numerical simulations found in the literature are presented.

In Chapter 3 the numerical algorithms involved in a simulation of a flow over an obstacle are discussed. Turbulent flow over bluff bodies is well suited to large eddy simulation since the wake regions are characterized by large-scale unsteady motions. The simulations use a collocated finite-volume code, which employs a semi-implicit fractional step method and a pressure correction equation to solve the velocity-pressure fields. The cylinder geometry is created on a Cartesian mesh using internal boundary conditions.

In Chapter 4 the time-averaged flow field over a wall-mounted finite-height square cylinder is numerically investigated at Re = 500. The wake of a finite-height square cylinder is studied for AR = 5. The time-averaged quantities are obtained for at least five complete vortex shedding cycles. Velocity vectors and vorticity contours were used to study the flow in two-dimensional

planes, while contours of the second invariant were used to visualize the three-dimensional vortex structure in the wake.

Chapter 5 examines some features of the instantaneous velocity field for the same case of flow over a finite-height square cylinder of AR = 5 at Re = 500. Based on the calculated Strouhal number, six consecutive instantaneous flow fields are chosen and are studied thoroughly. The Strouhal number is defined as St = fD/U_∞, where f is the frequency of the vortex shedding, D the cylinder diameter or width, and U_∞ the free stream velocity.

In Chapter 6 the solutions of three subgrid-scale (SGS) models are studied for a square cylinder with AR = 5 at Re = 500. Three different SGS models are employed on two different grid levels of 64 × 72 × 48 (coarser grid) and 128 × 144 × 96 (finer grid). Both time-averaged and instantaneous flow fields are presented.

In Chapter 7 the effect of the aspect ratio on the flow over a wall-mounted finite-height square cylinder is numerically investigated. The wake of a finite square cylinder is studied for three aspect ratios of AR = 3, 5 and 7 at Re = 500.

Conclusions and recommendations for further study are presented in Chapter 8. Several appendices are found at the end of the thesis. Appendix A examines the efficiency of the multi-grid approach. Appendix B introduces the Dynamic Smagorinsky model while the Non-linear Dynamic model is introduced in Appendix C. Appendix D presents the streamwise vorticity contours and velocity vectors at streamwise positions of x/D = 8 and 10, where x is the streamwise coordinate measured from the centre of the cylinder and D is the side length of the square cylinder.

Chapter 2

Physics (Literature Review)

2.1. Introduction

The majority of investigations of the flow over bluff bodies has focused on the flow around a circular cylinder (of diameter, *D*), while the flow around a square cylinder (of side length, *D*) has been less well studied. Although turbulence is three-dimensional (3-D), the mean flow around an "infinite" cylinder (where the length of the cylinder is much longer than its diameter and the ends of the cylinder do not influence the flow field at mid-length or mid-span) can be considered a two-dimensional (2-D) flow. In numerical simulations of the flow around an infinite cylinder, periodic boundary conditions are often employed for the side walls. Periodic boundary conditions are used in a particular direction for flows which do not vary (in the statistical sense) in a given direction (Ferziger and Peric, 1999).

2.2. "Infinite" Square Cylinder

The turbulent flow around a square cylinder has received far less attention than the flow around a circular cylinder (Lyn et al., 1995). Structures that typically have rectangular or near-rectangular cross-sections include architectural features on buildings, the buildings themselves, beams, fences and occasionally stays and supports in internal and external flow geometries (Sohankar et al., 1999). In cases where the geometry exhibits sharp corners, such as for a square cylinder or a cube, the separation points are fixed and the solution is less sensitive to modelling in the near-wall region (Frohlich et al., 1998). For the square cylinder a variety of numerical results are

available. The calculations all show qualitatively the correct basic shedding feature, but there are large quantitative differences in the results (Frohlich et al. 1998).

Although the geometry of the infinite square cylinder is simple, the surrounding flow structure is complex (Figure 1.1). The flow around an infinite cylinder involves the interactions of three shear flows in the same problem: a boundary layer, a separating free shear layer, and a wake.

In the present research, the flow around a square cylinder is studied for Re = 500. At this Reynolds number the wake flow is turbulent but it requires less numerical effort to simulate the flow compared to higher Reynolds number flows. Lin et al. (2008) conducted experiments for the flow around a surface-mounted square cylinder ranging from Re = 200 to 6,000 and showed that the flow structures are independent of Reynolds number. In the near-wake region of a two-dimensional cylinder, since the axes of the shed Karman vortices are parallel to the cylinder axis, the cylinder wake is assumed to be two-dimensional. However, in a strict sense, even a low Reynolds flow over a two-dimensional object is three-dimensional (Park and Lee, 2000). Park and Lee (2000) suggest that the main reasons for the three-dimensionality are the presence of longitudinal (streamwise) vortices.

At Re = 500, the flow separates from the upstream corners of the square cylinder, and the vortex shedding leads to an unstable and time-periodic oscillation in the wake region known as the von-Karman vortex street (Figure 1.1). This time-periodic unsteady motion makes the numerical simulation of this flow more challenging.

The longitudinal vortex structures have been extensively studied in the context of the circular cylinder, for Re = 100 to 500 and higher by Williamson (1996). In a review paper, Williamson

(1996) reported that, for a circular cylinder, a von-Karman vortex street first appears at Re ≈ 49 and the wake become three-dimensional at Re ≈ 149 resulting in a ‘‘mode A instability” which is characterized by a spanwise wavelength of around 3*D* - 4*D*. At Re ≈ 240 the mode A switches to mode B which is characterized by a reduction in size of the spanwise wavelength by a factor of three. Switching/moving from parallel laminar shedding to a “mode A instability” and ultimately “mode B instability”, Williamson (1996) found a discontinuity in the Strouhal number-Reynolds number relationship for vortex shedding.

Even though both mode A and mode B type behavior has been well-documented for the square cylinder, unlike the infinite circular cylinder, there is no particular classification method for various flow regimes for the infinite square cylinder. However, above some critical Reynolds number the flow around the infinite square cylinder exhibits the well-known time periodic phenomenon of vortex shedding. At Reynolds numbers below about unity, the flow is fully attached with no separation. As Re is increased, the flow separates, and a pair of steady symmetric vortices forms behind the body. For the circular cylinder, this occurs at around Re = 3–5. The recirculation region behind the body grows with increasing Re. The separation for Re < 100 occurs from the rear corners, predominantly from the rear corners at Re = 125 with occasional upstream corner separation, predominantly from the upstream corners at Re = 150, and, finally, at all times from the upstream corners for Re > 175 (Sohankar et al., 1999).

For a finite square cylinder, like the finite circular cylinder, the vortices and the wake have a strong three-dimensional character due to the effect of free end of the cylinder, and the features of vortex formation are different from that for the infinite cylinder (Okamoto et al., 1995).

Like the circular cylinder, flow around the square cylinder has been investigated both numerically and experimentally. Lyn et al. (1995) showed that, in comparison with an infinite circular cylinder, the length scales were larger in both streamwise and spanwise direction for an infinite square cylinder. This argument was also valid for the peak values of both turbulent and periodic stresses.

Bosch and Rodi (1998) presented the results of numerical simulations of vortex shedding past a free-standing square cylinder at $Re = 2.2\times10^4$ using RANS. Sohankar et al. (1999) used DNS for simulating the flow around a square cylinder for Re = 150–500. Okamoto et al. (1995) employed the laser-Doppler velocimetry method and demonstrated that the turbulence intensities increase in the recirculation region with an increase in the downstream distance, and they attain maximum values near the end of the recirculation region. After that they tend to decay gradually as the downstream distance increases from the recirculation region.

Murakami et al. (1999) conducted computational fluid dynamics analysis of turbulent flow past a square cylinder for $Re = 2.2\times10^4$ using LES. They implemented the three-dimensional LES computation based on the conventional standard Smagorinsky model and showed that the standard Smagorinsky model gives better results compared to the RANS models. Next, they carried out the computation using the dynamic Smagorinsky (DS) model and demonstrated the improvement by the use of the DS model. Lastly, they implemented the Lagrangian dynamic Smagorinsky model to overcome the disadvantages of the DS model. Lee (1998) simulated the wake structures behind a square cylinder at $Re = 2.2\times10^4$ using LES. He employed the finite-element method with isotropic linear elements.

Li and Wang (2004) developed an LES technique using the Immersed Boundary Method (IBM) to compute flow around a square cylinder for Re = 2.2×10^4. They employed a fractional-step, finite-difference method with a rectilinear non-uniform collocated grid. They reproduced the complex flow phenomena such as flow separation and vortex shedding and calculated the mean drag coefficient, mean lift coefficient, at incidence angle and pressure coefficient. They obtained good agreement between the numerical results and the experimental data.

Grigoriadis et al. (2003) considered the incompressible turbulent flow past a long square cylinder using LES for Re = 2.2×10^4 using the IBM concept. They used this model as one of the validation cases for the development of a numerical code designed for efficient, parallel, three-dimensional Navier-Stokes computations in complex geometrical configurations. The numerical method they used was based on the fractional-step method of Kim and Moin (1985) for different grid resolutions. They showed that the frequency of vortex shedding was in very good agreement with the experimental data. However, the comparison of vortex shedding frequency is not a safe indication of a successful prediction overall. They observed that an accurate prediction of the vortex shedding frequency was sensitive to the grid density close to the cylinder and not the overall resolution. On the other hand, the time-averaged length of the recirculation region was found to be more sensitive to the grid size. They demonstrated that an appropriate reproduction of the recirculation region was mainly related to the spatial resolution on the cylinder's surfaces particularly in the direction of the flow.

Liou et al. (2002) implemented LES for turbulent flows past a square cylinder with and without a nearby wall at a Re = 2.2×10^4. They used a finite-volume technique to solve the time-dependent filtered compressible Navier-Stokes equations with a dynamic subgrid-scale turbulence model.

Results showed some improvements in predicting the streamwise evolution of the long-time-averaged streamwise mean velocity and total fluctuation intensity along the centreline over those predicted by using Reynolds stress models.

Yen and Yang (2011) tested the flow over in infinite square prism under various angles of attack and Reynolds number ranging from Re = 4×10^3 to 3.6×10^4. For an infinite square prism with zero angle of attack, the flow separated from the two upstream corners of the prism and a wide wake formed downstream.

Okajima (1982), studied the variation of the Strouhal number in regards to the Reynolds number for the flow over an infinite rectangular cylinder, and showed that St of a square cylinder varies continuously around a constant value of St = 0.125, for a Reynolds number ranging from 100 to 1×10^4.

2.3. "Finite" Square Cylinder

Many high-rise buildings can be modeled as a wall-mounted finite-height cylinder with a free end. For a finite cylinder mounted on a ground plane (Figure 2.1), the flow over the free end, and the flow around the junction of the cylinder and the ground plane, change the vortex structure dramatically from the case of the flow over an infinite cylinder (Adaramola et al., 2006).

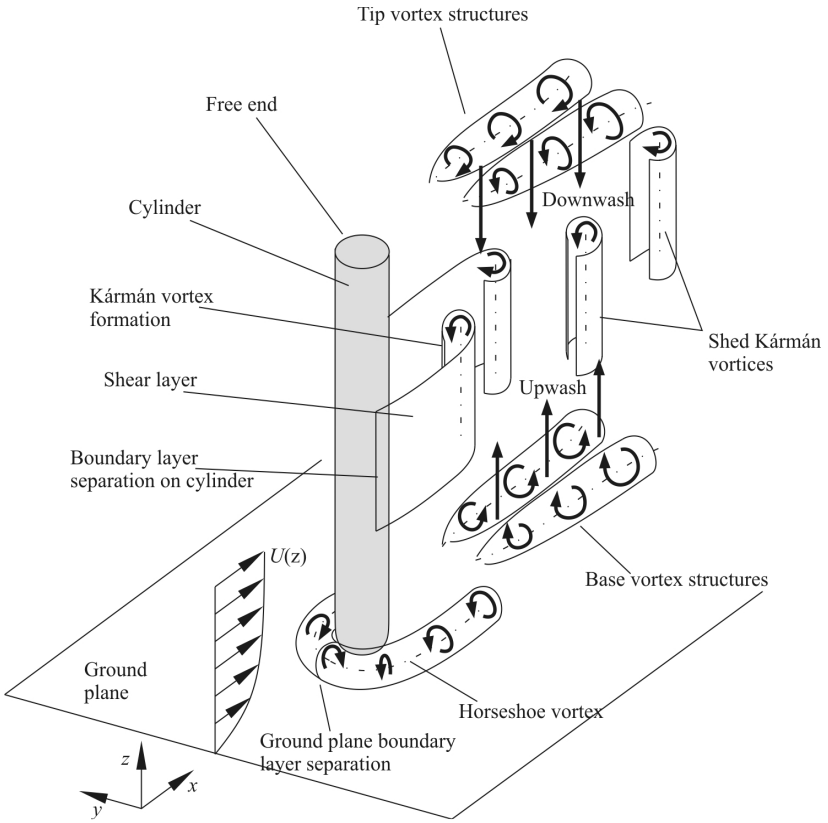

Figure 2.1: Sketch of the flow around a finite cylinder mounted normal to a ground plane.

2.3.1. End Effects

Cylinders with relatively small aspect ratios, the two ends affect the flow patterns directly and interact with each other at the same time. Fox and West (1993) showed that in regards to the mean pressure distribution, if the cylinder is of sufficiently high aspect ratio (AR > 13), the ends will be sufficiently separated that they will not affect each other. The free end of a finite-height cylinder is the main cause/source of the three-dimensionality of the flow. The free end alters the vortex formation region, vortex-shedding pattern and the surface pressure distribution (Park and Lee, 2000). The free end creates a pair of tip vortices, which induces a downward-directed velocity field along the wake centreline known as the downwash flow (Adaramola et al., 2006).

Around the junction point of the cylinder with the ground-plane, an adverse pressure gradient is produced. Consequently, the boundary layer is forced to separate from the ground-plane and ultimately a horseshoe vortex is formed wrapping around the base of the cylinder. These vortices carry on moving with the stream towards the downstream (Sakamoto and Arie, 1983). According to Okamoto and Sunabashiri (1992), the size of the horseshoe vortex is relative to the height of the cylinder, and decreases as the height of the cylinder increases. Bourgeois et al. (2011) showed that the horseshoe vortex is relatively weak in the wake region and does not have a major effect on the dynamics of the shed vortices.

In the wake region behind the wall-mounted cylinder, besides the tip vortices, a pair of weaker vortices close to the ground plane may also be also observed; these vortices are known as the base vortices (Figure 2.1, Sumner et al. 2004).

It should be noted that the main flow features in the wakes of both finite circular and square cylinders are similar (Wang and Zhou, 2009). There are many experimental and numerical studies in the literature for the flow around finite cylinders, with the majority of these studies focus on the finite circular cylinder.

2.3.2. Aspect Ratio Effect

Assuming a very long (or very slender) cylinder, it can be expected that the flow pattern in the middle of the cylinder should resemble the structure of an infinite cylinder.

However, for shorter (less slender) cylinders, the end effects will radically change the flow structure. In fact, the flow field of a surface-mounted finite-height cylinder is highly affected by the aspect ratio, AR (where AR = H/D, for cylinder height, H) (Adaramola et al., 2006).

Baban and So (1991) investigated the aspect ratio effect on the unsteady forces and the flow mechanism responsible for these forces. They studied the cross-flow over a finite-height cylinders of AR = 1 and 1.5 at Re = 46,000. In a similar work, Baban et al. (1989) had studied a circular cylinder with AR = 2. They observed an increase in the mean base pressure coefficient as AR decreased. The sectional mean drag coefficient C_D decreases as aspect ratio decreases and towards the cylinder-wall junction.

Sakamoto and Arie (1983) studied both finite circular and square cylinders experimentally at Reynolds number ranging from Re = 270 to 730 and showed that the vortex-shedding structure for a finite-height cylinder is mainly a function of aspect ratio. As the aspect ratio was reduced, the vortex shedding alters from the von-Karman to the arch type vortex. They also indicated that the Strouhal number decreases with decreasing aspect ratio for both a finite-height circular cylinder and a rectangular cylinder mounted on a ground-plane (Sakamoto and Arie, 1983).

For wall-mounted circular cylinders of AR = 2.5 and 10 at Re = 43,000, Lee et al. (2007) showed that the downwash flow behind the free end of the cylinder was much stronger for the more slender cylinder. The intensity of vorticity was stronger in the wake region of the longer cylinder. Their numerical simulations showed that the vortex shedding in the upper section of the more slender cylinder was not in the same phase with that of the lower region of the same cylinder.

Park and Lee (2000) investigated the aspect ratio effect on the vortex shedding frequency for a surface mounted finite circular cylinder and showed that at Re = 20,000, the vortex shedding frequency lowers as the aspect ratio decreases. The peak amplitude of the power spectral density decreases with decreasing aspect ratio. They also showed that the streamwise extent of vortex formation region decreases as aspect ratio increases. They also observed that near the free end, the vortex formation region is altered as the periodic vortex shedding disappears.

Okamoto and Sunabashiri (1992) showed that for a flow over a circular cylinder of finite-height and Reynolds number ranged from Re = 2.5×10^4 to 4.7×10^4, the size of the recirculation region increases as the aspect ratio increases for AR < $AR_{critical}$ ($AR_{critical}$ = 4 in their case), however after reaching the critical aspect ratio, the size of the recirculation zone decreases. Due to the free end effect the mean base pressure coefficient varied along the height of the cylinder for AR < $AR_{critical}$. For AR > $AR_{critical}$ the end effect is only limited to the near-end region. In the case of a circular cylinder, the separation line/point also varies as the aspect ratio crosses the critical value, shifting from $\theta < 90^o$ to $\theta = 140^o$, leading to a reduction of the size of the wake region. In terms of the power spectrum, the frequency is almost constant for AR < $AR_{critical}$, while for AR > $AR_{critical,}$ the magnitude of the peak varies along the height of the cylinder as the magnitude of the peak becomes smaller approaching the free end (Okamoto and Sunabashiri, 1992).

Okamoto et al. (1995) studied the turbulent near-wake behind rectangular cylinders for AR $\leq$ 1 for Re = 4,600. They studied the horseshoe vortices on the ground plane and the reverse flow region on the free end of the cylinder for various aspect ratios. As the aspect ratio becomes larger, reattachment occurs on the free end surface and the reverse flow region becomes larger.

Tanaka and Murata (1999) performed an experiment for flow over a finite circular cylinder at Re = 3.7×10^4 for aspect ratios ranging from AR = 1.25 to 10 with a very thin boundary layer on the ground plane. They observed that the downwash of AR < $AR_{critical}$ reaches the ground plane, while for higher aspect ratios the downwash never approaches the ground plane. As the aspect ratio decreases the center of the streamwise vorticity contours move downward, extending horizontally (in the spanwise direction) along the ground plane. While they observed a strong downwash, followed by a pair of tip vortices near the free end for all aspect ratios, they were unable to detect any upwash or base vortices even for a tall cylinder. Further away from the near wake of the cylinder ($x/D \approx$ 5-6), however, a pair of distinct streamwise base vortices is observed near the ground plane for AR = 10. Here x is defined as the streamwise extent of the flow field measured from the center of the cylinder. The recirculation region extends more widely in the spanwise direction as the aspect ratio increases, however at AR = 10, the recirculation region shrinks compared to AR = 5.

Lin et al. (2008) studied the horseshoe vortex structure near the juncture of the square cylinder and the ground plane for Re = 2×10^2 to 6×10^3 and AR = 0.5 to 3. They showed that the horseshoe vortex structure is independent of the Reynolds number and only depends on the boundary layer thickness and the aspect ratio. The overall flow structure for the finite square cylinder is similar to the finite circular cylinder. The flow structure for the finite square cylinders is almost independent of the Reynolds number (Lin et al. 2008).

Sousa (2002) used particle image velocimetry (PIV) to measure the turbulent flow around a wall-mounted cube for Re = 3210. Wang et al. (2004) studied the flow over surface-mounted finite-height square cylinders with aspect ratio ranging from AR = 3 to 7. A broad peak in the power

spectrum at the Strouhal number of St = 0.09 was obtained for AR = 3, while for AR = 5 and 7, pronounced sharp peaks of St ≈ 0.12 and 0.13 were observed, respectively. For an infinite square cylinder, St = 0.135 was reported.

Recently Wang et al. (2009) and Wang and Zhou (2009) presented PIV results of the near wake of a finite square cylinder for aspect ratios ranging from AR = 3 to 7 (for δ/D = 1.35), where δ is the thickness of the boundary layer on the ground plane at the location of the cylinder. They showed that, since a thick boundary layer existed for all three aspect ratios, the overall flow structure is independent of the aspect ratio as the base vortices are present for all three aspect ratios.

In terms of the instantaneous vortex structure, Wang and Zhou (2009) observed two distinct flow patterns. In the first case the spanwise shear flow swept across the central plane, the vortical structures were only observed on one side of the cylinder; leading to the concentrations of ω_x on the same side. Here ω_x is the streamwise vorticity and is defined as $\omega_x = \frac{\partial v}{\partial z} - \frac{\partial w}{\partial y}$. A similar vortex structure was reported for a two-dimensional cylinder wake by Wu et al. (1996). Wang and Zhou (2009) suggested that this flow pattern may correspond to the rollup of spanwise shear layer sweeping across the central plane. Similar to what was observed from the time-averaged flow field, the second flow pattern was characterized by two pairs of counter-rotating vortical structures, one pair near the free end of the cylinder linked to the downwash representing the tip vortices, and the other near the wall related to the upwash representing the base vortices.

2.3.3. Boundary Layer Thickness Effect

Studies show that besides the aspect ratio of the cylinder, the boundary layer thickness on the ground plane affects the creation of the base vortices and formation of the upwash flow. Where a thicker boundary layer is present, the base vortices are stronger and the upwash flow is more profound or enhanced. The presence of a stronger upwash flow also affects the free end region as it prevents the downwash flow to reach the ground plane and results in weaker tip vortices (Wang et al., 2006).

Park and Lee (2002) investigated the flow structure around the free end of a finite-height circular cylinder of AR = 6, and Re = 20,000 mounted on a ground plane and immersed in various boundary layers and a uniform inflow. They showed that the vortex-shedding frequency and vortex-formation length are both lower for a finite-height circular cylinder immersed in thick turbulent boundary layer compared to the uniform flow case. They showed that the vortex-shedding frequency decreases as the boundary layer thickness increases.

Sakamoto and Arie (1983) investigated that with increasing the boundary layer thickness, the Strouhal number decreases for all rectangular prisms.

Wang et al. (2006) studied the effect of the ground-plane boundary layer thickness on the flow around a finite square cylinder of AR = 5. They showed that the boundary layer thickness has a significant effect on the creation and the size of the base vortices. Unlike Sakamoto and Arie (1983), Wang et al. (2006) observed both symmetric and antisymmetric vortices in the near wake region of the wall-mounted square cylinder for a given aspect ratio. They observed that the probability of antisymmetrical vortex shedding varies with aspect ratio and the boundary layer

thickness. The probability of antisymmetrical vortex shedding considerably increases with increasing the boundary layer thickness, particularly near the free end and base of the cylinder.

2.3.4. Vortex Structure

In the near-wake region, depending on the aspect ratio and boundary layer thickness, two different vortex structures are observed. For flows around cylinders with low aspect ratios ($AR < AR_{critical}$, where $AR_{critical} \approx 2$ to 6), the tip vortices are dominant, and a symmetric arch-type vortex structure is observed. For higher aspect ratios ($AR > AR_{critical}$), an antisymmetric von-Karman vortex structure is present (Wang et al., 2006).

Okamoto and Sunabashiri (1992) studied the variation of the vortex formation in a wake region of a finite-height circular cylinder mounted on a ground plane for various aspect ratios and Re = 2.5×10^4 to 4.7×10^4. They showed that at $AR > AR_{critical}$ the vortex formation/pattern changed, from symmetric "arch" type to antisymmetric "von-Karman" type.

Sumner et al. (2004) investigated the wake of a wall-mounted finite circular cylinder for AR = 3, 5, 7 and 9 for Re = 6×10^4, using a seven-hole pressure probe and single-component thermal anemometry, where the boundary layer thickness was fixed at $\delta/D = 2.6$ They observed a pair of tip vortices near the free end for all four aspect ratios. However, near the ground plane, the base vortices were only observed for cylinders with $AR > AR_{critical}$. They also showed that as the flow moves downstream the tip vortices become weaker and their centers move toward the ground plane. The mean drag coefficient measurements showed that for the finite-height cylinders, the drag coefficient is lower than the drag coefficient for an "infinite" cylinder. The mean drag coefficient remained constant as long as $AR > AR_{critical}$, but below the critical aspect ratio, the

drag coefficient lowers considerably. A similar Strouhal number of St = 0.16 was measured at the mid-height location for all four aspect ratios. The measured Strouhal number was lower than the value for an "infinite" cylinder. The Strouhal number of St = 0.16 was independent of the position of the probe along the height of the cylinder for all four cylinders even for the small aspect ratios.

A similar study by Adaramola et al. (2006) noted the strong downwash velocity near the free end and weaker upwash near the ground plane. They also observed an overall reduction in turbulence intensity ($\frac{u'}{\overline{U}}$ and $\frac{w'}{\overline{U}}$) at the mid-height of the near wake region of the wall-mounted circular cylinder. Here $\overline{U}$ is the mean streamwise velocity and u' and w' are the streamwise and wall-normal fluctuations and are defined as $u' = u - \overline{U}$ and $w' = w - \overline{W}$. While the turbulence intensity was the lowest for AR < $AR_{critical}$, the profiles for AR = $AR_{critical}$ ($AR_{critical}$ = 3-5 in this case), suggested a transitional wake structure towards AR > $AR_{critical}$ where the profiles nearly collapse. The streamwise development of the Reynolds shear stress distribution $\frac{u'w'}{\overline{U}^2}$ at the wake centreline (y/D = 0) showed two regions of prominent Reynolds shear stress, each of opposite sign for AR > $AR_{critical}$, while for AR < $AR_{critical,}$ the Reynolds shear stress profiles are indicating the absence of the base vortex structures and upwash flow.

Recently, Bourgeois et al. (2011) used a phase averaging method to study the configuration and energetics of the large-scale vortex structure for quasi-periodic shedding in the turbulent wake of a finite square-cross-section surface-mounted cylinder with AR = 4, immersed in a thin boundary layer of δ/H = 0.18 (δ/D = 0.72), measured with particle image velocimetry (PIV). They observed a pair of tip vortices at the leading edge of the free end of the cylinder. The second

invariant iso-surfaces obtained by the numerical simulations contain structures that are similar in shape to the prototypical structure suggested by Bourgeois et al. (2011), albeit the current results are instantaneous while Bourgeois et al. (2011) presented the phase-averaged results.

In terms of the effect of the initial turbulence intensity, Bourgeois et al. (2011) believed that the initial turbulence intensity does not play a role in the final structures of large scale vortices and its only effects are earlier transition and increased spreading of turbulence intensity.

Beside the tip and base vortices, the spanwise vortices (von-Karman vortices) are observed in the near wake of the finite-height cylinders. These vortices are enhanced near the free end and reduced near the wall, affecting the cycle of the symmetric/antisymmetric vortex structure. The spanwise vortex structure is only observed for finite-height cylinders with $AR > AR_{critical}$ (Wang et al., 2006).

Sumner et al. (2004) and Wang and Zhou (2009) showed that the Strouhal number measured remained constant along the height of the cylinder for reasonably small aspect ratios. Besides the major peak, a minor peak was observed near the free end of the cylinder of $AR > AR_{critical}$. Near the free end the major peak of the streamwise velocity spectrum weakened due to the interaction of the downwash flow.

2.4. Numerical Studies

In terms of numerical studies, Frohlich and Rodi (2004) employed both Smagorinsky and dynamic Smagorinsky LES models to study the flow over a finite circular cylinder with AR = 2.5 and Re = 43,000. They concluded that even a simple Smagorinsky model can lead to

acceptable results. Frederich et al. (2009) employed a proper orthogonal decomposition (POD) technique to capture the unsteady nature of the flow around a wall-mounted circular cylinder of AR = 2 for Re = 2×10^6. Sau et al. (2003) investigated numerically the three-dimensional unsteady vortex interactions of the flow in the near-wake field of a wall-mounted rectangular cylinder of AR = 1.7 for Re = 300 and 500. They observed a large horseshoe vortex behind the cylinder and a downwash flow in the near-wake field. Afgan et al. (2007) investigated the aspect ratio effect for AR = 6 and 10 using LES. They implemented a uniform velocity profile with no fluctuation at the inlet. As for the sub-grid scale model, they employed a Smagorinsky model along with a damping function near the walls. They had observed a very weak upwash flow for AR = 6.

Frederich et al. (2009) studied the turbulent separated flow around a wall-mounted finite circular cylinder at high Reynolds number. While the results obtained from their LES were in very good agreement with the experiments, the non-zonal hybrid RANS-LES approach of Detached-Eddy Simulation exhibits problems in the attached laminar boundary layer.

Salvador et al. (2010) presented both experimental and numerical results for the flow around a surface-mounted circular cylinder at the two aspect ratios of AR = 2.5 and 5 using the immersed boundary method along with the LES. The Reynolds number based on the diameter was set twice as large for AR = 2.5 at Re = 4.3×10^4 compared to AR = 5, with Re = 2.2×10^4. The cylinders were immersed in a turbulent boundary layer with a thickness of about 10% of the cylinder height. Both numerical and experimental results presented a stronger horseshoe vortex for a shorter cylinder. In terms of the vortex structure, even for a short cylinder of AR = 2.5, an antisymmetric vortex structured is observed.

In the short cylinder case, the *u*-fluctuations (*u′*) were not representative of the shear layer bordering but followed the *w*-fluctuations (*w′*) pattern. Salvador et al. (2010) suggested that the elevated *u*-fluctuations might be originated by an energy transfer from the much larger *w*-fluctuations in this region. For the long cylinder, however the *u*-fluctuations were originated from the shear layer while the *w*-fluctuations were not as large as the *u*-fluctuations. Their results from the numerical computation were in a good agreement with the experiments.

Recently, Krajnovic (2011) studied the flow around a finite circular cylinder of AR = 6 and Re = 2×10^4 using the LES. The 2nd invariant iso-surfaces of the instantaneous flow field showed that the distance between the subsequent vortices was quite constant in the near-wake region of the cylinder. For a finer grid the Strouhal number was calculated as St = 0.149 which was slightly higher than the corresponding number with a coarser grid. In terms of numerical calculations this study showed that the grid refinement improves the agreement with the experimental data.

2.5. Summary of the Reviewed Papers

Table 2.1 summarizes the main variables and characteristics of the reviewed papers in this chapter.

Table 2.1: Summary of the reviewed papers

Author	**Year**	**Re**	***δ/D***	**Aspect Ratio**	**Experimental/ Numerical**	**Cylinder's Shape**
Adaramola et al.	2006	6×10^4	2.6	3 to 9	Experimental	Circular
Afgan et al.	2007	2.0×10^4		6 to 10	Numerical	Circular

Author	**Year**	**Re**	***δ/D***	**Aspect Ratio**	**Experimental/ Numerical**	**Cylinder's Shape**
Baban and So	1991	4.6×10^4		1 to 2	Experimental	Circular
Bosch and Rodi	1998	2.2×10^4		Infinite	Numerical	Square
Bourgeois et al.	2011	1.2×10^4	0.72	4	Experimental	Square
Fox and West	1993	4.4×10^4		4 to 30	Experimental	Circular
Frederich et al.	2009	2.0×10^6		2	Numerical	Circular
Frohlich and Rodi	2004	4.3×10^4	Thin	2.5	Numerical	Circular
Grigoriadis et al.	2003	2.2×10^4		Infinite	Numerical	Square
Krajnovic	2011	2×10^4		6	Numerical	Circular
Lee	1998	2.2×10^4		Infinite	Numerical	Square
Li and Wang	2004	2.2×10^4		Infinite	Numerical	Square
Lin et al.	2008	200 to 6000		0.5 to 3	Experimental	Square
Liou et al.	2002	2.2×10^4		Infinite	Numerical	Square
Lyn et al.	1995	21400		Infinite	Experimental	Square
Murakami et al.	1999	2.2×10^4		Infinite	Numerical	Square
Okajima	1982	100 to $\times10^4$		Infinite	Experimental	Rectangular
Okamoto et al.	1995	4.6×10^3		≤ 1	Experimental	Rectangular

Author	**Year**	**Re**	***δ/D***	**Aspect Ratio**	**Experimental/ Numerical**	**Cylinder's Shape**
Okamoto and Sunabashiri	1992	2.5×10^4 to 4.7×10^4	0.13	2.5 to 10	Experimental	Circular
Park and Lee	2000	2.0×10^4		Infinite	Experimental	Circular
Park and Lee	2002	2.0×10^4		6	Experimental	Circular
Sakamoto and Arie	1983	270 to 730		1 to 5	Experimental	Square & circular
Salvador et al.	2010	2.210^4 and 4.3×10^4	0.1 *h*	2.5 to 5	Experimental/ Numerical	Circular
Sau et al.	2003	300 to 500		1.7	Numerical	Rectangular
Sohankar et al.	1999	<500		Infinite	Numerical	Square
Sousa	2002	3,210		1	Experimental	Square
Sumner et al.	2004	6×10^4	2.6	3 to 7	Experimental	Circular
Tanaka and Murata	1999	3.7×10^4	Very thin	1.25 to 10	Experimental	Circular
Williamson	1996	100 to 500		Infinite	Experimental	Circular
Wissink and Rodi	2008	3.3×10^4		Infinite	Numerical	Circular
Wang et al.	2004	9.3×10^3	thin	3 to 7	Experimental	Square

Author	**Year**	**Re**	***δ/D***	**Aspect Ratio**	**Experimental/ Numerical**	**Cylinder's Shape**
Wang et al.	2006	11500	0.07-0.245	5	Experimental	Square
Wang et al.	2009	7.3×10^3	1.35	3 to 7	Experimental	Square
Wang and Zhou	2009	9.3×10^3	1.35	3 to 7	Experimental	Square
Yen and Yang	2011	4×10^3-3.6×10^4		infinite	Experimental	Square

Chapter 3

Numerical Algorithm

3.1. Introduction

In using a mathematical method to describe a physical system, e.g. the Navier-Stokes equations, the level of approximation associated with building the model should be identified. In classical fluid mechanics, continuum mechanics gives a macroscopic description of the flow. Strictly speaking, the Navier-Stokes equations are valid for the instantaneous flow field. The Navier-Stokes equations are based on Newton's second law of mechanics. In this study, an isothermal, single Newtonian fluid with a constant density is considered (Sagaut, 2005).

3.2. Navier-Stokes Equations

The differential form of the Navier-Stokes and continuity equations is given below:

$$\frac{\partial u_i}{\partial t} + \underbrace{\frac{\partial}{\partial x_j}\left(u_i u_j\right)}_{\text{convection}} = -\underbrace{\frac{1}{\rho}\frac{\partial p}{\partial x_i}}_{\text{pressure}} + \underbrace{\nu \frac{\partial}{\partial x_j}\left(\frac{\partial u_i}{\partial x_j} + \frac{\partial u_j}{\partial x_i}\right)}_{\text{diffusion}} \qquad 3.1$$

and

$$\frac{\partial u_i}{\partial x_i} = 0. \qquad 3.2$$

Here p, t, ρ and v are and pressure, time, density and kinematic viscosity, respectively. u_i and x_i are the i^{th} velocity and coordination components. To fully resolve the unsteady Navier-Stokes equations for turbulent flow, all the spatial and temporal scales should be resolved. This means that the space and time scales Δx and Δt, respectively should be small enough to capture all of the fluid's dynamic behavior. According to Kolmogorov's (Pope, 2000) model the ratio of the largest to smallest scales can be estimated as $L/\eta = O\ (\mathrm{Re}^{9/4})$, where η and L are defined as the Kolmogorov's and the largest and smallest characteristic length scales, respectively.

Therefore, for a Reynolds number, based on the diameter of the cylinder, of Re = 500, the length scale ratio is $L/\eta \approx 1.18\times10^{6}$.

Although this number is manageable for low Reynolds number flows, for higher Reynolds numbers resolving all the time and length scales would require enormous grid and computational resources. Spatially filtered turbulence models such as large eddy simulation (LES) can provide a more viable approach for simulating high Reynolds number unsteady flows (Sagaut, 2005).

In LES, the large energy-containing scales of motion, which are responsible for most of the momentum transport, are resolved directly and the small-scale turbulent fluctuations are modeled (Wikstrom et al., 2004). In other words, in LES the effect of the large scales is directly computed while that of the small sub-grid scales is modeled. Since the small scales tend to be more isotropic than the larger ones, it should be possible to parameterize them using simpler and more universal models than standard Reynolds stress models (Germano et al., 1991).

3.3. The Filtered Navier-Stokes Equations

Filtering is used to divide the fluid motion into a large-scale component that can be calculated exactly and a smaller sub-grid scale component. The filtering operation is given by,

$$\bar{f}(x_i) = \int_{\Omega} f(x_i')\, G(x_i, x_i') dx_i' \qquad 3.3$$

where G is the filter function and Ω is the flow domain. Here $f(x)$ is the function of space, $\overline{f}(x)$ is the resolved/filtered function of space and x and x' are the coordinates. With this definition, the incompressible Navier-Stokes and continuity equations filtered with a spatial filter of characteristic width, Δ, can be written as follows:

$$\frac{\partial \overline{u}_i}{\partial t} + \frac{\partial}{\partial x_j}\left(\overline{u}_i \overline{u}_j\right) = -\frac{1}{\rho}\frac{\partial \overline{p}}{\partial x_i} + \nu \frac{\partial^2 \overline{u}_i}{\partial x_j \partial x_j} - \frac{\partial \tau_{ij}}{\partial x_j} \qquad 3.4$$

and

$$\frac{\partial \overline{u}_i}{\partial x_i} = 0. \qquad 3.5$$

Here, $\overline{u}_i$ and $\overline{p}_i$ are the resolved velocity components and pressure, respectively; the bar over the variable denotes filtering. In this case, the spatial filter uses a characteristic width, Δ, which is defined as the local grid scale.

The viscous stress tensor $\bar{\tau}_{ij}$ is defined as:

$$\bar{\tau}_{ij} = < u'v' > . \qquad 3.6$$

Using an eddy viscosity model (EVM) formulation, the Reynolds stress tensor can be written as a function of the local flow field as follows:

$$- < u'v' > = \nu_t \frac{\partial \bar{u}}{\partial x}. \qquad 3.7$$

Even though defining the cut-off point is a very difficult task, especially for a multi-dimensional complex flow field, the idea is to find a satisfactory and functional basis for the decomposition of the large scale eddies from the small scale ones.

3.4. Discrete Equations and Solution Method

In order to solve the partial differential equations governing the flow, these equations must be discretised and then numerically solved. Noting that for the Navier-Stokes equations, the elliptic character of the flow is assumed to be only due to the pressure and the other parts are considered to be of parabolic nature, Kim and Moin (1985) proposed a numerical method for computing three-dimensional, time-dependent incompressible flows, which is often referred to as the fractional-step method. The major difficulty in solving the Navier-Stokes equations arises from the fact that the continuity equation is not time-dependent. On the other hand, the momentum

equations involve both pressure and velocity fields as unknowns. To address the mentioned issues, an implicit coupling between the continuity and momentum equations is required.

The current code is based on a code inherited from Prof. Bergstrom's research group. A two-step fractional-step method is used to solve the filtered Navier-Stokes equations in terms of momentum and pressure steps.

The fractional-step method will be applied to the discrete Navier-Stokes and continuity equations, which were obtained following the finite-volume method. Using the finite-volume technique, the integral form of the governing equations is discretized and the geometrical information from the grid is incorporated directly into the discretization. The main advantage of the finite-volume method is that the grid transformations are not required in the numerical simulations (Mittal and Iaccarino, 2005). Also, finite-volume methods are used because of their general applicability to flows with complex geometries (Salvetti and Banerjee, 1995). Considering energy conservation, the finite-volume method would seem a logical choice because it is intrinsically conservative. A conservative finite-volume discretization of mass and momentum will not, however, guarantee conservation of kinetic energy (Ham et al., 2002). On the other hand, Wesseling and Oosterlee (2001) suggest that the motivation to use a finite-volume scheme is to conserve the mass locally.

In the thesis research, the finite-volume method is used to discretize the above equations on a non-uniform collocated grid. In the collocated grid all the variables are stored at the same set of grid points and an identical control volume is employed for all the variables. In this arrangement, since many of the terms in each of the equations are basically the same, the number of coefficients that must be computed and stored is minimized and the programming is simplified

by this choice. In addition, when multi-grid procedures are used, the same operators for transfer of information between the different grids can be used for all variables. The collocated arrangement also has important advantages in complex solution domains, especially when the boundaries have slope discontinuities or the boundary conditions are discontinuous (Ferziger and Peric, 1999).

Employing a second order fractional step method for solving the discrete form of the Navier-Stokes equations leads to the following set of equations:

$$\rho \frac{\overline{u}_i^* - \overline{u}_i^n}{\Delta t} = \frac{1}{2}\left[3H_i^n - H_i^{n-1}\right] + G_i \qquad 3.8$$

and

$$\rho \frac{\overline{u}_i^{n+1} - \overline{u}_i^*}{\Delta t} = -\overline{p}_{,i}^{n+1}, \qquad 3.9$$

where the operators H and G are the convection and diffusion terms and are defined as, $H_i = -\frac{\partial}{\partial x_j}\left(\overline{u}_i \overline{u}_j\right)$, and $G_i = \frac{1}{2}\nu \frac{\partial^2 \overline{u}_i}{\partial x_j \partial x_j} - \frac{\partial \tau_{ij}}{\partial x_j}$, where n indicates the time step and Δt is the discrete time interval between two time steps n and $n + 1$. It should be noted that using the semi-implicit Crank-Nicolson method half of the viscous term is made implicit and the second half is used as the source term. Also, $\overline{u}_i^*$ indicates an intermediate velocity computed from the momentum equation. The pressure field used in the second step of Eq. 3.9 includes a pressure

correction that assures the final n+1 field will conserve mass, which is explained in details in section 3.5.

A semi-implicit Crank-Nicolson method was used to solve the momentum equations. A TDMA (Tri-Diagonal Matrix Algorithm) solver is used to construct the main solver for the discrete equations. When it comes to accuracy and simplicity the second order semi-implicit Crank-Nicolson method is employed where:

$$\phi_i^{n+1} = \phi_i^n + \frac{\Delta t}{2} f\left(\phi_i^{n+1}\right) + \frac{\Delta t}{2} f\left(\phi_i^n\right). \qquad 3.10$$

where ϕ is a generic term. In this method the contribution from the previous time step is used as an additional source term (Ferziger and Peric, 2003).

In terms of spatial derivatives, in general a second-order central-difference method was used to discretize the equations. However, for a zero-turbulence intensity inflow and use of a relatively short flow domain, the cylinder obstruction was observed to cause an erroneous spatial variation in the approach flow upstream of the cylinder, which in turn triggered anomalies in the subgrid-scale stress. To resolve this numerical issue, a third-order QUICK scheme was used to provide enhanced dissipation in regions of high Peclet number upstream of the cylinder, where the Peclet number Pe = $u\Delta x/v$ indicates the local ratio of advection to diffusion. Since the QUICK upwind scheme is relatively diffusive, it was avoided in the near wake region. Furthermore, given that only one fictitious node is used on each side of the computational domain, near the outer walls the code switched back to the central-difference scheme. The result of this ad hoc use of the

QUICK scheme was that the erroneous spatial variations in the velocity field upstream of the cylinder were eliminated. For the temporal integration, the maximum CFL number was set to 0.8, where the CFL number is defined as CFL = $u\Delta t/\Delta x$. It should be noted that the CFL number, which represents a constraint based on convection, is not the only constraint for the time step, since the pressure and velocity components are coupled to each other due to the non-linear nature of the Navier-Stokes equations. Furthermore, in regions very close to the wall, the diffusion stability constraint can be more important than that due to convection.

The intermediate nodal velocity components were obtained by solving Equation 3.8. Since the flux velocities are required at the faces of the cell for solving Equation 3.9, a second-order interpolation scheme is used to compute the flux velocities at the face locations. It should be noted that the computed flux values do not necessarily satisfy the continuity. Therefore in a fractional-step method, the next step would be to correct the velocity based on pressure information. In the present code, a pressure correction equation was used which ensured mass conservation at each time step, to replace the fractional step given in Equation 3.9. The pressure correction equation was solved using a multi-grid method with a control strategy, as described below.

3.5. Pressure-Correction Method

A representative control volume is shown in Figure 3.1, together with the flux velocities defined at the faces of the control volume. Using the finite-volume method (FVM) to discretize the continuity equation on a non-uniform collocated grid gives

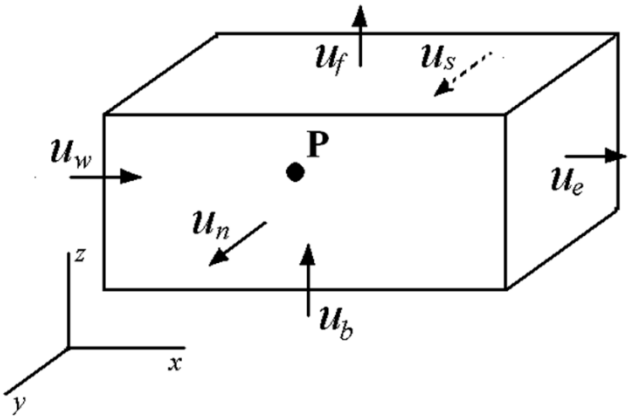

Figure 3.1: Sketch of a control volume.

$$(\overline{u}_e - \overline{u}_w)A_x + (\overline{u}_n - \overline{u}_s)A_y + (\overline{u}_f - \overline{u}_b)A_z = 0, \qquad 3.11$$

where the areas of the control volume faces are given by $A_x = \Delta y \times \Delta z$, $A_y = \Delta x \times \Delta z$ and $A_z = \Delta x \times \Delta y$. Here $\overline{u}_e, \overline{u}_w, \overline{u}_n, \overline{u}_s, \overline{u}_f, \overline{u}_b$ are the resolved velocity components at the east, west, north, south, front and back faces, respectively. As mentioned above, the intermediate velocity u^* obtained from the solving the first fractional step does not necessarily satisfy continuity. Instead, a pressure correction will be implemented in order to ensure mass conservation. The development of the pressure correction methodology is described below.

For the collocated grid arrangement, the face velocities can be approximated in terms of the nodal velocities, e.g. for the east flux velocity one obtains

$$\overline{u}_e^* = \frac{\Delta x_i \overline{u}_E^* + \Delta x_{i+1} \overline{u}_P^*}{\Delta x_{i_e}} + \frac{A\Delta t}{\rho \Delta V}(\overline{p}_E - \overline{p}_P). \qquad 3.12$$

In this equation, upper case subscriptions are used to represent the nodal velocity at the center of a cell, while lower case scripts are used to represent the face velocity. Note that face velocities as defined above do not guarantee mass conservation for the cell. To ensure mass conservation,

the face values should be adjusted by adding a correction based on a pressure correction field, p', i.e.

$$\bar{u}_e = \bar{u}_e^* + \frac{A_x \Delta t}{\rho \Delta V}\left(\bar{p}'_P - \bar{p}'_E\right). \qquad 3.13$$

From continuity:

$$\bar{u}_e A_e - \bar{u}_w A_w + \bar{u}_n A_n + \bar{u}_s A_s + \bar{u}_f A_f + \bar{u}_b A_b = 0. \qquad 3.14$$

Substituting Equation 3.13 and the corrections to the other five face velocities into Equation 3.14 gives the following equation

$$a_P \times \bar{p}'_P = a_E \times \bar{p}'_E + a_W \times \bar{p}'_W + a_N \times \bar{p}'_N + a_S \times \bar{p}'_S + a_F \times \bar{p}'_F + a_B \times \bar{p}'_B + b, \qquad 3.15$$

where, for an orthogonal grid, $a_E = a_W = \frac{A_X^2 \Delta t}{\Delta V}$, $a_N = a_S = \frac{A_Y^2 \Delta t}{\Delta V}$, $a_F = a_B = \frac{A_Z^2 \Delta t}{\Delta V}$, $a_P = a_E + a_W + a_N + a_S + a_F + a_B$ and $b = -\rho\left[A_X\left(\bar{u}_e^* - \bar{u}_w^*\right) + A_Y\left(\bar{u}_n^* - \bar{u}_s^*\right) + A_Z\left(\bar{u}_f^* - \bar{u}_b^*\right)\right]$.

After the p' field is obtained by solving Equation 3.15, the nodal pressure field is updated as

$$p^{n+1} = p^n + p'. \qquad 3.16$$

The updated (corrected) pressure field is used to complete the second fractional-step equation and obtain the new velocity field. Therefore, Equation 3.13 is rewritten as

$$\bar{u}_e^{n+1} = \bar{u}_e^{n+1} \times (1-f) + \left[\bar{u}_e^{*} + \frac{A_x \Delta t}{\rho \Delta V} (\bar{p}'_P - \bar{p}'_E) \right] \times f, \qquad 3.17$$

where f is the relaxation factor and $0 < f < 1$.

Note that the pressure correction equation is typically a discrete Poisson equation, which is well-known for its critical role in the overall solution algorithm, due to the high computational cost of solving it. Therefore, a multi-grid strategy, along with an alternating direction implicit (ADI) solver based on a TDMA, was used for solving the pressure correction equation, as described below.

3.6. Multi-Grid Approach

The main computational challenge in solving the above equations relates to the pressure correction equation. Since it is an elliptic equation, a change at one location influences the entire domain. As the grid becomes larger, this elliptic coupling becomes problematic and slows down the solver. To accelerate the performance of the pressure solver, a four-level multi-grid method had been adapted into the present code, where the local agglomeration of a finer grid is used for creation of the coarser grid. The pressure-correction equation was solved by employing the multi-grid approach to accelerate a basic iterative solution process through adequate coarse grid corrections. The main advantage of the multi-grid approach is that it is has the unique potential of solving numerous kinds of mathematical problems with N unknowns with O(N) work (Wesseling and Oosterlee, 2001). In geometric multi-grid, which had been adapted into the code, coarse grids are constructed from the given fine grid, and coarse grid corrections and

coefficients are computed using discrete systems constructed on the coarse grids (Wesseling and Oosterlee, 2001).

It was observed that after the solution becomes stable, a four-level-controlled W cycle functions in a similar way to a non-controlled V cycle, where the solution uses the regular hierarchy of grids and each coarse grid is composed of eight adjacent control volumes. As shown in Figure 3.2, the solution starts from the finest grid, with a spacing of h, and then the solution is transferred to the next coarse grid for which the spacing is $2h$. This procedure is called *smoothing* or *restriction*. After this procedure is repeated a number of times and the equations are solved at the coarsest grid level, the solution proceeds upward by local subdivision of the coarse grids to the finer ones. This procedure is called *prolongation*.

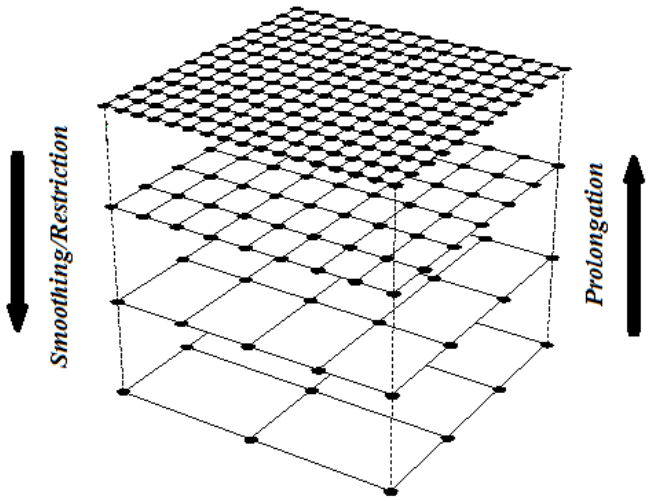

Figure 3.2: The schematics of a four level multi-grid approach (Computation and Information System Library's website).

Since a structured grid was used to discretize the solution domain, making coarse grids from fine grids by agglomeration of fine grid cells was relatively straightforward. However, since the square cylinder was a solid obstacle located in the interior of the solution domain, special care

had to be taken to ensure that on all grid levels, the fluid cells remained separated from the solid cells. For solid cells, the pressure correction coefficients were set to predict a constant value (of zero), and these values were not used in correcting the velocity components at the faces of the cylinder or just interior to the face. The boundary absorption approach was employed for the solid walls of the square cylinder and the residuals were set to zero for the (internal) cells inside the solid body/ square cylinder.

The computational effort required for one complete inner cycle using a multi-grid method consisting of a four-level V cycle can be estimated as $2\times 1+1\times\left(\frac{1}{2}\right)^3+1\times\left(\frac{1}{4}\right)^3+10\times\left(\frac{1}{8}\right)^3\approx 2.16$, where the value of 1 is used to indicate the computational effort for a single solution on the fine mesh. Considering the fact that smoothing in each level reduces the computational cost by half, in three directions, this number would be $(1/2)^3$. Figure A.7 of Appendix A shows the sequence and the number of occurrence at each grid level.

In Appendix B, the performance of a multi-grid approach is studied in detail for both high-resolution and low-resolution grids, and the results are compared to the base solver solution for a flow around a wall-mounted square cylinder of AR = 3 and Re = 500. Based on the maximum residual rates for a coarser grid of 64 × 72 × 48, the multi-grid scheme is 100/(17×2.16) = 2.29 times more efficient than the base solver. Since, in the TDMA scheme, the information travels one grid per sweep iteration, the number of iterations is linearly proportional to the number of nodes in each coordinate (Ferziger and Peric, 2002). However, all iterative solvers converge more slowly on finer grids and this number should be higher for a finer grid. The comparison

indicates that not only is the residual reduction rate larger for the coarser grid, the base solver performs much more quickly on the coarse grid. Although the residual magnitudes are different for fine and coarse grids, both the base solver and multi-grid residuals follow the same pattern. Interestingly, even after 100 iterations with a multi-grid approach for a fine grid the residual reduction has not stopped and further calculations may improve the solution.

Based on the maximum residual rates for a 128 × 144 × 96 grid, the multi-grid scheme is 100/(10×2.16) = 4.63 times more efficient than the base solver. This demonstrates that as the grid size increases, the benefit of using a multi-grid scheme increases

3.7. Large Eddy Simulation Schemes

Recalling the filtering procedure inherent to LES, although Equation 3.4 resembles the Reynolds Average Navier-Stokes (RANS) equation for the mean flow, the SGS tensor contained in this equation is significantly different from the Reynolds stress tensor. The SGS tensor in large eddy simulations deals with rapidly fluctuating fields in space and time, provided Δx and Δt are sufficiently small (Lesieur and Metais, 1996). In contrast, the Reynolds stress represents the entire contribution of the turbulent motions, both large- and small-scale, to the mean momentum balance.

Note that in the filtered Navier-Stokes equations, the filtered product of the velocity components is replaced by the product of the filtered velocity components, and these are not equal, i.e.

$$\overline{u_i u_j} \neq \overline{u_i}\ \ \overline{u_j}. \qquad 3.18$$

Instead, their difference is represented by the sub-grid scale stress tensor, i.e.

$$\tau_{ij} = \overline{u_i u_j} - \overline{u_i}\ \ \overline{u_j}. \qquad 3.19$$

As in the case of some RANS models, many SGS models are expressed in terms of an eddy viscosity model of the form

$$\tau_{ij} - \frac{1}{3}\delta_{ij}\tau_{kk} = -2\nu_t \bar{S}_{ij}\,. \qquad 3.20$$

Here τ_{ij} and S_{ij} are the SGS stress and strain rate tensors, respectively, ν_t is the SGS viscosity and δ_{ij} is the Kronecker delta. The most popular SGS model is the Smagorinsky model which is based on Prandtl's mixing-length theory (Lesieur et al., 2005). Based on Prandtl's theory the eddy viscosity is a function of the mixing length, representing a local turbulent length scale, multiplied by a turbulent velocity scale. In the same way, Smagorinsky proposed that for LES, the SGS eddy viscosity be proportional to the local grid scale, Δx, multiplied by a SGS velocity scale (Lesieur et al., 2005), $\Delta x\,|\bar{S}|$, so that

$$\nu_t = (C_S \Delta x)^2 \left|\bar{S}\right|, \qquad 3.21$$

where $\overline{S}_{ij} = \frac{1}{2}\left(\frac{\partial \overline{u}_i}{\partial x_j} + \frac{\partial \overline{u}_j}{\partial x_i}\right)$ is the resolved rate-of-strain tensor, $\left|\overline{S}\right| = \left(2\overline{S}_{ij}\overline{S}_{ij}\right)^{\frac{1}{2}}$ is its magnitude, and C_s is a model coefficient. Then, the form of the SGS stress becomes

$$\tau_{ij}^{*} = \tau_{ij} - \frac{1}{3}\delta_{ij}\tau_{kk} = -2C_S\overline{\Delta}^2 \left|\overline{S}\right| \overline{S}_{ij}, \qquad 3.22$$

where the superscript * denotes a traceless form of the tensor. In this study, for the standard Smagorinsky model the value of the coefficient C_s was set to 0.1 (Frohlich and Rodi, 2004).

The Smagorinsky SGS model has a number of deficiencies. First, the Smagorinsky constant, C_S, must be adjusted for different flows. Second, the model is often observed to be overly dissipative (Murakami et al., 1999). Third, the model does not inherently reduce to zero in near-wall regions where the turbulence is strongly damped. For the current flow, a van Driest damping function was employed near the ground plane and the cylinder walls as follows:

$$f_\mu = C_S\Delta\left(1 - \exp\left(\frac{-y^+}{25}\right)^3\right)^{1/2} \qquad 3.22$$

where $y^+ = \frac{u^* y}{\nu}$, and $u^* = \sqrt{\tau_w / \rho}$ (Frohlich and Rodi, 2004). This required that the local wall shear stress be estimated from the velocity component parallel to the wall at the first computational node near the wall.

To overcome the limitations of the Smagorinsky model, several other models have been proposed. Among them is the so-called dynamic Smagorinsky model (DSM) which was first

introduced by Germano et al. (1991) and then revised by Lilly (1992). In the DSM, the coefficient C_S is determined as a variable of space and time, utilizing two filters with different characteristic scales: a grid filter and a test filter. This treatment of C_S is designed to enable the model to naturally adapt to laminar and near-wall flows. However, just as for the multi-grid scheme, in designing the grid used for the test filter, care had to be taken to ensure that cells with solid and fluid were not combined.

Although the DSM has significant advantages over the SM, it still needs further improvement. One of the main problems with the DSM is the potential for large fluctuations of the value of C_S, which can then lead to divergence. For cases such as fully developed channel flow, plane averaging is typically employed to remove the large fluctuations; however, for inhomogeneous unsteady flow, such as flow around bluff bodies, this method will not work. Instead, in this simulation an upper limit was set to constrain the fluctuation of C_S and local volume-averaging was also implemented to obtain a robust model. Frohlich and Rodi (2004) showed that for a cylinder flow the DSM is sensitive to the grid size and yields a smaller recirculation zone for coarser grids. In the near-wake region, the DSM is expected to perform better than the Smagorinsky model.

The main drawback of the conventional methods like SM and DSM is that in these models a strict alignment between the τ_{ij} and S_{ij} tensors is required (Wang and Bergstrom, 2005). To resolve this issue, a non-linear model is proposed which involves a finite number of tensorial terms.

The Dynamic Smagorinsky and Non-linear Dynamic models are described in detail in Appendices B and C, respectively.

3.8. Boundary Conditions

Recall that the flow geometry being considered is a surface-mounted finite square cylinder immersed in a uniform stream flowing over a ground plane. Initially a uniform velocity profile without any turbulence was prescribed at the inlet following the approach of Frohlich and Rodi (2004). It was observed that employing a uniform velocity profile at the inlet produces high residual areas at the intersection of the ground plane and the inlet, which then decelerates the pressure solver's performance. To remedy this problem, a thin laminar boundary layer was implemented at the inlet.

Due to the presence of a boundary layer near the ground plane and also the disturbance originating from the wake region behind the square cylinder, specifying the outlet boundary conditions was more challenging. For nodal velocity components, a convective boundary condition was implemented as follows,

$$\frac{\partial \overline{u_i}}{\partial t} + U \frac{\partial \overline{u_i}}{\partial x} = 0, \qquad 3.24$$

where U was the local flux velocity. In addition, mass conservation was enforced on the flux velocities.

No-slip boundary conditions were implemented on the walls of the cylinder and on the ground plane. Slip boundary conditions were imposed on the side walls as well as the top wall of the domain. Due to the limited distance between the inlet plane and the square cylinder, and given the use of a laminar boundary layer inflow, the resulting boundary layer thickness (δ) on the

ground plane at the location of the cylinder was thin relative to the cylinder width and height, i.e. $\delta / D < 0.3$.

Flags were set to distinguish the solid nodes from the fluid ones. The coefficients in the different transport equations were set to calculate zero velocity and zero pressure for the solid nodes, except for the first layer of the nodes which were used as ghost nodes to implement the no-slip boundary conditions on the walls of the cylinder. For the nodes located in the corners of the cylinder two or even three different values were implemented, depending on the velocity component being considered.

3.9. Numerical Grid

Hyperbolic-tangent functions were used to create a non-uniform grid. The grid was refined in both the spanwise and wall normal directions near the corners of the square cylinder (Figure 3.3 and Figure 3.4). In the current study two levels of resolution were used to discretize the fluid domain: a coarser grid consisting of 64 × 72 × 48 (221,184) control volumes and a finer grid consisting of 128 × 144 × 96 (1,769,472) control volumes, as shown in Figures 3.3 and 3.4.

The domain size was chosen based on other numerical studies such as Frohlich and Rodi (2004) and through various preliminary studies it had been ensured that flow structure in the wake region is not affected by the domain boundaries.

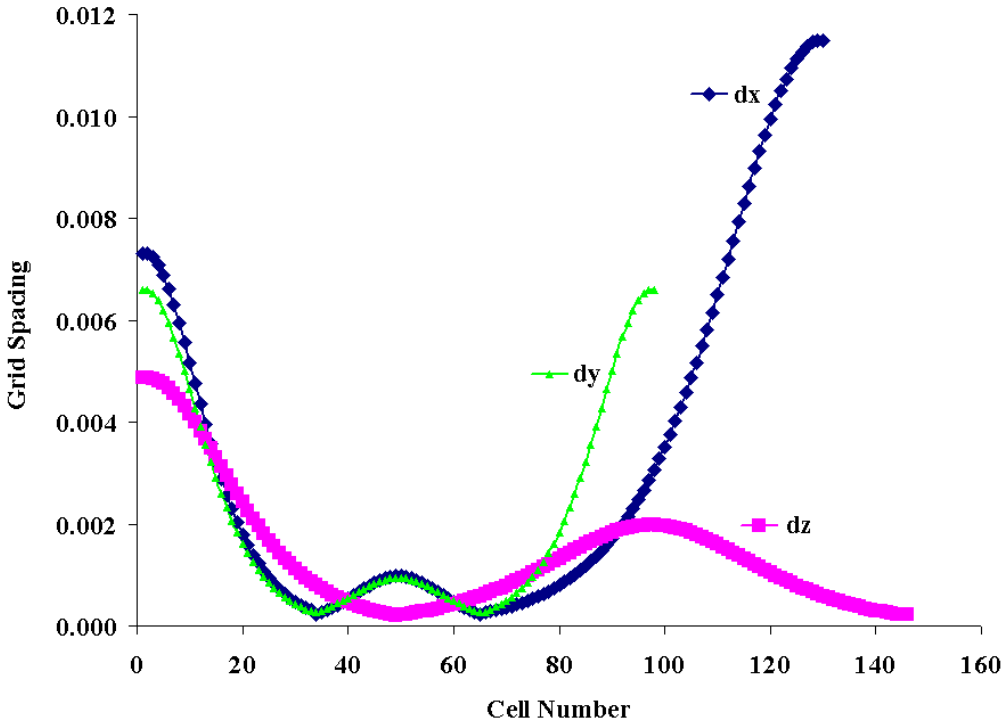

Figure 3.3: Grid spacing of a computational domain for a square cylinder of AR = 5.

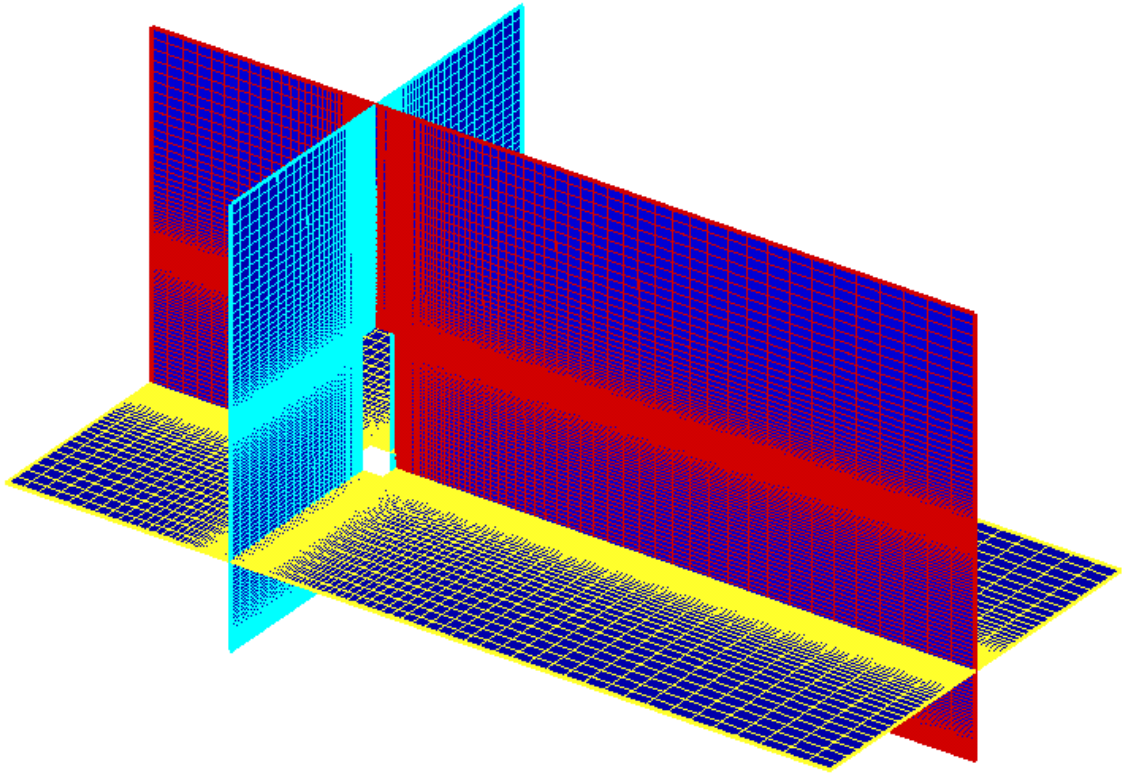

Figure 3.4: Three dimensional cuts of the computational domain for a flow over a square cylinder of AR = 5.

The numerical method and SGS models have been validated by previous simulation of channel flows. All of the mean flow patterns – e.g. streamlines – and other quantities such as St number are qualitatively and even quantitatively consistent with the limited results available for comparison. This will become apparent in the next chapters which discuss the simulation results.

3.10 Clock Time

Setting a CFL number of 0.8 imposed a limiting time-step of $\Delta t \sim 2\times10^{-4}$ for the fine grid solutions. Consequently for a grid of higher resolution at least two to three weeks were required for the completion of one shedding cycle. To achieve a time-averaged flow field, simulations were carried out for at least 20 shedding cycles. To obtain the time-averaged data, the flow had to reach the fully developed state first, meaning that the flow had to grow out of the initial uniform condition and its effects on the flow domain had to subside. This procedure imposed additional run time for the solution.

3.11. Discussion

The main computational challenge in simulating the flow over a finite-height square cylinder involved the solid obstacle, inlet and outlet boundary conditions and the LES models. The coefficients in the different transport equations were set to calculate zero velocity and zero pressure for the solid nodes, except for the first layer of the nodes which were used as ghost nodes to implement the no-slip boundary conditions on the walls of the cylinder. For the nodes located in the corners of the cylinder two or even three different values were implemented, depending on the velocity component being considered.

Due to the erroneous spatial variation near the sharp corners of the square cylinder, a QUICK scheme was added into a general second-order central-difference method. As for the multi-grid scheme, in designing the grid used for the test filter, solid and fluid cells were kept separated. Similar to the multi-grid scheme, employing a pressure correction method, the fluid cells were also kept separated from the solid cells. Implementing the DSM and DNM for a flow around bluff body, a three-dimensional filtration was applied instead of a plane averaging technique which was prescribed for the channel flow. An upper limit was set to constrain the fluctuation of C_S and local volume-averaging was also implemented to obtain a robust model. Implementing a Smagorinsky method, a damping function was employed near the ground plane and the cylinder walls.

Since employing a uniform velocity profile at the inlet produced high residual areas at the intersection of the ground plane and the inlet, instead a thin laminar boundary layer was implemented at the inlet. For nodal velocity components, besides implementing a convective boundary condition the mass conservation was enforced on the flux velocities.

Chapter 4

Time-Averaged Velocity Field for a Flow over a Finite-height Square Cylinder of AR = 5

4.1. Introduction

In this chapter the time-averaged flow field over a wall-mounted finite-height square cylinder of AR = 5 is investigated numerically. The cylinder was mounted on a ground plane and immersed in a thin laminar boundary layer with $\delta/D = 0.01$ at the inlet plane. Note that given the short development length upstream of the cylinder, the boundary layer thickness at the location of the cylinder is about $\delta/D \sim 0.3$.

The solution domain extended 5.5D upstream and 14.5D downstream of the cylinder (in the x direction). The total cross-stream extent of the solution domain was 10D and the height (in the z-direction) of the flow domain was set to be twice the height of the cylinder (2H). A 128 × 144 × 96 non-uniform collocated grid was used to discretize the domain. To resolve the boundary layers on the cylinder surfaces, the grid was refined in both the cross-stream (y) and wall-normal (z) directions near the corners of the square cylinder using hyperbolic-tangent functions. Frohlich and Rodi (2004) used the solution domain of 7.5D upstream and 12.5D downstream with the total cross-stream extent of 10D for a flow over a finite-height circular cylinder of AR = 2.5 and $Re = 4.3\times10^4$. For AR = 6, Krajnovic (2011) selected a much larger solution domain of 8D upstream and 19D downstream with the total cross-stream extent of 24D for a flow over a finite-height circular cylinder for $Re = 2.0\times10^4$.

The time-averaged quantities were obtained for at least five complete flow-through cycles. Time signals of the velocity field predicted by the DSM recorded at three points over 10,000 time-

steps were used to calculate the vortex shedding frequency and the number of vortex shedding cycles.

The Reynolds number was set to Re = 500 based on width of the cylinder D and the free stream velocity U. Streamlines and both velocity and vorticity contours are presented at various planes to investigate the features of the time-averaged flow. Iso-surfaces of the 2nd invariant of the velocity gradient tensor are also used to visualize vortices.

4.2. Flow Structure

The first set of figures will describe the flow in the near-wake region directly behind the cylinder in terms of contour plots based on the time-averaged velocity and vorticity fields. Attention will be focused on the vertical symmetry plane (x-z plane at y/D = 0) as well as multiple horizontal planes located at different heights above the ground plane.

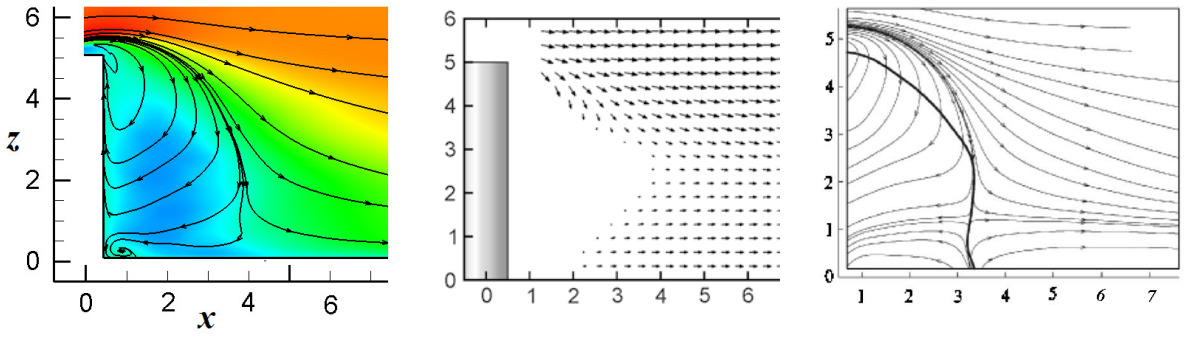

Figure 4.1: Time-averaged velocity field along the wake centre-line y/D = 0; a) LES solution, b) Sumner et al. (2004) for a circular cylinder at Re = 6×10^4, c) Wang et al. (2006) at Re = 1.15×10^4.

Figure 4.1 presents the time-averaged velocity field in the wake along the centreline (y/D = 0). Figure 4.1(a) shows the time-averaged streamwise velocity contours and streamlines obtained from the numerical prediction for the resolved-scale field. Figure 4.1(b) presents the time-

average velocity vectors obtained by Sumner et al. (2004) for a wall-mounted finite circular cylinder for AR = 5 and Re = 6×10^4, using a seven-hole pressure probe, for a much thicker approach flow with a boundary layer thickness of δ/D = 2.6. In Figure 4.1(b) the triangular shaped region of recirculating flow is indicated by the absence of velocity measurements. Figure 4.1(c) shows the time-averaged streamlines obtained by Wang et al. (2006) for flow around a finite square cylinder of AR = 5 for a much higher Reynolds number, Re = 1.15×10^4 and also a relatively thin boundary layer of δ/D = 0.07.

All three cases indicate a strong downwash originating from the free end. A weaker upwash is observed near the ground plane. The streamwise extent of the recirculation zone is similar for all three cases: approximately 3.75D for the numerical solution, 3.5D for Sumner et al. (2004) and 4D for Wang et al. (2006). The measurements of Wang et al. (2006) show a slightly stronger upwash compared to the LES solution.

Recall that a saddle point is defined as a point where four tangent curves meet. Generally in a flow over a finite-height cylinder the saddle point results from interaction of the upwash and downwash flows. Where iso-surfaces enclose a region of flow a focal point is formed (Smits and Lim, 2000). The streamline patterns for both saddle and focal points are sketched in Figure 4.2. While a focal point corresponds to a region of vorticity, the saddle point indicates approximately irrotational flow. In Figure 4.1(c), the saddle point (the interaction point of downwash and upwash flow) is located at about 1.2D from the ground plane, while for the LES solution the saddle point is located at about 1D. At the cylinder-wall junction in the LES field, a focal point associated with the upwash flow was observed. Although this focal point is not reported by the

experimental studies, both Afgan et al. (2007) and Salvador et al. (2009) observed a focal point near the cylinder-wall junction for a finite-height circular cylinder.

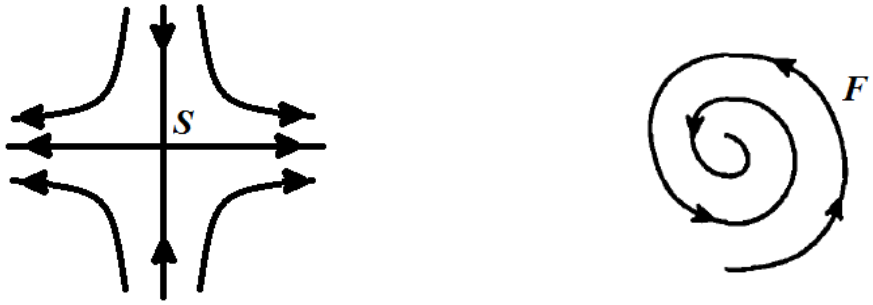

(a) (b)

Figure 4.2: Critical points: a) Saddle point, b) focal point (Smits and Lim, 2000).

4.3. Time-Averaged Velocity Contours in Center Plane

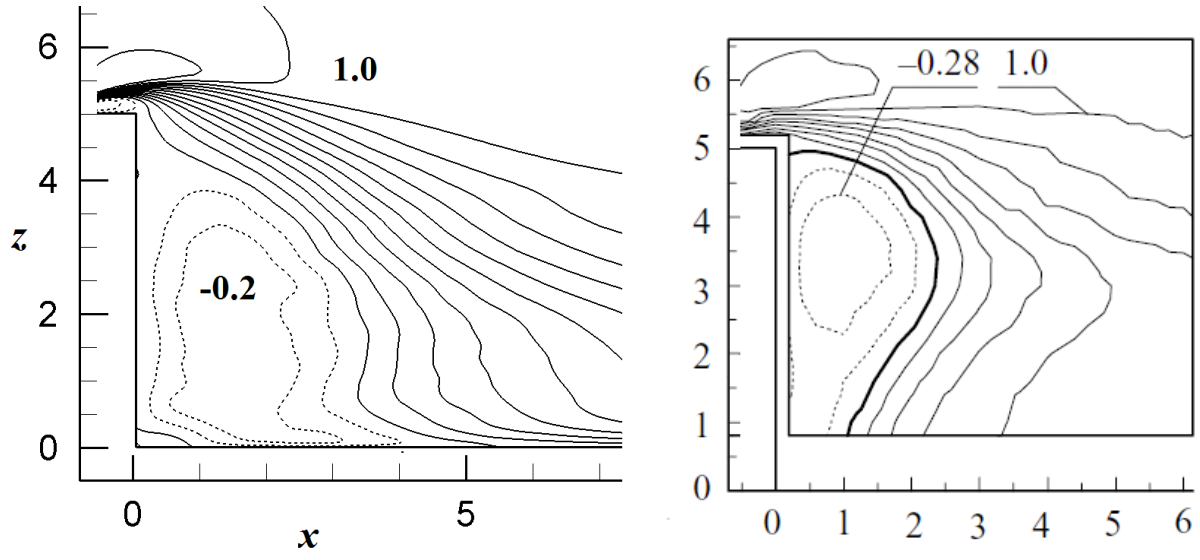

(a) (b)

Figure 4.3: Time-averaged streamwise velocity contours u/U_∞, solid lines: positive values, dashed lines: negative values: a) LES solution at Re = 500 and δ/D = 0.3 with contour increments of u/U_∞ = 0.1, b) Wang et al. (2009) at Re = 9300 and δ/D = 1.35.

Figure 4.3 compares contours of the time-averaged streamwise velocity component obtained from the LES solution to the experimental measurements of Wang et al. (2009) for flow over a wall-mounted cylinder with a much thicker boundary layer thickness of δ/D = 1.35 and a higher

Reynolds number of Re = 9300. Their measurements indicate the recirculation zone is displaced upward toward the tip of the cylinder and is relatively narrow near the ground plane. In contrast, for the LES results, the recirculation zone is displaced down toward the ground plane and remains relatively thick near the cylinder base. This difference may be due to the relatively thin boundary layer characterising the LES study (δ/D = 0.3 laminar boundary layer vs. δ/D = 1.35 turbulent boundary layer for Wang et al. 2009).

Figure 4.4 compares the time-averaged normal velocity contours obtained from the LES solution to the experimental measurements of Wang et al. (2009). Near the free end, the numerical solution is in good agreement with the experimental results. Near the ground plane, however, the normal velocity contours are different. The experimental measurements which are for a flow with a thicker boundary layer of δ/D = 1.35 indicate significant upwash, while the numerical solution predicts a weaker upwash effect which is restricted to the region of the ground plane and rear surface of the cylinder. Both Figures 4.3 and 4.4 suggest that the boundary layer thickness on the ground plane affects the upwash flow, more specifically where a thicker boundary layer is present, the upwash becomes stronger.

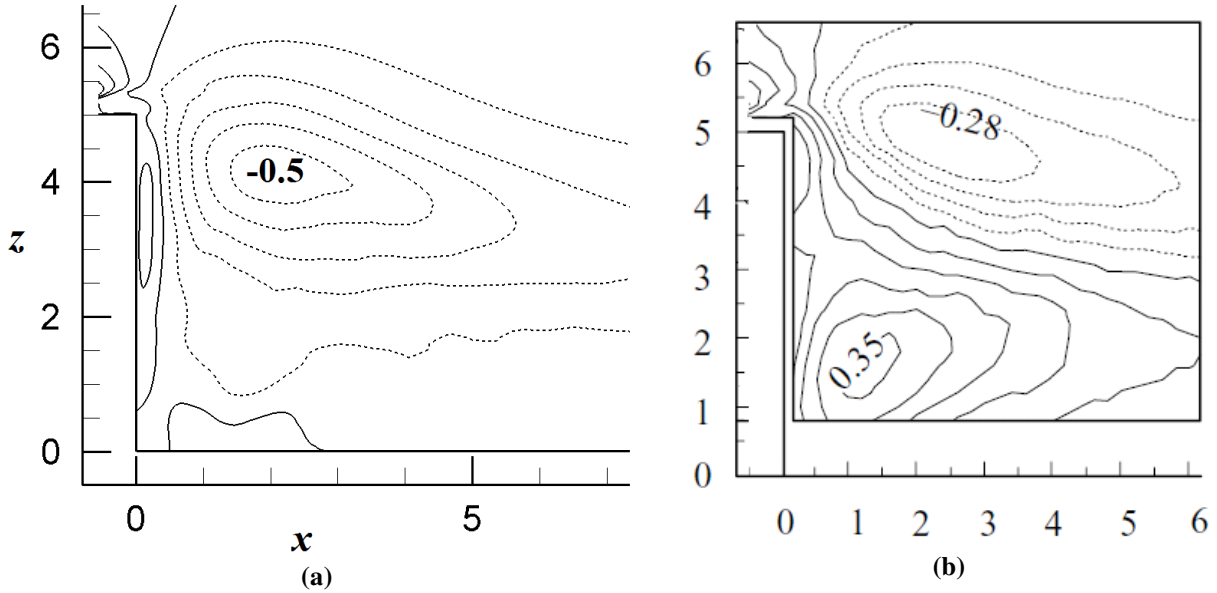

Figure 4.4: Time-averaged normal velocity contours w/U_∞, solid lines: positive values, dashed lines: negative values: a) LES solution at Re = 500 and δ/D = 0.3 with contour increments of w/U_∞, = 0.1, b) Wang et al. (2009) at Re = 9300 and δ/D = 1.35.

4.4. Variation of Wake along Cylinder Height

Figure 4.5 shows the time-averaged streamlines on the rear wall, side wall and top of the half-cylinder, as well as the ground plane and centre plane. The streamline patterns on the ground plane and also on the walls of the cylinder can be used to obtain insight into the flow structures within the wake. On the ground plane, upstream of the front wall of the cylinder, the horseshoe vortex is formed. The flow just above the ground plane is deflected outward by the cylinder, and then turns back, moving upstream and toward the center plane of the wake.

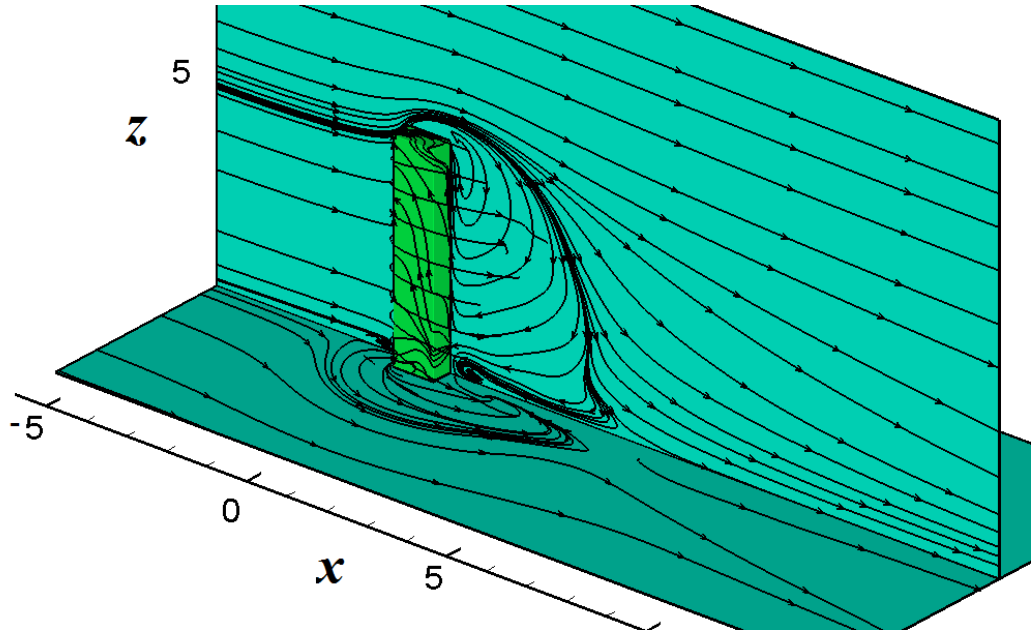

Figure 4.5: Time-averaged streamlines showing structure of wake.

Streamlines in the centerplane indicate a strong downwash originating from the free end. The streamlines on the front wall of the cylinder show a saddle point located at about $z/D = 1$ from the ground plane. Even near the ground plane, the downwash flow is dominant. The streamlines at the top wall tend to curve, as the flow is pulled towards the side edges. This might be an indication of separation of the tip vortices near the free end of the cylinder and stretching of in the spanwise direction.

Transverse profiles of the time-averaged streamwise velocity component in the wake behind the finite-height square cylinder are presented in Figure 4.6.

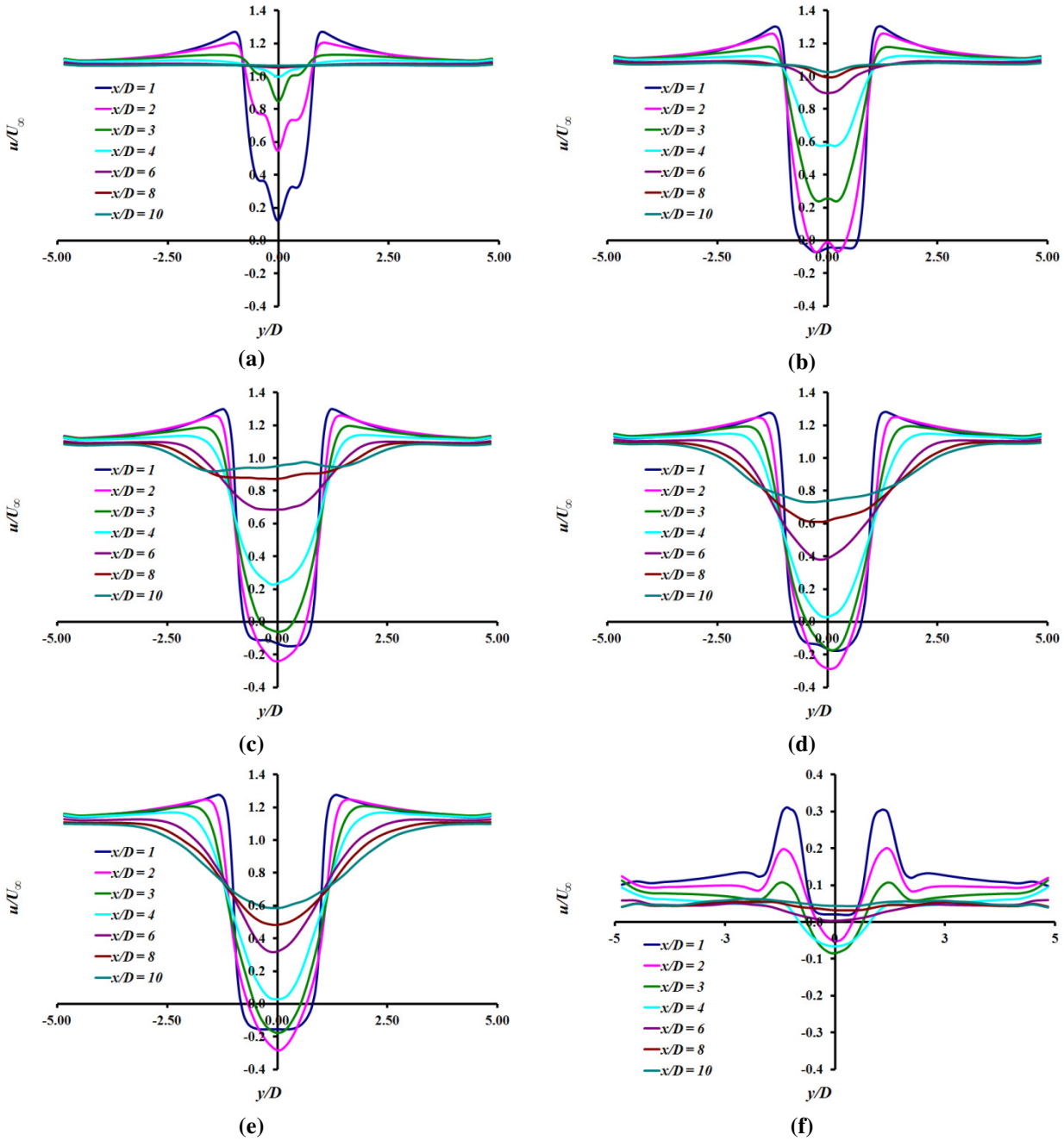

Figure 4.6: Time-averaged streamwise velocity components u/U_∞ obtained at a): z/D = 5, b) z/D = 4, c) z/D = 3, d) z/D = 2, e) z/D = 1, and f) $z/D \sim 0$.

For each figure, a series of profiles is presented, beginning at x/D = 1 and extending downstream to x/D = 10. Note that for most vertical locations, near the cylinder the velocity component becomes negative at the centreline, indicating a recirculation zone. Close to the cylinder, one also observes accelerated flow just outside the cylinder sidewalls. Overall, Figure 4.6 indicates a

larger velocity deficit in the central wake region compared to the tip region. As seen in Figure 4.6, the recirculation zone generally expands laterally as the flow descends towards the ground plane.

One of the characteristics of a finite cylinder is that the wake structure changes significantly from the tip to the base of the cylinder. In the next set of figures, the flow structure in the wake will be explored using six different horizontal planes, i.e. at z/D = 5, 4, 3, 2, 1, and 0, where the zero plane is just above but on the ground plane. Figure 4.7 shows the streamlines of the time-averaged velocity field in the wake. Since the time-averaged velocity field is symmetric, only half of the domain is shown in Figure 4.7.

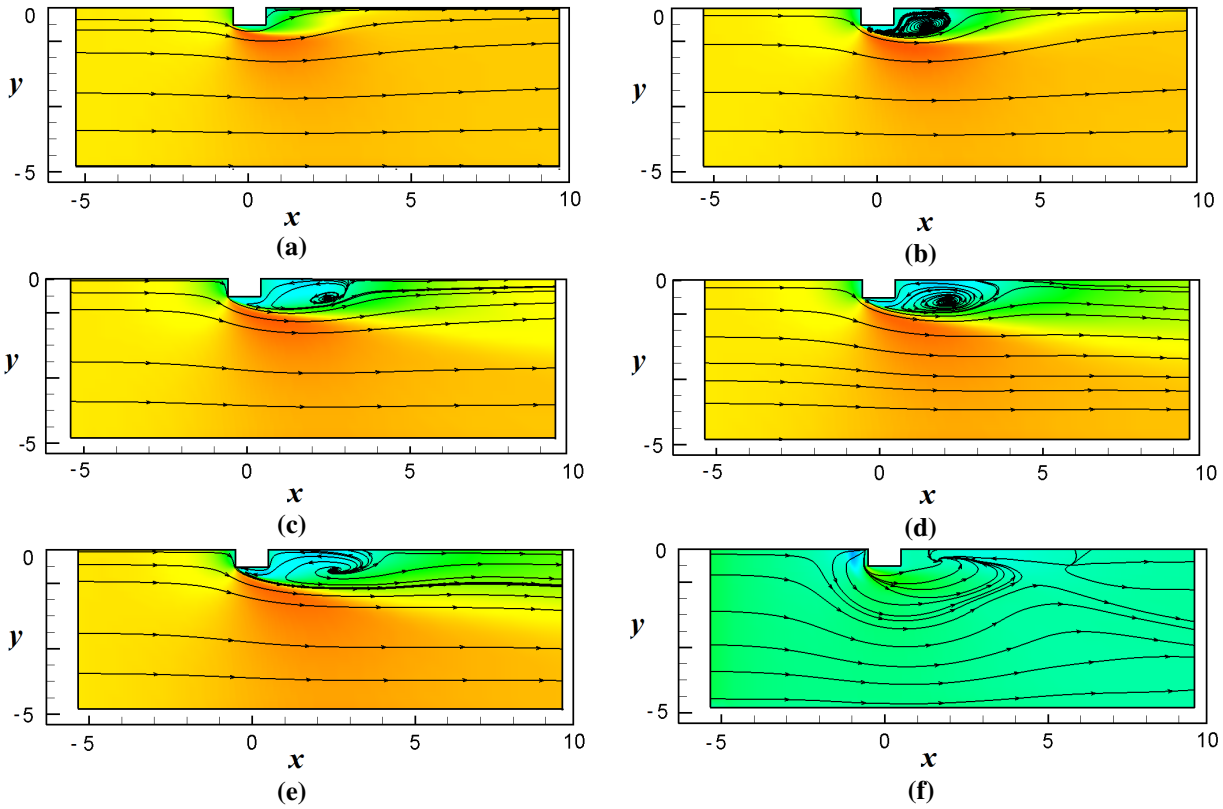

Figure 4.7: Time-averaged streamlines and streamwise velocity contours u/U_∞: a) z/D = 5, b) z/D = 4, c) z/D = 3, d) z/D = 2, e) z/D = 1, and f) z/D ~ 0.

Based on Figure 4.7(a), near the free end minimal vortex structure is observed. At z/D = 4, Figure 4.7(b), a small recirculation zone is formed. Further from the free end, the recirculation zone grows larger as the flow approaches the ground plane. Although the size of the recirculation zone remains almost the same moving from z/D = 3 in Figure 4.7(c) to z/D = 1 in Figure 4.7(d), the shape and the location of the recirculation zone has changed. At both z/D = 3 and z/D = 1, the center of the recirculation zone is closer to the edge of the wake region and the free stream. At z/D = 2, the recirculation zone is slightly larger and is located nearer to the centreline of the wake region. In Figure 4.7(f) at $z/D \sim 0$, the flow is observed to move away from the front surface of the cylinder.

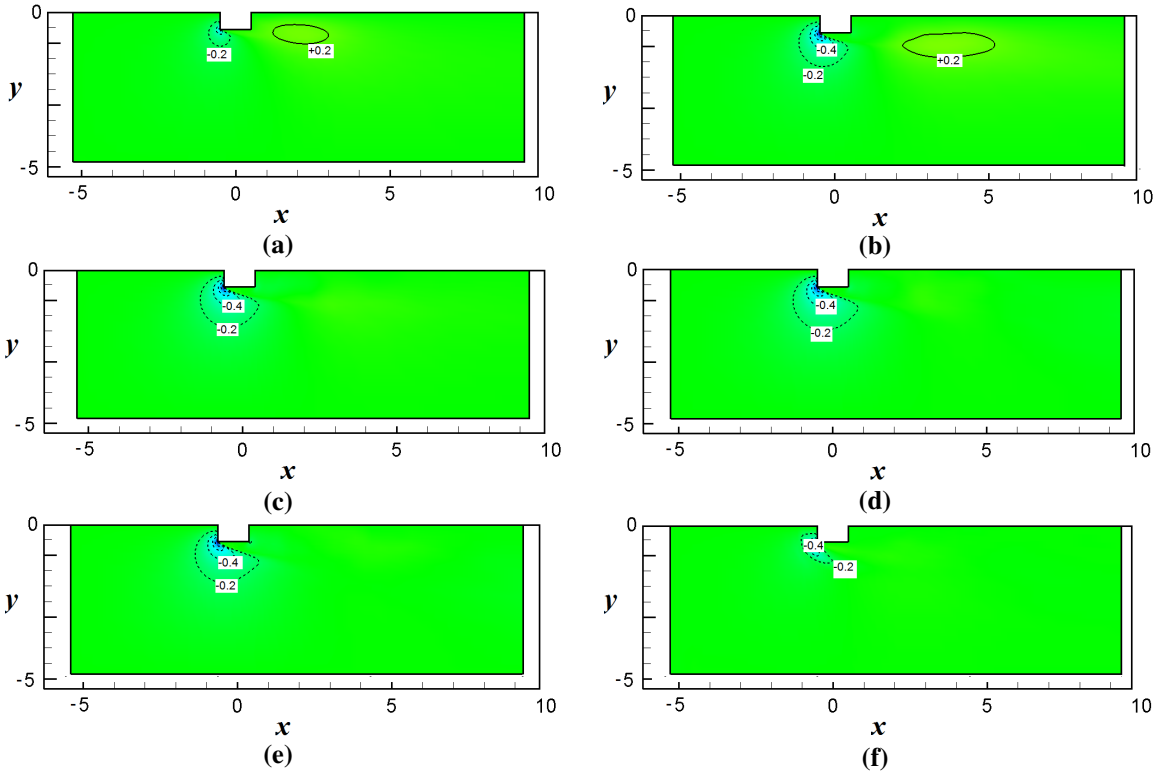

Figure 4.8: Time-averaged lateral velocity contours v/U_∞ with a contour increments of v/U_∞ = 0.2, solid lines: positive values, dashed lines: negative values: a) z/D = 5, b) z/D = 4, c) z/D = 3, d) z/D = 2, e) z/D = 1, and f) $z/D \sim 0$.

Figure 4.8 shows the time-averaged lateral velocity contours. At the front corners of the square cylinder the lateral velocity component is strongest. The lateral velocity reaches its maximum

value at z/D = 3 and 2, Figures 4.8(c) and 4.8(d), at the front corners of the cylinder. Near the free end, the spanwise velocity values are lower since the flow is able to escape over top of the cylinder. Near the ground plane the spanwise velocity is minimal due to the presence surface shear. As the flow descends towards the ground plane, the spanwise velocities disappear directly behind the cylinder.

Figure 4.9 shows the time-averaged normal velocity contours. The concentration of contour lines near the front corners in the upper half of the cylinder, Figures 4.9(a), (b) and (c), indicate flow being deflected over top of the cylinder. In contrast, behind the cylinder in the wake, the flow moves down from the top, Figures 4.9(a), (b) and (c), and then loses any significant downward momentum near the ground plane, Figures 4.9(e) and (f). The maximum normal velocity appears to be at z/D = 4 and near the free end, Figure 4.9(a) and (b).

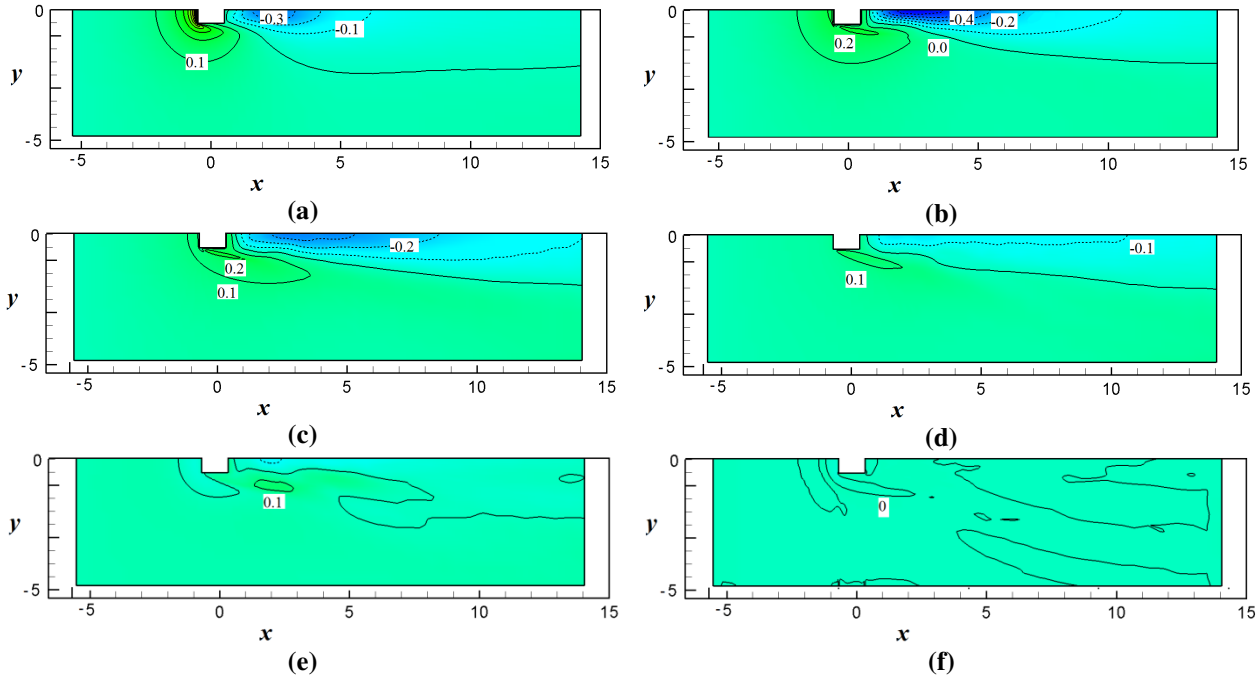

Figure 4.9: Time-averaged normal velocity contours w/U_∞ with a contour increments of w/U_∞ = 0.1, solid lines: positive values, dashed lines: negative values: a) z/D = 5, b) z/D = 4, c) z/D = 3, d) z/D = 2, e) z/D = 1, and f) z/D ~ 0.

4.5. Variation of Time-Averaged Pressure

Figure 4.10 presents the time-averaged pressure coefficient contours. Here pressure coefficient is defined as $C_p = (p-p_\infty)/½\rho_\infty U_\infty^2$. A high pressure region is observed in front of the cylinder all the way from the free end to the ground plane, with the pressure being lowest near the free end. Near the ground plane at the front of the cylinder the pressure reaches the maximum value.

In the near-wake region, the pressure is characterised by much lower values, which reach a minimum value at about z/D = 1, Figure 4.10(e), which is the region where the upwash and downwash merge. Behind the cylinder, the pressure exhibits its minimum value near the free end.

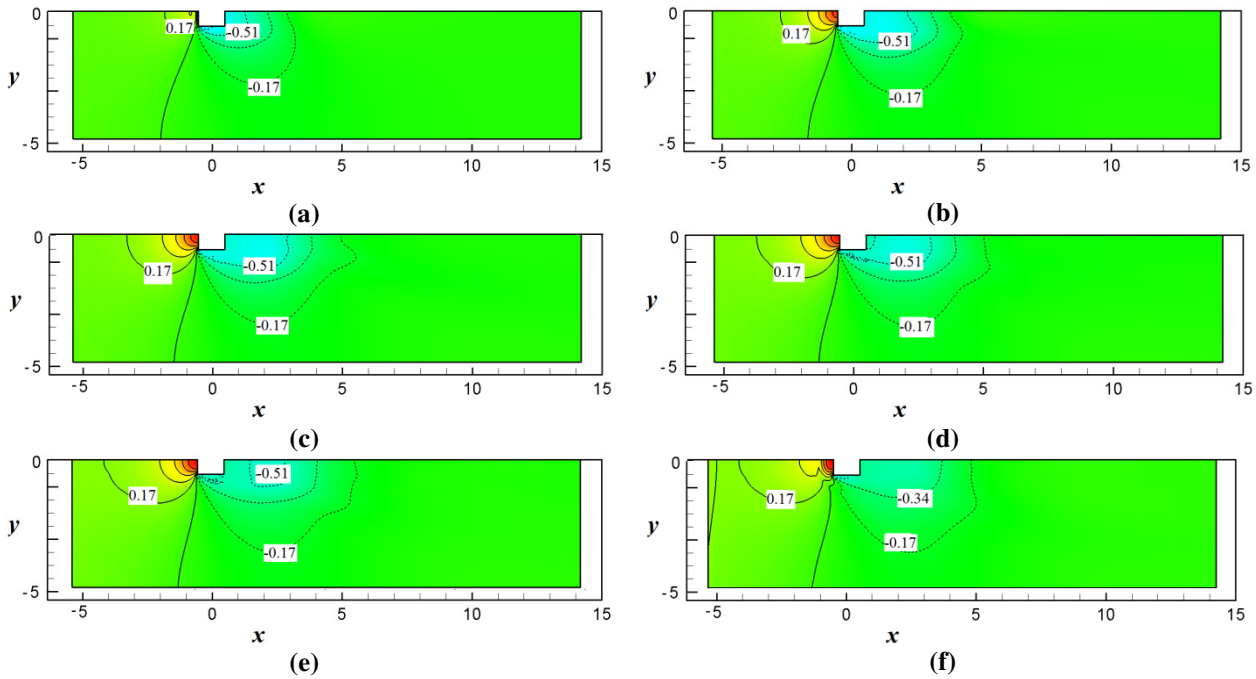

Figure 4.10: Time-averaged pressure coefficient contours, *Cp* with a contour increments of *Cp* = 0.17, solid lines: positive values, dashed lines: negative values: a) *z/D* = 5, b) *z/D* = 4, c) *z/D* = 3, d) *z/D* = 2, and e) *z/D* = 1, f) *z/D* ~ *0*.

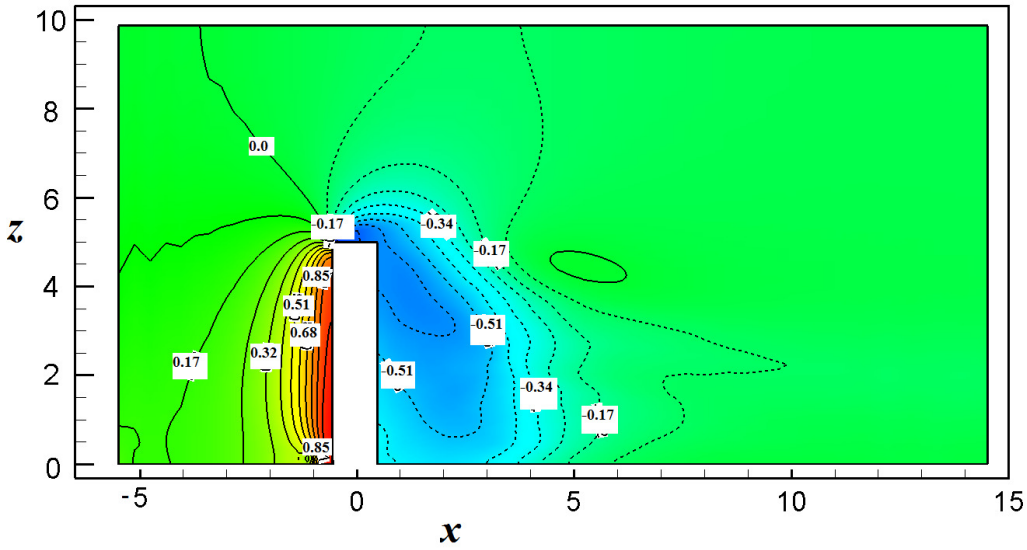

Figure 4.11: Time-averaged pressure coefficient (*Cp*) contours along the wake centre-line *y*/*D* = 0 with a contour increments of w/U_∞ = 0.34, solid lines: positive values, dashed lines: negative values.

Figure 4.11 presents the time-averaged pressure contours in the wake along the centre-plane (*y*/*D* = 0). The pressure contours change significantly from the tip to the base of the cylinder. In the near-wake region, the pressure is characterised by much lower values, particularly near the free end and as the ground-plane approaches pressure raises. Behind the cylinder, the pressure exhibits its maximum value near the ground-plane.

4.6. Variation of Time-Averaged Vorticity along Height of the Cylinder

Figure 4.12 presents contours of the time-averaged normal vorticity in various horizontal planes. Since these contours exhibit a symmetric behaviour, only half the domain is shown in Figure 4.12. According to the figure, the normal vorticity is maximum near the front corners of the square cylinder, and remains strong along the boundary between the recirculating and external uniform flow.

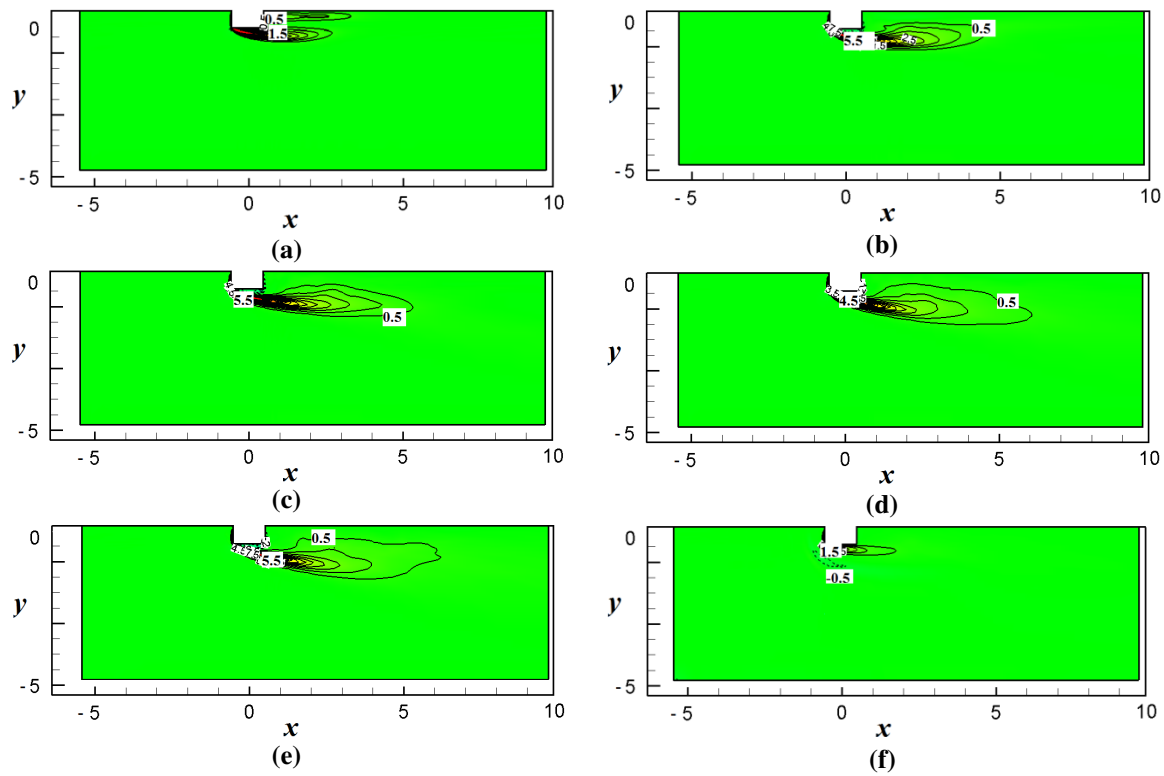

Figure 4.12: Time-averaged normal vorticity contours ω_z/U_∞, with a contour increments of ω_z/U_∞ = 0.5, solid lines: positive values, dashed lines: negative values: a) z/D = 5, b) z/D = 4, c) z/D = 3, d) z/D = 2, e) z/D = 1, and f) $z/D \sim 0$.

The vorticity is weakened as the flow moves downstream. The recirculating flow near the symmetry plane at the rear of the cylinder exhibits a relatively low level of vorticity. The vorticity originates with the extension of the separated shear layers from the sidewalls of the cylinder. The distribution of the vorticity contours changes as the flow descends from the free end towards the ground plane. At z/D = 5, Figure 4.12(a), besides the vorticity generated from the side walls, another vortex structure is formed near the symmetry plane. As the flow moves towards the ground plane, the side wall vorticity expands in both the streamwise and spanwise directions. Near the ground plane, Figure 4.12(f), a second vortex structure of opposite sign is evident near the front corners of the square cylinder, which most likely pertains to the horseshoe vortex.

4.7. Model of the Flow Structure

A persistent question for researchers studying this flow scenario is the specific nature of the vortex structure in the near-wake of the cylinder. In particular, it is of interest to understand how the vertically aligned vorticity being shed from the cylinder transforms downstream into streamwise vortical structures, which seem to be indicated by time-averaged measurements, e.g. Adaramola et al. (2006).

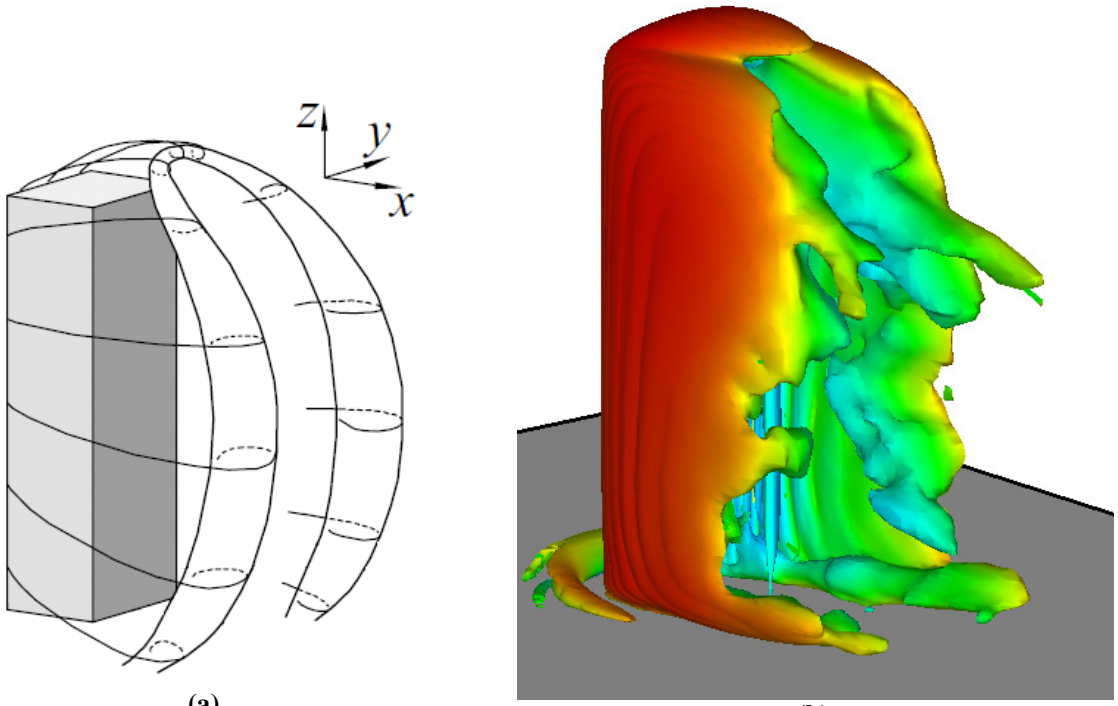

(a) (b)

Figure 4.13: Comparison of: a) model of Wang et al. (2009) for the flow structure, and b) *Q* iso-surfaces based on LES flow field.

The second invariant of the velocity gradient tensor can be used to analyse the vortical structures in the near-wake region of the finite square cylinder. The second invariant is defined as follows,

$$Q = ½ (\Omega_{ij} \Omega_{ij} - S_{ij} S_{ij}), \quad 4.1$$

where $S_{ij} = ½ (u_{i,j} + u_{j,i})$ is the strain rate tensor and $\Omega_{ij} = ½ (u_{i,j} - u_{j,i})$ is the vorticity tensor (which are the symmetric and antisymmetric components of $u_{i,j}$). Therefore, Q can be considered to represent the local balance between rotation and strain. Positive Q iso-surfaces represent areas where the strength of rotation dominates strain, indicating a vortex core. The main advantage of the second invariant over the vorticity, for vortex visualization, is that unlike the vorticity, Q becomes zero at the wall (Dubief and Delcayre, 2004).

Figure 4.13 compares the model of the wake structure proposed by Wang et al. (2009) for a wall-mounted finite-height square cylinder to the structure created by using iso-surfaces of the 2nd invariant of the velocity gradient tensor to visualise the LES flow field. Both of these pertain to the time-averaged flow structure. As proposed by Wang et al. (2009), their model suggests a symmetric flow structure for most parts of the wake region. Wang and Zhou (2009) made PIV measurements of the near wake of a finite square cylinder for aspect ratios ranging from AR = 3 to 7 (for δ/D = 1.35). They constructed both symmetric and antisymmetric flow structures models based on the existing experimental flow fields. They attributed the existence of the upwash and the corresponding base vortices to the thick boundary layer effect. Away from the free end the flow is characterized by von-Karman vortex structure. Approaching the ground plane however, the convection velocity of the spanwise vortices is reduced by the shear stress exerted by the wall, resulting in an inclination of the spanwise vortex roll near the ground-plane (Wang and Zhou, 2009).

The results for the mean velocity field shown in Figures 4.1 through 4.12 offer some support for the model of Wang et al. (2009). First, note that all of the results based on the time-averaged velocity field as predicted by the LES are symmetric, which agrees with the model of Wang et al (2009). Evidence of vortex cores is provided in Figure 4.12 for the wall-normal vorticity. Based on this figure, the cores appear to vary in both streamwise location and diameter for different horizontal planes. Although the cores are smallest and weakest at the tip and ground plane, the LES does not predict as strong a curvature as shown in the model of Wang et al (2009). Figure 4.9 implies that the normal velocity is a maximum near the free end of the cylinder. As the flow descends towards the ground plane, this value decreases which indicates that the downwash is stronger in the upper part of the wake region of the cylinder.

For comparison, the second invariant is used to visualise the time-averaged flow field in Figure 4.13(b). Figure 4.13(b) shows a weak horseshoe vortex at the front of the cylinder on the ground plane. A pair of the vortices originates from the free end, and then roll down towards the ground plane. These vortices appear to be symmetric near the free end. They are attached near the free end of the square cylinder, but become detached from each other as the flow develops towards the ground plane. Away from the free end, the vortices remain within the same vertical plane and do not expand in the cross-stream direction. This feature is also observed Figure 4.8, where as the flow approaches the ground plane, the spanwise velocity decreases to zero. The symmetric vortices separate near the middle of the cylinder. There is no evidence of antisymmetric Kármán vortex shedding. However, even if it existed in the instantaneous motion, if it was sufficiently regular, it would mostly be eliminated by the time-averaging used in these plots. Returning to Figure 4.13(b), two streamwise structures are observed above the ground plane.

4.8. Resolved Stresses

Figure 4.14 shows the resolved streamwise stress contours in multiple planes. Based on Figure 4.14, in the near wake region of the wall-mounted square cylinder, the u-fluctuations are minimal near the symmetry plane, but dominant in the separated shear layers.

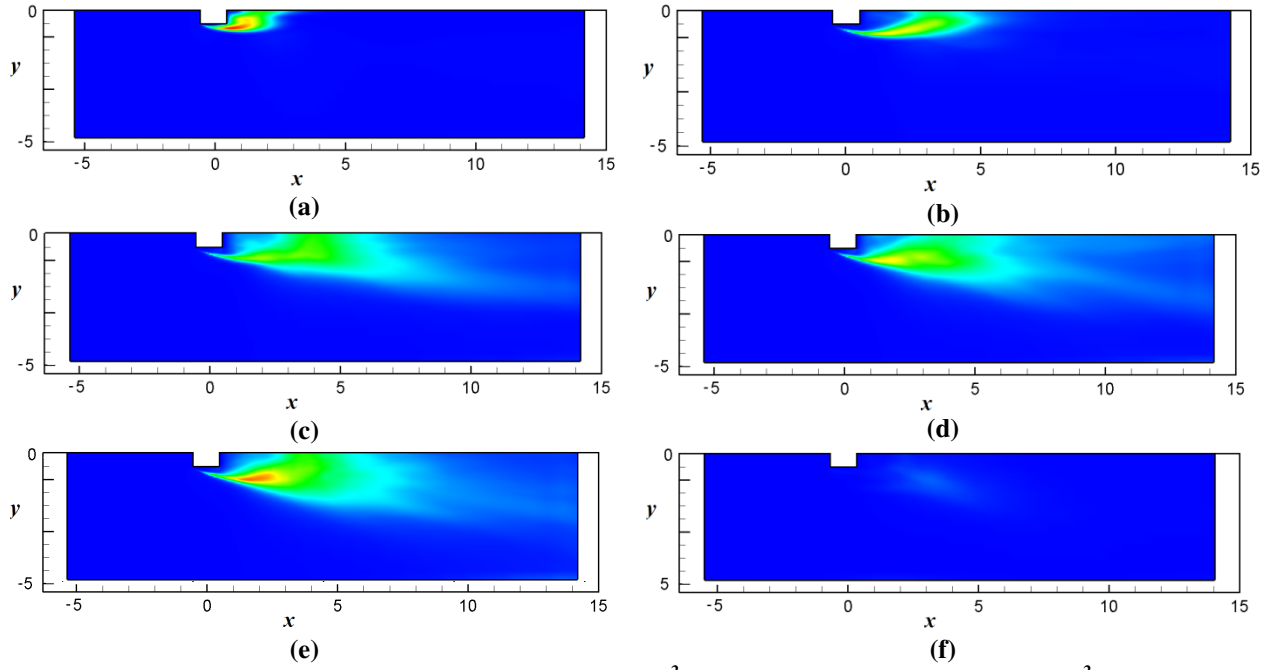

Figure 4.14: Resolved streamwise stress contours $\langle u'u' \rangle / U^2_\infty$ with maximum value of $\langle u'u' \rangle / U^2_\infty = 0.35$ at: a) $z/D = 5$, b) $z/D = 4$, c) $z/D = 3$, d) $z/D = 2$, e) $z/D = 1$, f) $z/D \sim 0$.

Note that these fluctuations indicate wider separated shear layers, Figure 4.14(c, d, e), compared to the time-averaged wake velocity field shown in Figure 4.4 and the time-averaged normal vorticity contours presented in Figure 4.12. Frohlich and Rodi (2004) also observed that the resolved stress components imply wider shear layers compared to the streamlines of the time-averaged flow field.

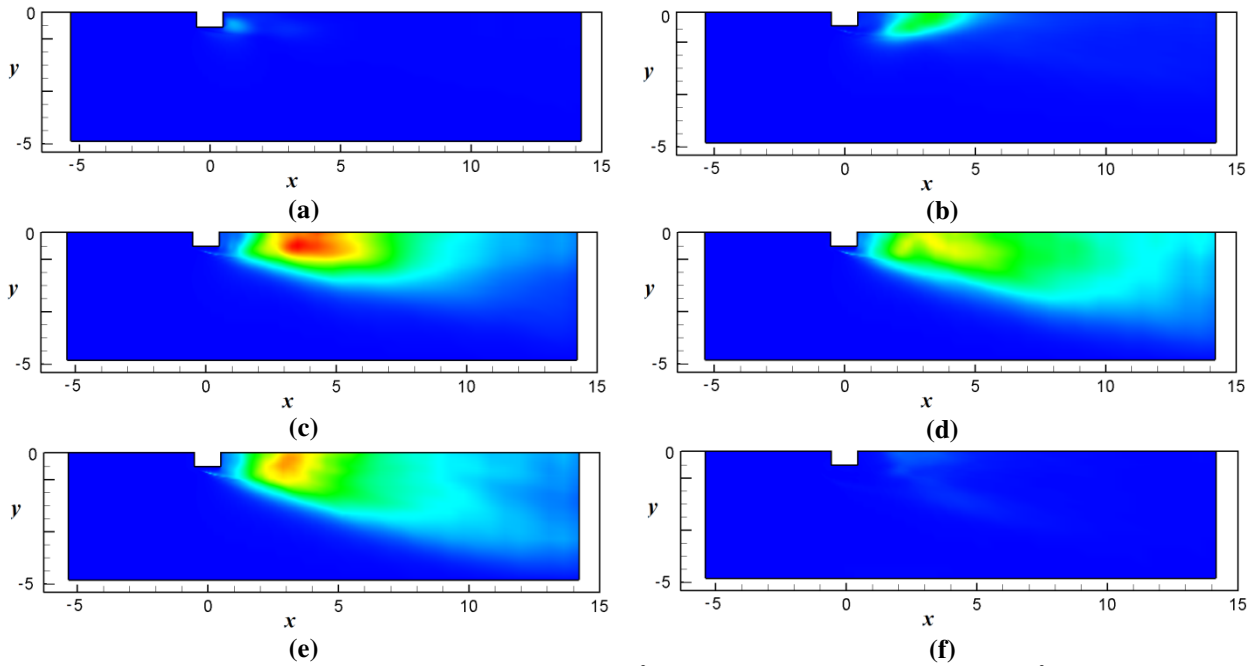

Figure 4.15: Resolved spanwise stress contours $\langle v'v' \rangle / U^2_\infty$ with maximum value of $\langle v'v' \rangle / U^2_\infty = 0.17$ at: a) $z/D = 5$, b) $z/D = 4$, c) $z/D = 3$, d) $z/D = 2$, e) $z/D = 1$, f) $z/D \sim 0$.

Figure 4.15 shows the resolved spanwise stress contours in multiple planes along the height of the cylinder. According to this figure, compared to the streamwise velocity fluctuations, the normal fluctuations (or resolved normal stress, $\langle v'v' \rangle / U^2_\infty$) are larger in magnitude near the symmetry plane. Figure 4.15(c) shows that the normal velocity fluctuations are largest at $z/D = 3$. Comparison between the resolved spanwise stress contours, Figure 4.14, and the corresponding fluctuations show that although in the near-wake region the spanwise velocity is a maximum near the free end, at this location the velocity fluctuation is minimal. This may be another indication of the presence of the time-variant nature of vortices in the near-wake region of the cylinder farther away from the free end.

Figure 4.16 shows the resolved normal stress contours in multiple planes located along the height of the square cylinder. According to this figure, like the spanwise fluctuations, the normal fluctuations $\langle w'w' \rangle / U^2_\infty$ are maximum near the symmetry plane. Figure 4.16(c) shows that $\langle w'w' \rangle / U^2_\infty$ reaches its maximal at $z/D = 3$.

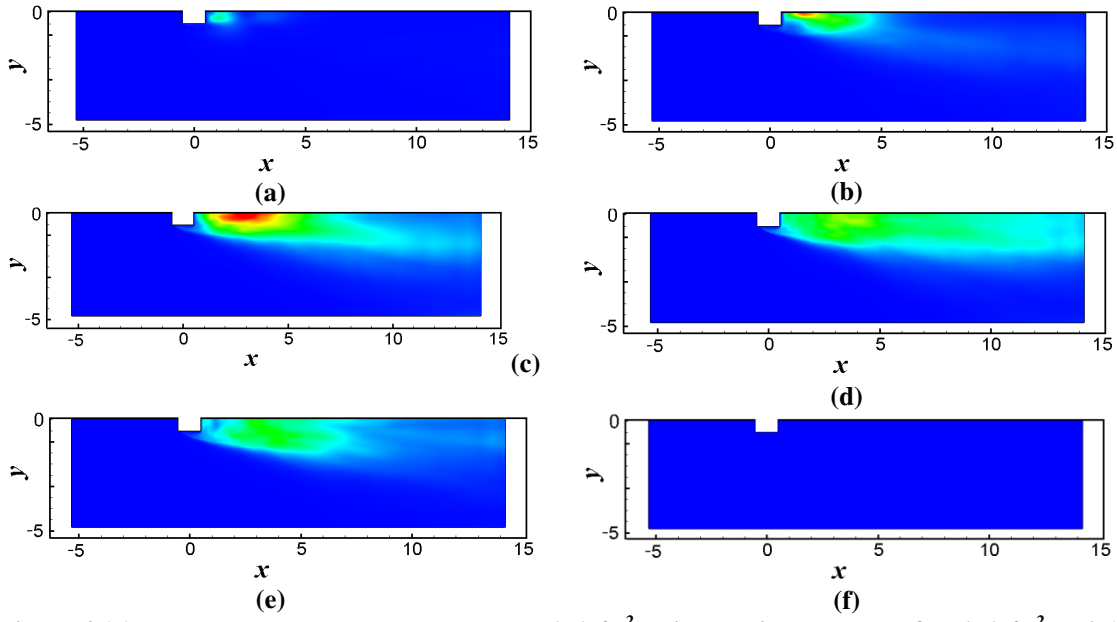

Figure 4.16: Resolved normal stress contours $\langle w'w' \rangle / U^2_\infty$ with maximum value of $\langle w'w' \rangle / U^2_\infty = 0.15$ at: a) $z/D = 5$, b) $z/D = 4$, c) $z/D = 3$, d) $z/D = 2$, e) $z/D = 1$, f) $z/D \sim 0$.

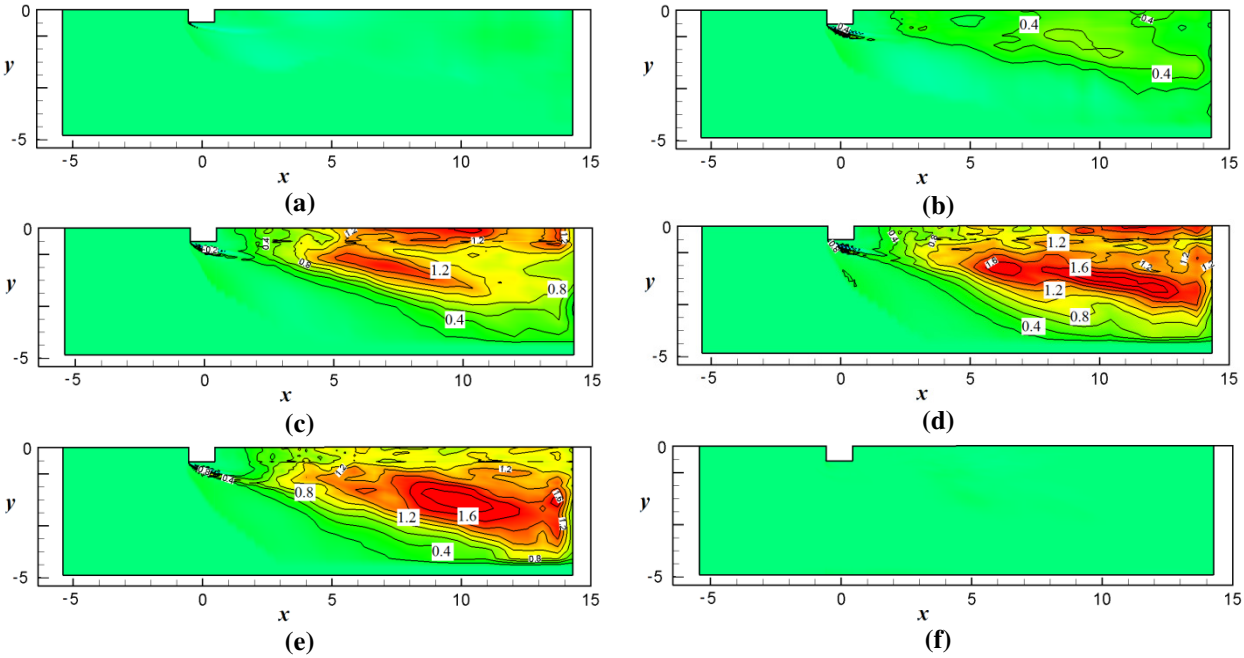

Figure 4.17: Time-averaged eddy viscosity contours ν_T/ν with contour increments of $\nu_T/\nu = 0.4$ at: a) $z/D = 5$, b) $z/D = 4$, c) $z/D = 3$, d) $z/D = 2$, e) $z/D = 1$, f) $z/D \sim 0$.

Figure 4.17 illustrates the time-averaged eddy viscosity contours in the six different horizontal planes. The time-averaged eddy viscosity is significantly higher at $z/D = 3$ to $z/D = 1$. Recalling

the fluctuating velocity values shown in Figures 4.14, 4.15 and 4.16, the eddy viscosity is higher in the same planes as the velocity fluctuations. This is an indication that in the bottom section of the wake region, the flow is more turbulent compared to the free end region, where the time-averaged eddy viscosity is smaller in magnitude. The range of the SGS viscosity predicted by the DSM indicates that the LES solution is fairly well resolved, as the ratios of the SGS viscosity to the molecular viscosity are close to unity.

4.9. Time-Averaged Streamwise Vorticity

Figure 4.18 shows the time-averaged streamwise vorticity at different streamwise locations downstream of the cylinder. A pair of tip vortices is observed near the free end of the cylinder. Initially, these vortices are stretched toward the ground plane and two distinct peak values are observed for each vortex. Also a pair of weak base vortex structures (with opposite sense of rotation to the tip vortex pair) can be identified close to the ground plane. These smaller vortices have the same sign as the base vortex structures observed by Sumner et al. (2004) and Wang et al. (2006) but are much smaller in size. It is noted that the size of the base vortices depends on various factors, most importantly the boundary layer thickness on the ground plane (Wang et al., 2006). Finally, in addition to these two sets of vortices, another pair of smaller vortices is observed on top of the tip vortices at $x/D = 1$, Figure 4.18(a). These vortices have an opposite sign in regards to the tip vortices and are absent in the planes further downstream.

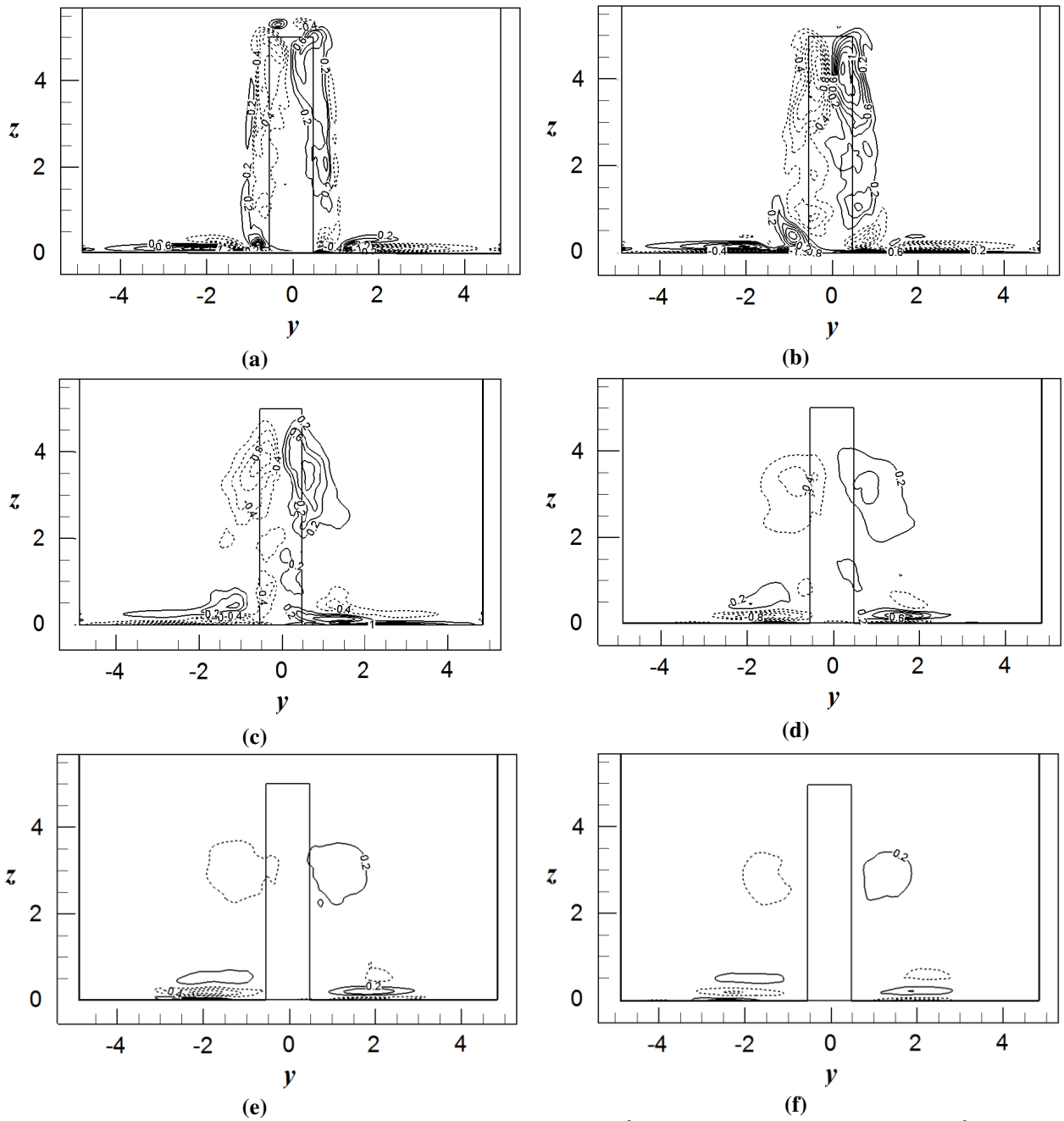

Figure 4.18: Time-averaged streamwise vorticity contours ω_x/U^2_∞ with contour increments of ω_x/U^2_∞ = 0.2, solid lines: positive values at: a) *x/D* = 1, b) *x/D* = 2, c) *x/D* = 4, d) *x/D* = 6, e) *x/D* = 8, f) *x/D* = 10.

In the near-wake region, as the flow moves downstream, the vortices become weaker, the tip vortices move towards the ground plane and the vortices are expanded in the cross-stream direction and become rounder in shape. Overall, the vortex structure changes significantly as the

wake develops downstream. The numerical solutions are consistent with the experimental results of Sumner et al. (2004) for a circular cylinder.

4.10. Conclusion

It should be noted that the experimental data in the literature for flow over a finite square prism at Re = 500 is extremely limited: the author could not find any quantitative measurements for comparison. Therefore, such features as the extent of recirculation zone on the centre plane and the streamline patterns were compared qualitatively with the results of other finite cylinder flows. The general agreement of these features with other studies suggests that the predictions of the LES are realistic.

The analysis above of itself does not offer strong support for the structural model advanced by Wang et al. (2009), although some similarities exist between their model and the mean field predicted by the LES. One possible reason for the lack of agreement may be the challenge of identifying vortex structures, e.g. using vorticity distributions versus visualisation using the 2^{nd} invariant. Another issue is whether the characteristic vortex structure is the same for the time-averaged and the instantaneous flow. The time-averaged results are in good agreement with the measurements of Wang et al. (2006) for flow over a finite-height square cylinder immersed in a thin boundary layer. Comparison of the LES results with the velocity field for a square cylinder immersed in a thicker boundary layer, Wang et al. (2009), suggests that the boundary layer thickness especially affects the upwash flow. More specifically, a thicker boundary layer causes the upwash to become stronger. A pair of counter-rotating tip vortices is observed near the free end. As the flow moves downstream, these vortices move towards the ground plane, lose their

strength and become rounder in shape. Also a pair of weak base vortex structures is observed near the ground plane. The base vortices are smaller in size than those observed in the experiments of Sumner et al. (2004) and Wang et al. (2009), most likely due to the boundary layer thickness on the ground plane (Wang et al., 2006).

The following chapter examines some features of the instantaneous velocity field. After that the streamwise vorticity structure of the wake is investigated using vertical sections at different values of *x/D*. The subsequent section examines periodic motions within the wake, and the final section returns to reconsider visualisation of the 3-D structure of the wake based on the instantaneous flow field.

Chapter 5

Instantaneous Flow Field over a Finite-Height Cylinder of AR = 5

5.1. Introduction

In this chapter the instantaneous flow field over a wall-mounted finite-height square cylinder is investigated by LES. The wake of a finite square cylinder is studied for the aspect ratio of AR = 5 at Re = 500. The cylinder was immersed in a thin laminar boundary layer of $\delta/D = 0.01$ at the inlet.

Three probes were chosen to store the velocity and pressure variation throughout the simulation located at $x/D = 3$ and $y/D = 1.5$ and along the height of the cylinder at $z_1/D = 2.7$, $z_2/D = 2.1$ and $z_3/D = 1.2$. These locations were chosen so that the probes were able to detect the periodic passing of vortices while the flow was relatively low in turbulence. It should be noted that, for the square cylinder, wake is wider than for a circular cylinder. The length of the time series is important and also the number of power spectra that are averaged to produce the final result are important.

Time signals of the velocity field predicted by the LES solution were recorded at the three points selected within the near-wake region for over 10,000 time-steps storing every 10th point in time. The instantaneous flow fields were extracted and processed for a characteristic time period based on the calculated Strouhal number of St = 0.127. A single time period was arbitrarily divided into six phases, and the instantaneous features of the flow visualised for different phases within a single period. Streamlines, velocity and vorticity contours were analysed for various planes, to represent the two-dimensional features of the instantaneous flow. Iso-surfaces of the 2^{nd} invariant were also used to visualize the vortex structures.

5.2. Power Spectra

Matlab's Fourier transform was used to process the velocity time series to obtain the corresponding power spectra. Figure 5.1 shows the power spectra at three locations along the height of the square cylinder. A significant peak is observed at St = 0.127 for all three sample locations, which is slightly higher than the value for an infinite cylinder St = 0.122 (Sohankar et al., 1999) at Re = 500. For a wall-mounted circular cylinder with aspect ratios ranging from AR = 3 to 9 and a boundary layer thickness of δ/D = 2.6 at Re = 6×10^4, Sumner et al. (2004) measured the Strouhal number to be St = 0.16 and showed that it is lower for a finite cylinder than for an infinite cylinder. For a finite square cylinder with aspect ratio's of $1.5 < AR < 8$, and boundary layer thicknesses of $0.68 < \delta/D < 2.85$, Sakamoto and Arie (1983) obtained St = 0.14 for Re ~ 500. The peak Strouhal number obtained by Wang and Zhou (2009) for a square cylinder with AR = 7 and δ/D = 2.6 was St = 0.11 for Re = 9.3×10^3, while Wang et al. (2004) obtained peak values of St = 0.09 for AR = 3 and St ~ 0.12 and 0.13 for AR = 5 and 7, respectively for Re = 9.3×10^3. They also concluded that the flow over cylinders with AR = 5 and 7 may be dominated by von-Karman type vortices. In addition to aspect ratio and geometry, e.g. the shape of the cylinder, the boundary layer thickness may also affect the value of the Strouhal number.

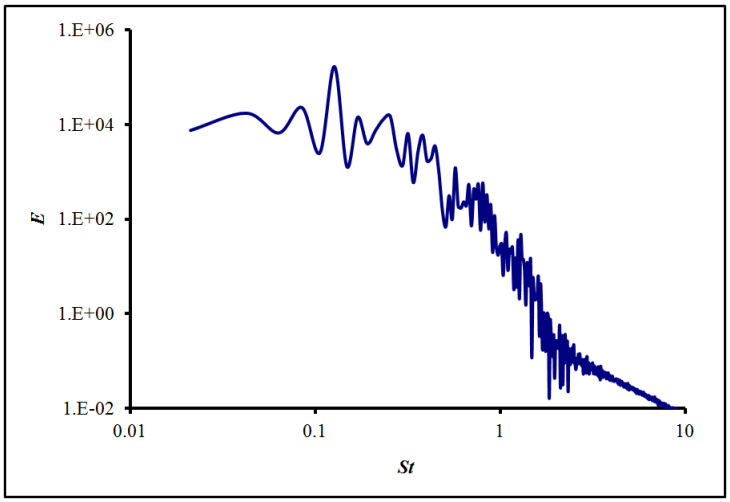

a)

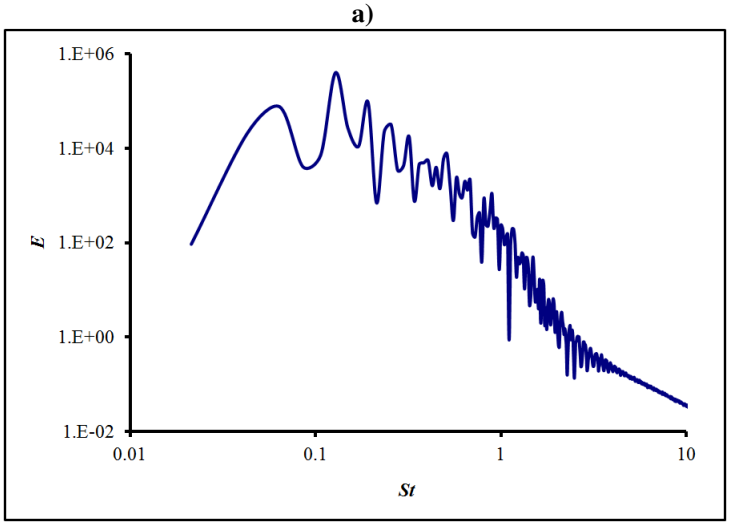

b)

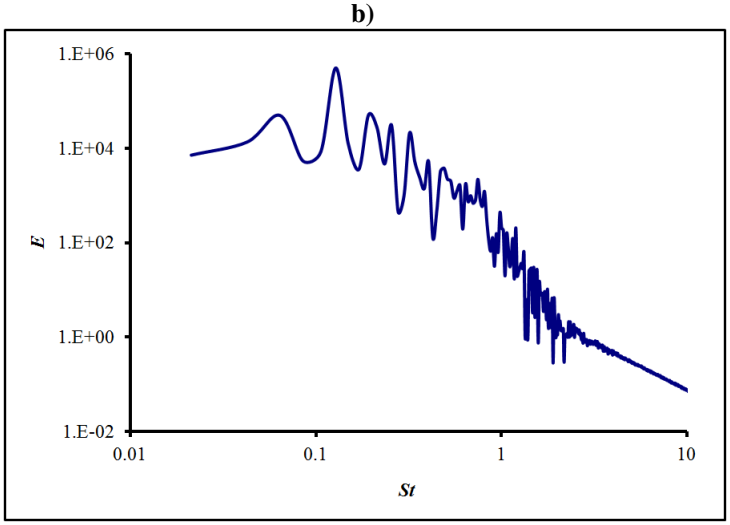

c)

Figure 5.1: Variation of the power spectra along the height of the cylinder, at *x/D* = 3, *y/D* = 1.5: a) *z/D* = 2.7, b) *z/D* = 2.1, c) *z/D* = 1.2.

The following instantaneous flow fields were extracted and processed for a characteristic time period of $T = 0.79$s based on a Strouhal number of St = 0.127. As noted above, the instantaneous features of the flow were visualised for six different phases within a single period. It is not expected that all of the flow features will exhibit strongly periodic behaviour. On the other hand, certain of flow features explored in the following figures do demonstrate some aspects of periodicity.

5.3. Instantaneous Flow Structure in the Center-plane

The first set of figures considers the instantaneous velocity field in a vertical plane along the centreline of the wake. The figures below are so "rich" with information, it is practically impossible to give a complete analysis. Figure 5.2 presents the instantaneous velocity vectors for each phase. A strong downwash flow is observed originating from the free end interacting with a weak upwash flow originating from the ground plane. Near the rear wall of the cylinder the flow moves swirling both away from and toward the cylinder wall. The vector fields show that the reverse flow along the ground plane into the wake separates and reattaches to the ground plane. The calculation of reattachment point varies along the ground plane for each phase.

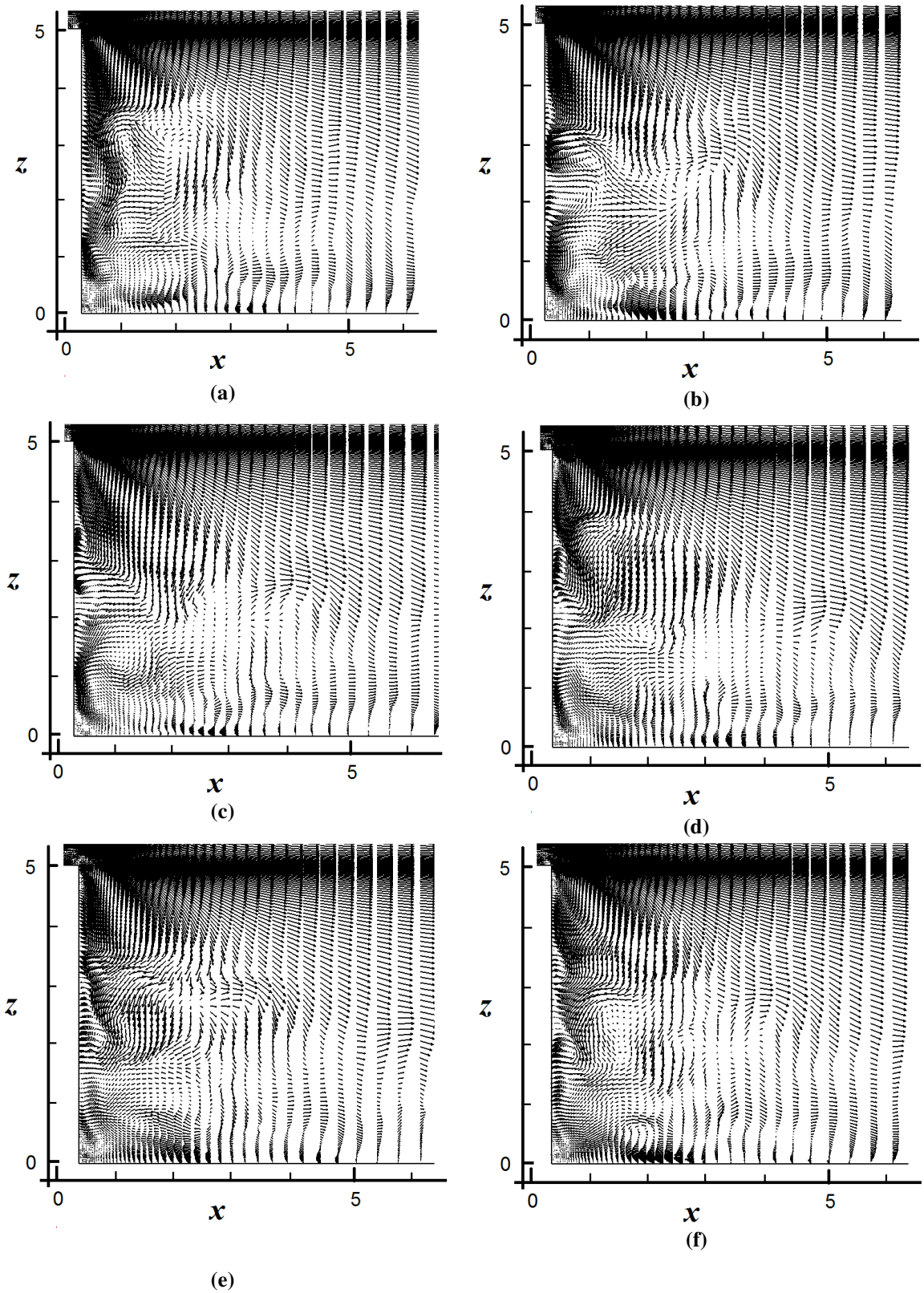

Figure 5.2: Instantaneous velocity vectors at six consecutive time frames: a) 1/6*T*, b) 2/6*T*, c) 3/6*T*, d) 4/6*T*, e) 5/6*T*, and f) *T*.

Figure 5.3 also presents the instantaneous flow field in terms of streamlines at six consecutive time frames, any two separated by a time increment of $\Delta t = 1/6T$. In all six cases the flow is characterized by the strong downwash flow from the free end interacting with a weak upwash flow originating from the ground plane. Recall that a saddle point shows the interaction point of downwash and upwash flow; where they are clearly evident, they are marked by the symbol '+'. Figure 5.3(d) (as well as 5.2(d)) specifically portray the free end downwash flow meeting the upwash flow from the ground plane, where the downwash flow is limited to the upper half of the wake. For this flow scenario, only one saddle point is observed in Figure 5.3(d). On the other hand, Figure 5.3(e) portrays a more complex flow field, with more than one saddle point, while Figure 5.3(b) exhibits three focal points. Based on Figure 5.3, the downwash and upwash flow regions as well as the number and locations of critical points varies from one case to another. Wang and Zhou (2009) observed an instantaneous flow field with two saddle points for AR = 7 and boundary thickness of $\delta/D = 1.35$. Two saddle points and focal points are generally observed for higher aspect ratio prisms (Wu et al., 1996), which they suggest are associated with the von-Karman type vortex shedding parallel to the axis of the cylinder (Wang and Zhou, 2009). In the present study, although the downwash flow is dominant, the existence of a pair of saddle points at specific times would be an indication of vortex shedding. To explore the existence of the spanwise vortices, the same instantaneous flows fields are processed in terms of spanwise vorticity ω_y in Figure 5.4.

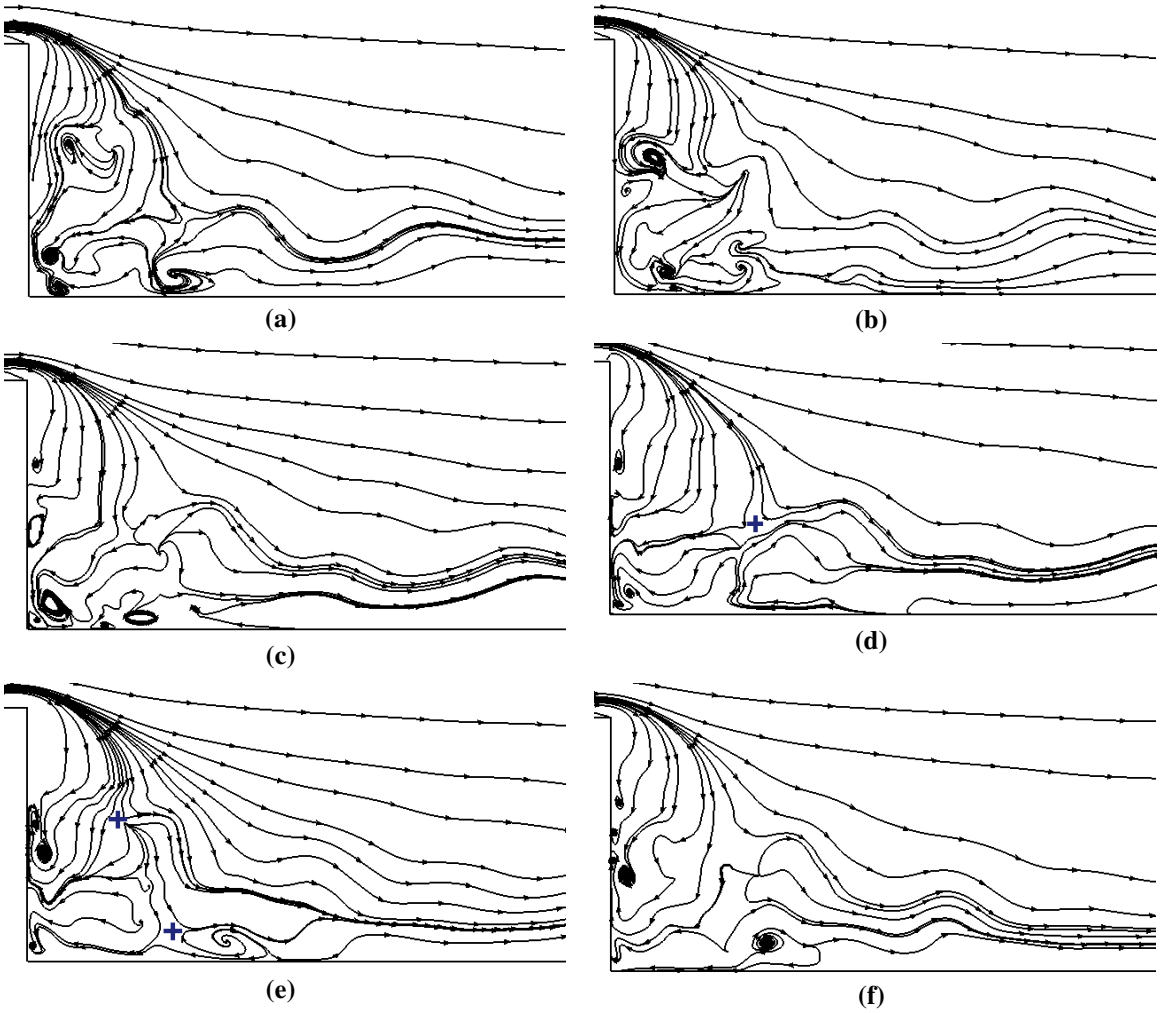

Figure 5.3: Instantaneous streamlines at six consecutive time intervals: a) 1/6*T*, b) 2/6*T*, c) 3/6*T*, d) 4/6*T*, e) 5/6*T*, and f) *T*.

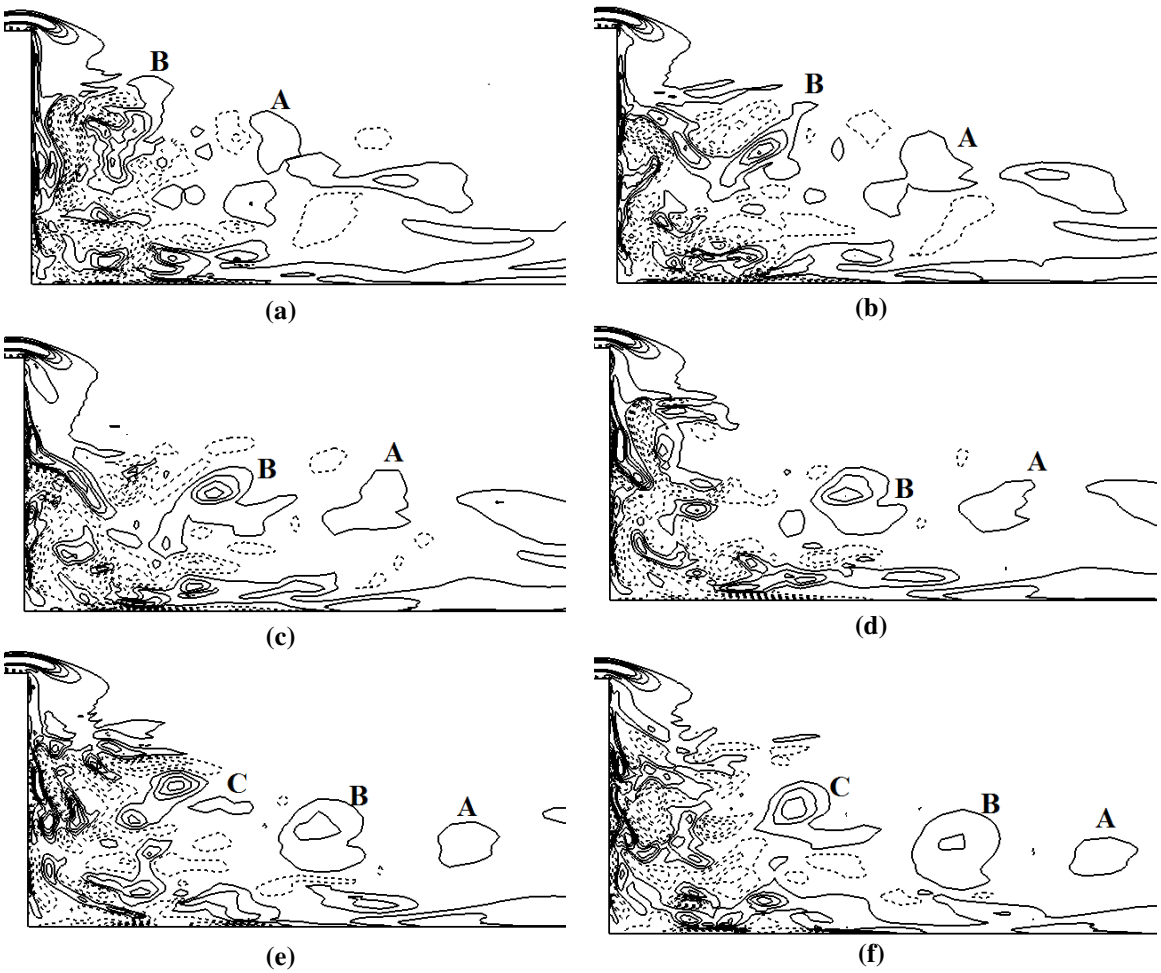

Figure 5.4: Instantaneous spanwise vorticity contours ω_y at six consecutive time intervals: a) 1/6*T*, b) 2/6*T*, c) 3/6*T*, d) 4/6*T*, e) 5/6*T*, and f) *T*.

Figure 5.4 indicates a complex vorticity field. Continuous shedding of spanwise vorticity from the top rear edge is observed for all six consecutive time intervals associated with the descending shear layer. The size and location of the vortex structures vary in time. The flow first rolls up against the rear wall, and then is convected out of the near wake into the downstream flow. According to Figure 5.4, in the near wake region, closer to the cylinder wall, the spanwise vortices are negative and mainly the positive vortices are carried out downstream.

5.4. Instantaneous Development of the Flow in Wall-Normal Planes

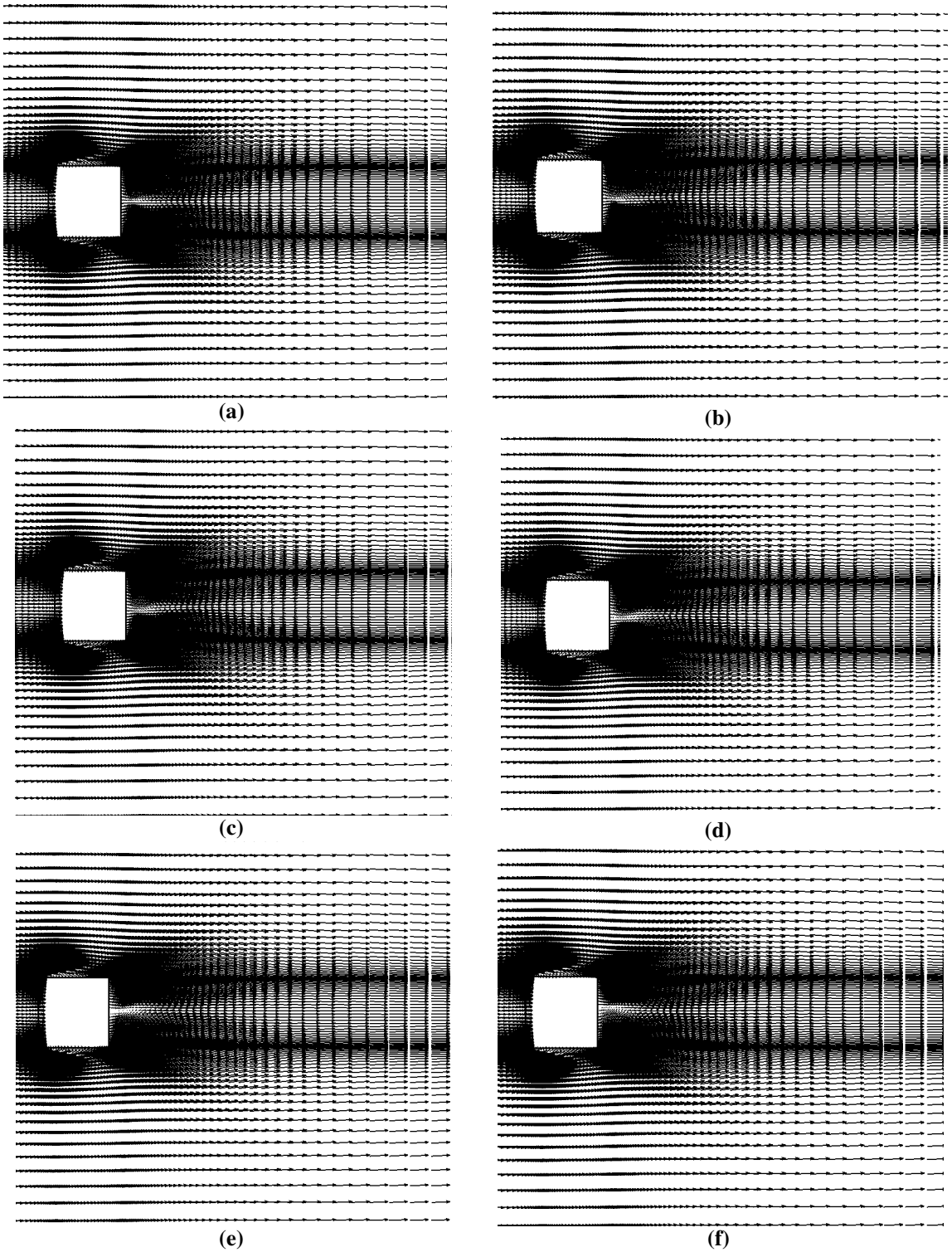

Figure 5.5: Instantaneous velocity vectors located at z/D = 5 at six consecutive time intervals: a) 1/6T, b) 2/6T, c) 3/6T, d) 4/6T, e) 5/6T, and f) T.

Figures 5.5 and 5.6 show the instantaneous velocity vectors and contours of the wall-normal vorticity ω_z, respectively, in a horizontal plane at $z/D = 5$. Although the details in many regions are blurred by the concentration of velocity vectors in Figure 5.5, the overall pattern is strongly symmetric near the free end. Figure 5.6 sugests that a pair of symmetric vortices is formed in the inner wake region near the free end. These vortices are relatively small in size and rounded in shape. A second pair of symmetric vortices originate at the front corners of the square cylinder and extend downstream into the near-wake region.

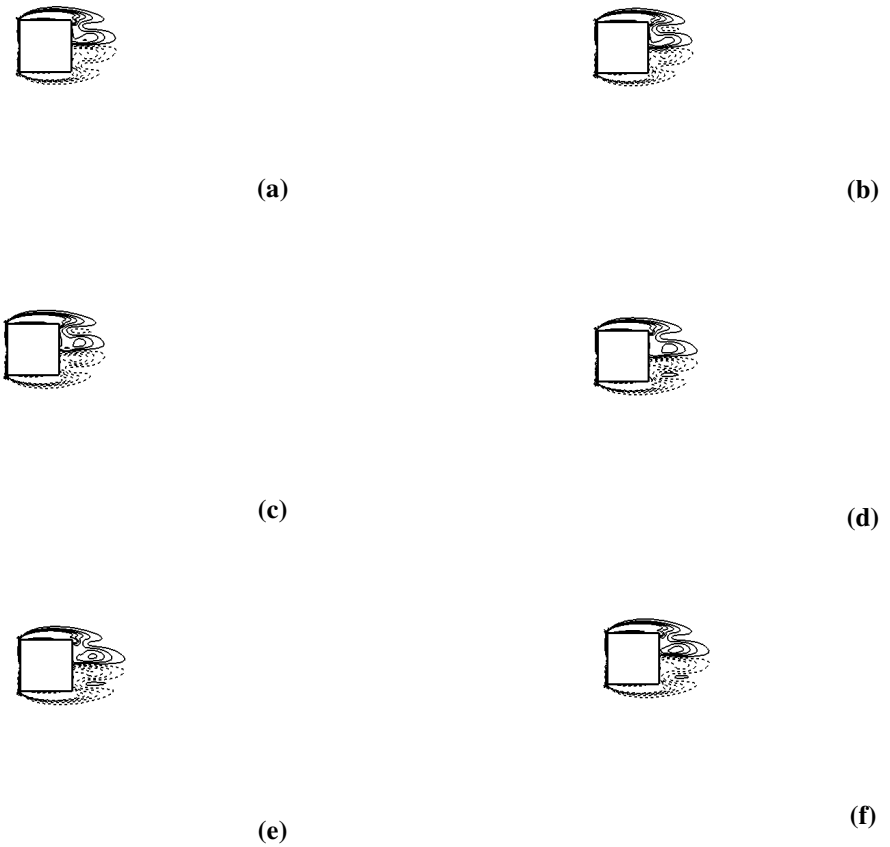

(a) **(b)** **(c)** **(d)** **(e)** **(f)**

Figure 5.6: Instantaneous normal vorticity contours ω_z located at $z/D = 5$ for six consecutive time intervals: a) 1/6*T*, b) 2/6*T*, c) 3/6*T*, d) 4/6*T*, e) 5/6*T*, and f) *T*.

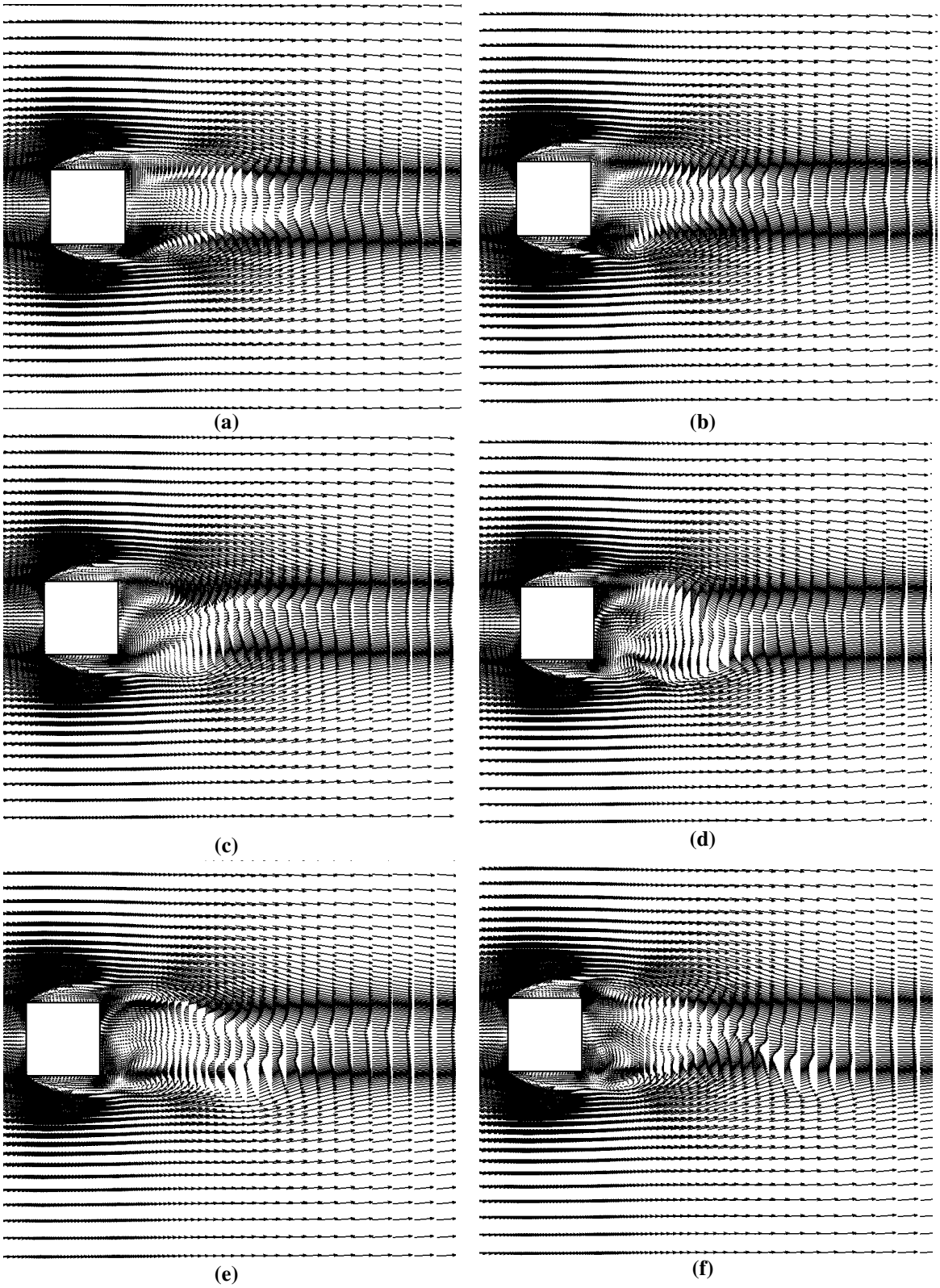

Figure 5.7: Instantaneous velocity vectors located at z/D = 4 for six consecutive time frames: a) 1/6T, b) 2/6T, c) 3/6T, d) 4/6T, e) 5/6T, and f) T.

Figures 5.7 and 5.8 show the instantaneous velocity vectors and contours of the wall-normal vorticity ω_z, respectively, at z/D = 4. According to Figure 5.7, the flow begins to become antisymmetric and more complex. For example, whereas the outer flow continues to move downstream, the flow inside the wake region at times is observed to move upstream toward the cylinder. The inclination of this flow changes as the flow evolves in time, as does the reverse flow into the near-wake region. The associated vortical structures shown in Figure 5.8 also exhibit a weak periodicity. Both pairs of vortices extend further in the streamwise direction compared to the corresponding structures at z/D = 5 in Figure 5.6. They also alternate in terms of which structure extends furthest into the wake.

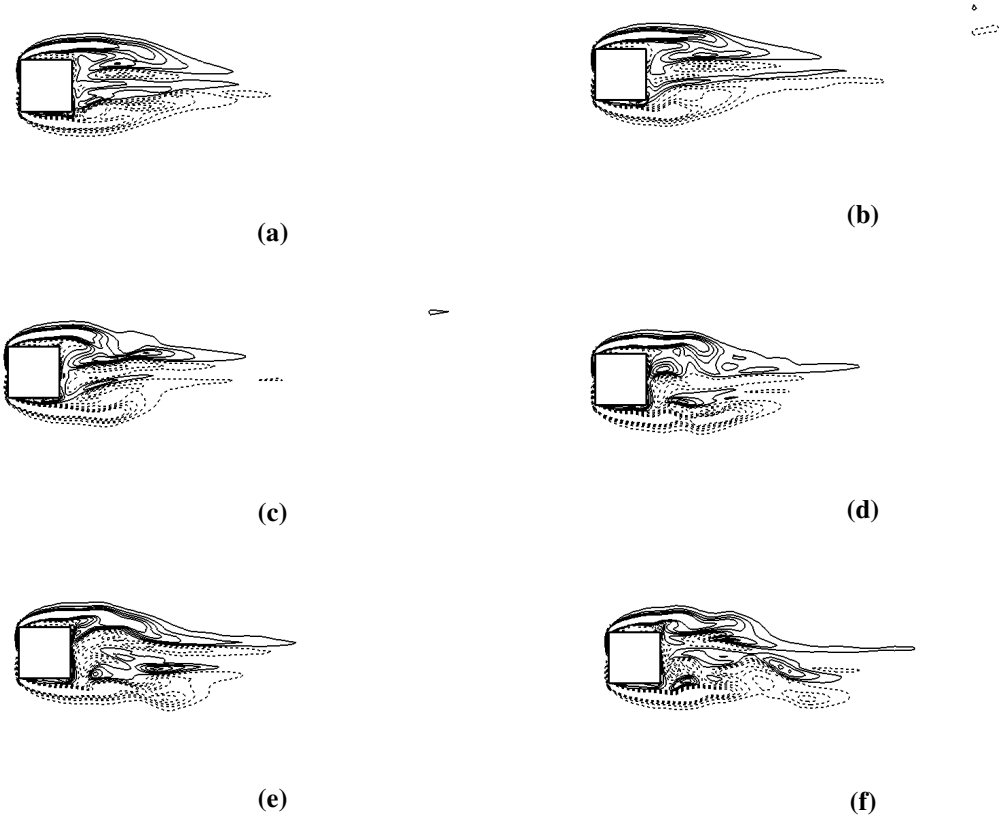

Figure 5.8: Instantaneous normal vorticity contours ω_z located at z/D = 4 for six consecutive time intervals: a) 1/6*T*, b) 2/6*T*, c) 3/6*T*, d) 4/6*T*, e) 5/6*T*, and f) *T*.

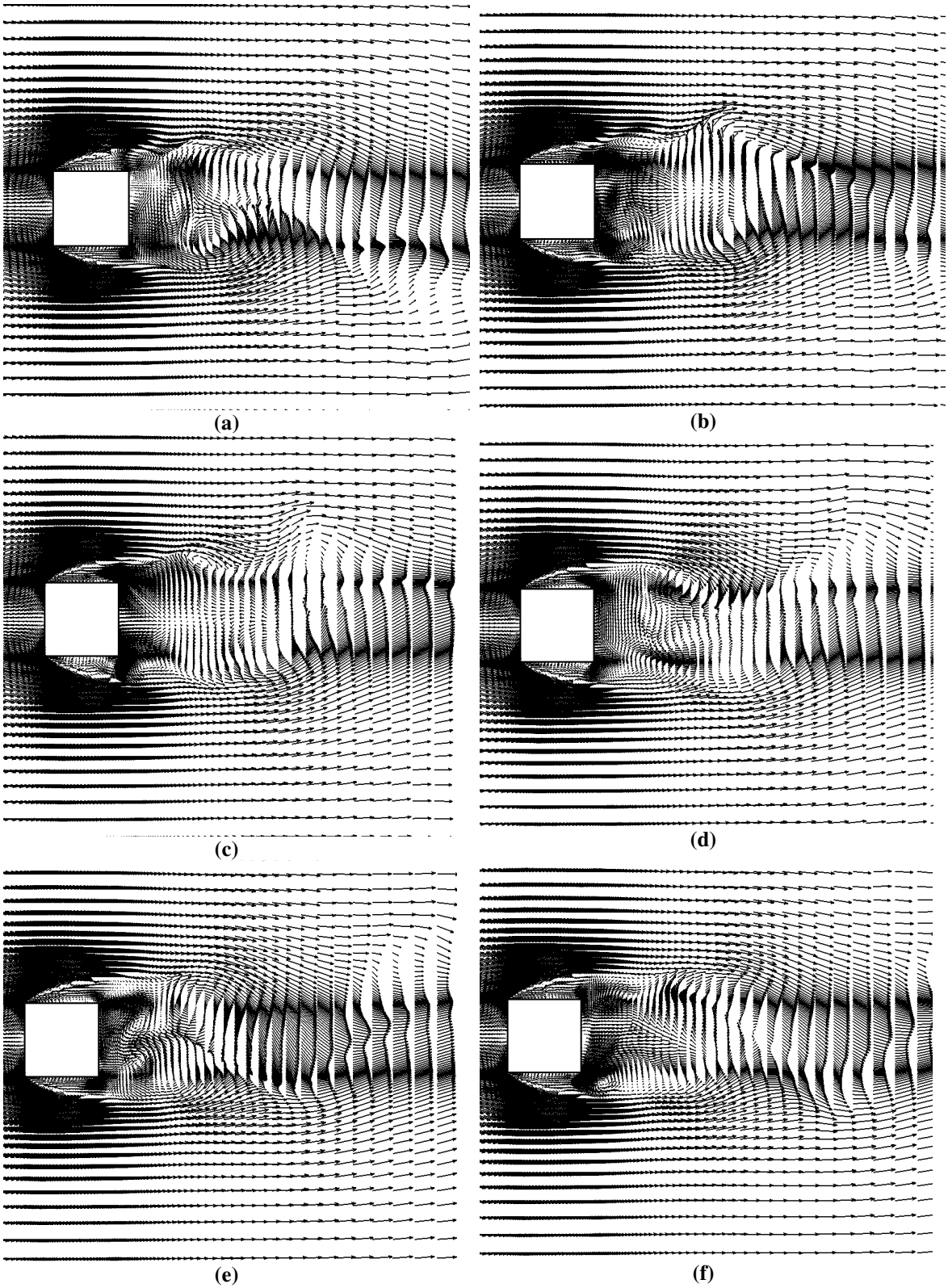

Figure 5.9: Instantaneous velocity vectors located at z/D = 3 for six consecutive time intervals: a) 1/6T, b) 2/6T, c) 3/6T, d) 4/6T, e) 5/6T, and f) T.

Figures 5.9 and 5.10 show the instantaneous velocity vectors and contours of the wall-normal vorticity ω_z, respectively, at $z/D = 3$. Figure 5.9 indicates that strong antisymmetric recirculation patterns are formed in the near-wake region, and as before include fluid being swept back upstream toward the rear face of the cylinder. Due to the evident enlargement of the recirculation zones, as shown in Figure 5.10, the side vortices extend further downstream compared to $z/D = 5$ and 4. The location of these vortices is beginning to alternate with time in a manner that resembles von-Karman vortex shedding. On the other hand, there are also features that imply symmetric shedding, such as a simultaneous breaking away of vortex structures as observed in Figure 5.10(d) and 5.10(f).

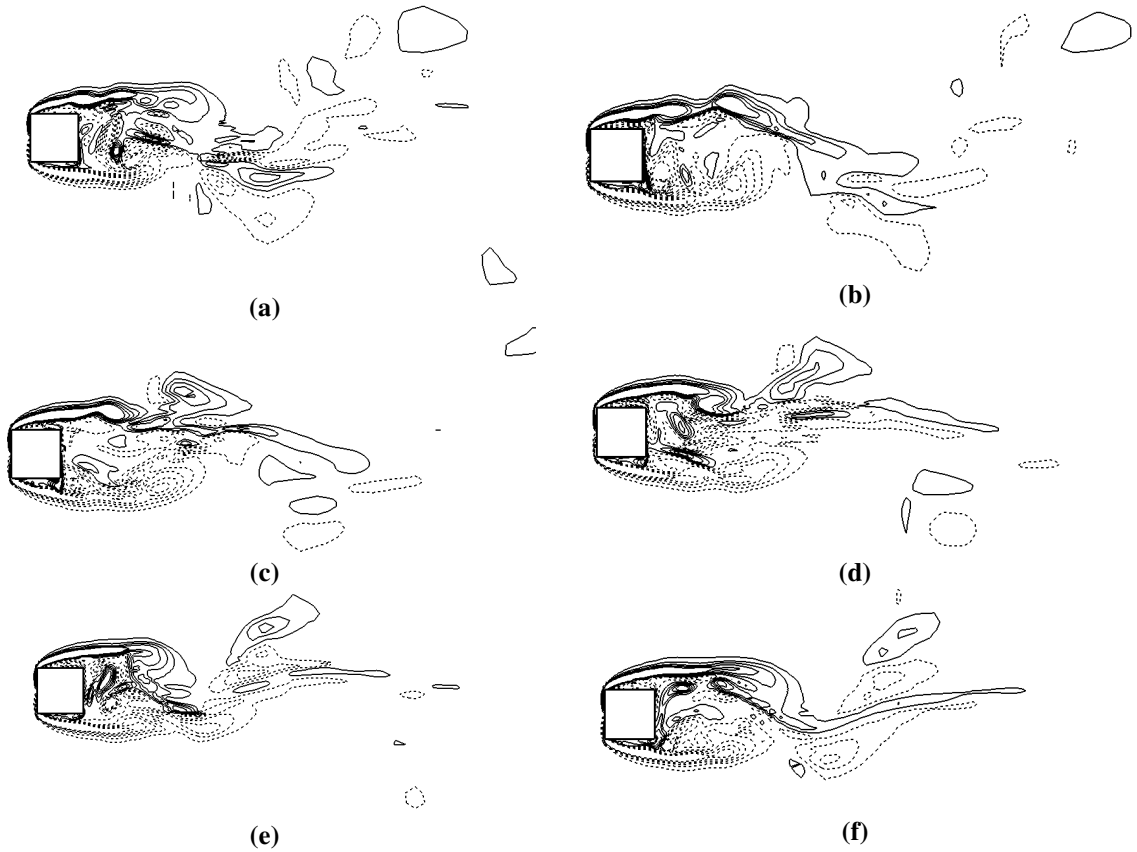

Figure 5.10: Instantaneous normal vorticity contours ω_z located at $z/D = 3$ for six consecutive time intervals: a) 1/6*T*, b) 2/6*T*, c) 3/6*T*, d) 4/6*T*, e) 5/6*T*, and f) *T*.

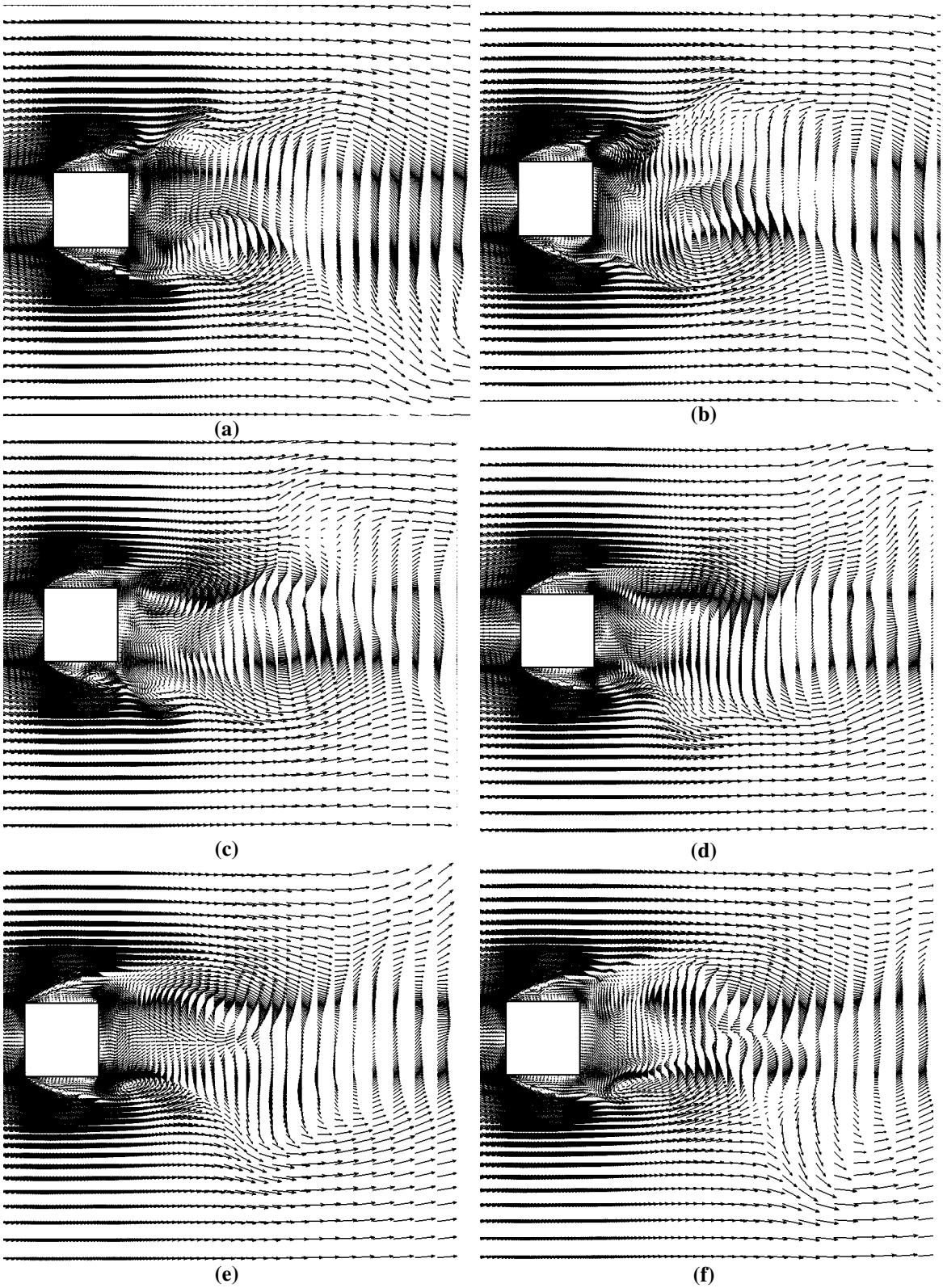

Figure 5.11: Instantaneous velocity vectors located at z/D = 2 for six consecutive time intervals: a) 1/6T, b) 2/6T, c) 3/6T, d) 4/6T, e) 5/6T, and f) T.

Figures 5.11 and 5.12 show the instantaneous velocity vectors and contours of the normal vorticity ω_z, respectively, at $z/D = 2$. The velocity vectors in Figure 5.11 indicate large recirculation zones, which significantly perturb the flow outside the nominal extent of the wake. The contours in Figure 5.12 illustrate many features of periodic von-Karman vortex shedding such as release of a vortex structure into the wake from alternate sides of the rear face of the cylinder. For example, comparison between figures 5.12(b) and 5.12(e) show that the dominant vortex has shifted from the lower side at 5.12(b) to the upper side at 5.12(e). The vortical structures have grown larger in size and expanded in the spanwise direction compared to the ω_z contours at $z/D = 3$ in Figure 5.10. Their effect on the wake as they move downstream is much more pronounced.

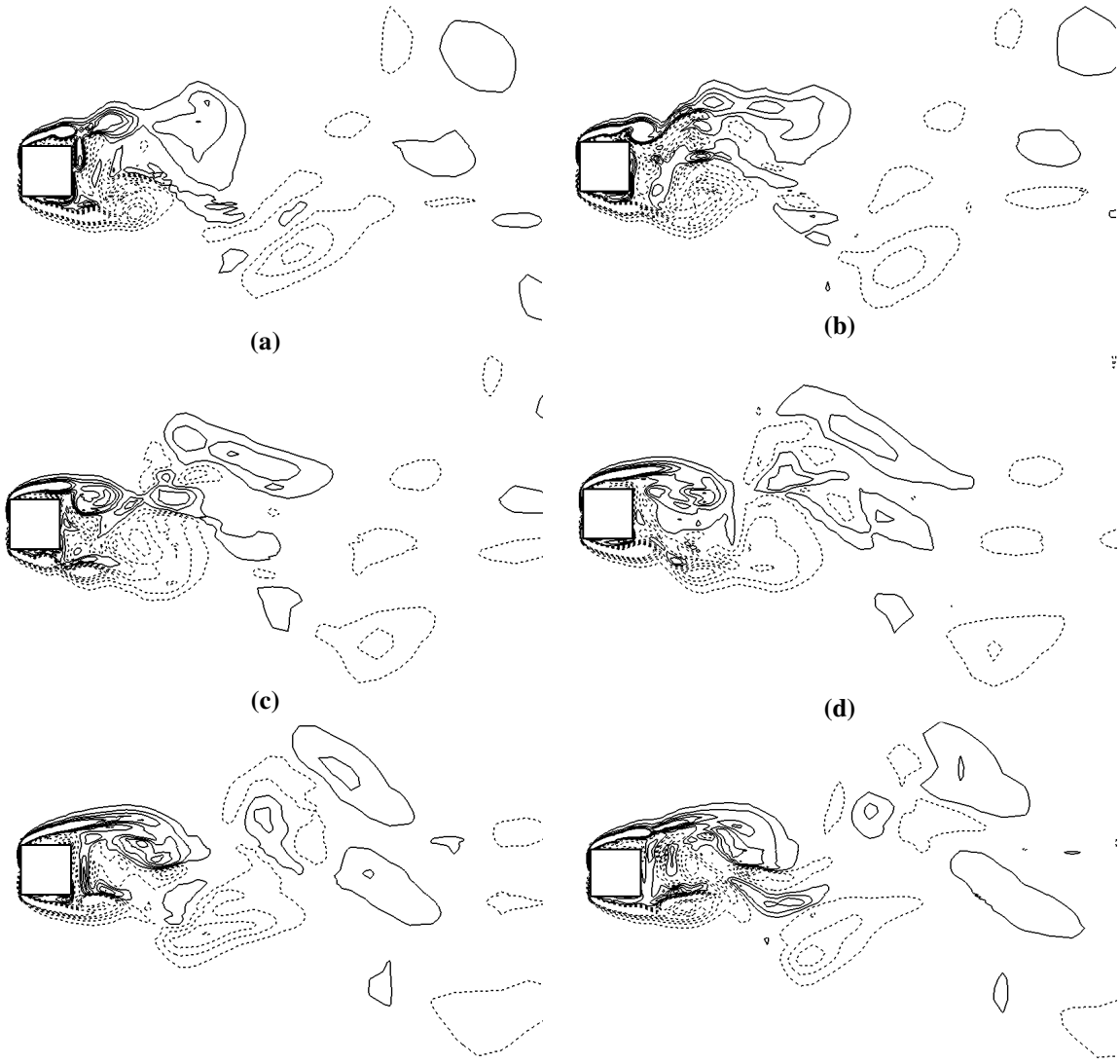

Figure 5.12: Instantaneous normal vorticity contours ω_z located at $z/D = 2$ for six consecutive time intervals: a) 1/6T, b) 2/6T, c) 3/6T, d) 4/6T, e) 5/6T, and f) T.

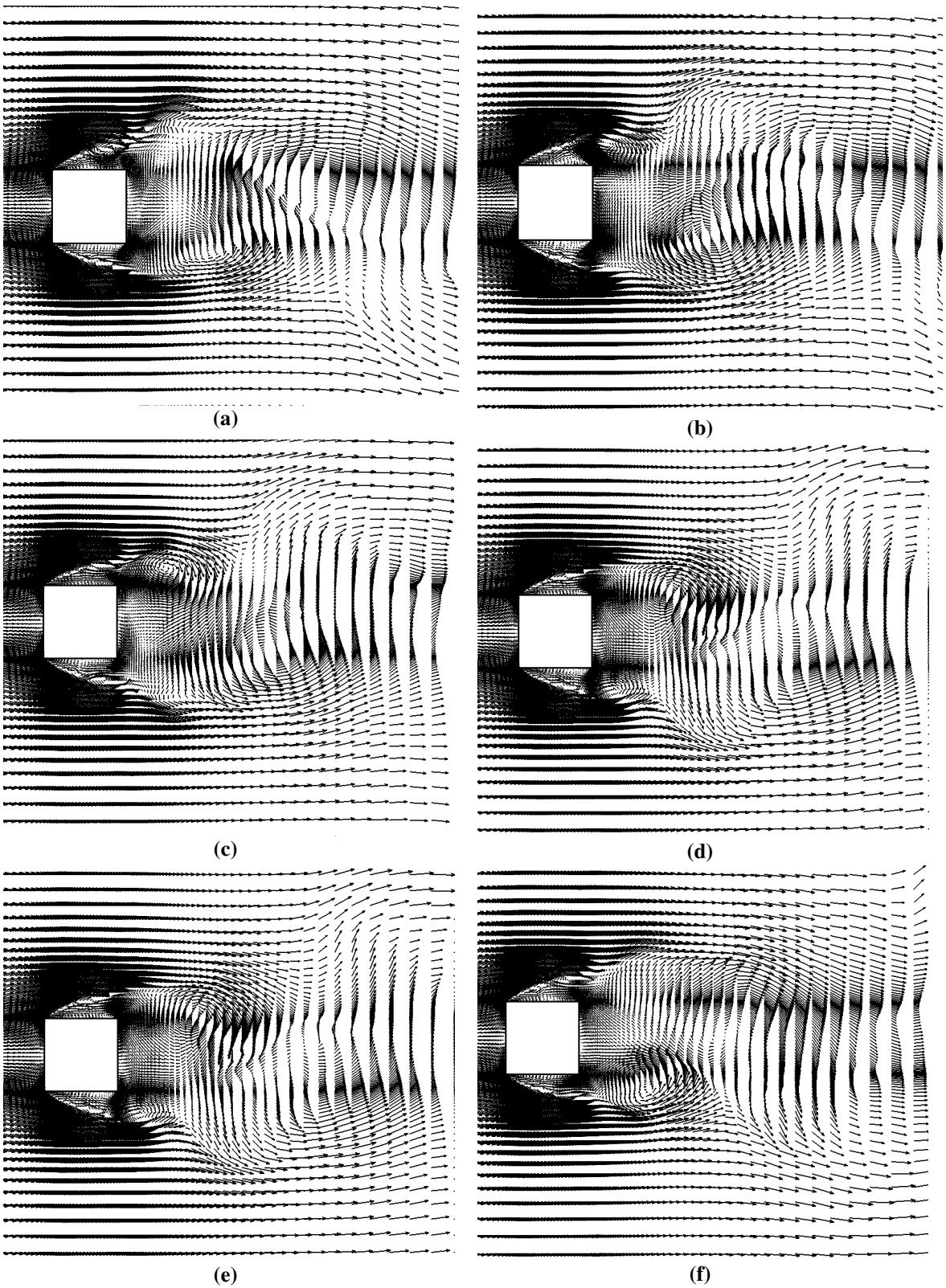

Figure 5.13: Instantaneous velocity vectors located at z/D = 1 for six consecutive time-steps: a) 1/6T, b) 2/6T, c) 3/6T, d) 4/6T, e) 5/6T, and f) T.

Figures 5.13 and 5.14 show the instantaneous velocity vectors and contours of the wall-normal vorticity ω_z, respectively, at $z/D = 1$. All of the features previously noted in Figures 5.11 and 5.12 are even more pronounced in Figures 5.13 and 5.14. Time variant von-Karman vortex shedding is observed downstream of the wall-mounted square cylinder. However, the size of the vortical structures is somewhat suppressed compared to those shown in Figure 5.12, which might be attributed to the influence of the friction forces on the ground plane.

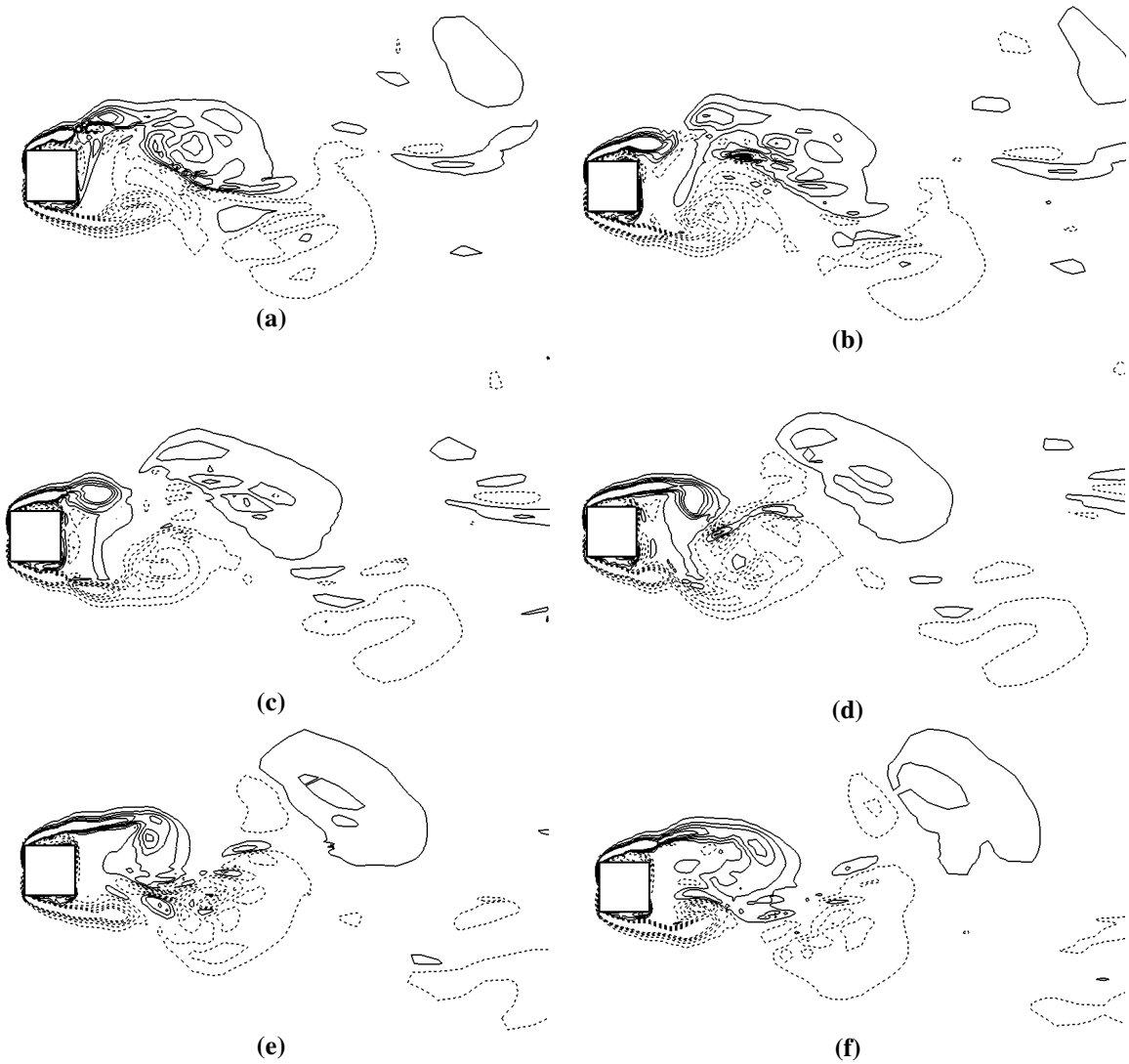

Figure 5.14: Instantaneous normal vorticity contours ω_z located at $z/D = 1$ for six consecutive time intervals: a) 1/6*T*, b) 2/6*T*, c) 3/6*T*, d) 4/6*T*, e) 5/6*T*, and f) *T*

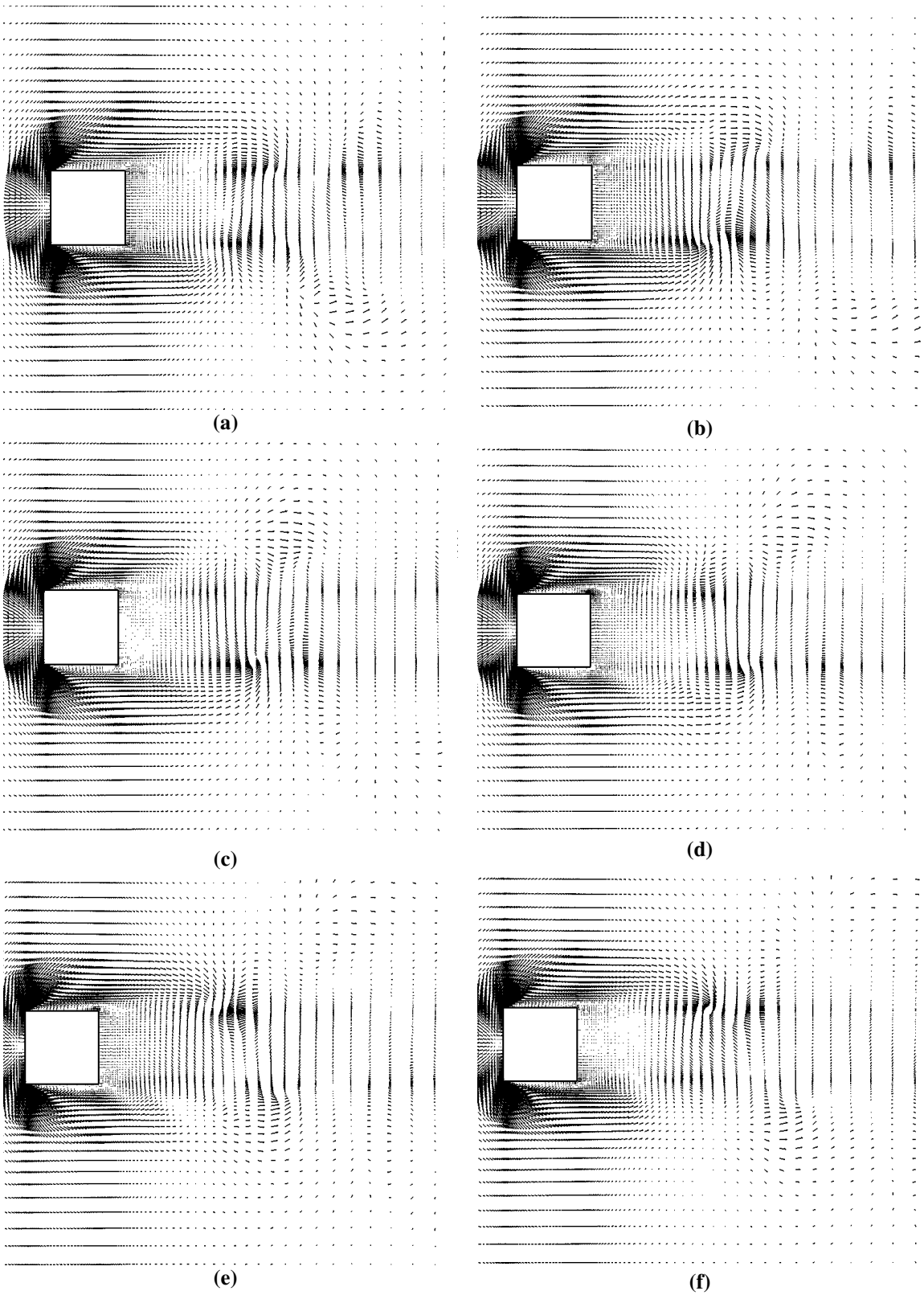

Figure 5.15: Instantaneous velocity vectors located at *z/D ~ 0* for six consecutive time intervals: a) 1/6*T*, b) 2/6*T*, c) 3/6*T*, d) 4/6*T*, e) 5/6*T*, and f) *T*.

Finally, Figures 5.15 and 5.16 show the instantaneous velocity vectors and contours of the normal vorticity ω_z, respectively, at $z/D \sim 0$, or just above the ground plane. In Figure 5.15, the velocity vectors indicate a much more regular flow structure and a much weaker velocity deficit in the wake. In Figure 5.16, the contours reveal a more symmetric vortex structure, although the shear layers from the sides of the cylinder still appear to be weakly shedding. Upstream of the front edges of the cylinder one can observe evidence of the horseshoe vortex on the ground plane. All of these effects may be attributed to the immediate presence of the ground plane.

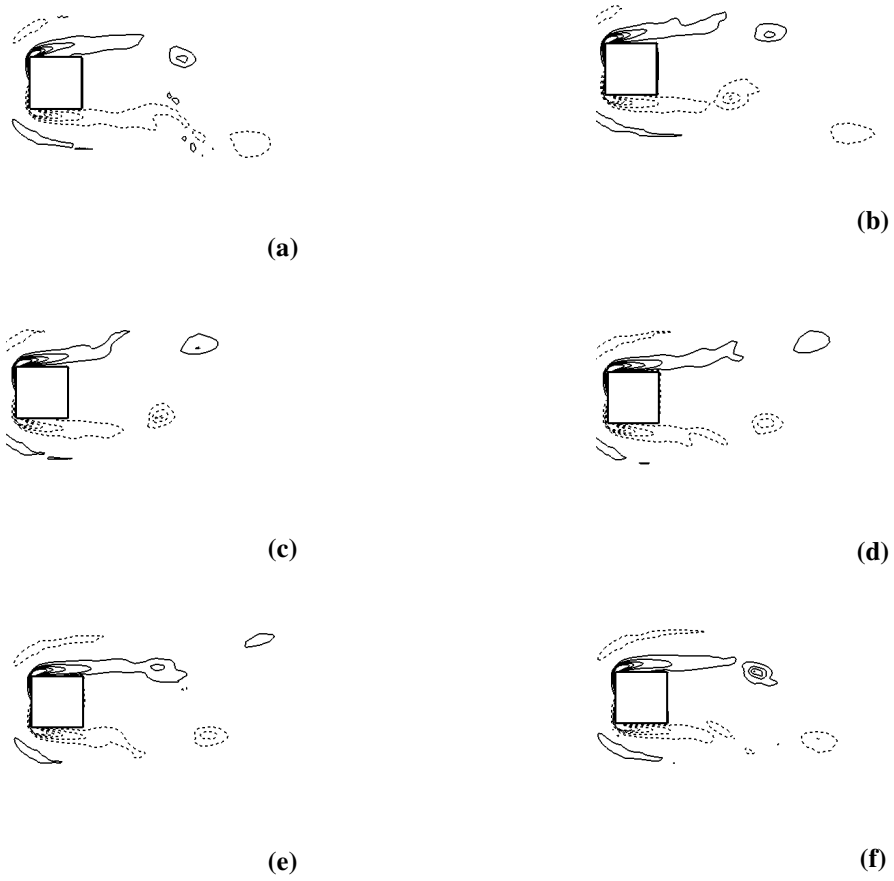

Figure 5.16: Instantaneous normal vorticity contours ω_z located at $z/D \sim 0$ for six consecutive time intervals: a) 1/6*T*, b) 2/6*T*, c) 3/6*T*, d) 4/6*T*, e) 5/6*T*, and f) *T*.

Kawamura et al. (1984) and Sakamoto and Arie (1983) introduced a theory based on the concept of critical aspect ratio, AR_c. Based on their theory, for $AR < AR_c$ the near-wake vortices are

dominated by the free end tip vortices and are of the symmetric arch-type. For $AR > AR_c$, near the free end the flow is still dominated by the tip vortices, but away from the tip, vortices are of the antisymmetric von-Karman type. For cylinders near the critical aspect ratio, i.e. for $AR \approx AR_c$, there is a combination of both symmetric and antisymmetric vortices. Note that near the free end, even for $AR > AR_c$, the vortices are symmetric. Wang and Zhou (2009) observed both antisymmetric von Karman-type vortices and symmetric arch-type vortices behind a wall-mounted finite-height square cylinder of AR = 7. Near the free end, however, the symmetric arch type vortices were dominant. Based on the flow behavior shown in Figures 5.5 to 5.16, the near-wake vortices near the free end are of the symmetric arch-type, which is in agreement with the theory of Kawamura et al. (1984) and Sakamoto and Arie (1983). Away from the tip, the near-wake vortices begin to be dominated by antisymmetric von-Karman type vortices, and this behavior becomes specially pronounced in the lower region.

5.5. Development of the Instantaneous Flow Field in the Spanwise Direction

The next set of figures also considers the instantaneous velocity field over a set of time intervals that spans one period. In this case, the spanwise and wall-normal velocity components and streamwise vorticity are investigated using vertical planes located in the wake of the cylinder at different streamwise distances from the cylinder.

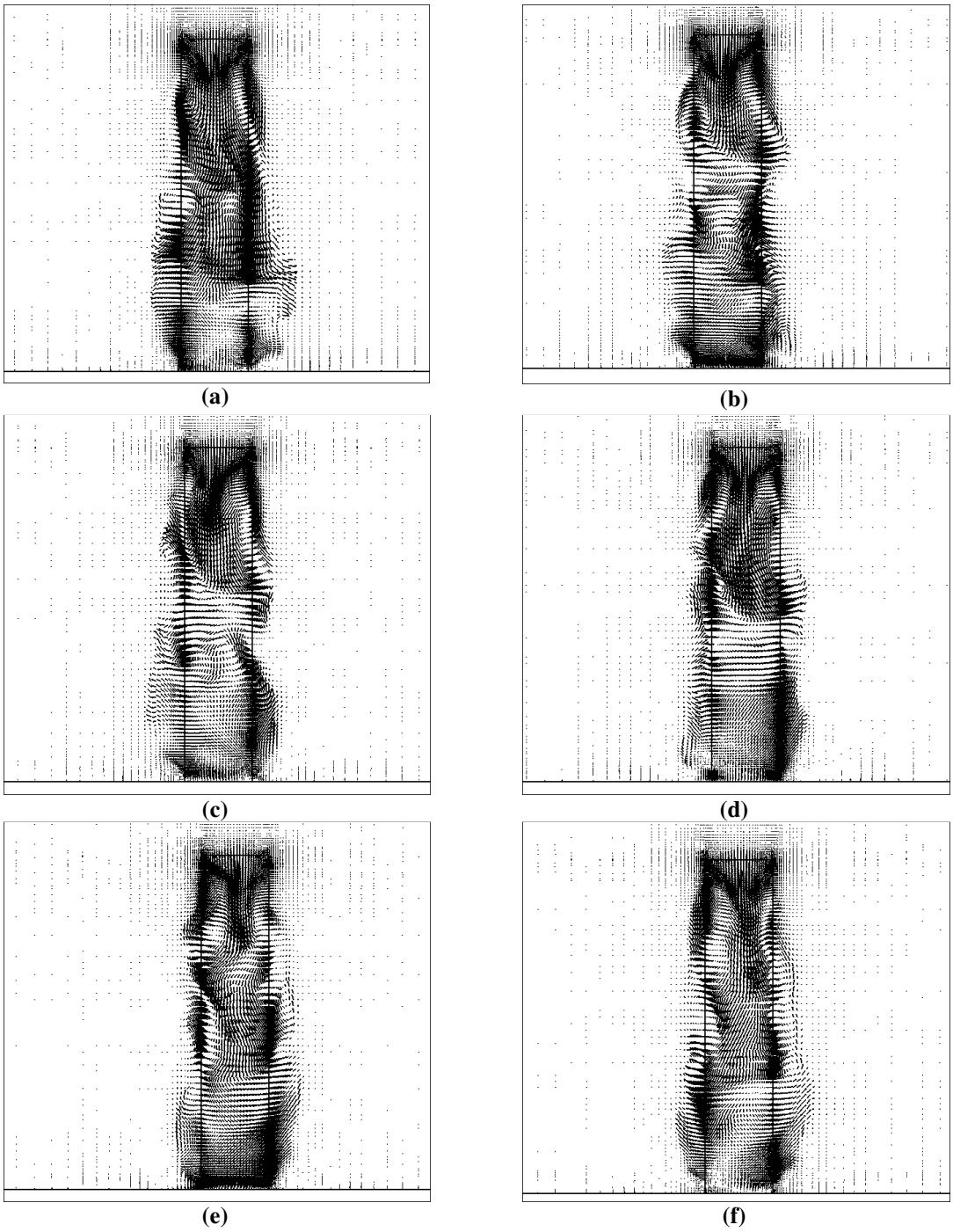

Figure 5.17: Instantaneous velocity vectors located at x/D = 1 for six consecutive time intervals: a) 1/6T, b) 2/6T, c) 3/6T, d) 4/6T, e) 5/6T, and f) T.

Figures 5.17 and 5.18 show the instantaneous velocity vectors and streamwise vorticity contours, ω_x, in a vertical plane located at x/D = 1. Both figures indicate a complex flow field that changes significantly over the time interval considered. There is no strong evidence of periodicity in the

flow. A pair of tip vortices is formed near the free end. The tip vortices are relatively symmetric at all time steps. A pair of very weak vortices is formed above the tip vortices with opposite sign. A series of vortex structures extends all the way from the free end to the ground plane, often centered near the side walls. A pair of vortices is observed near the ground plane for all six time steps which may be interpreted as the base vortices; their direction of rotation is opposite to that of the tip vortices. Note that although the instantaneous vortex structure is dynamic and changing in time, overall it retains the tip and base vortex structure which characterized the time-average flow (see Figure 4.19). However, in the lower region there is some indication of periodic behavior, i.e. positive and negative vortex structures occupy the same location at different times.

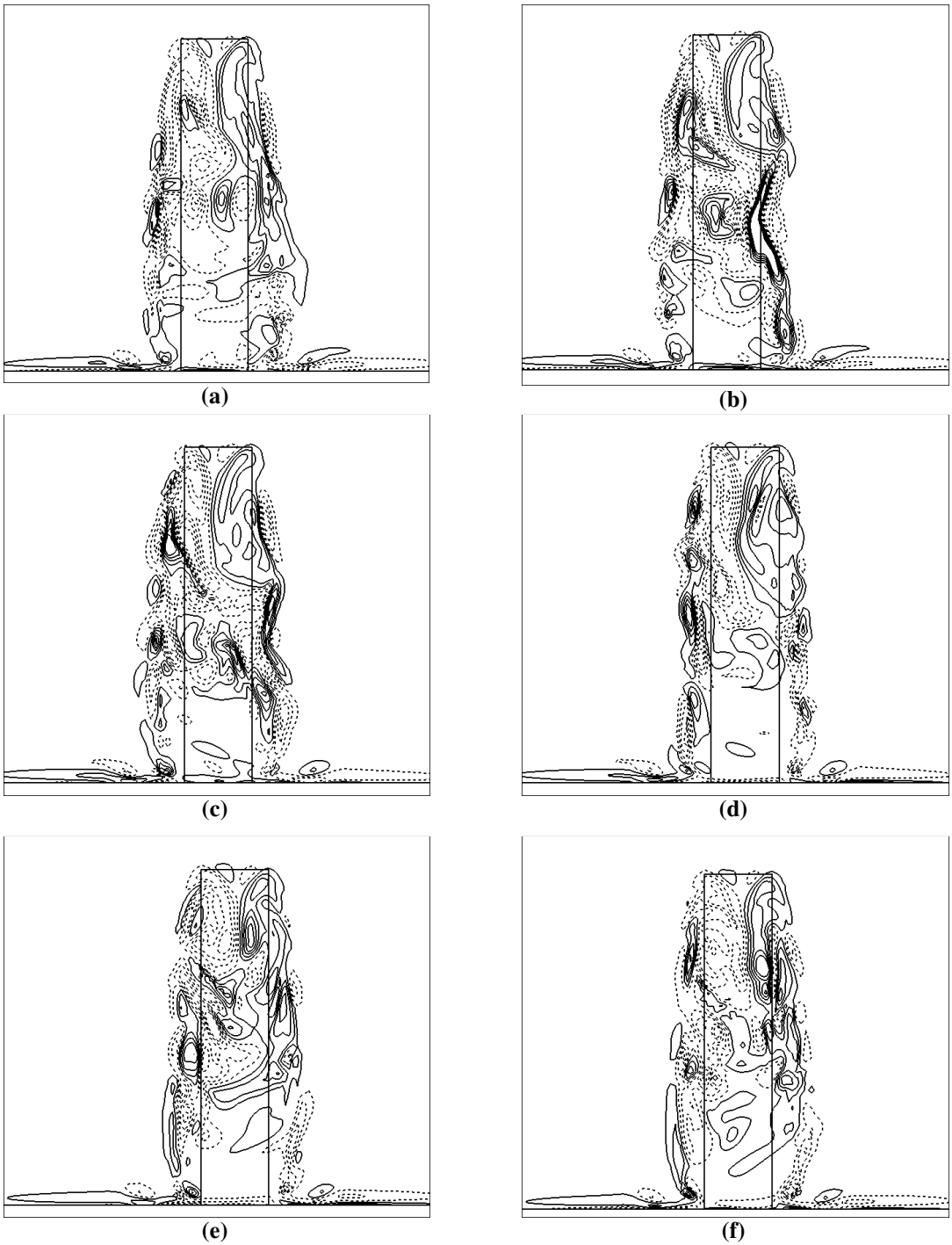

Figure 5.18: Instantaneous streamwise vorticity ω_x contours located at x/D = 1 for six consecutive time intervals: a) 1/6T, b) 2/6T, c) 3/6T, d) 4/6T, e) 5/6T, and f) T.

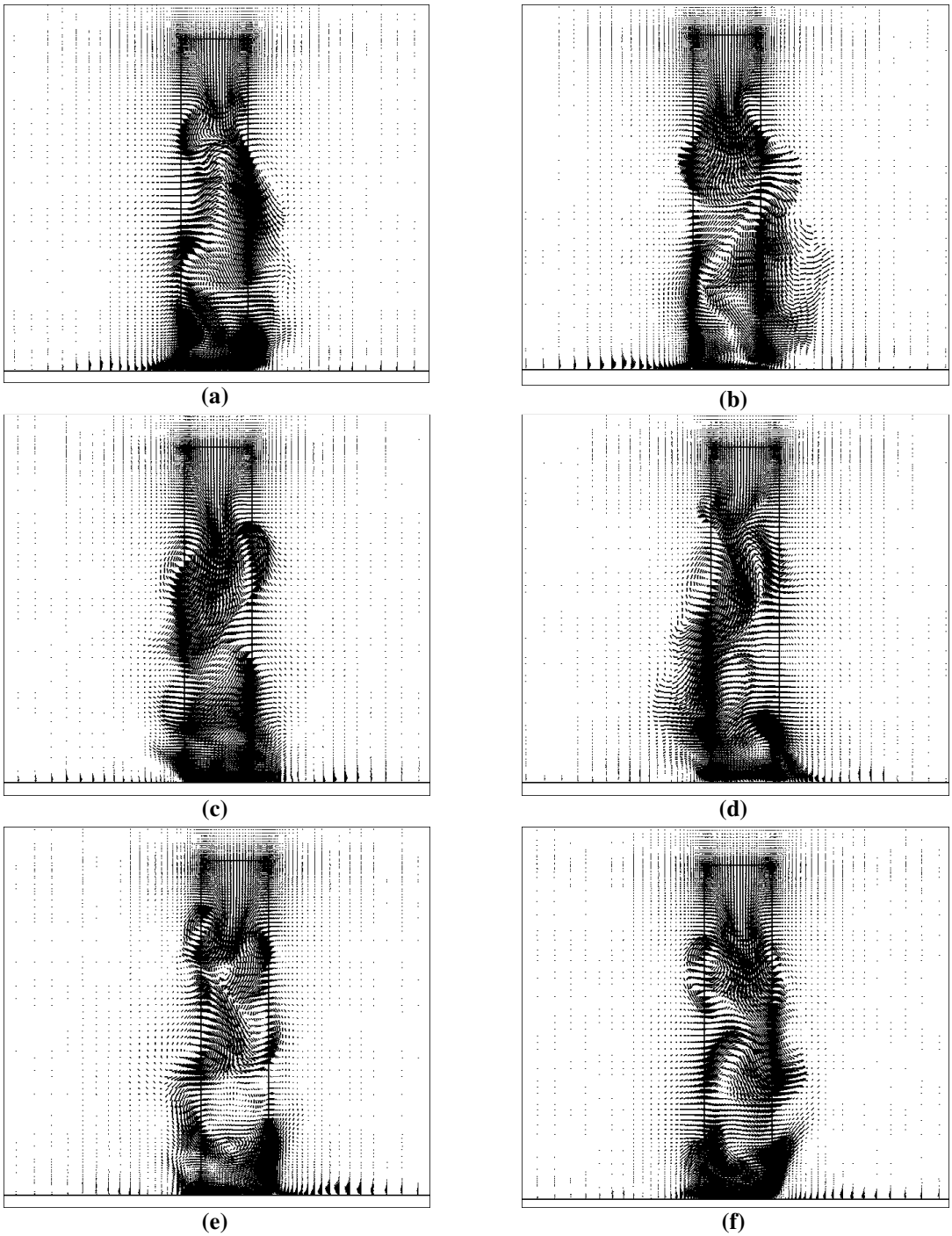

Figure 5.19: Instantaneous velocity vectors located at x/D = 2 for six consecutive time intervals: a) 1/6T, b) 2/6T, c) 3/6T, d) 4/6T, e) 5/6T, and f) T.

Figures 5.19 and 5.20 show the instantaneous velocity vectors and streamwise vorticity contours, ω_x, in a vertical plane located at x/D = 2 for six different time intervals. The velocity vectors indicate a stronger and more active flow pattern. The velocity field presented in Figure 5.19

shows strong motions further away from the free end of the cylinder, causing the entire wake to move in a periodic fashion across the centreline. The tip vortices have grown larger and have moved away from the free end towards the ground plane compared to $x/D = 1$. The additional pair of vortices which was observed above the tip vortices for $x/D = 1$ has disappeared. The vertical series of vortices observed at $x/D = 1$ is no longer concentrated near the side walls, and has extended into the central part of the cylinder wake. The base vortices are extended further upward towards the mid-height of the cylinder.

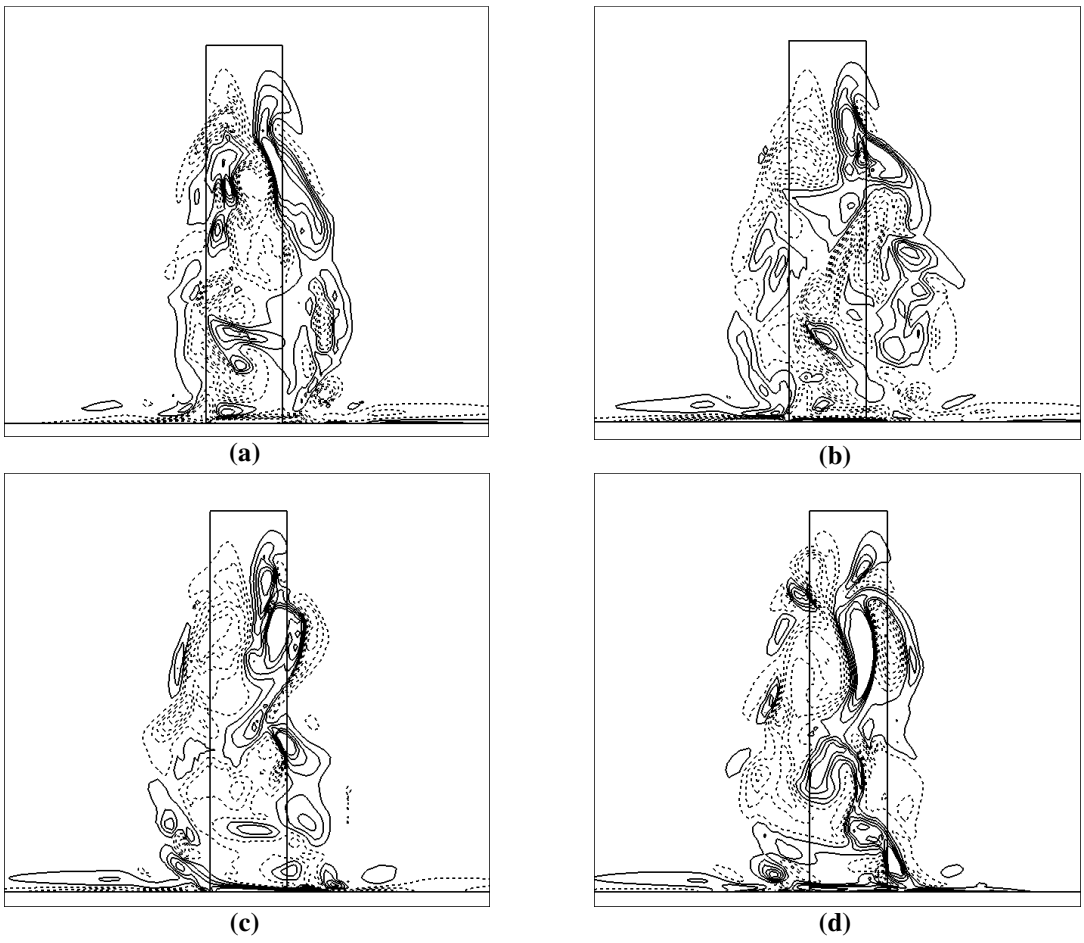

(a) **(b)** **(c)** **(d)**

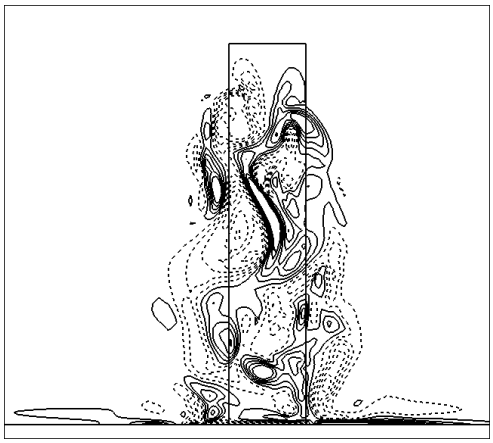

(e)

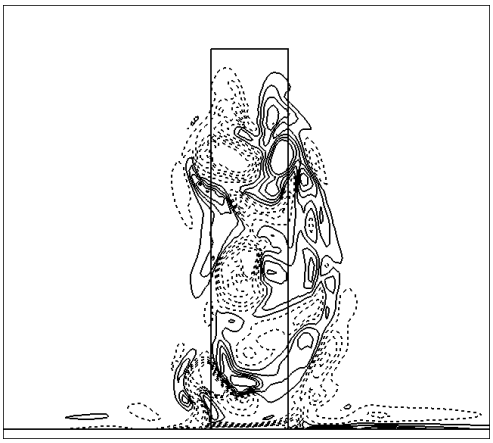

(f)

Figure 5.20: Instantaneous streamwise vorticity contours ω_x located at x/D = 2 for six consecutive time intervals: a) 1/6T, b) 2/6T, c) 3/6T, d) 4/6T, e) 5/6T, and f) T.

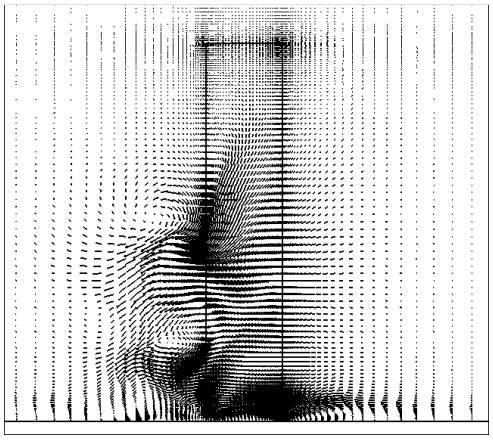

(a)

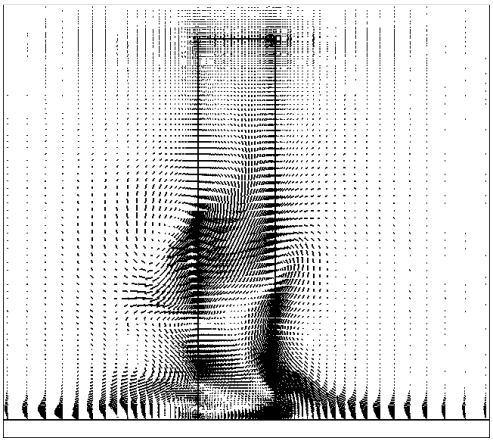

(b)

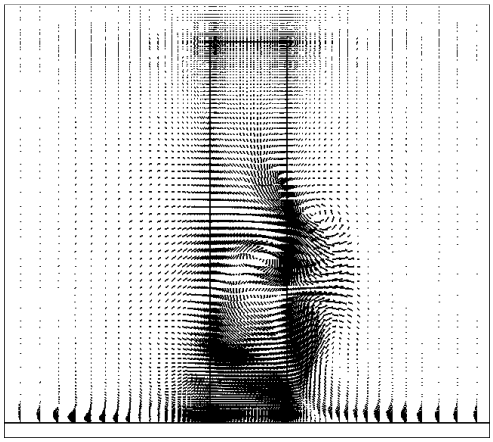

(c)

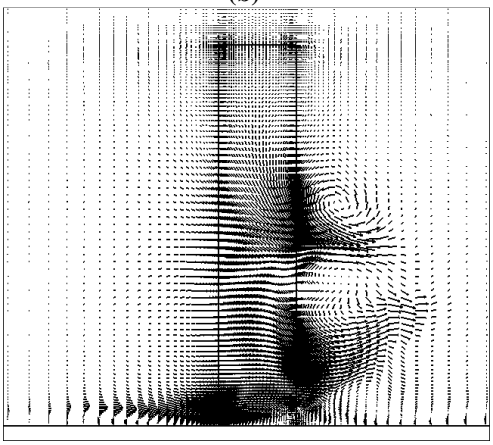

(d)

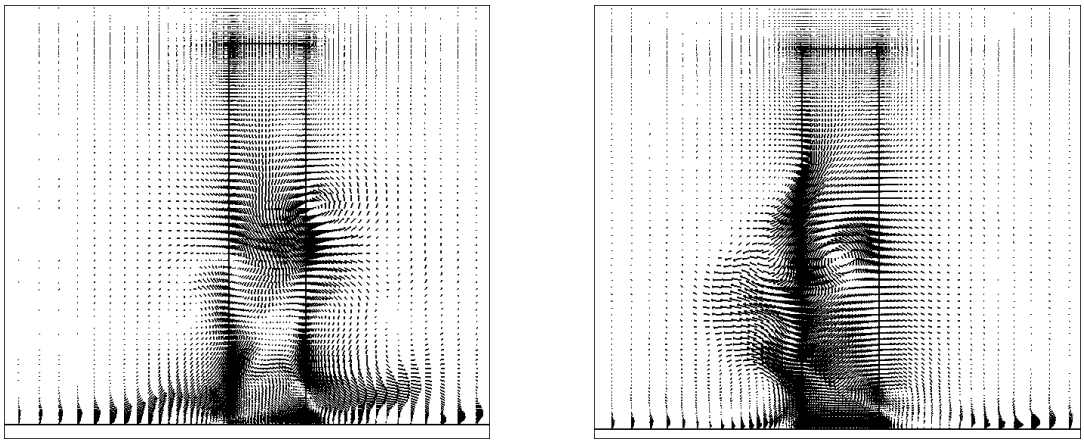

(e) (f)

Figure 5.21: Instantaneous velocity vectors located at x/D = 4 for six consecutive time intervals: a) 1/6T, b) 2/6T, c) 3/6T, d) 4/6T, e) 5/6T, and f) T.

Figures 5.21 and 5.22 show the instantaneous velocity vectors and the streamwise vorticity contours, ω_x, in a vertical plane located at x/D = 4 at six different time intervals. Note that this location is close to the downstream edge of time-average recirculation zone directly behind the cylinder. The velocity field in Figure 5.21 shows strong and irregular motions, which extend relatively far away from the cylinder centreline in the cross-stream direction, especially along the ground plane, where narrow jets moving into and out of the wake are also observed. The pair of tip vortices that had been observed at the two previous sections appears quite different: these vortices are neither symmetric nor near the free end. The vorticity distribution is entirely antisymmetric and concentrated on different sides of the cylinder at different times. For example, the location of these vortices has moved from left hand side in Figure 5.22(a) to the right hand side in Figure 5.22(d) and then returns to the left hand side in Figure 5.22(f), which may be indicative to some degree of periodic motion. The vortices have expanded significantly in the spanwise direction.

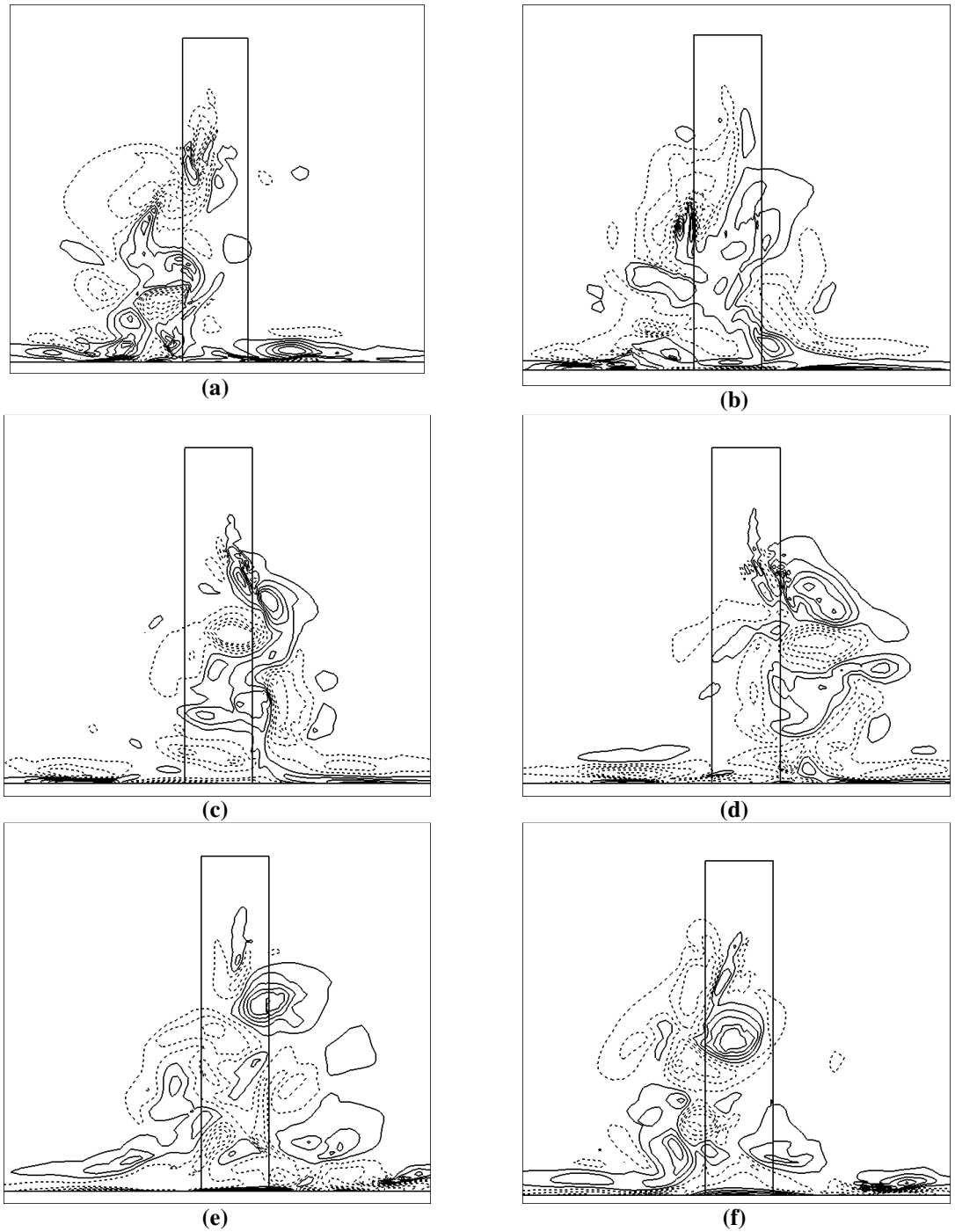

Figure 5.22: Instantaneous streamwise vorticity contours ω_x located at x/D = 4 for six consecutive time intervals: a) 1/6T, b) 2/6T, c) 3/6T, d) 4/6T, e) 5/6T, and f) T.

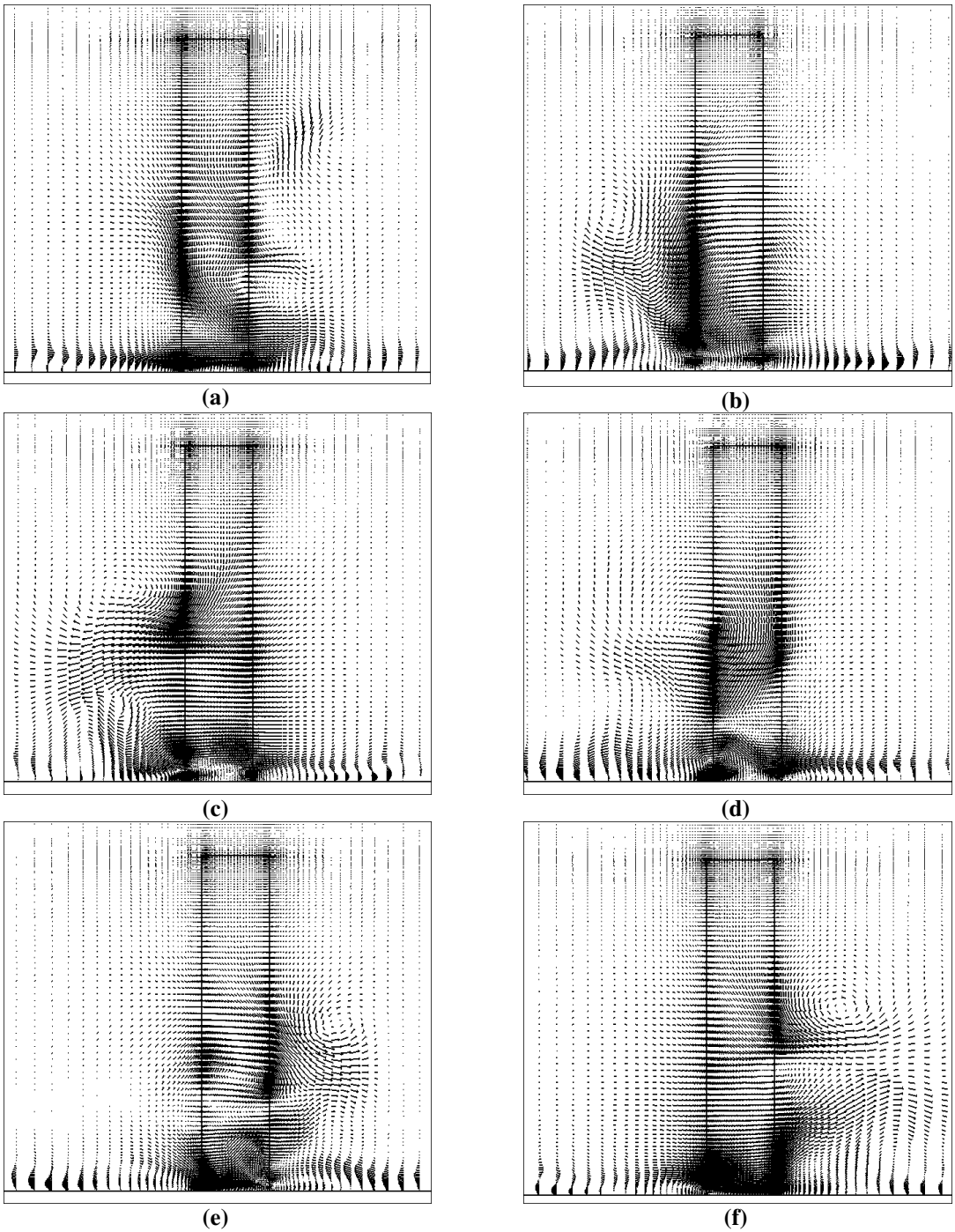

Figure 5.23: Instantaneous velocity vectors located at x/D = 6 for six consecutive time intervals: a) 1/6T, b) 2/6T, c) 3/6T, d) 4/6T, e) 5/6T, and f) T.

Figures 5.23 and 5.24 show the instantaneous velocity vectors and the streamwise vorticity contours, ω_x, in a vertical plane located at x/D = 6. The velocity vectors indicate a weaker and more diffuse flow pattern. As shown in Figures 5.23 and 5.24, the shear layer tends to sweep

across the central plane, and streamwise vorticity is observed to move from one side to the other side of the cylinder. This motion is in some ways periodic. A similar flow pattern was observed in the wake of an infinite cylinder (Wu et al., 1996). Wang and Zhou (2009), who observed a similar flow pattern for flow over a wall mounted square cylinder of AR = 7, suggested that these flow patterns may correspond to the roll-up of the spanwise shear layer sweeping across the central plane. On the other hand, Figures 5.23(d) and 5.24(d) present two pairs of highly distorted counter-rotating vortices, similar to what was observed in the near-wake region, one pair originating from the free end of the cylinder and the other pair near the ground plane.

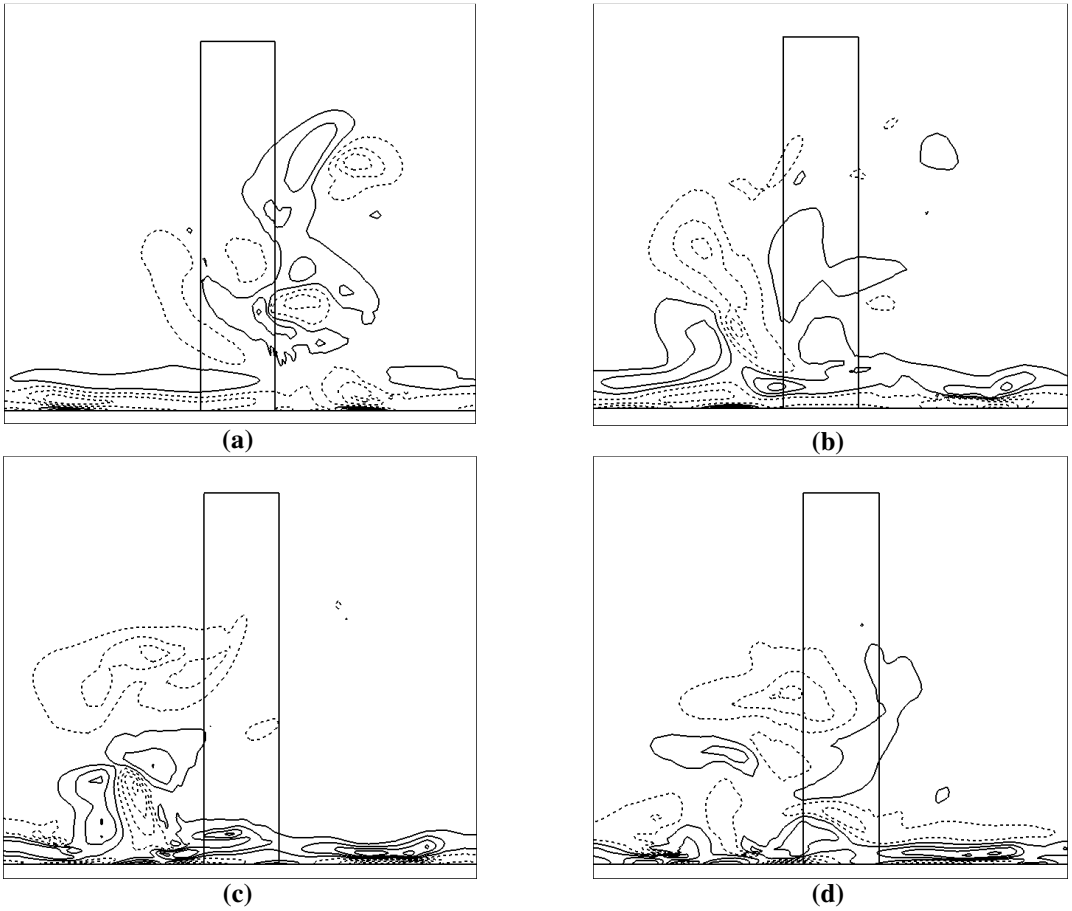

(a) **(b)** **(c)** **(d)**

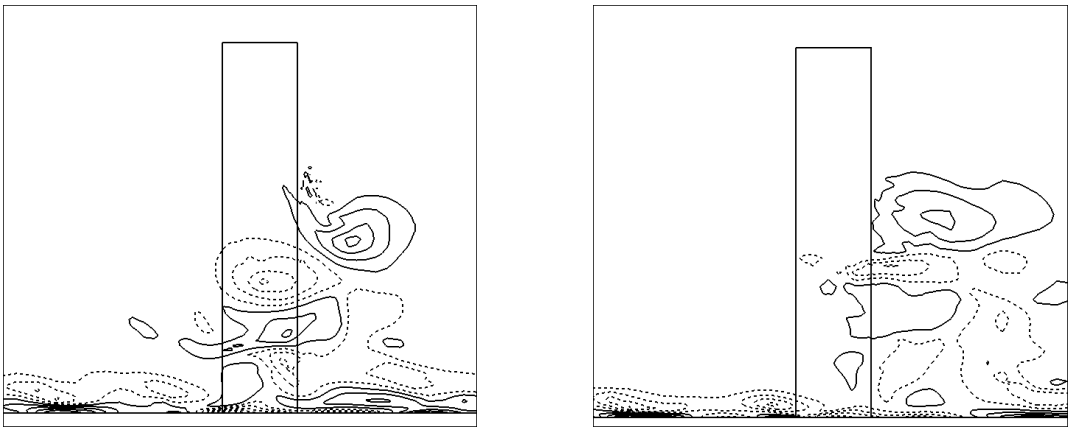

(e) (f)

Figure 5.24: Instantaneous streamwise vorticity contours ω_x located at x/D = 6 for six consecutive time intervals: a) 1/6T, b) 2/6T, c) 3/6T, d) 4/6T, e) 5/6T, and f) T.

According to the set of figures above, as the flow moved downstream, the vortices became weaker, and the vortex centers slowly moved away from the free end towards the ground plane. For a finite circular cylinder of AR = 5, Sumner et al. (2004) observed a similar behavior for the time-averaged streamwise vortices at x/D = 4, 6, 8 and 10. They also noted that as the flow moves downstream, the vortices become more rounded in shape. Park and Lee (2000) obtained the vortex structure very close to a circular cylinder of AR = 6 at x/D = 0, 0.25 and 0.6 and observed similar behavior in the near-wake region. Wang et al. (2004) showed that for a square cylinder of AR = 5, at x/D = 1, 3 and 5, as the flow moves downstream, the vortices became weaker and also larger. Interestingly, in their study, while the base vortices decay with increasing x/D, the tip vortices became stronger as the flow proceeded downstream reaching a maximum value at x/D = 3.

5.6. Second Invariant Iso-Surfaces of the Instantaneous Velocity Field

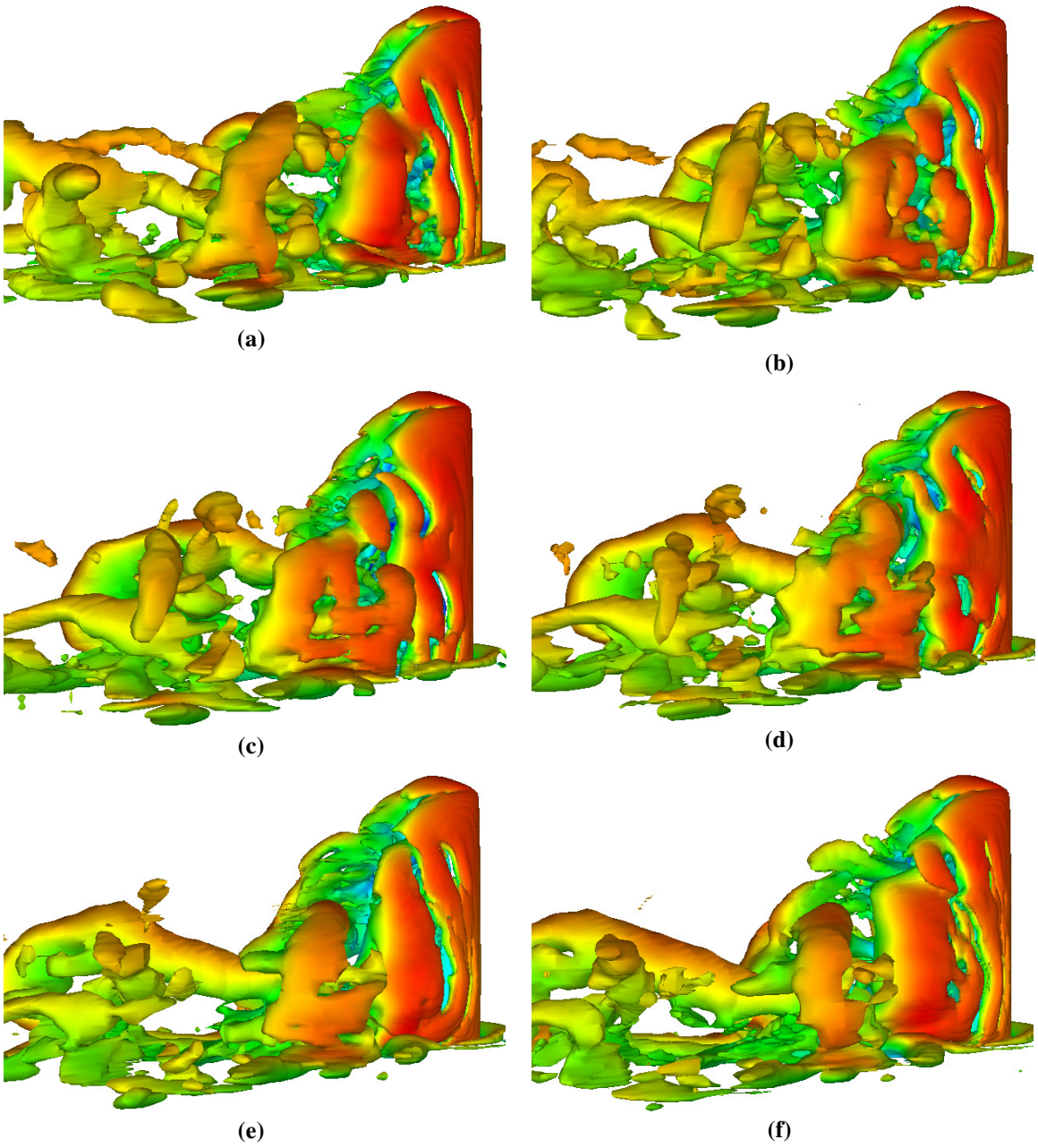

Figure 5.25: Instantaneous 2nd invariant iso-surfaces for six consecutive time-steps: a) 1/6*T*, b) 2/6*T*, c) 3/6*T*, d) 4/6*T*, e) 5/6*T*, and f) *T*.

Figures 5.25 and 5.26 show iso-surfaces of the second invariant of the instantaneous velocity field at six consecutive time-steps. These surfaces reveal a complex network of vortex tubes aligned in different directions, but retaining a similar pattern. A strong downwash is observed,

particularly near the free end. Even for the instantaneous field, symmetric structures are observed near the free end. The streamwise structures formed near the free end tilt downwards and connect to the vertical structures shed from the sides. The wake region is much larger compared to the time-averaged flow field (see Figure 3.14(b)), as the vortex structures are expanded in the cross-stream direction in the instantaneous flow field. The growth of the structures in the transverse direction is especially evident in Figure 5.26. The wake region is also observed to extend further in the streamwise direction. Near the ground plane, some quasi-antisymmetric behaviour with time-periodic features is observed in the vortex structures, which may indicate Kármán vortex shedding in the near-wake region.

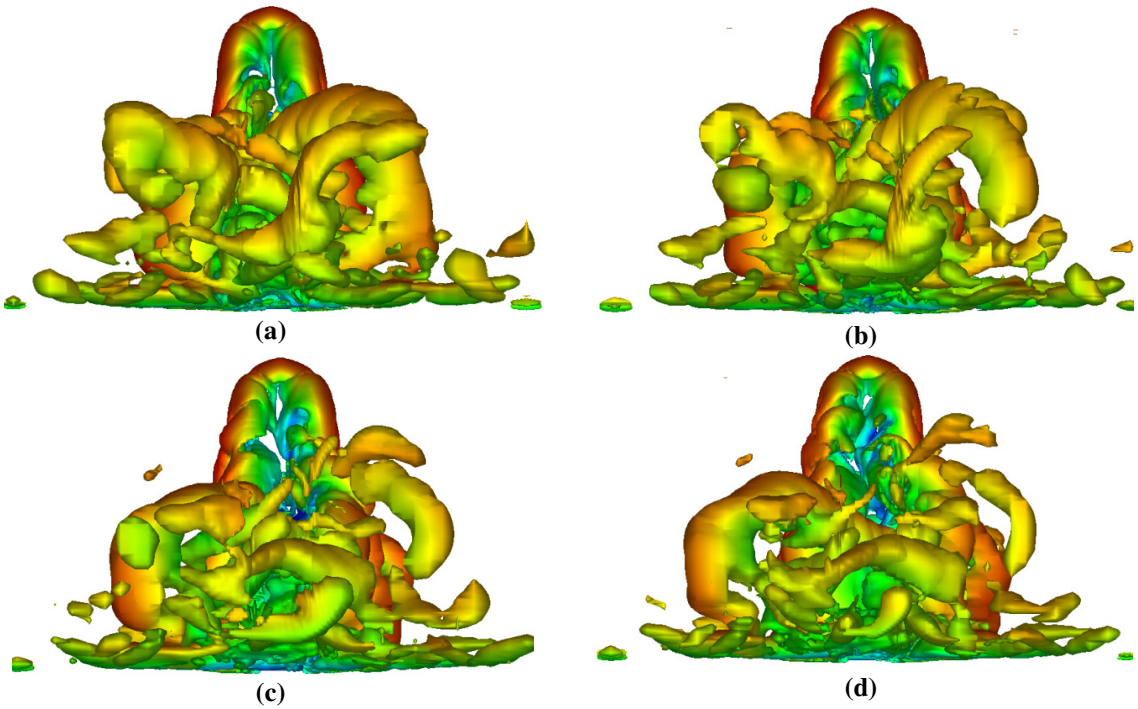

(a) **(b)** **(c)** **(d)**

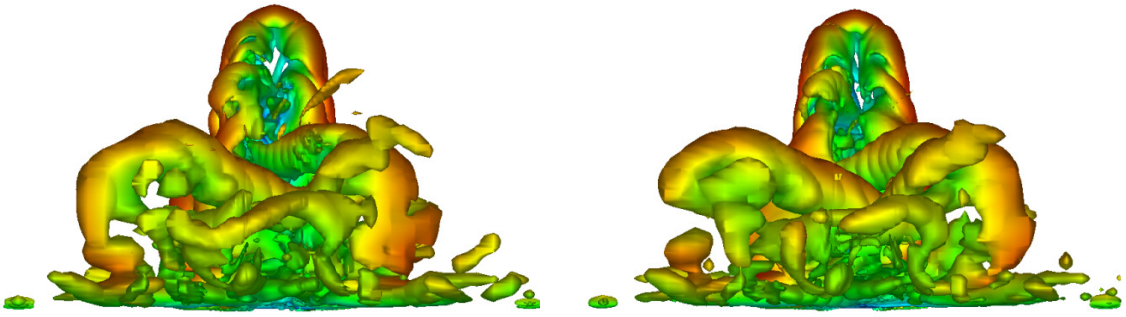

(e) (f)

Figure 5.26: Instantaneous 2nd invariant Iso-surfaces for six consecutive time-steps: a) 1/6*T*, b) 2/6*T*, c) 3/6*T*, d) 4/6*T*, e) 5/6*T*, and f) *T*.

5.7. Conclusion

The instantaneous velocity fields from LES of flow over a wall-mounted finite-height square cylinder with AR = 5 have been presented. A Strouhal number of St = 0.127 was obtained for three sample locations along the height of the cylinder, which is in a good agreement with the experimental measurements.

The instantaneous flow fields were characterized by the strong downwash flow from the free end interacting with a weak upwash flow originating from the ground plane. Two distinct flow fields are observed: in the first scenario the free end downwash flow met the upwash flow from the ground plane and was limited to the upper half of the wake, and only one saddle point was observed. The second scenario involved a more complex flow pattern with multiple saddle and focal points.

The instantaneous velocity fields suggest a symmetric flow near the free end. However, further downstream from the cylinder, the velocity field in the wake becomes strongly antisymmetric. The antisymmetric patterns observed downstream may be an indication of the presence of periodic von-Karman type vortices.

The streamwise vorticity contours in a normal plane located at various distances from the cylinder indicate that as the flow moved downstream, the vortex structures became weaker and concentrated closer to the ground plane. The structures also extended in the transverse direction, and exhibited the asymmetry observed in the velocity vector fields.

Chapter 6

Sub-grid Scale Modeling Effect

6.1. Introduction

In this chapter the solutions of three different SGS models are studied for a square cylinder with AR = 5 at Re = 500. The SM, DSM and DNM are performed on two different grids, a coarse grid of 64 × 72 × 48 control volumes and a fine grid of 128 × 144 × 96 control volumes to investigate the sensitivity of the SGS model to grid resolution. Table 6.1 summarizes the minimum and maximum residuals for both coarse and fine grids.

Table 6.1: Minimum and maximum residuals for both coarse and fine grids.

		dx/D	*dy/D*	*dz/D*
Fine Grid	min	1.15E-02	1.30E-02	1.01E-02
	max	5.75E-01	3.29E-01	5.75E-01
Coarse Grid	min	2.50E-02	2.79E-02	2.20E-02
	max	1.02E+00	5.40E-01	4.01E-01

Both time-averaged and instantaneous flow fields are presented. Streamlines, velocity vectors, and contours of velocity, eddy viscosity and vorticity are presented for various planes, while iso-surfaces of the 2nd invariant are employed to visualize the flow field in three dimensions.

6.2. Time-Averaged Streamlines of a Flow Field

Figure 6.1 shows the time-averaged velocity field along the centreline of the wake, corresponding to $y/D = 0$. In this figure, the predictions on both the coarse and fine grids are presented for each SGS model. The streamline patterns for all simulations share a common

structure. For example, there is a strong downwash component to the velocity field that originates from the free end of the cylinder and extends in the streamwise direction (Sumner et al., 2004). A much weaker upwash is observed near the ground plane. The streamlines indicate the presence of a horseshoe vortex in front of the cylinder at the junction of the cylinder with the ground plane, although in some cases it is not well resolved. Comparing the fine grid simulations presented in Figure 6.1 reveals that the maximum streamwise extent of the recirculation zone is observed for the SM solution, while the wake region predicted by the DSM has the smallest streamwise extent. The two dynamic SGS models, i.e. the DSM and DNM solutions are more similar to each other than to the SM prediction.

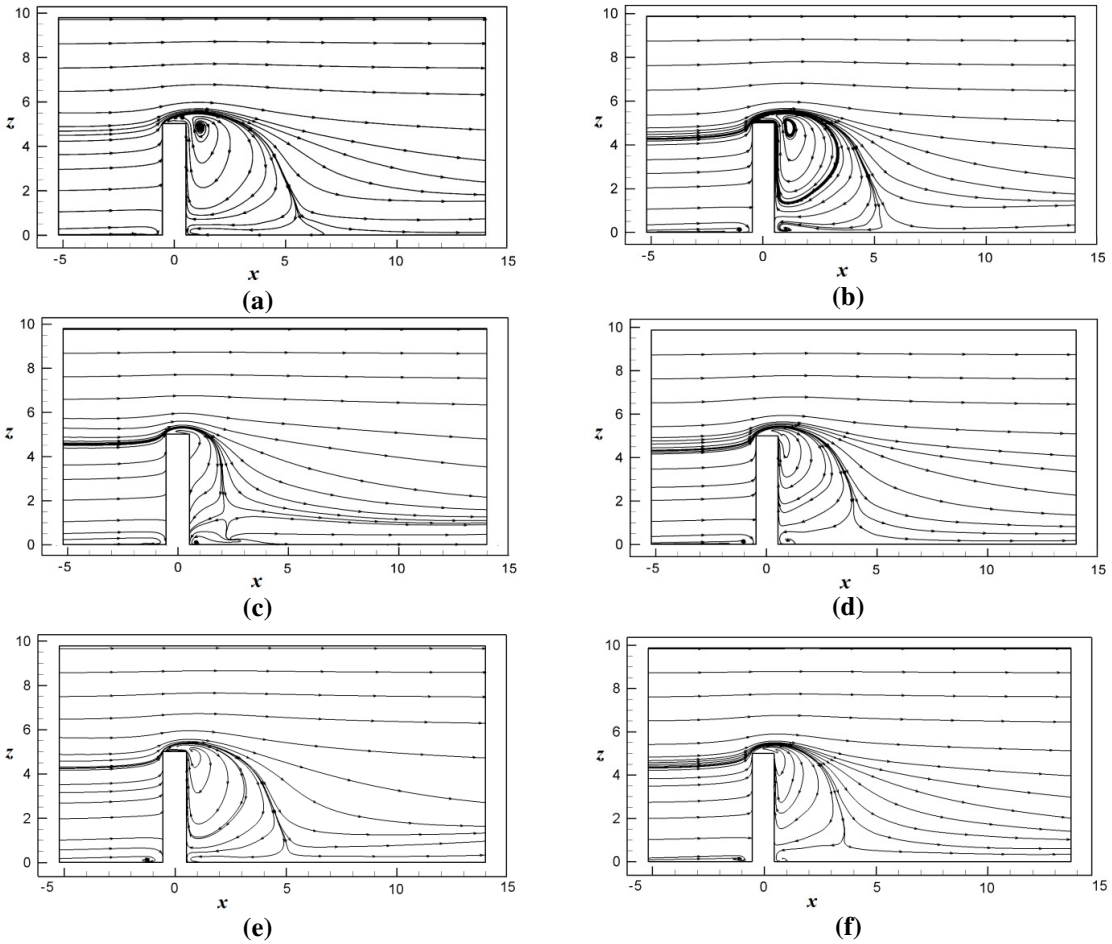

Figure 6.1: Time-averaged streamlines in the center-plane: a) SM coarse grid, b) SM fine grid, c) DSM coarse grid, d) DSM fine grid, e) DNM coarse grid, f) DNM fine grid.

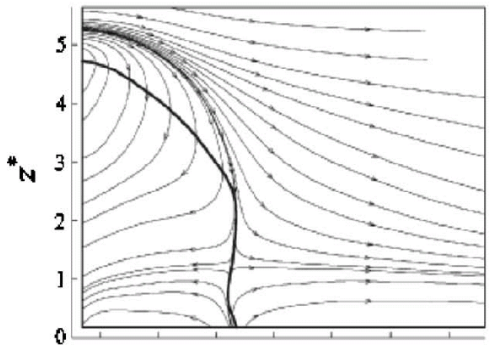

Figure 6.2: Time-averaged sectional streamlines in the *x*-*z* plane at *y*/*D* = 0 from Wang et al. (2006).

Figure 6.2 presents similar streamlines based on a PIV study by Wang et al. (2006) for the case of a square cylinder with the same aspect ratio and a relatively thin boundary layer (case 1) at a much higher Reynolds number of approximately Re = 11,500. Although the recirculation zone in the wake is similar, there are also important differences; most notably the upwash obtained by Wang et al. (2006) is slightly stronger than predicted by the LES's. In Chapter 4, a more comprehensive comparison was presented between the DSM solution on the fine grid and these experimental measurements.

Unlike the other two SGS models, the DSM on a coarser grid is unable to accurately predict the wake region, and instead the streamwise extent of the predicted recirculation zone is much smaller than for both other cases. There is also an absence of upwash along the rear surface of the cylinder. For this model, insufficient grid resolution has a severe effect on the predicted recirculation region. According to Frohlich and Rodi (2004), this behaviour comes from the fact that for the DSM, the test filter operation projects the velocity onto a coarser grid. Surprisingly, for the DNM, which also uses a test filter operation, the insufficient resolution only results in a slightly larger recirculation region.

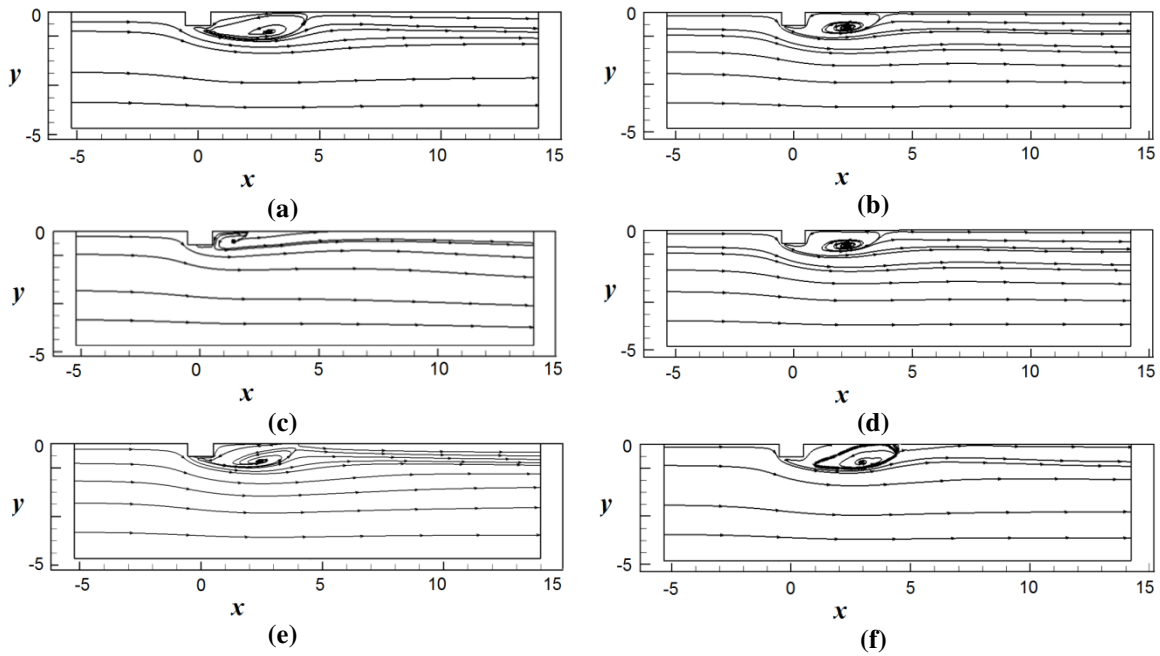

Figure 6.3: Time-averaged streamlines in a plane at *z/D* = 2.5: a) SM coarse grid, b) SM fine grid, c) DSM coarse grid, d) DSM fine grid, e) DNM coarse grid, f) DNM fine grid.

Figure 6.3 shows the streamlines of the time-averaged velocity field of the wake in a plane located at $z/D = 2.5$ from the ground plane. Since the time-averaged wake velocity field consists of two symmetric recirculation zones, only half the domain is shown in Figure 6.3. The streamline plots show that the shear layers separating from the cylinder are drawn toward the symmetry plane behind the cylinder, leading to the formation of a recirculation region. As noted above, the DSM exhibits a strong sensitivity to level of grid resolution that is not apparent in the simulations using the other two models. On the fine grid, the SM solution exhibits the largest recirculation region.

6.3. Time-Averaged Normal Vorticity Contours

Figure 6.4 presents the time-averaged normal vorticity contours (in the z direction) in a plane located at $z/D = 2.5$ for all six cases. Since these contours also exhibit a symmetric behavior, only half the domain is shown in Figure 6.5.

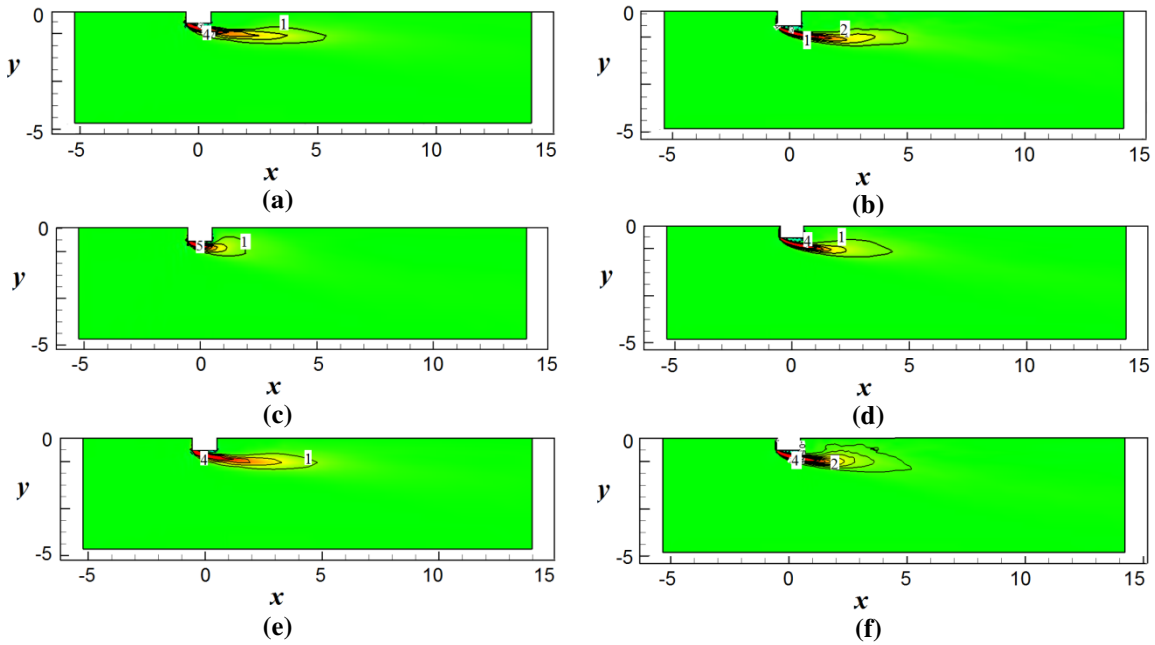

Figure 6.4: Time-averaged normal vorticity contours ω_z/U_∞ in a plane located at z/D = 2.5: a) SM coarse grid, b) SM fine grid, c) DSM coarse grid, d) DSM fine grid, e) DNM coarse grid, f) DNM fine grid.

With respect to grid resolution effects, as before the DSM predicts a much smaller vortex structure on the coarse grid. On the fine grid, the vortex structure predicted by all three models is very similar. The peak normal vorticity occurs at the front corners of the square cylinder, and as the flow moves downstream, the vorticity spreads in the spanwise direction. The vorticity is associated with the extension of the separating shear layers and is concentrated along the boundary of the recirculating flow and the external uniform flow. The recirculating flow behind the cylinder only exhibits a low level of vorticity.

6.4. Resolved Reynolds Stresses

The next set of figures will explore the level of the resolved fluctuating velocity components in plane sections through the wake of the cylinder. Recall that the time-averaged product of the resolved-scale velocity fluctuations can also be regarded as a resolved-scale Reynolds stress.

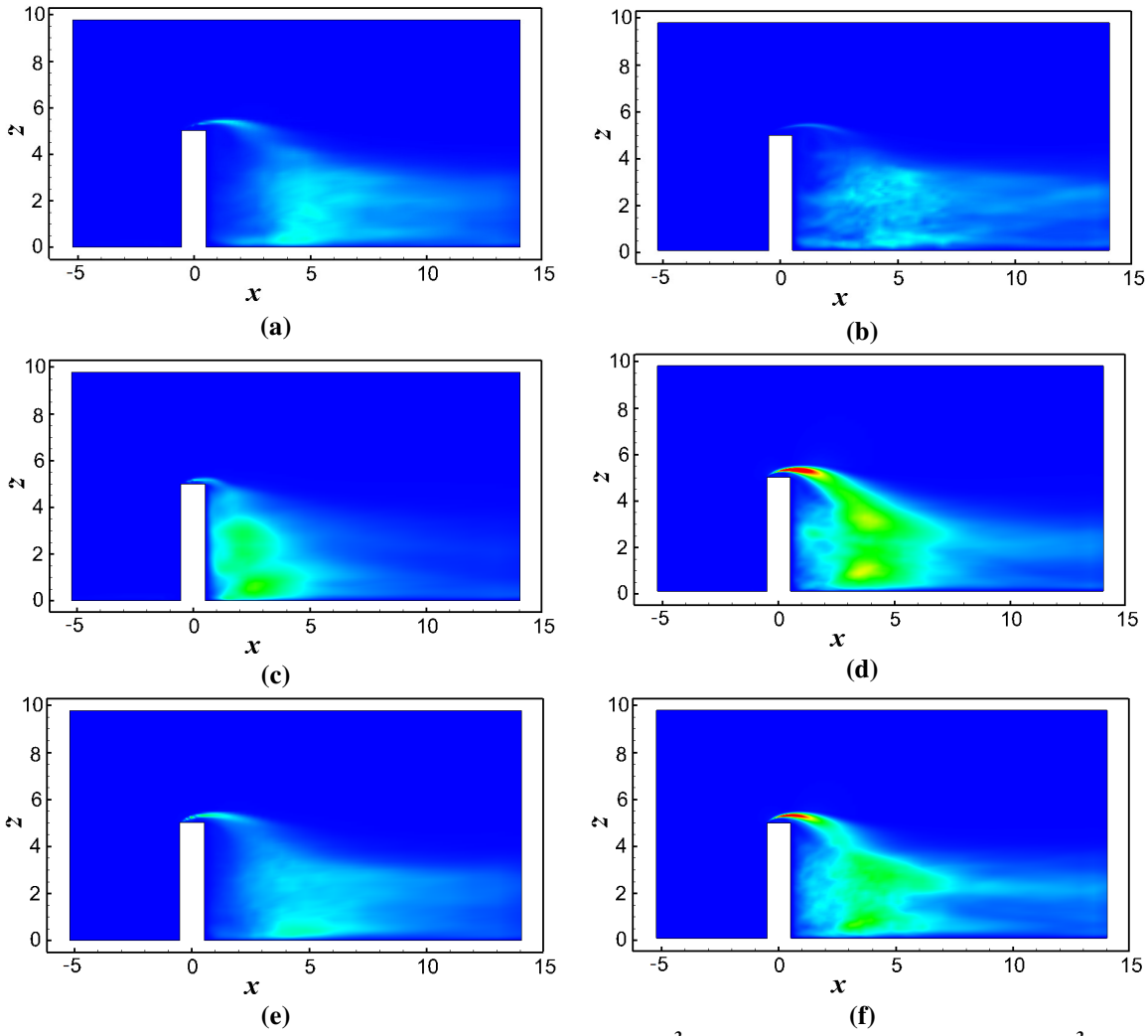

Figure 6.5: Resolved streamwise stress contours $\langle u'u' \rangle / U^2_\infty$ with maximum value of $\langle u'u' \rangle / U^2_\infty = 0.2$ in a center-plane: a) SM coarse grid, b) SM fine grid, c) DSM coarse grid, d) DSM fine grid, e) DNM coarse grid, f) DNM fine grid.

Figure 6.5 shows contours of the resolved-scale streamwise stress $\langle u'u' \rangle / U^2_\infty$ in the center-plane for all six combinations of grid and SGS model. For the two dynamic models, the peak value of the resolved-scale stress is significantly higher on the finer grids. Two distinct peaks are observed for the stress in the near-wake region for all cases. The stronger peak is located near the ground plane, while the weaker peak is located near the top boundary of the wake region. These high stress regions might be an indication of high shear regions, since often shear regions are regions of strong production of turbulence kinetic energy. For the dynamic models, a high value of $\langle u'u' \rangle / U^2_\infty$ is observed near the free end of the cylinder, where the separated flow at the

front end of the cylinder is drawn into the downwash. Overall, the DSM (on the fine grid) predicts the highest stress values, while the SM (on both grids) predicts the lowest values.

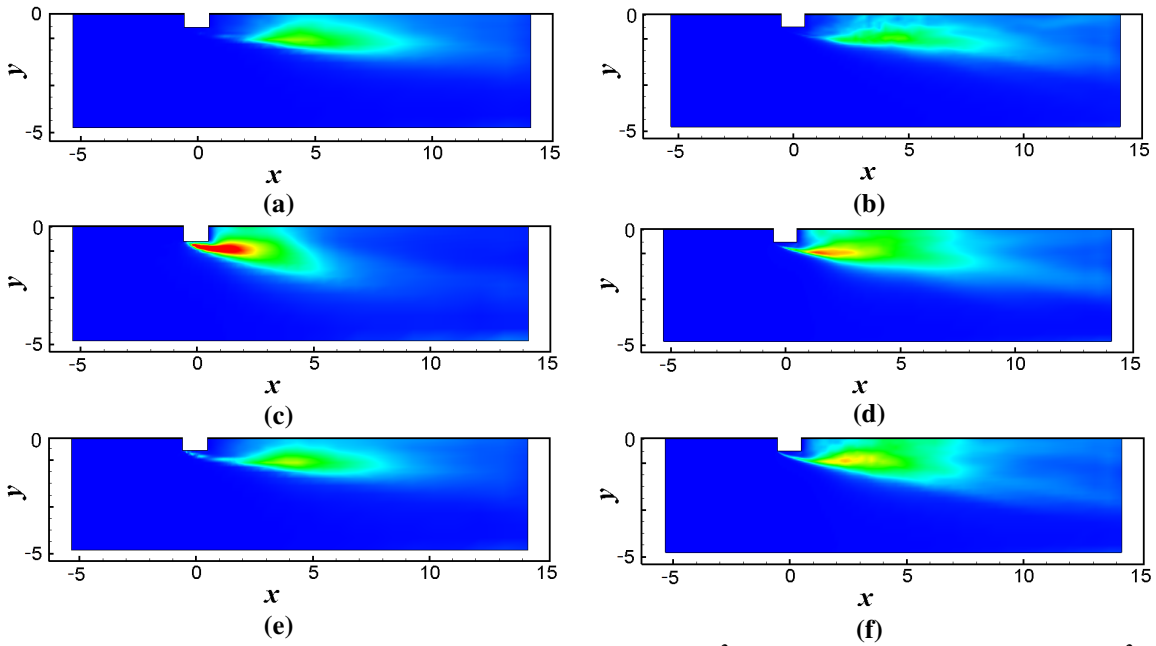

Figure 6.6: Resolved scale streamwise stress contours $\langle u'u' \rangle / U^2_\infty$ with maximum value of $\langle u'u' \rangle / U^2_\infty = 0.2$ in a plane located at $z/D = 2.5$: a) SM coarse grid, b) SM fine grid, c) DSM coarse grid, d) DSM fine grid, e) DNM coarse grid, f) DNM fine grid.

In the next three figures, consideration shifts to a comparison of the three resolved-scale normal stress components in a horizontal plane located at half the cylinder height. Figure 6.6 shows contours of the resolved-scale streamwise stress in a plane located at $z/D = 2.5$ for all six cases. The stress typically exhibits a peak value just downstream from the rear corner of the cylinder, and relaxes to a minimum value near the center-plane. Like the vorticity in Figure 6.4, the region of high stress tends to spread laterally into the wake region. Both dynamic models predict higher peak values, however, on the coarse grid the DSM predicts a much higher stress value than the other two models.

Figure 6.7 shows contours of the resolved-scale wall-normal stress in a horizontal plane located at $z/D = 2.5$ for all six cases. According to this figure, the peak value of the wall-normal stress

occurs directly downstream of the outer edge of the cylinder and closer to the centreline than was the case for the streamwise stress component. Consistent with the erroneous behavior previously noted, the DSM on the coarse grid exhibits too high a peak value and the high stress levels extend over too large a region compared to the other model predictions. Recall that previously (see Figure 6.2) the recirculation zone predicted by the DSM on the coarse grid was much smaller than for the other models. On the finer grid, the DNM predicts the largest peak value for the wall-normal stress.

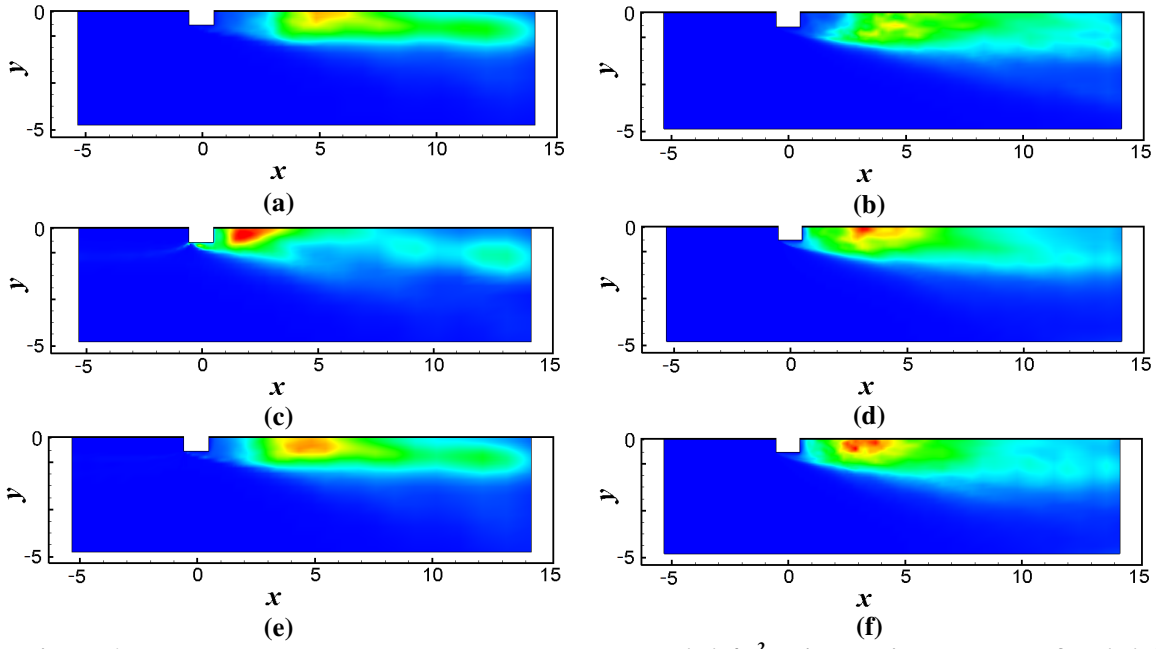

Figure 6.7: Resolved-scale wall-normal stress contours $\langle w'w' \rangle / U^2_\infty$ with maximum values of $\langle w'w' \rangle / U^2_\infty$ = 0.15 in a plane located at z/D = 2.5: a) SM coarse grid, b) SM fine grid, c) DSM coarse grid, d) DSM fine grid, e) DNM coarse grid, f) DNM fine grid.

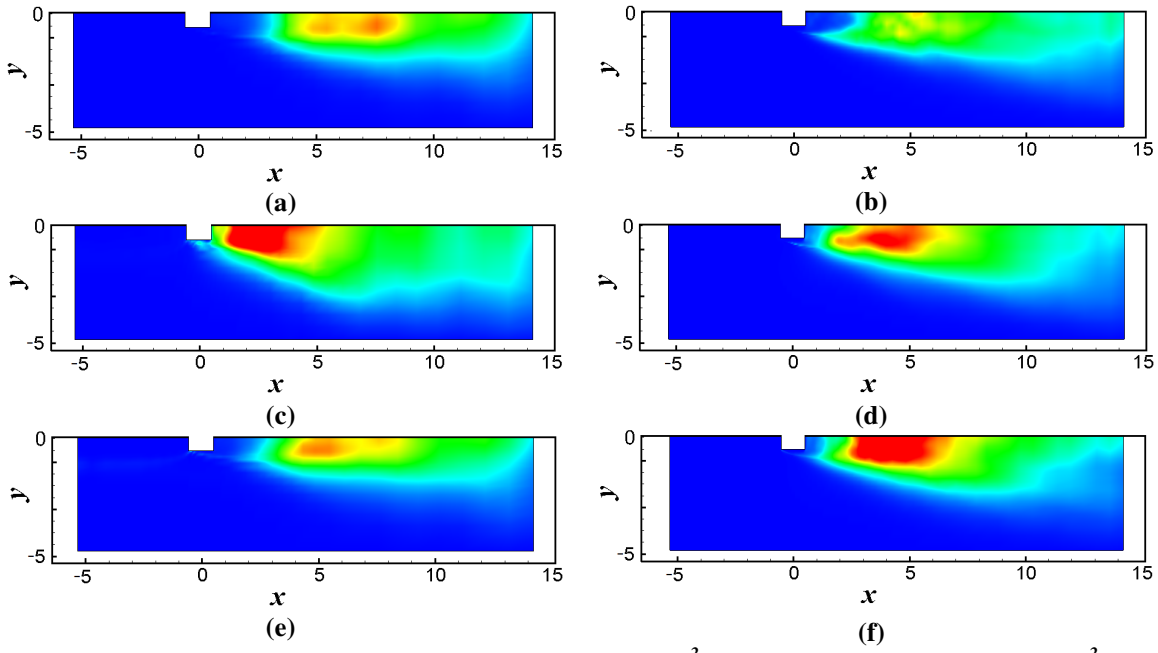

Figure 6.8: Resolved-scale spanwise stress contours $\langle v'v' \rangle / U^2_\infty$ with maximum value of $\langle v'v' \rangle / U^2_\infty = 0.15$. in a plane located at $z/D = 2.5$: a) SM coarse grid, b) SM fine grid, c) DSM coarse grid, d) DSM fine grid, e) DNM coarse grid, f) DNM fine grid.

Figure 6.8 shows contours of the resolved-scale spanwise stress in a horizontal plane located at $z/D = 2.5$ for all six cases. According to this figure, as for the wall-normal stress, the spanwise stress $\langle w'w' \rangle / U^2_\infty$ contours show a maximum directly behind the cylinder, and for the two dynamic models, the peak occurs near the symmetry plane. As before, on the coarse grid the DSM, see Figure 6.8(c), appears to over-predict the peak value, and the area where the stress reaches its largest values is smaller than for the other cases. On the fine grid, all SGS models predict similar contour patterns for the spanwise stress component except for the SM that predicts the peak off centreline and further away from the cylinder's rear wall.

Comparison between the three resolved-scale stress components reveals that the streamwise stress exhibits the highest peak value of 0.3, while the wall-normal and spanwise stresses display the peak values of 0.2. The streamwise stress is more dominant in the separated shear layers compared to the other two normal stress components. It also appears that the streamwise stress

distribution is more representative of the shear layers, and in fact implies a wider spread of the separated shear layers compared to that indicated by the time-averaged wake velocity field shown in Figure 6.3 and the time-average normal vorticity contours presented in Figure 6.4. Frohlich and Rodi (2004) also observed that the resolved-scale stress components imply a wider spread of the separated shear layers compared to the streamlines of the time-averaged flow field.

6.5. Time-Averaged Streamwise Vorticity Contours

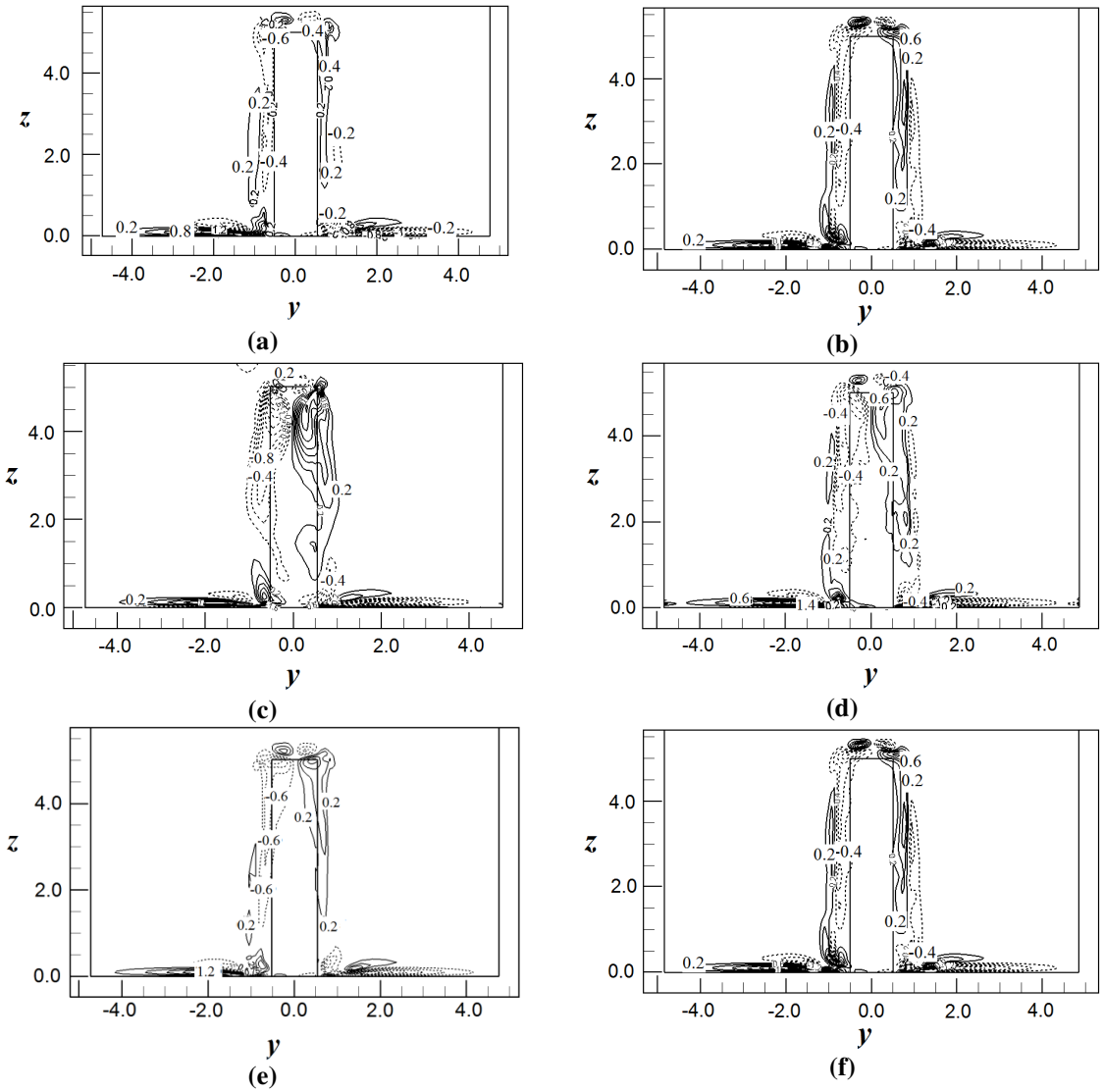

Figure 6.9: Time-averaged streamwise vorticity contours ω_x in a plane located at x/D = 1: a) SM coarse grid, b) SM fine grid, c) DSM coarse grid, d) DSM fine grid, e) DNM coarse grid, f) DNM fine grid.

Figure 6.9 shows the streamwise vorticity at x/D = 1 for all six cases. In general, a pair of tip vortices is formed near the free end and a pair of vortices with opposite signs (from the tip vortices) is formed near the ground plane for all cases. In addition to these two sets of vortices, except for Figure 6.9(c), another pair of smaller vortices is observed above the tip vortices. These vortices have an opposite sign compared to the tip vortices. In general, the simulation on the finer mesh is able to resolve a finer vortex structure, especially for the SM and DNM predictions. Based on the fine mesh solutions, the tip vortices predicted by the SM are narrower and concentrated around the corners of the cylinder. The DSM and DNM exhibit a similar vortex structure which is unlike the SM prediction: the tip vortices are larger and extend into the wake of the cylinder. While the fine grid predictions show the vortex pairs extending along most of the span for both dynamic models; for the SM, these vortices are continuous and narrow.

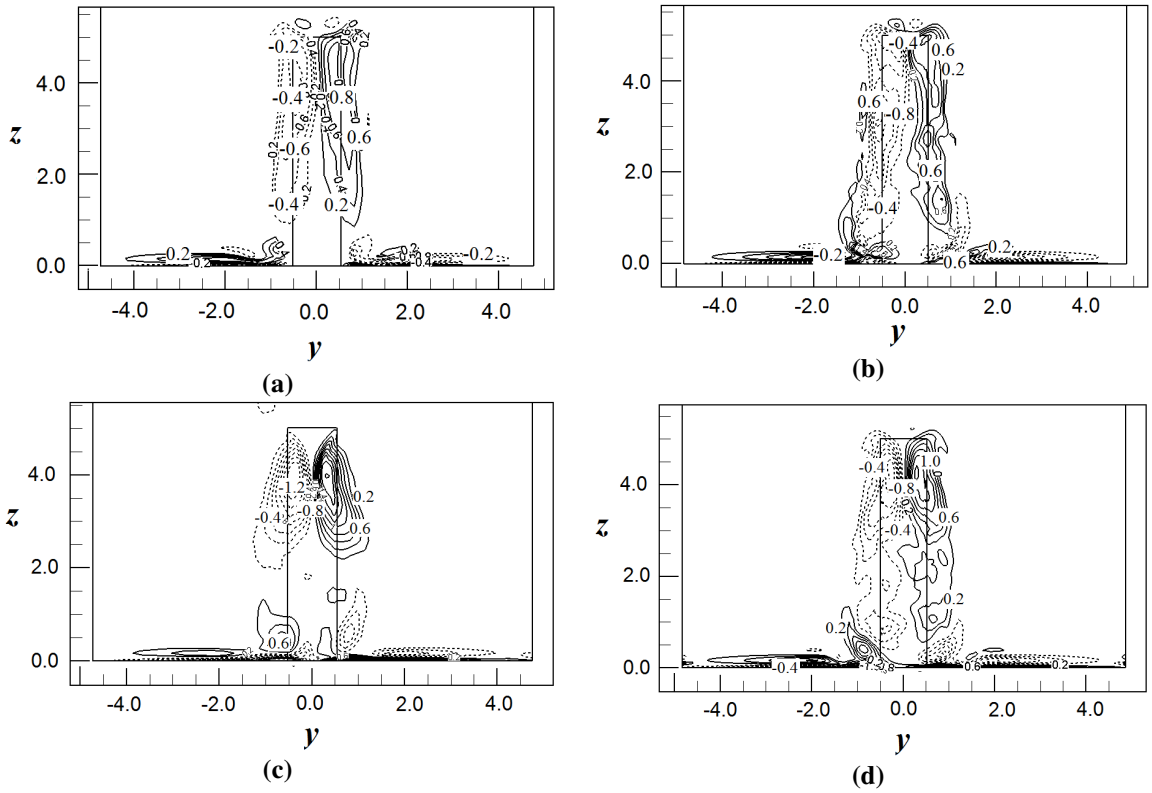

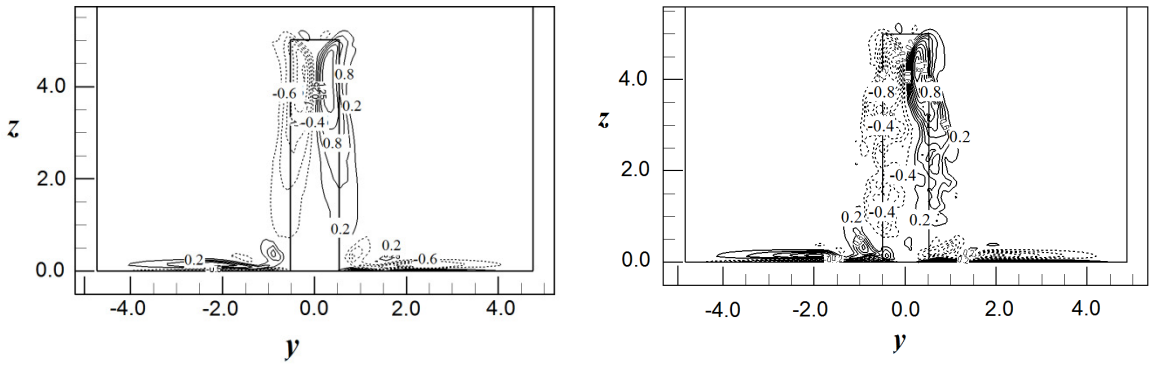

(e) (f)

Figure 6.10: Time-averaged streamwise vorticity contours ω_x in a plane located at x/D = 2: a) SM coarse grid, b) SM fine grid, c) DSM coarse grid, d) DSM fine grid, e) DNM coarse grid, f) DNM fine grid.

Figure 6.10 indicates that at a section one diameter further downstream, the tip vortices identified in Figure 6.9 have grown larger and broader, and their centers have descended away from the free end towards the ground plane. The base vortices also have grown somewhat stronger. The secondary tip vortices observed in Figure 6.9 are absent for the DSM, and much weaker for the SM and DNM predictions. As before, for all three SGS models, the vortex patterns on the coarse grid are much smoother and regular than on the fine grid; furthermore, this effect is most pronounced for the DSM.

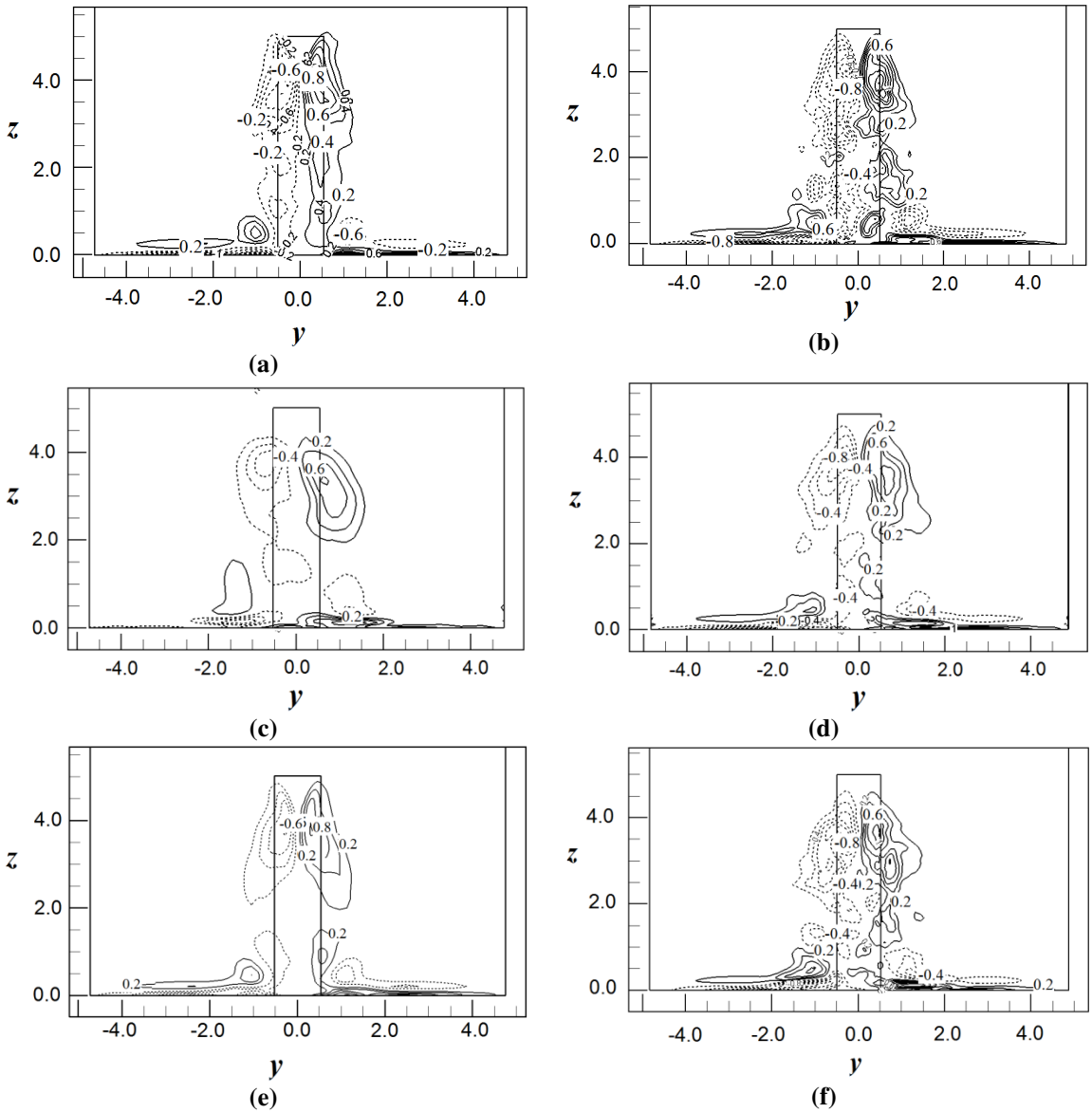

Figure 6.11: Time-averaged streamwise vorticity contours ω_x in a plane located at x/D = 4: a) SM coarse grid, b) SM fine grid, c) DSM coarse grid, d) DSM fine grid, e) DNM coarse grid, f) DNM fine grid.

Figure 6.11 shows contours of the time-averaged streamwise vorticity at x/D = 4. In terms of structure, the center of the tip vortices has moved further down toward the ground plane and the base vortices are grown larger for all cases. In general the base vortices have been displaced to the outside by the penetration of the tip vortices almost to the ground plane. Based on the fine grid simulations, even though the location of the vortices for all cases is approximately the same, their shape and strength (magnitude) varies from one case to another. The SM predicts the

strongest vortex structure with a triangular shape to the contours, while the DNM predicts a slightly narrower vortex which is also longer. The DSM predicts the weakest vortex pattern.

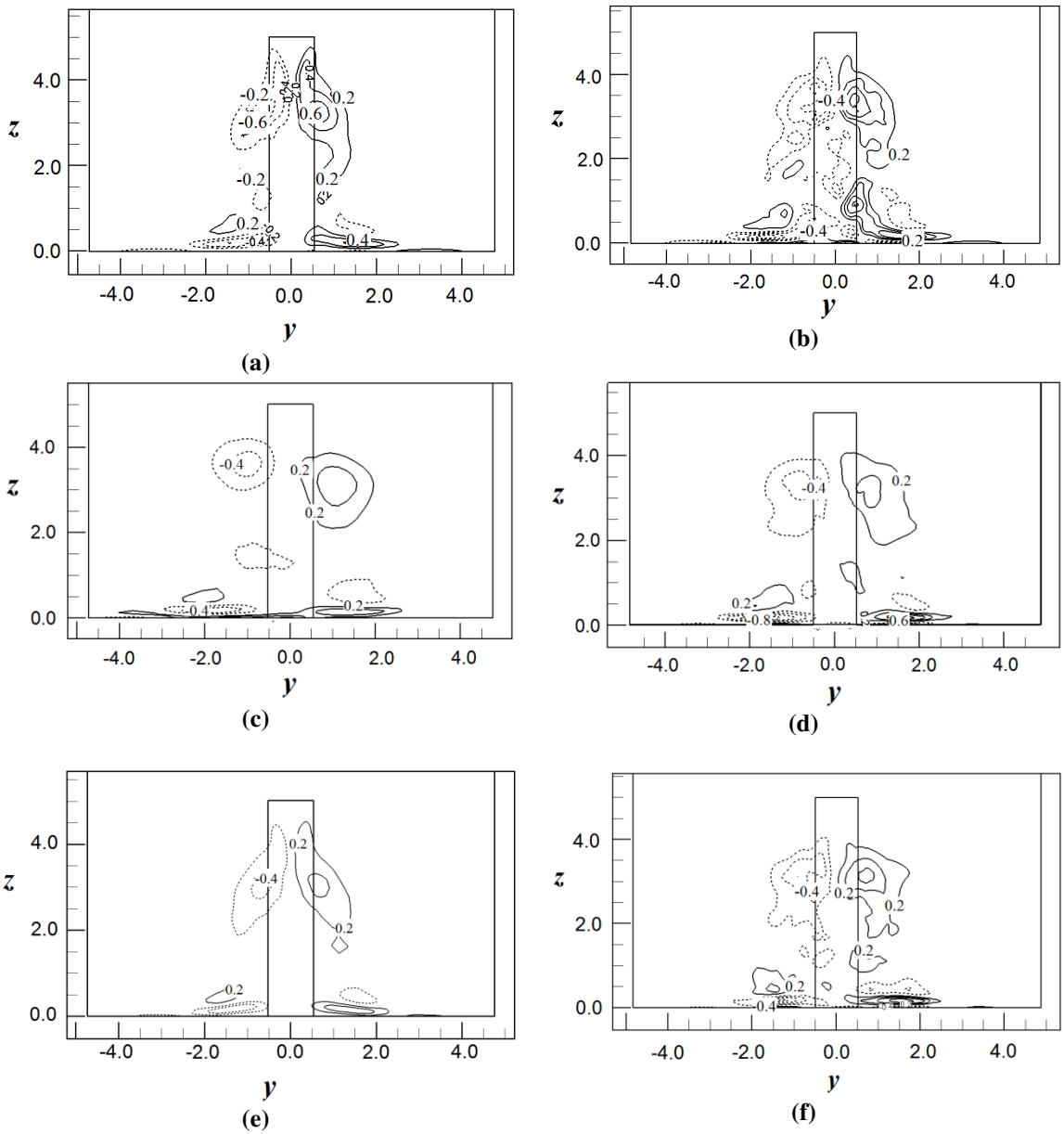

Figure 6.12: Time-averaged streamwise vorticity contours ω_x in a plane located at x/D = 6: a) SM coarse grid, b) SM fine grid, c) DSM coarse grid, d) DSM fine grid, e) DNM coarse grid, f) DNM fine grid.

Figure 6.12 shows contours of the time-averaged streamwise vorticity at x/D = 6. For the two dynamic models, the coarse grid solution is becoming relatively weak, and even the fine grid solution is less detailed than the prediction of the SM. Furthermore, the contour patterns for both

DSM solutions, Figure 6.12(c,d), are weaker and rounder compared to the other two cases. According to fine grid simulations, the vertical location of the tip vortices is very close to that observed at $x/D = 4$. The centers of these vortices have moved away from the cylinder towards the side walls of the flow domain; this behaviour is especially noticeable in Figure 6.12(c). The vortex structures next to the ground plane and underneath the base vortices are growing thicker.

Contours of streamwise vorticity for vertical sections at $x/D = 8$ and $x/D = 10$ are shown in Appendix D. In all cases, the contours are much weaker in magnitude and rounder in shape, and in fact barely captured on the coarse grids. The tip vortices tend to remain at the same height and move further away from the cylinder towards the exterior walls of the domain. This is consistent with the experimental observations of Sumner et al. (2004) for the case of a circular cylinder. Overall, for the fine resolution grids all three SGS models predicted similar but not identical vorticity contours. In particular, within the near-wake region the different SGS models predict different patterns of vorticity. The figures also show that typically the DSM solution on the coarse resolution grid yields patterns noticeably different from the other two models. However, right behind the cylinder i.e. at $x/D = 1$ and 2, the dynamic models on the fine grid tend to predict a more complex vortex pattern.

6.6. Time-Averaged Iso-Surfaces of the 2nd Invariant

The second invariant of the velocity gradient tensor was used to analyse the vortical structures in the near-wake region of the finite square cylinder. A detailed description of the method of using iso-surfaces of the 2nd invariant to visualize vortex structures was given in Chapter 4.

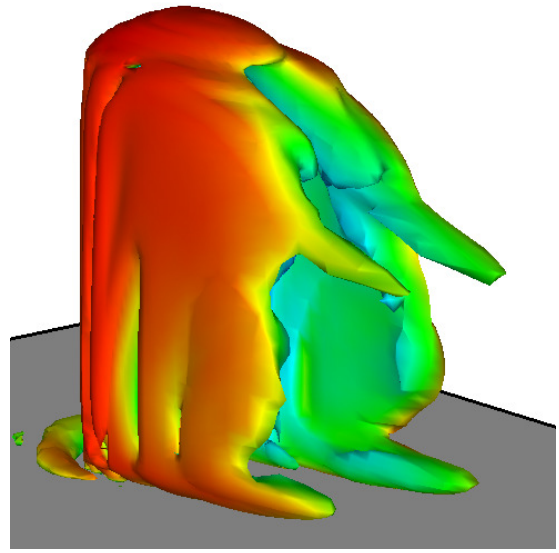

(a)

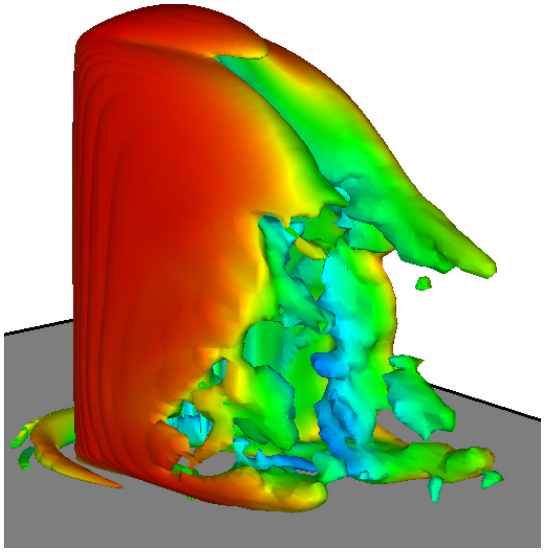

(b)

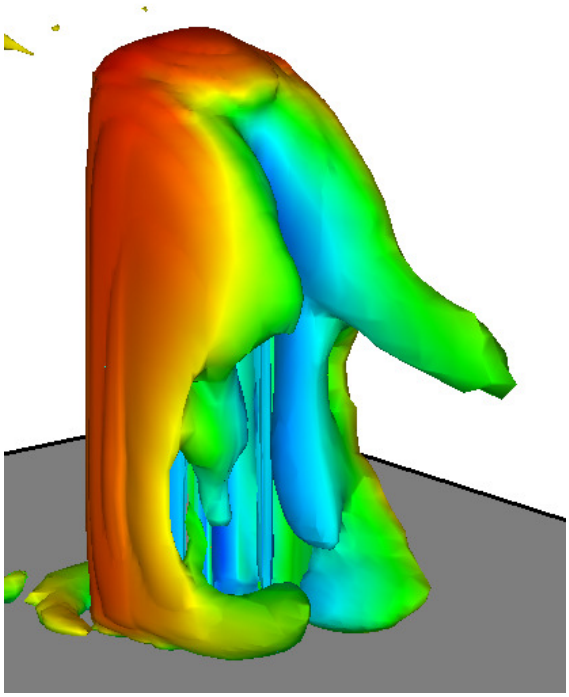

(c)

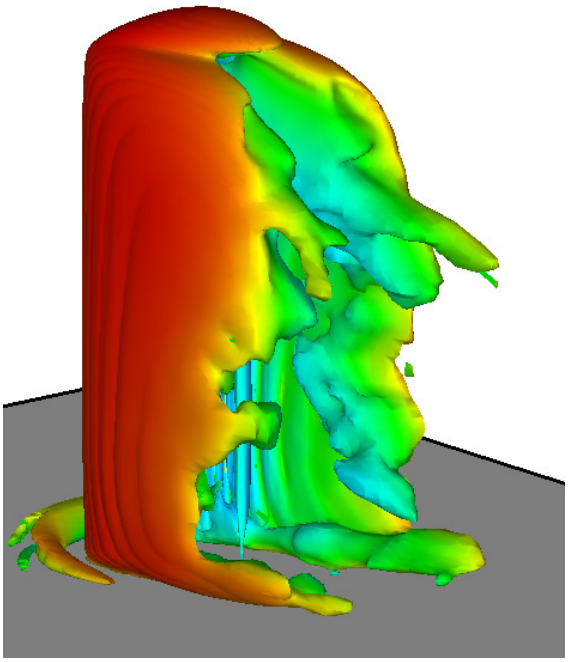

(d)

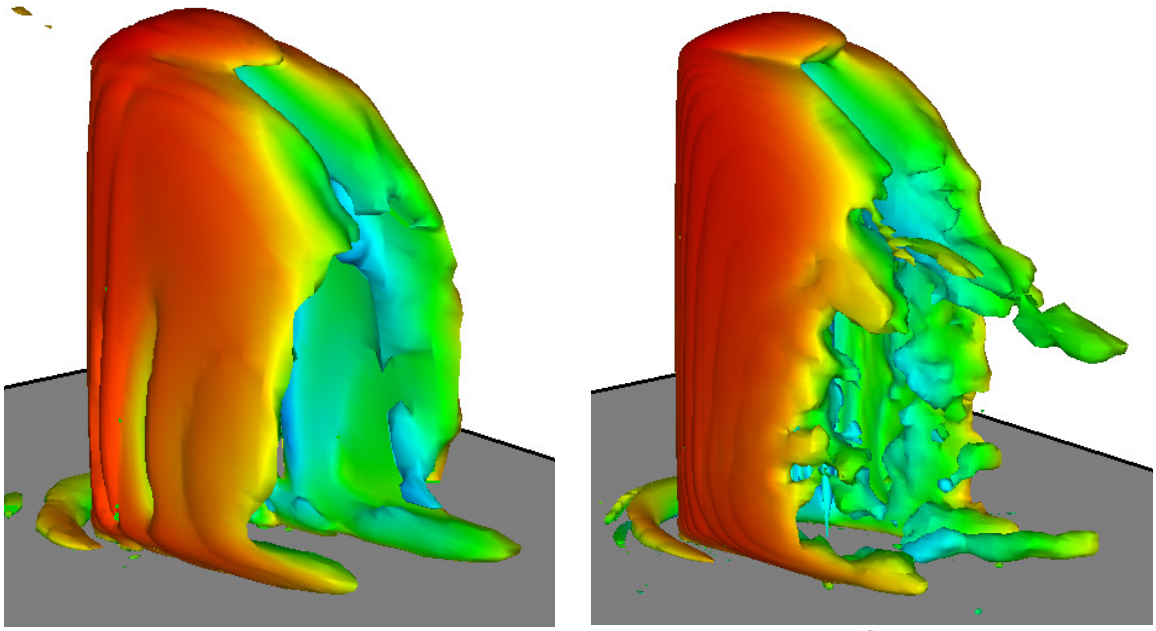

(e) (f)

Figure 6.13: Time-averaged *Q* iso-surfaces of the time-averaged flow-field: a) SM coarse grid, b) SM fine grid, c) DSM coarse grid, d) DSM fine grid, e) DNM coarse grid, f) DNM fine grid.

Figure 6.13 presents the iso-surfaces of the 2nd invariant of the velocity gradient field in the near-wake of the cylinder for all six cases. Note that a thin horseshoe vortex is always observed at the front of the cylinder on the ground plane. A pair of tip vortex structures tips down towards the ground plane and together with the vortex structures being shed from the vertical sides of the cylinder for a quasi-symmetric arch-type vortex in the near-wake region. The main vortex legs are attached near the free end of the square cylinder, but detach from each other as they move away from the free end towards the ground plane. The vortex structure does not immediately expand in the cross-stream direction. Near the ground plane a second pair of vortex structures is formed, which extend in the streamwise direction. There is no sign of antisymmetric Kármán vortex shedding of the vertical structures being shed from the cylinder, which reflects the time-averaged nature of these structures.

On the coarse grid, all SGS models predict smoother but less detailed structures. This is especially true for the DSM shown in Figure 6.13(c), which has pronounced tip and base vortex structures. In terms of a comparison among the different SGS models on the fine grid, Figure 6.13(b) indicates that the largest recirculation zone is observed for the SM, and the vortex structures appear to be more stretched in the streamwise direction compared to other cases. The DNM also predicts a more complicated vortex structure near the ground plane.

6.7. Instantaneous Iso-Surfaces of the 2nd Invariant

Figure 6.14 shows the iso-surfaces of the 2nd invariant of the velocity gradient tensor for the instantaneous flow-field for all six cases. As in the case of the mean flow field, a horseshoe vortex is typically observed in front of the cylinder on the ground plane. In general, the solutions with higher grid resolution exhibit more refined structures, with rounder vortex tubes. Side shear layer vortices are also observed near the cylinder walls. The separated shear layers roll up for all the above cases to produce segregated vortex structures. Antisymmetric vortex shedding instabilities begin to appear half-way through the wake region. These antisymmetric vortices are more clearly exhibited by the high resolution simulations. The vortex structure for the finer solutions is more extended in both the lateral and longitudinal directions. In some ways, the instantaneous structure is very similar for each fine grid solution, which is perhaps significant; however, both dynamic models show more instabilities, e.g. the waves on the initial long vertical side-wall vortex structures

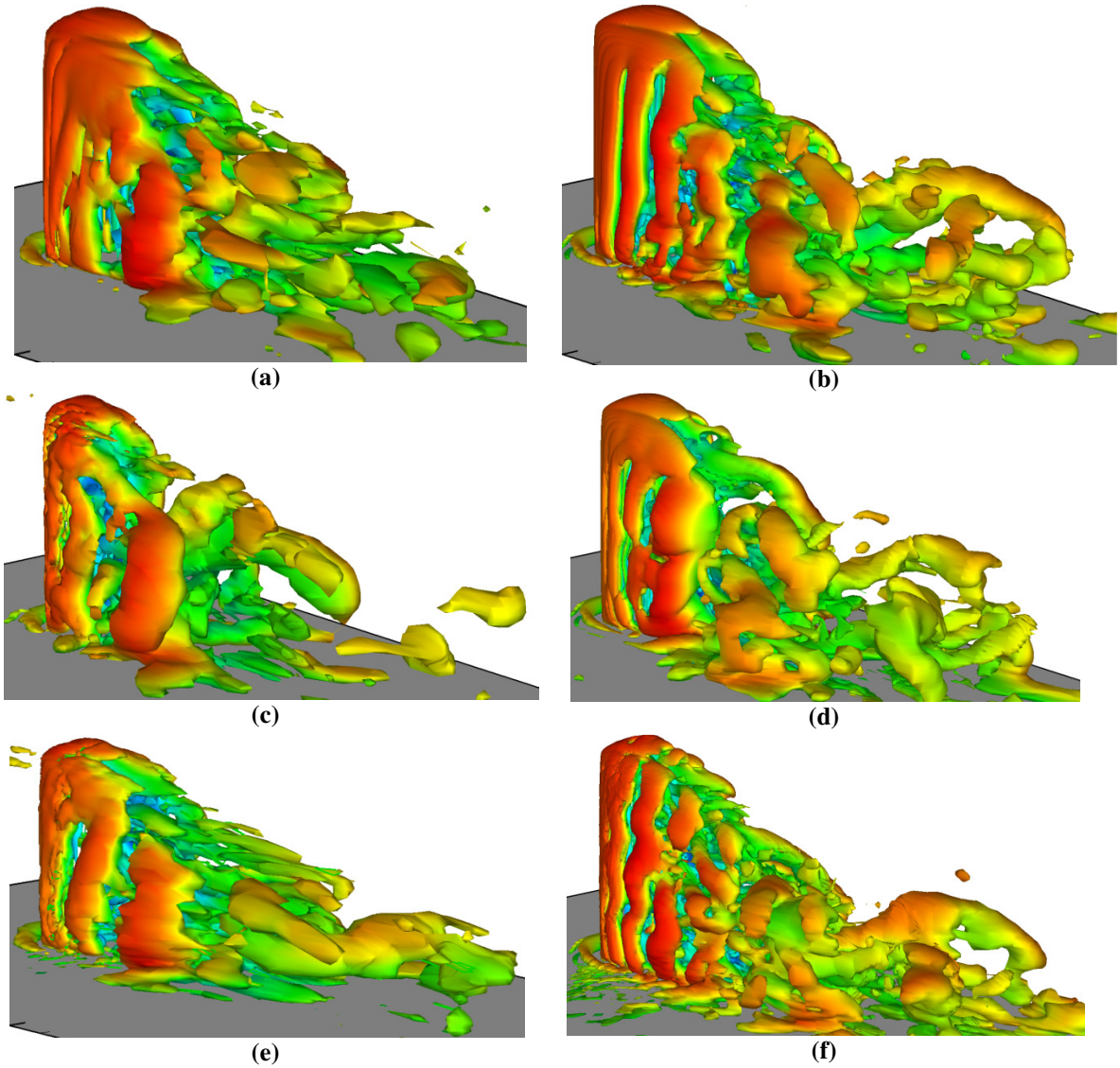

Figure 6.14: Instantaneous Q Iso-surfaces of the time-averaged flow-field: a) SM coarse grid, b) SM fine grid, c) DSM coarse grid, d) DSM fine grid, e) DNM coarse grid, f) DNM fine grid.

6.8. Conclusion

The LES predictions of three SGS models, i.e. SM, DSM and DNM, performed on two different grid levels of 64 × 72 × 48 and 128 × 144 × 96 for a square cylinder with AR = 5 at Re = 500 are studied. The time-averaged velocity fields in the wake, Figures 6.1 and 6.3, showed that the DSM, with a low resolution, predicted a much smaller recirculation zone than did the other models. The eddy viscosity contours also shed light on the SGS models and the grid effect. For

example, the DSM with a low resolution yields a shorter recirculation zone, but exhibits the highest *u*-fluctuations (see Figure 6.6). The DSM with a low resolution solution shows the highest fluctuations for both the normal and spanwise components.

In terms of the streamwise vorticity contours, all three SGS models with a high resolution grid predicted similar vorticity contours. According to Figures 6.9-6.12, although the DSM solution with a low resolution grid was unable to predict the near-wake region accurately, outside the wake region the streamwise vorticity contours are similar to the predictions of the other two models. This might be due to the fact that further away from the cylinder, outside of the wake region the turbulence is minimal. In the near-wake region, the various SGS models present different behavior.

Overall, it can be said that in the case of the DSM solutions insufficient grid resolution leads to erroneous predictions. The DNM is a major improvement as the predictions are similar on both the coarse and fine grids.

All in all, the DNM is much less sensitive to grid resolution and is able to predict the flow structure even with lower resolution. The SM, however, appears to lead to different time-averaged vorticity fields in the wake, and does not resolve some of the detail captured by the dynamic models.

Chapter 7

Effect of Aspect Ratio

7.1. Introduction

As discussed in Chapter 4, three types of vortex structures, i.e. tip, base and spanwise, are observed in the near-wake region of the finite-height cylinders. The vortex structure of the near-wake region is characterized by interactions of these vortex structures, the size and strength of which vary with aspect ratio. For example, as the aspect ratio increases, the base vortices grow larger but there is less interaction between tip and base vortices (Sumner et al., 2004).

In this chapter, the effect of aspect ratio on the flow over a wall-mounted finite-height square cylinder is investigated based on numerical simulations using LES at Re = 500. A dynamic Smagorinsky model as described in Chapter 3 was used for the subgrid-scale model. The near-wake region of a finite square cylinder is studied for three aspect ratios, AR = 3, 5 and 7. The cylinder was mounted on a ground plane and immersed in an exterior stream with a thin laminar boundary layer. The boundary layer thickness on the ground plane, at the location of the cylinder, was $\delta/D = 0.01$. The Reynolds number was set to Re = 500 based on width of the cylinder D and the free stream velocity U.

The solution domain extended $5D$ upstream and $14D$ downstream of the cylinder (in the x direction). The total cross-stream extent of the solution domain was $10D$ and the height (in the z-direction) of the flow domain was set to be twice the height of the surface-mounted cylinder ($2H$). A relatively fine $128 \times 144 \times 96$ non-uniform collocated grid was used to discretize the domain. Since the same size of grid was used for all three aspect ratios, the resolution for the smallest aspect ratio was the highest. To resolve the boundary layers on the cylinder surfaces,

the grid was refined in both the cross-stream (y) and wall-normal (z) directions near the corners of the cylinder. The grid was also refined in the streamwise direction to accommodate the cylinder. Table 7.1 summarizes the minimum and maximum residuals for all three aspect ratios.

Table 7.1: Minimum and maximum residuals for all three aspect ratios.

		dx/D	*dy/D*	*dz/D*
AR 3	min	1.15E-02	1.30E-02	6.08E-03
	max	5.75E-01	3.29E-01	1.46E-01
AR 5	min	1.15E-02	1.30E-02	1.01E-02
	max	5.75E-01	3.29E-01	5.75E-01
AR 7	min	1.15E-02	1.30E-02	1.42E-02
	max	5.75E-01	3.29E-01	3.42E-01

The time-averaged quantities were averaged over at least five complete shedding cycles. Streamlines, velocity and vorticity contours, were obtained at various planes to capture some two dimensional features of the time-averaged flow. The analysis also considered the two-dimensional drag-coefficient, obtained from the time-averaged pressure field along the height of the cylinder and power spectra at three different locations along the height of the cylinder. Finally, iso-surfaces of the 2nd invariant of the velocity gradient were used to visualize the vortical structures in the wake.

7.2. Time-Averaged Velocity Field

Figure 7.1 shows the time-averaged streamlines in a vertical plane parallel to the approach flow and located on the wake centreline; results are shown for the three aspect ratios studied, AR = 3, 5 and 7. The recirculation zone immediately behind the cylinder is clearly illustrated by the streamline pattern.

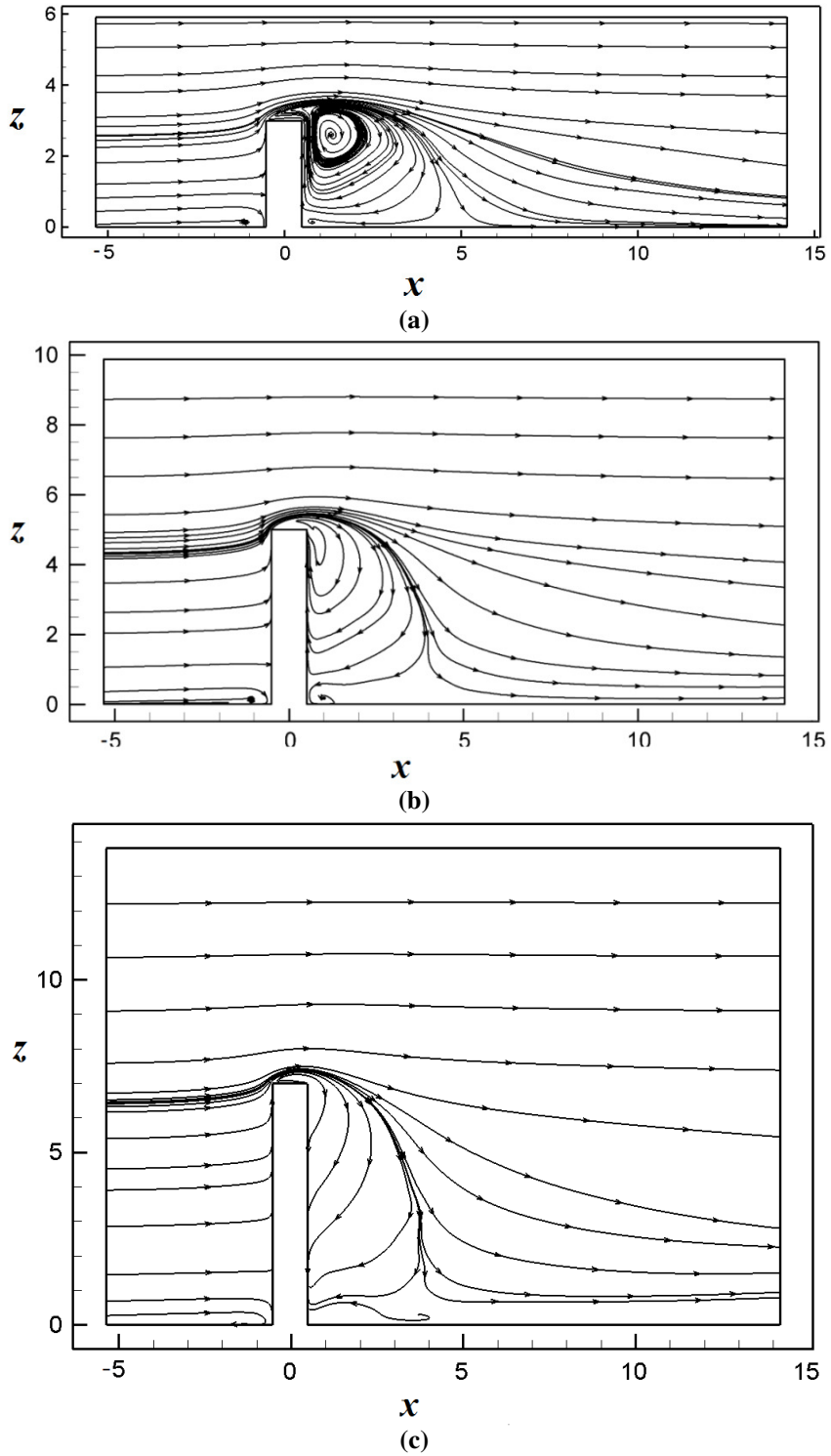

Figure 7.1: Time-averaged streamlines in a vertical plane along the wake centre-line *y/D* = 0: a) AR = 3, b) AR = 5, c) AR = 7.

For all aspect ratios, the influence of the free end leads to a strong downwash velocity field on the wake centreline. For AR = 3 (Figure 7.1(a)), the downwash flow reaches the ground plane

and there is no sign of upwash flow originating near the ground plane. There is also a relatively large area of reverse flow immediately above the cylinder. For AR = 5 and 7 (Figures 7.1(b) and 7.1(c)), the flow reattaches to the cylinder's rear wall and a weak upwash flow is observed close to the ground plane. The reverse flow region above the cylinder is much smaller and almost nonexistent for AR = 7. The results in Figure 7.1 are in good agreement with the various experimental studies in the literature, which indicate that for aspect ratios smaller than the critical value, the shear layer reattaches onto the ground plane (Tanaka and Murata, 1999; Wang et al., 2006).

The streamwise extent of the recirculation zone is the largest for AR = 3, and as the height of the cylinder increases the streamwise extent of the recirculation zone decreases. In addition, for AR = 3, the recirculation zone adjacent to the tip of the cylinder is the strongest and as the height of the cylinder increases, the recirculation zone loses its strength especially near the tip region.

It should be noted that the center of the recirculation zone changes dramatically with AR. For AR = 3, the center of the recirculation zone is distinctively apart from the cylinder wall and is moved in the streamwise direction. For AR = 5 and 7 (Figures 7.1(b) and 7.1(c)), since the flow reattaches to the cylinder's rear wall it is difficult to locate the center of the recirculation zone.

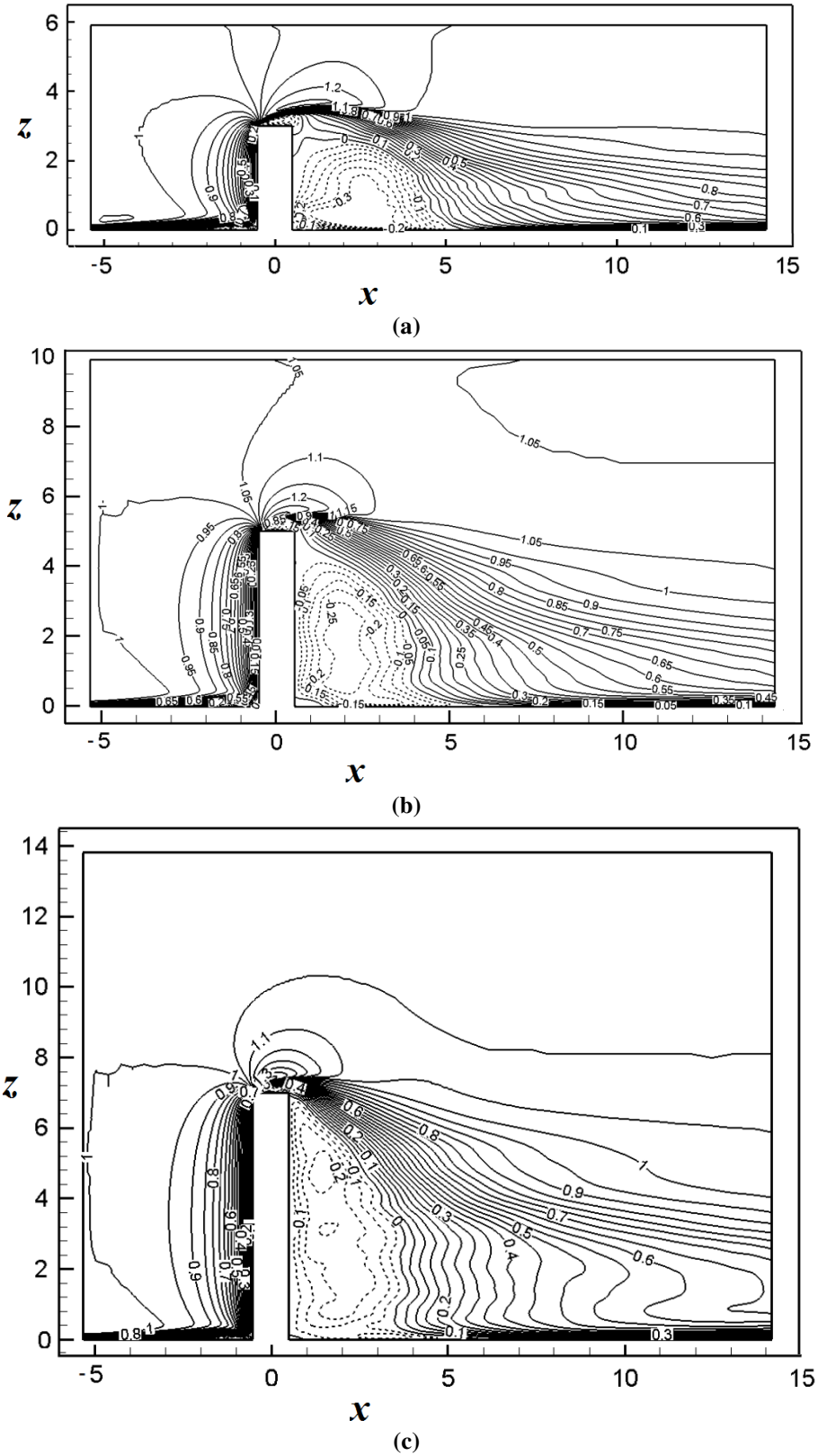

Figure 7.2: Time-averaged streamwise velocity contours u/U_∞ along the wake centreline, solid lines: positive values, dashed lines: negative values: a) AR = 3, b) AR = 5, c) AR = 7.

Figure 7.2 documents the time-averaged streamwise velocity contours for all three aspect ratios. The contours also indicate that the downstream extent of the near-wake region decreases as the aspect ratio increases. Near the free end the streamwise velocity contours are different for AR = 3 compared to the two other higher aspect ratios. According to Figure 7.2(a) the reverse flow begins some distance below the free-end, while in Figure 7.2(c) for AR = 7, the reverse flow occurs right at the free-end. Park and Lee (2000) showed that the size of the recirculation region increases as the aspect ratio increases for aspect ratios below the critical value, while thereafter the size of the recirculation zone decreases (also seen by Wang and Zhou (2009)). Since AR = 3 is the only aspect ratio below the critical aspect ratio (assumed to be between 2 to 4 for this study), this study did not allow the effect of aspect ratio below the critical value to be assessed.

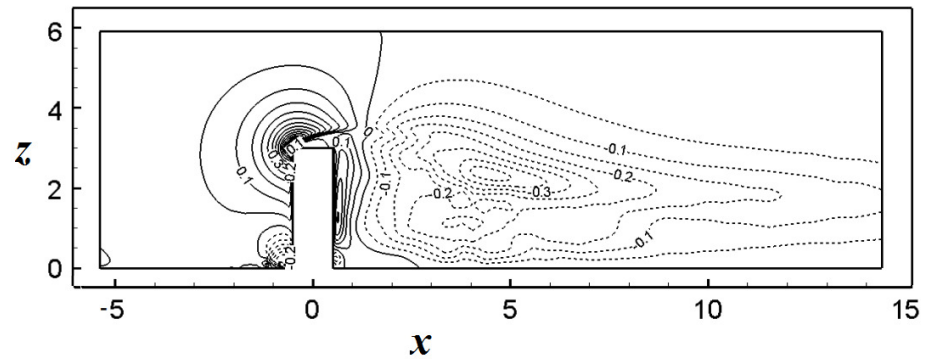

(a)

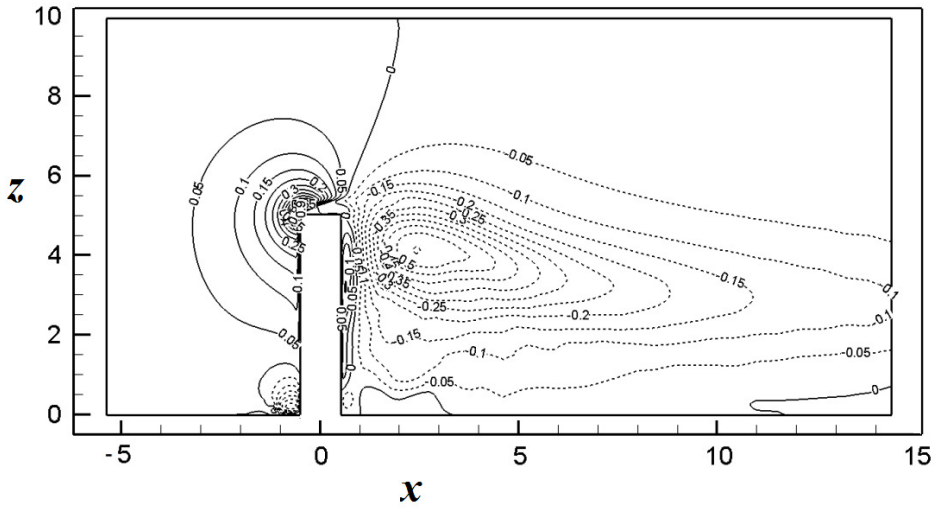

(b)

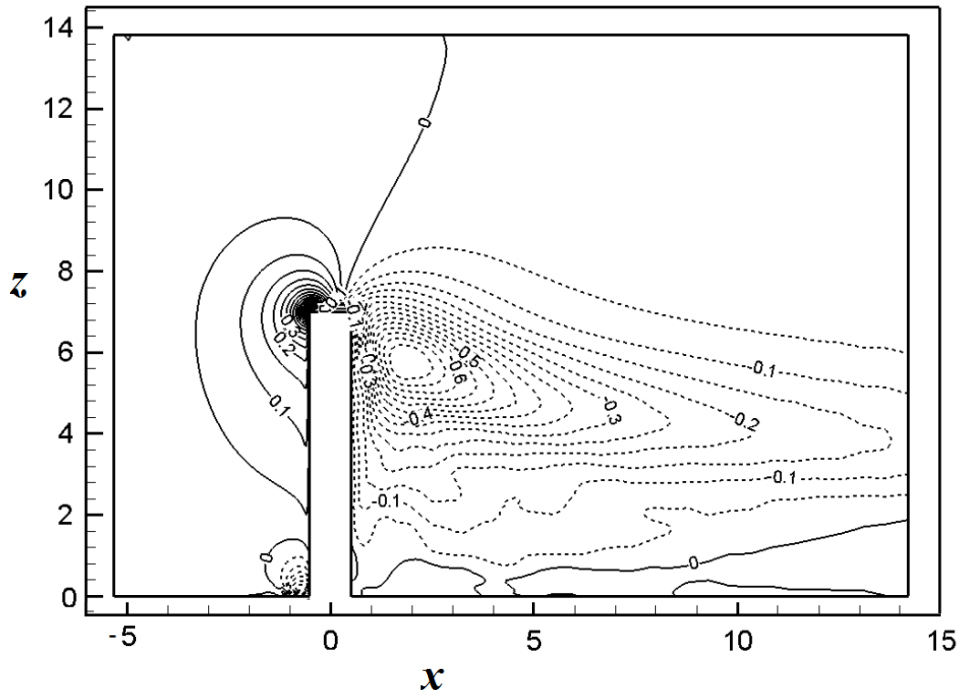

(c)

Figure 7.3: Time-averaged normal velocity contours w/U_∞ along the wake centreline, solid lines: positive values, dashed lines: negative values: a) AR = 3, b) AR = 5, c) AR = 7.

Figure 7.3 compares the time-averaged normal velocity contours in the center plane. It indicates a strong downwash for AR = 3 and a weaker upwash for AR = 5 and AR = 7. Also the center of the normal velocity contour pattern has shifted from the downstream of the wake region closer towards the square cylinder's wall as the aspect ratio increases. A strong upwash is observed immediately behind the cylinder for AR = 3. As the aspect ratio rises to AR = 5, the near-wall upwash becomes weaker and eventually no near-wall upwash is observed at AR = 7. This phenomena is consistent with the streamlines in Figure 7.1 and a small negative region behind the cylinder at the ground plane.

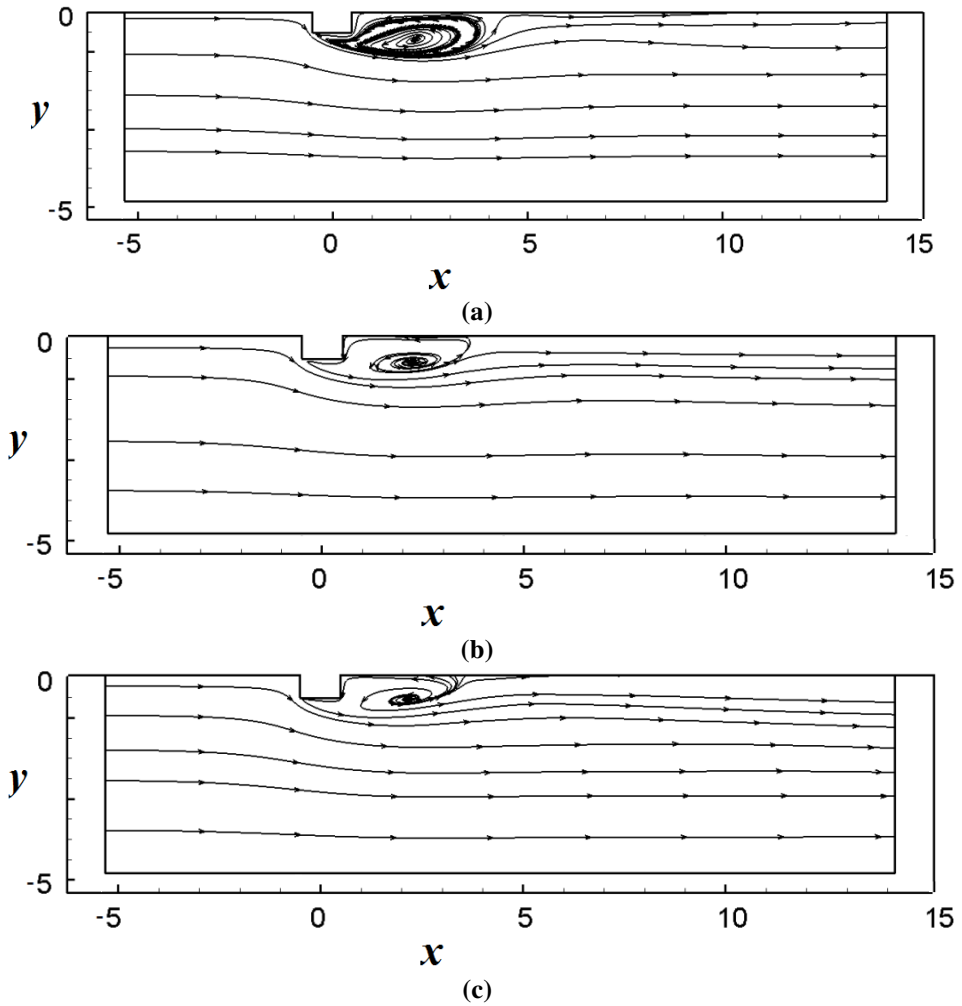

Figure 7.4: Time-averaged streamlines located at the mid-height of the cylinder: a) AR = 3, b) AR = 5, c) AR = 7.

Figure 7.4 presents the streamlines of the time-averaged velocity field in a plane located at mid-height of the cylinder, i.e. for AR = 3 at z/D = 1.5, for AR = 5 at z/D = 2.5, and for AR = 7 at z/D = 3.5. Based on Figure 7.4(a), the vortex structure or recirculation region is stronger and larger for AR = 3. The location of the center of the recirculation region also varies with aspect ratio. Compared to AR = 3, for AR = 5 and 7, the core of the recirculation region moves closer to the border of the recirculation zone (near-wake region) and the free stream.

7.3. Surface Flow Patterns

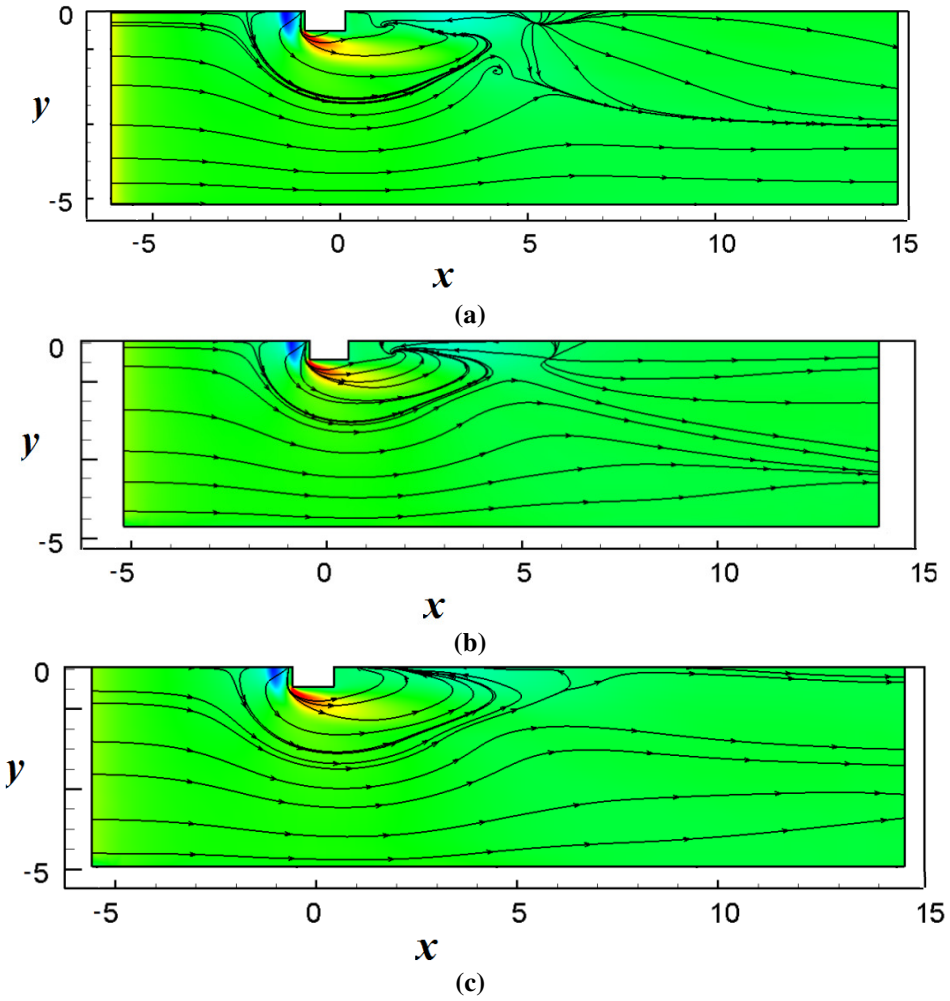

Figure 7.5: Time-averaged streamwise velocity contours and streamlines adjacent to the ground plane: a) AR = 3, b) AR = 5, c) AR = 7.

The streamline patterns on the ground plane can be used to obtain insight into the flow structures within the wake. Figure 7.5 shows the time-averaged streamwise velocity contours and streamlines just above the ground plane. Upstream of the front wall of the cylinder where the horseshoe vortex is formed, the streamlines are identical for all three aspect ratios and a saddle point is observed at approximately x/D = -2.0. Within the near-wake region of the cylinder, the streamline patterns begin to show some differences. The recirculation zone extends further downstream as the aspect ratio increases. Outside the wake region the streamlines are more

converged towards the center plane as the aspect ratio increases. For AR = 3 and maybe AR = 5, the saddle point is associated with stronger upstream flow compared to AR = 7, which might be a signature of downwash reaching the ground plane.

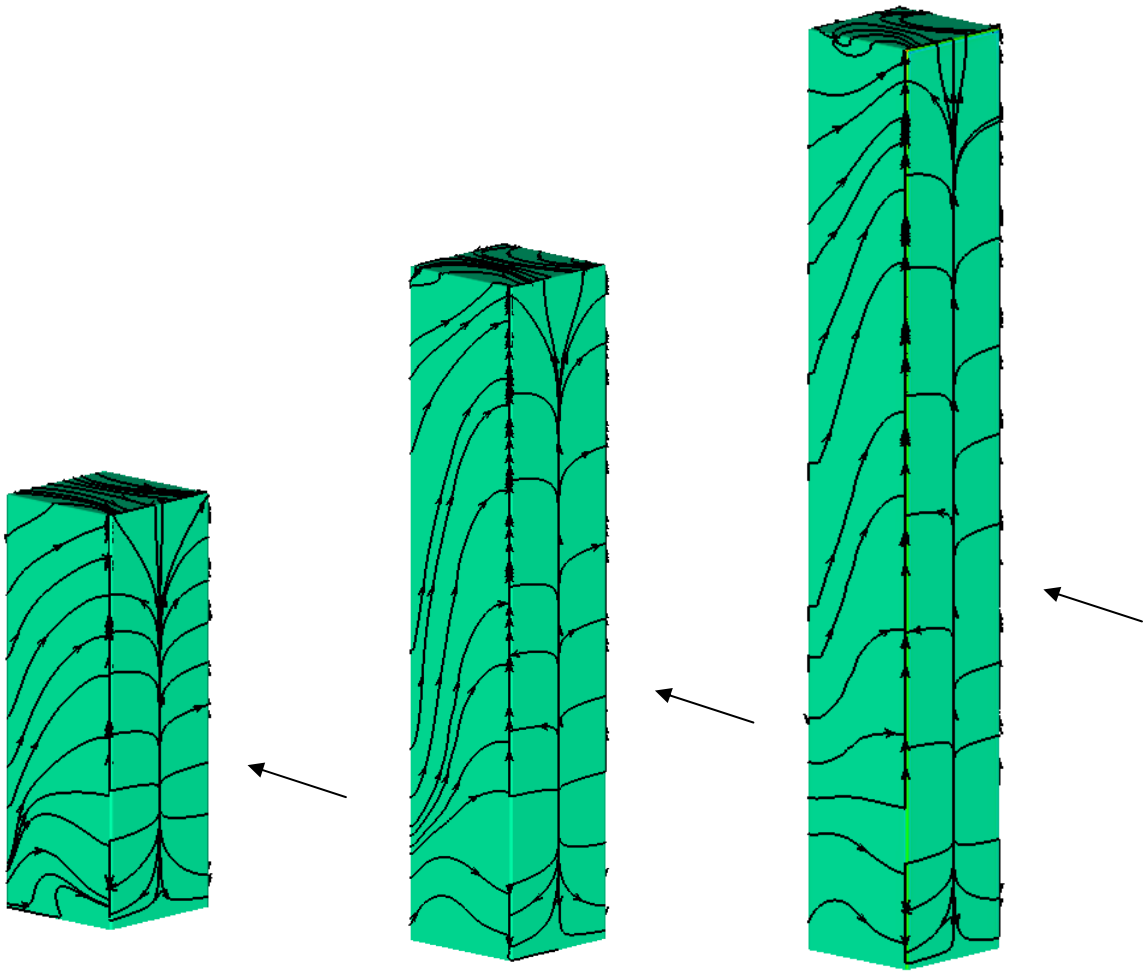

(a) (b) (c)

Figure 7.6: Time-averaged streamlines on the front and side walls of the cylinder: a) AR = 3, b) AR = 5, c) AR = 7.

Figure 7.6 shows the time-averaged streamlines on the front wall and one side wall of the cylinder. In general the streamlines on the front wall of the cylinder reveal a similar flow pattern for all three aspect ratios. For each case, a saddle point is located on the front wall at about z/D = 1 above the ground plane. On the other hand, the flow patterns on the side wall of the cylinder change somewhat with aspect ratio. For example, AR = 3 exhibits a strong upward

flow, from the ground plane to the free end, with only a very small region of downward flow close to the ground plane. The upward flow on the side wall joins with the upward flow on the front wall at the leading vertical edge. For AR = 5, the upward flow is still dominant, but near the ground plane, the region of downward flow is larger. For AR = 7, the downward flow region becomes even more extensive. The streamlines on the top wall also vary with the aspect ratio. While the streamlines are relatively straight for AR = 3, for higher aspect ratios the streamlines tend to curve away from the centreline, as the flow is pulled towards the side edges.

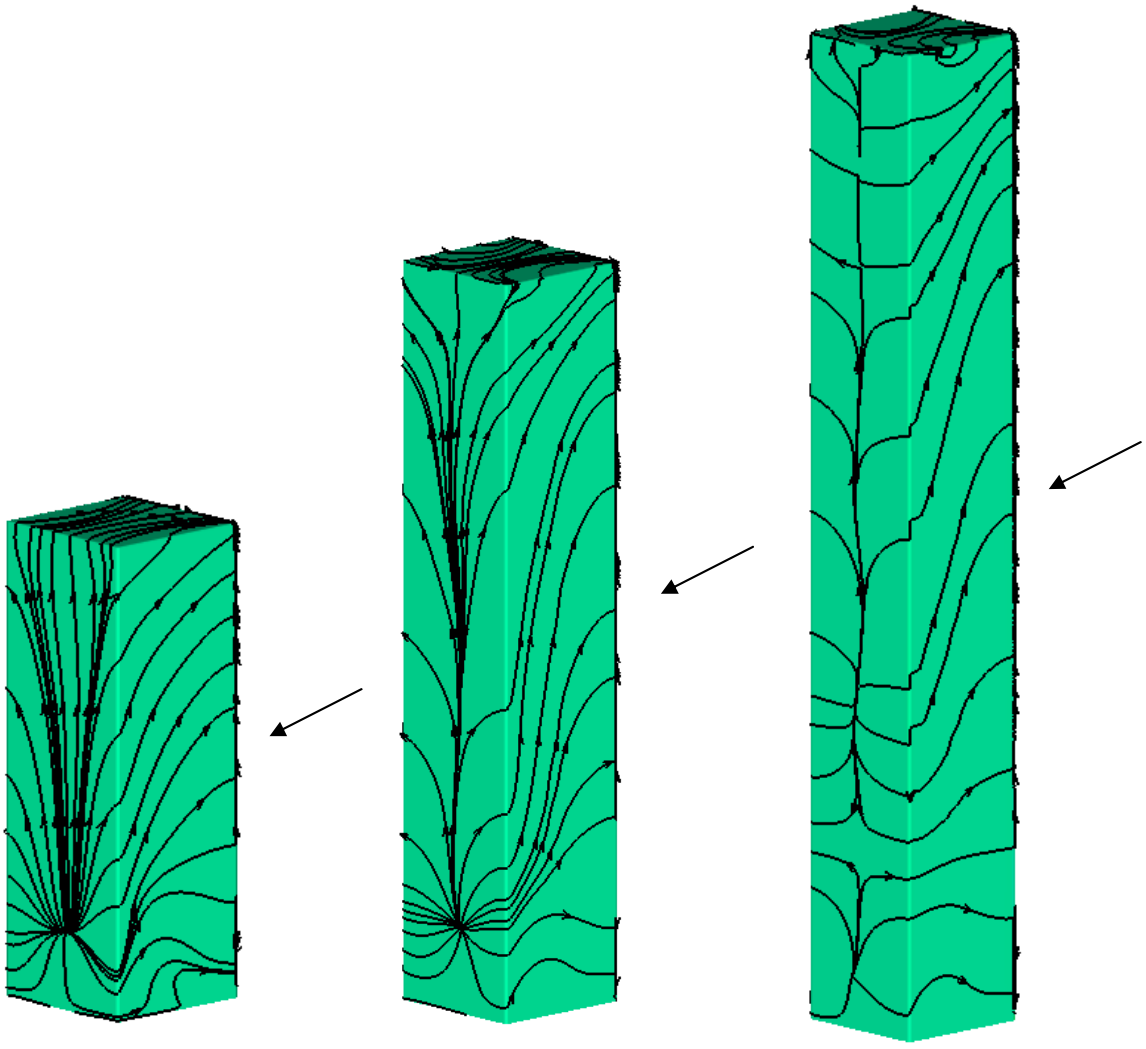

(a) **(b)** **(c)**

Figure 7.7: Time-averaged streamlines on the rear and side walls of the cylinder: a) AR = 3, b) AR = 5, c) AR = 7.

Figure 7.7 presents the time-averaged streamlines on the rear wall of the cylinder for all three aspect ratios. The time-averaged streamlines at the back wall of cylinder exhibit a node at about $z/D = 1$ for both AR = 3 and AR = 5. For both cases, the flow along the rear wall is dominantly upwards. The flow pattern, however, changes as the aspect ratio increases and the flow begins to be directed towards the side walls of the cylinder and upwash becomes weaker. As shown in Figure 7.3 a stronger upwash is observed immediately behind the cylinder for AR = 3 and as the aspect ratio rises to AR = 5 and 7, the near-wall upwash becomes weaker. For AR = 7, a saddle point exists and the movement of the streamlines towards the side walls is more pronounced

7.4. Resolved Stresses

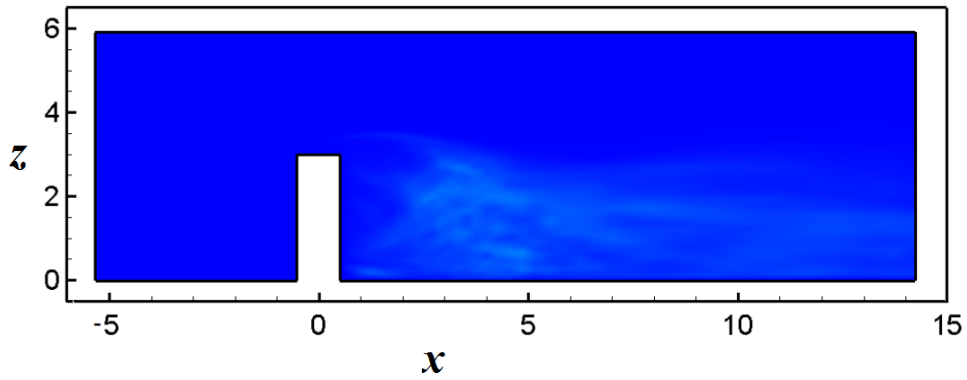

(a)

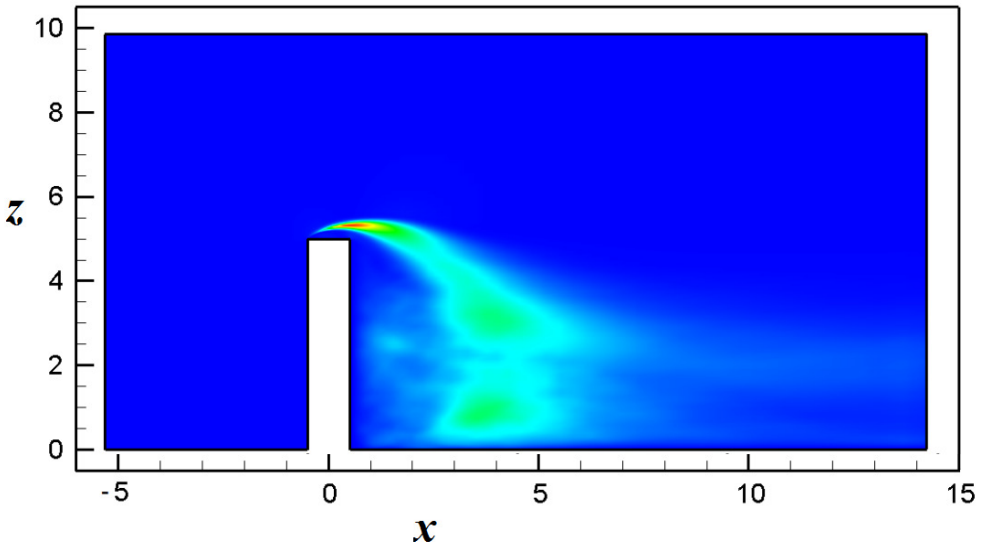

(b)

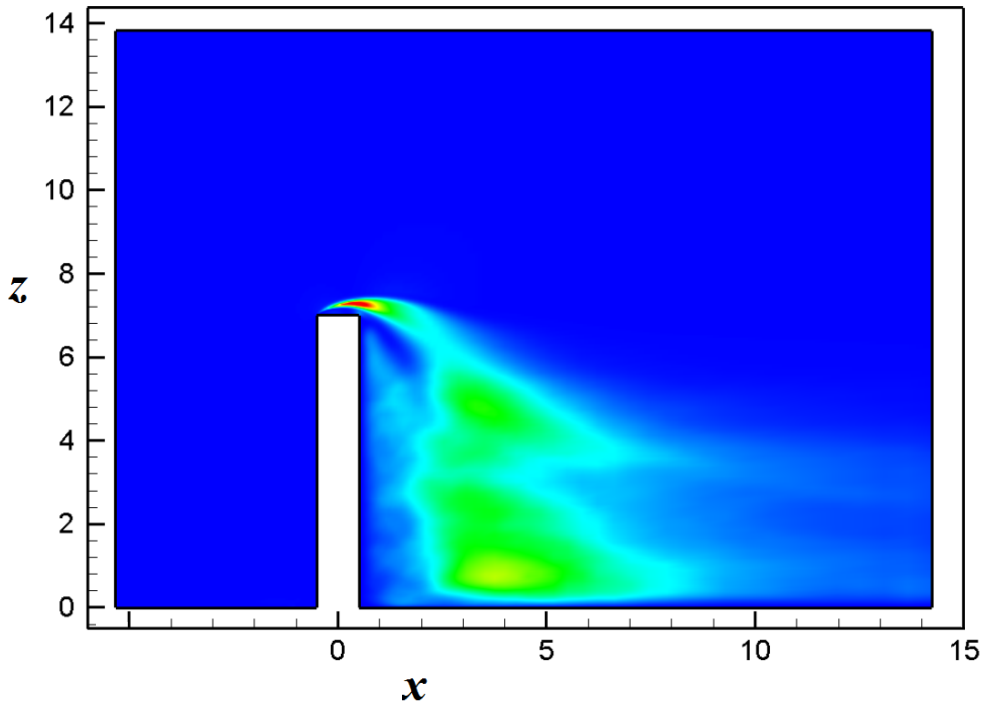

(c)

Figure 7.8: Resolved streamwise stress $\langle u'u' \rangle / U^2_\infty$ with maximum value of $\langle u'u' \rangle / U^2_\infty = 0.3$ in center-plane: a) AR = 3, b) AR = 5, c) AR = 7.

Figure 7.8 shows contours of the resolved streamwise stress component $\langle u'u' \rangle / U^2_\infty$ in a center-plane located at $y/D = 0$. Based on Figure 7.8, the value of the resolved-scale stress is highest for AR = 7, and almost negligible for AR = 3. Two distinct regions of high stress levels are observed for the stress in the near-wake region for AR = 5 and AR = 7. These high-stress

regions might be an indication of local regions of high shear. A high value of $\langle u'u' \rangle / U^2_\infty$ is also observed near the free end of the cylinders for AR = 5 and AR = 7, where the separated flow at the front end of the cylinder is drawn into the downwash. The significant levels of $\langle u'u' \rangle / U^2_\infty$ observed for cylinders with higher aspect ratios may signify the presence of time-variant vortices in the near-wake region of the cylinder, particularly near the ground plane. Figure 7.9 shows contours of the streamwise resolved-scale stress component $\langle u'u' \rangle / U^2_\infty$ in a horizontal plane located at the mid-height of each cylinder, i.e. at z/D = 1.5 for AR = 3, at z/D = 2.5 for AR = 5, and at z/D = 3.5 for AR = 7. Consistent with the flow behavior observed in Figure 7.10, the maximum value of the resolved-scale stress occurs for AR = 7, while the minimum value occurs for AR = 3.

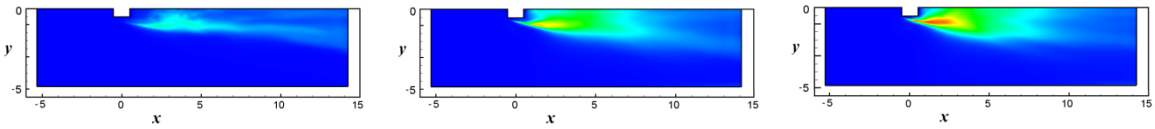

(a) (b) (c)

Figure 7.9: Resolved streamwise stress $\langle u'u' \rangle / U^2_\infty$ with maximum value of $\langle u'u' \rangle / U^2_\infty$ = 0.3 in a horizontal plane at the mid-height of the cylinder: a) AR = 3, b) AR = 5, c) AR = 7.

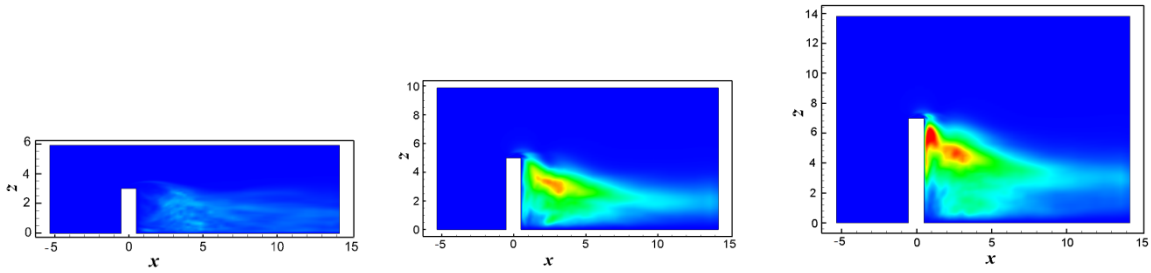

(a) (b) (c)

Figure 7.10: Resolved spanwise stress $\langle w'w' \rangle / U^2_\infty$ with maximum value of $\langle w'w' \rangle / U^2_\infty$ = 0.2 in a center-plane: a) AR = 3, b) AR = 5, c) AR = 7.

Figure 7.10 plots contours of the resolved spanwise stress $\langle w'w' \rangle / U^2_\infty$ in the center-plane of the wake. According to this figure, the magnitude of the spanwise fluctuations is greatest for AR = 7. For AR = 3, the spanwise stress is highest near the outer boundary of the near-wake region. For AR = 3, the resolved stress level is much less compared to AR = 5 and 7 due to the presence of the arch type vortices, which tend to reduce the level of unsteady motion. For AR = 5 and 7,

significant stress levels extend throughout the wake region particularly near the free end of the cylinder, whereas for AR = 3, the stress level is only significant further downstream from the rear wall.

7.5. Time-Averaged Vorticity Contours

Figure 7.11 presents contours of the time-averaged normal vorticity ω_z/U_∞ in a horizontal plane at the mid-height locations for all three aspect ratios.

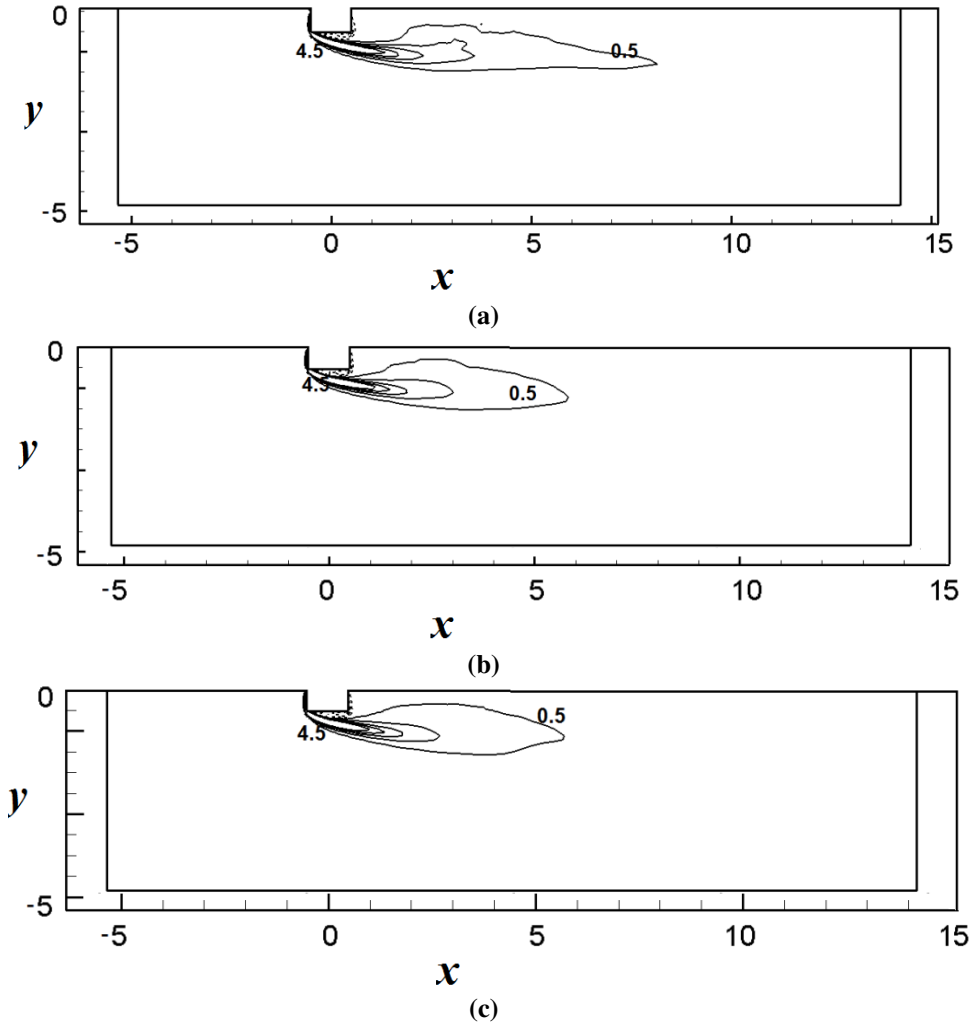

Figure 7.11: Time-averaged normal vorticity contours ω_z/U_∞ located at the mid-height of the cylinder: a) AR = 3, b) AR = 5, c) AR = 7.

As noted in Chapter 4, the normal vorticity is strongest at the front corners of the square cylinder. The extension of the vorticity contours downstream from the cylinder varies with aspect ratio; the extension of the contours in the streamwise direction is the most pronounced for AR = 3, Figure 7.11(a). For AR = 5 and 7, the normal vorticity contours are shorter and rounder in shape, and are wider in the spanwise direction. This might be an indication of the existence of antisymmetric type von-Karman vortices, since the von-Karman type vortices are more extended in the spanwise direction.

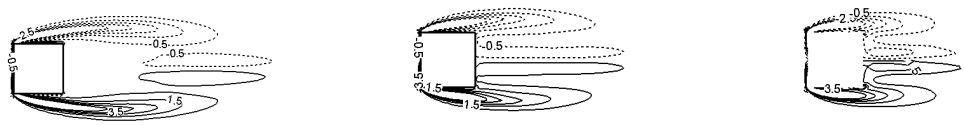

(a) **(b)** **(c)**

Figure 7.12: Time-averaged normal vorticity contours ω_z/U_∞ near the free end located at z/l = 1: a) AR = 3, b) AR = 5, c) AR = 7.

Figure 7.12 shows contours of the time-averaged wall-normal vorticity ω_z/U_∞ in a horizontal plane near the free end of each cylinder, i.e. at z/H = 1. According to Figure 7.12, a pair of symmetric vortices is formed within the wake region near the free end. The center of these vortices moves towards the cylinder as the aspect ratio increases. These vortices are attached for the cylinder at AR = 5 and 7, but not for AR = 3. A comparison between the ω_z/U_∞ contours in the near-wake region for AR = 5 and AR = 7 indicates that the vortices are smaller in size and more rounded in shape for AR = 7. Outside the wake region, a pair of symmetric vortices originates from the front corners of the square cylinder and stretch all the way to the end of the wake region. Like the center vortices, the side-wall vortices become smaller and begin to connect to the central vortices as the aspect ratio increases.

7.6. Development of Streamwise Vorticity in the Near-Wake Region

Figures 7.13 to 7.19 show the spatial development of the time-averaged streamwise vorticity in the wake region of the cylinder using vertical sections located at different distances downstream from the cylinder. In Figure 7.13 which considers a plane section located at x/D = 1, a pair of tip vortices is observed near the free end of the cylinder for all three aspect ratios. These tip vortices are stretched towards the ground plane and two distinct peak regions are observed for each individual vortex. For AR = 3, the tip vortices almost reach the ground plane and the tip and base vortices overlap along the outer edges of the cylinder; as the aspect ratio increases, the distance between the lower part of the streamwise vortex and the ground-plane increases. The tip vortices are also shifted towards the center of the cylinder in the spanwise plane as the aspect ratio increases. In addition to these two sets of vortices, another pair of smaller vortices is observed above the tip vortices at x/D = 1. These vortices appear similar for all three aspect ratios. In terms of the base vortices, due to the fact that the contours of vorticity near the ground plane are very compressed it is difficult to distinguish any specific structures from Figure 7.13.

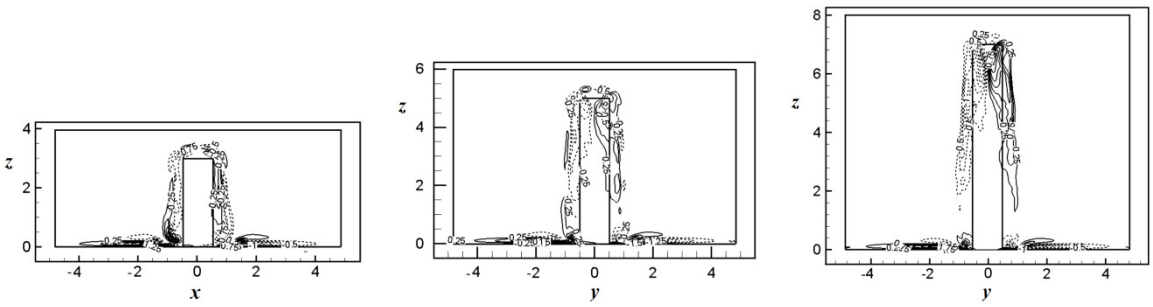

Figure 7.13: Time-averaged streamwise vorticity contours ω_x/U_∞ in a normal plane located at x/D = 1: a) AR = 3, b) AR = 5, c) AR = 7.

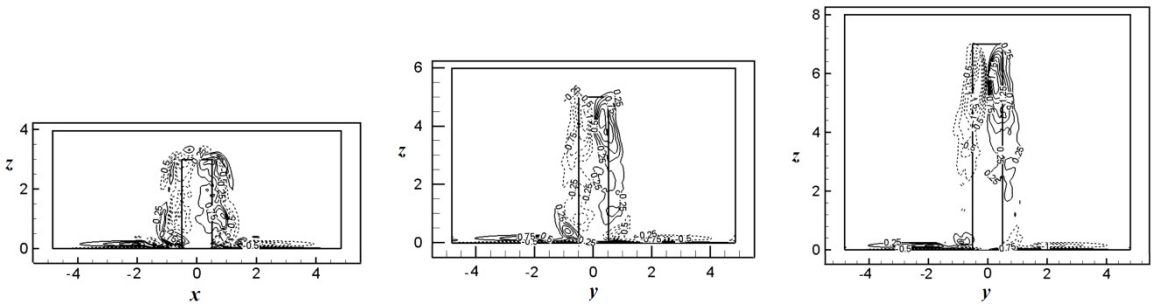

Figure 7.14: Time-averaged streamwise vorticity contours ω_x/U_∞ in a normal plane located at x/D = 2: a) AR = 3, b) AR = 5, c) AR = 7.

Further downstream at x/D = 2, Figure 7.14 indicates that for all three aspect ratios, the tip vortices identified in Figure 7.13 have grown larger and their centers have moved away from the free end towards the ground plane. Weak base vortices are visible for AR = 5 and 7 near the ground plane. The secondary tip vortices observed in Figure 7.13 are absent for AR = 5 and 7, but still persist for AR = 3, likely due to the stronger downwash for the taller cylinders.

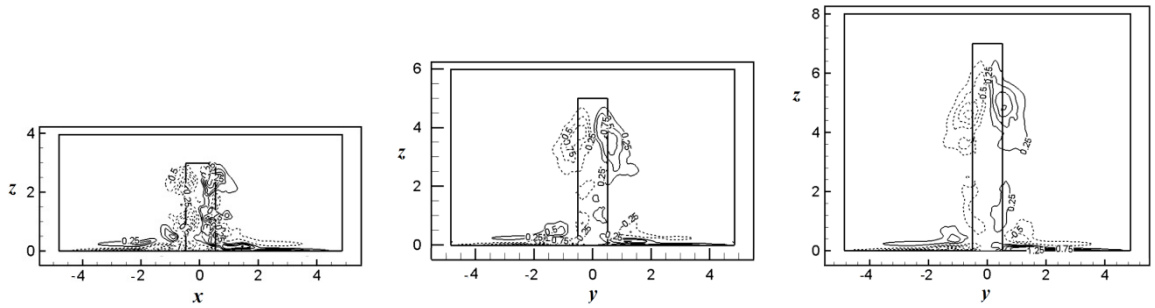

Figure 7.15: Time-averaged streamwise vorticity contours ω_x/U_∞ at a normal plane located at x/D = 4, a) AR = 3, b) AR = 5, c) AR = 7.

Moving farther downstream to x/D = 4, Figure 7.15 shows that for both aspect ratios AR = 5 and 7, the tip vortices have moved farther down towards the ground plane and the base vortices have grown larger. For AR = 3, a pair of small base vortices is now observed near the ground plane. Compared to the higher aspect ratios, the base vortices for AR = 3 are located farther away from the side walls of the cylinder. In contrast, the centers of the base vortices for AR = 7 are still

aligned with the tip vortices. As the aspect ratio increases, the vortices become longer and narrower in shape.

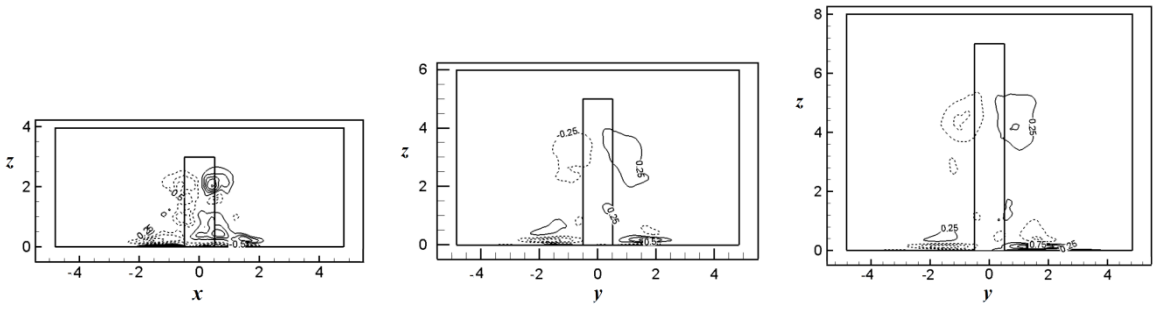

Figure 7.16: Time-averaged streamwise vorticity contours ω_x/U_∞ in a normal plane located at x/D = 6: a) AR = 3, b) AR = 5, c) AR = 7.

Finally, Figure 7.16 presents contours of the time-averaged streamwise vorticity for a plane section located at x/D = 6. The base vortices observed for AR = 3 at x/D = 4 no longer exist near the ground plane, and instead the tip vortex structure extends over the entire length of the cylinder. For aspect ratios of AR = 5 and 7, the centers of the base vortices have moved farther down towards the ground plane and also moved outwards in the lateral direction.

According to these figures, with increasing streamwise distance from the cylinder, the streamwise vortex structures become weaker, while their centers slowly move away from the free end towards the ground plane. The vortices also become more rounded in shape. A similar behaviour was observed by Sumner et al. (2004) for the case of a circular cylinder at a higher Reynolds number. Park and Lee (2000) showed that the vortex formation region decreases as the aspect ratio increases. This may explain the fact that at x/D = 6, both the tip and base vortices are well defined for AR = 3 but are reduced in strength for the two higher aspect ratios (Figure 7.16). The observation that as the aspect ratio decreases, the center of the streamwise vorticity

contours moves downward, and also extends horizontally in the cross-stream direction along the ground plane was also noted by Tanaka and Murata (1999).

7.7. Mean Drag Coefficient

Figure 7.17 demonstrates the time-averaged two-dimensional sectional pressure drag coefficient for all three aspect ratios. The mean pressure drag coefficients are obtained from integration of the mean pressure on the front and rear walls of the cylinder. For AR = 3, the sectional mean drag coefficient remains constant from near the free end to the mid-height of the cylinder, and then decreases near the ground plane. For AR = 5, the change is more gradual. For AR = 7, the sectional drag coefficient drops to its minimal value at about z/H = 0.3 from the ground plane, and a second peak is observed in close proximity to the ground plane. For all three cases right near the ground plane there is a rise due to the wall effect. Baban and So (1991) and Baban et al. (1989) showed that the local mean drag coefficient decreases as the aspect ratio decreases and for individual cases near the cylinder's base.

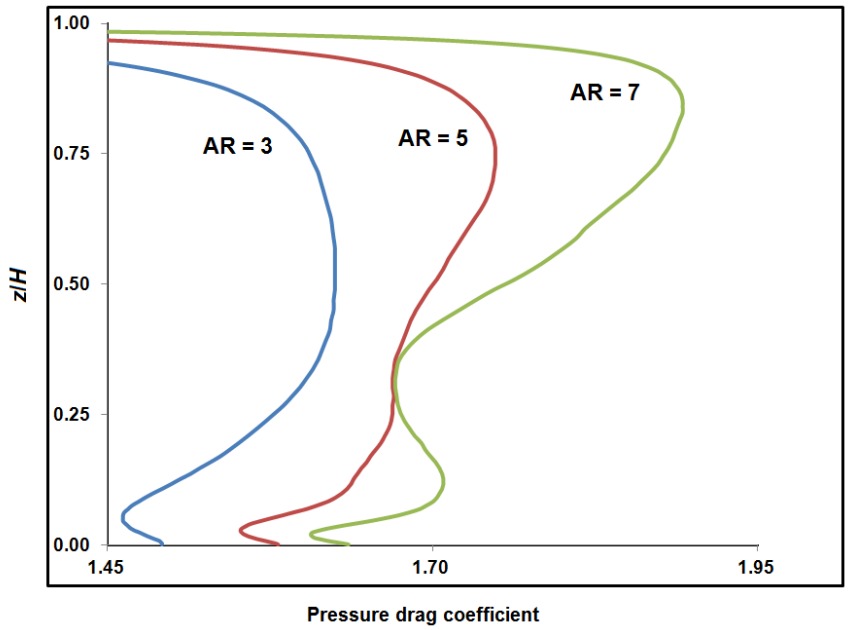

Figure 7.17: Two dimensional (sectional) pressure drag coefficients C_D for the three aspect ratios AR = 3, 5 and 7.

Fox and West (1993) showed that for circular cylinders with AR < 13, the distribution of the mean drag coefficient along the cylinder is unique for each case. As the aspect ratio increased, a steady increase of C_D was observed for 4 < AR < 20. Near the free end, however, a large reduction in the wake pressure resulted in high local mean pressure drag coefficient (Fox and West, 1993).

7.8. Power Spectra

The variation of the power spectra with Strouhal number (based on the resolved scale streamwise velocity fluctuation along the height of the cylinder) is explored in Figure 7.18 for the three different aspect ratios. The probes are located at x/D = 3, y/D = 1.5: a) z/D = 1.8, b) z/D = 1.5, c) z/D = 1.2, d) z/D = 2.7, e) z/D = 2.1, f) z/D = 1.2, g) z/D = 4.2, h) z/D = 3.6, i) z/D = 2.9. The specific plots indicate a distinct peak for both AR = 5 and AR = 7; in contrast, no single dominant peak is observed for AR = 3. This behaviour seems reasonable as the flow for lower

aspect ratios does not exhibit time-variant vortex shedding as shown by Kawamura et al., (1984) and Sakamoto and Arie (1983).

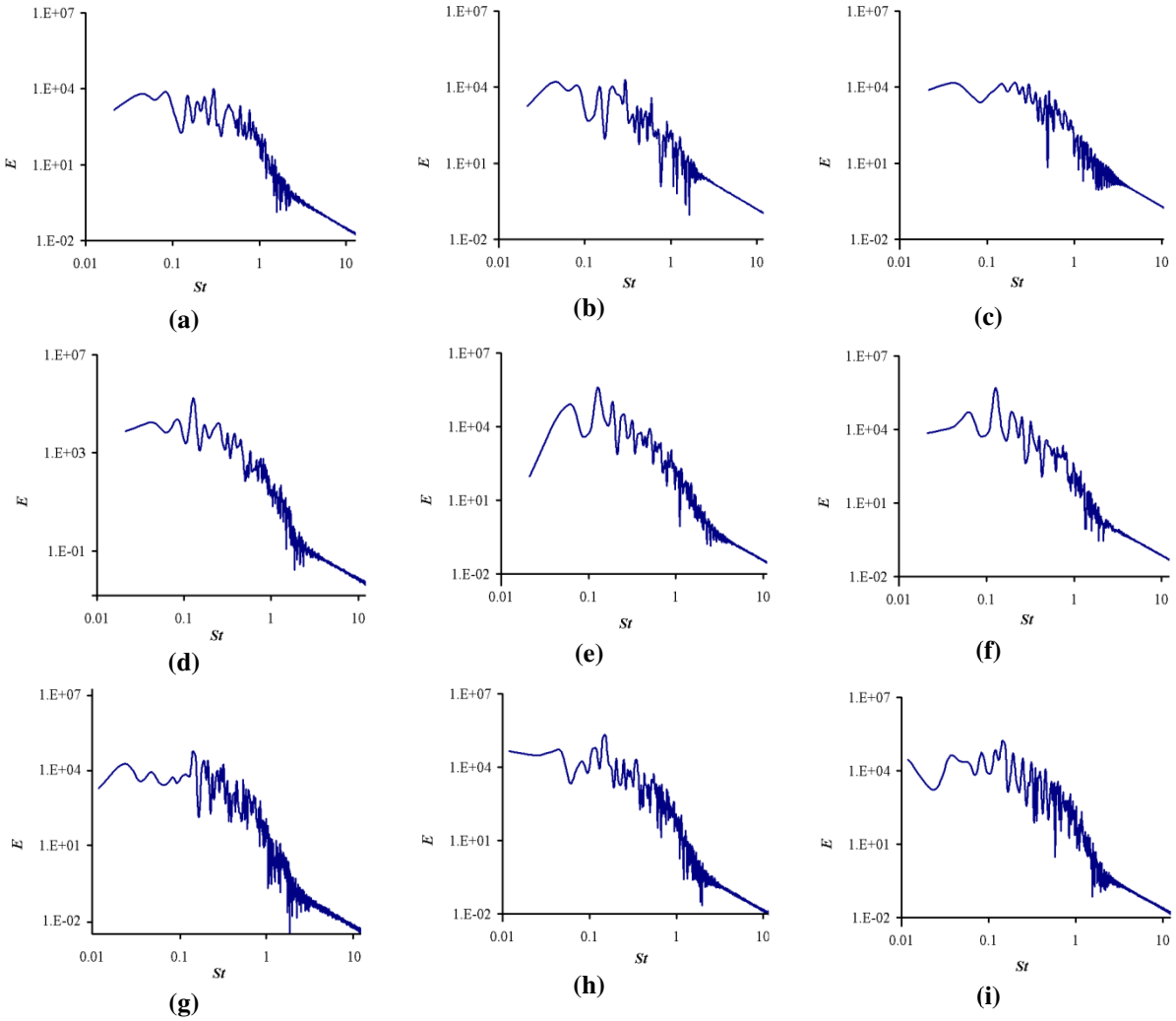

Figure 7.18: Variation of the power spectra along the height of the cylinder, at *x/D* = 3 and *y/D* = 1.5 for all three aspect ratios. From top to bottom: AR = 3 (a,b,c), AR = 5 (d,e,f), AR = 7 (g,h,i). From left to right: near the free end (a,d,g), mid-height (b,e,h), near the ground plane (c,f,i).

For AR = 5, Figure 7.18 (d,e,f) indicates the same Strouhal number St = 0.127 for all three heights, which implies the Strouhal number does not vary along the cylinder and is independent of vertical location. For this aspect ratio, as the location moves from the free end towards the ground plane, the peak becomes stronger. For AR = 7, the Strouhal number varies along the height of the cylinder: St = 0.142 near the free end and ground plane, while at the mid-height St

= 0.166. This is consistent with the numerical simulations of Lee et al. (2007) who showed that the vortex shedding in the upper section of a taller cylinder was not in phase with that of the lower region of the same cylinder. Compared to AR = 5, the peak values for AR = 7 are less distinct especially near the free end. For AR = 7, Wang and Zhou (2009) obtained a peak Strouhal number of St = 0.11. In a previous study Wang et al. (2004) had reported St = 0.13 for AR = 7. Wang and Zhou (2009) proposed that the presence of the downwash flow affects the frequency hence the Strouhal number is lower for finite cylinders than for an infinite cylinder, for which typically St = 0.125 ~ 0.13 at Re = 9.3×10^3. Wang and Zhou (2009) also obtained power spectra at different streamwise locations. For all three locations considered, the major peak value of the spectra indicated a Strouhal number of St = 0.11 at Re = 9.3×10^3, although further from the square cylinder a second value of St = 0.22 was observed near the ground plane. For a circular cylinder of aspect ratio AR = 3 to 9, Sumner et al. (2004), observed that the Strouhal number of St ≈ 0.16 was independent of the position along the height of the cylinder at Re = 6×10^4. Sakamoto and Arie (1983) indicated that the Strouhal number decreases with decreasing aspect ratio for both a finite-height circular cylinder and a rectangular prism mounted on a ground-plane.

7.9. Visualization of Mean Vortex Structure in Wake

Figure 7.19 presents iso-surfaces of the time-averaged vortex structures using the 2^{nd} invariant of the velocity gradient field in the near-wake of the cylinder for all three aspect ratios. Note that a small horseshoe vortex is observed in front of the cylinder on the ground plane for all three aspect ratios.

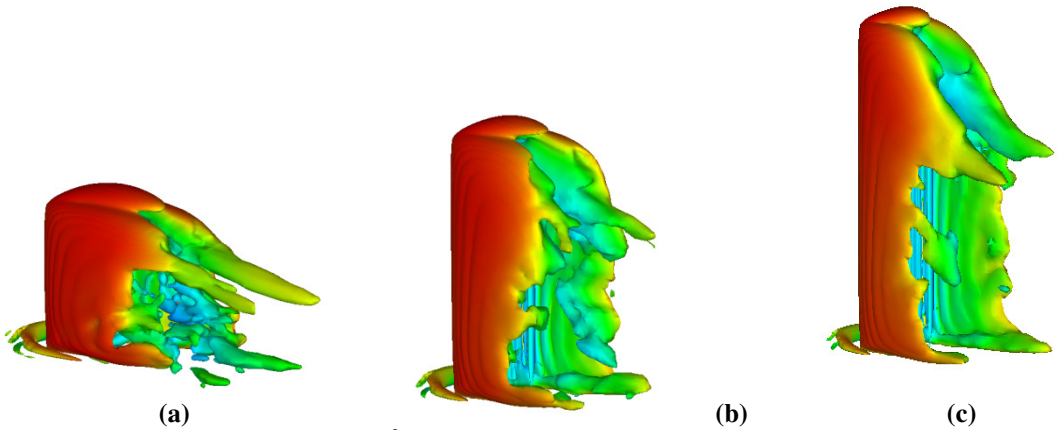

(a) (b) (c)

Figure 7.19: Time-averaged 2nd invariant iso-surfaces: a) AR = 3, b) AR = 5, c) AR = 7 colored by the magnitude of the streamwise velocity.

The horseshoe vortex formed at the front of the square cylinder with AR = 3 is somewhat more well defined than that for AR = 5 and AR = 7. This agrees with the observation of Okamoto and Sunabashiri (1992) that the size of the horseshoe vortex depends on the height of the cylinder, and decreases as the height of the cylinder increases.

A pair of tip vortex structures and a quasi-symmetric arch-type vortex are formed in the near-wake region. These vortex structures are formed at the free end and as the aspect ratio increases they become weaker and move further away from the free-end. Next to the ground plane a second pair of vortex structures is formed for all three aspect ratios. The shear layers on the side walls are also observed to form irregular vortical structures which bend inward toward each other. In the interior of the near-wake region, the AR = 3 cylinder has more streamwise structures than the other two aspect ratios. The streamwise extent of these side wall shear layers is a function of the aspect ratio and tends to decrease as the aspect ratio increases. As noted previously, the lack of any sign of antisymmetric Kármán vortex shedding reflects the time-averaged nature of these structures.

7.10. Conclusions

The wake of a finite square cylinder mounted on a ground plane was investigated numerically using a dynamic Smagorinsky SGS model. The cylinder aspect ratio was set at AR = 3, 5 and 7, and the Reynolds number was Re = 500. Each cylinder was immersed in a thin laminar boundary layer.

The time-averaged velocity field in the near-wake region showed the presence of a strong downwash for all three aspect ratios, and a weaker upwash for AR = 5 and 7. A strong upwash is observed near the cylinder for AR = 3. The time-averaged vorticity was shown to vary with aspect ratio, e.g., as the aspect ratio increases, the vortex structures in a horizontal plane at mid-height become shorter and rounder in shape. In terms of resolved scale stress, the $\langle u'u' \rangle / U^2_\infty$ contours extended further downstream at higher aspect ratios, which may be due to the existence of vortex shedding in the near-wake region of the cylinder, particularly near the ground plane. The time-averaged streamwise vorticity fields showed the presence of a counter-rotating vortex pair near the free end (the tip vortex structures) and a pair of weaker base vortices near the ground plane. Tip vortex structures were observed for all three aspect ratios, and weakened as the flow moved downstream. In terms of the magnitude, the tip vortices are strongest for AR = 3 and reduce in strength as the aspect ratio increases.

Consideration of the vortex shedding frequency indicated a different wake structure for the cylinder with AR = 3. While a distinct peak was observed for AR = 5 and AR = 7, no dominant peak value was detected for AR = 3. This behaviour is consistent with the notion that at lower aspect ratios the flow does not exhibit time-variant vortex shedding. For AR = 5 the Strouhal number did not vary along the height of the cylinder, whereas for AR = 7 it did. Finally,

visualisation of the time average velocity field using 2^{nd} invariant iso-surfaces indicated a horseshoe vortex in front of the cylinder and an arch-type vortical structure in the wake region.

Chapter 8

Conclusions and Future Work

8.1. Review of Major Contributions

The main objective of this research was to develop, document and study numerically the flow around finite-height square cylinders mounted on a ground plane, particularly in the near-wake region, under various geometrical conditions. Both the time-averaged and instantaneous flow fields were studied. The secondary objective of the research was to study the effect of various sub-grid scale (SGS) models. Ultimately the effect of aspect ratio was studied for three aspect ratios of AR = 3, 5 and 7.

This study is one of few studies to perform an LES simulation of the flow around a surface-mounted finite square cylinder. This study provides new physical insight into the complex, three-dimensional, turbulent, and unsteady near-wake flow structures, including both the time-averaged representation and instantaneous behavior. It should be noted that this type of information is very difficult to obtain with conventional experimental techniques. The only technique that could be used would be Tomographic PIV, which is very new and probably does not have the temporal resolution.

In Chapter 4 the time-averaged flow field over a wall-mounted finite-height square cylinder of AR = 5 at Re = 500 was studied in detail. The time-averaged results were in good agreement with the measurements of Wang et al. (2006) for flow over a finite-height square cylinder immersed in a thin boundary layer. Comparison of the LES results with the velocity field for a square cylinder immersed in a thicker boundary layer, Wang et al. (2009), suggested that the boundary layer thickness especially affects the upwash flow. More specifically, a thicker

boundary layer causes the upwash to become stronger. A pair of counter-rotating tip vortices was observed near the free end. As the flow moved downstream, these vortices moved towards the ground plane, lost their strength and became rounder in shape. Also, a pair of weak base vortex structures was observed near the ground plane. The base vortices were smaller in size than those observed in the experiments of Sumner et al. (2004) and Wang et al. (2009), most likely due to the boundary layer thickness on the ground plane (Wang et al., 2006).

The instantaneous velocity fields from LES of flow over a wall-mounted finite-height square cylinder with AR = 5 were presented in Chapter 5. A Strouhal number of St = 0.127 was obtained for three sample locations along the height of the cylinder, which is in a good agreement with the experimental measurements. The instantaneous flow fields were characterized by the strong downwash flow from the free end interacting with a weak upwash flow originating from the ground plane. Two distinct flow fields were observed: in the first scenario the free end downwash flow met the upwash flow from the ground plane and was limited to the upper half of the wake, and only one saddle point was observed. The second scenario involved a more complex flow pattern with multiple saddle and focal points. The instantaneous velocity fields suggested a symmetric flow near the free end. However, further downstream from the cylinder, the velocity field in the wake became strongly antisymmetric. The streamwise vorticity contours in a normal plane located at various distances from the cylinder indicated that as the flow moved downstream, the vortex structures became weaker and concentrated closer to the ground plane. The structures also extended in the transverse direction, and exhibited the asymmetry observed in the velocity vector fields.

In Chapter 6, the LES predictions of three SGS models, i.e. SM, DSM and DNM, performed on two different grid levels of $64 \times 72 \times 48$ and $128 \times 144 \times 96$ for a square cylinder with AR = 5 at Re = 500 were presented. The flow field around a bluff body includes various types of flow features such as separation, free shear layers and vortex shedding, which makes it difficult to pre-select one specific value of C_S as required by a SM. The DSM with a low resolution yielded a shorter recirculation zone, but exhibited the highest u-fluctuations. In terms of the streamwise vorticity contours, all three SGS models with a high resolution grid predicted similar vorticity contours. Although the DSM solution with a low resolution grid was unable to predict the near-wake region accurately, outside the wake region the streamwise vorticity contours were similar to the predictions of the other two models. In the case of the DSM solutions, insufficient grid resolution led to erroneous predictions. The DNM is a major improvement as the predictions were similar on both the coarse and fine grids. Both time-averaged and instantaneous results indicate that the DNM is less dependent on the grid resolution than the DSM. In addition, it appears to result in a finer-scale vortex structure than the DSM. The SM, appeared to lead to different time-averaged vorticity fields in the wake, and did not resolve some of the detail captured by the dynamic models. All in all, the DNM was much less sensitive to grid resolution and was able to predict the flow structure even with lower resolution.

In Chapter 7, the wake of a finite square cylinder mounted on a ground plane was investigated numerically using LES using a dynamic Smagorinsky SGS model. The cylinder aspect ratio was set at AR = 3, 5 and 7, and the Reynolds number was Re = 500. Each cylinder was immersed in a thin laminar boundary layer.

The time-averaged velocity field in the near-wake region showed the presence of a strong downwash for all three aspect ratios, and a weaker upwash for AR = 5 and 7. A strong upwash is observed near the cylinder for AR = 3. The time-averaged vorticity was shown to vary with aspect ratio, e.g. as the aspect ratio increases, the vortex structures in a horizontal plane at mid-height became shorter and rounder in shape. In terms of resolved scale stress, the $\langle u'u' \rangle / U^2_\infty$ contours extended further downstream at higher aspect ratios, which might be due to the existence of vortex shedding in the near-wake region of the cylinder, particularly near the ground plane. The time-averaged streamwise vorticity fields showed the presence of a counter-rotating vortex pair near the free end (the tip vortex structures) and a pair of weaker base vortices near the ground plane. Tip vortex structures were observed for all three aspect ratios, and weakened as the flow moved downstream. In terms of the magnitude, the tip vortices were strongest for AR = 3 and reduced in strength as the aspect ratio increased. Consideration of the vortex shedding frequency indicated a different wake structure for the cylinder with AR = 3. While a distinct peak was observed for AR = 5 and AR = 7, no dominant peak value was detected for AR = 3. This behaviour was consistent with the notion that at lower aspect ratios the flow does not exhibit time-variant vortex shedding. Finally, visualisation of the time average velocity field using 2nd invariant iso-surfaces indicated a horseshoe vortex in front of the cylinder and an arch-type vortical structure in the wake region.

8.2. Comments on Future Studies

In this thesis, the flow over a finite-height square cylinder is studied. Although useful information has been obtained from the simulation of the flow over a square cylinder, the model is restricted to the simple geometry of a square cylinder. Therefore an important next step in

developing the code is to enable the simulation over different geometric shapes such as a circular cylinder. A key issue for complex geometries is the grid generation process. In the past different body-fitted grids such as O-type and C-type grids were usually used, which generally required significant effort and could lead to a loss of accuracy. The grid generation effort becomes even more complex and time-consuming for moving or deforming geometries. The advantage of structured Cartesian grids over curvilinear or unstructured grids is the relative ease of the grid generation process, the lower computational effort, and the lower book-keeping requirements. The immersed boundary method (IBM) has opened the doors to simulate complex geometries, maintaining the simplicity and efficiency of the Cartesian grid. In the IBM, the boundaries do not necessarily conform to the grid, and the governing equations are usually discretized on fixed Cartesian meshes. The advantage of the IBM is that bodies of almost arbitrary shape can be implemented without grid restructuring, a procedure which is often time-consuming (Mohd-Yusof 1998). Furthermore, multiple bodies may be simulated with different arrangements and the interference effects between various bluff bodies can also be studied. In view of the above, implementation of the IBM should be considered in the future.

Also related to the grid, developing a parallel algorithm along with a multi-block scheme would enable the code to perform much faster and hence enable the numerical simulation of higher Reynolds numbers and finer grids.

As it was discussed before, the boundary layer thickness affects the wake region particularly near the ground plane. A thicker boundary layer causes the base vortices to become stronger and the upwash becomes more pronounced. In this thesis the cylinders were immersed in a thin laminar boundary layer, whereas in most experimental cases, thicker turbulent boundary layers are

generally employed. Future work should therefore consider thicker and turbulent boundary layers. To properly implement a thick turbulent boundary layer in LES, an instantaneous velocity profile with realistic turbulence characteristics must be introduced at the inlet.

Finally, even though the experiments of Lin et al. (2008) for a flow around a surface-mounted square cylinder for Reynolds numbers ranging from Re = 200 to 6,000 showed that the flow structures are mostly independent of Reynolds number, it would be useful to perform simulations at higher Reynolds numbers to confirm this behaviour.

References

M.S. Adaramola, O.G. Akinlade, D. Sumner, D.J. Bergstrom and A.J. Schenstead. Turbulent Wake of a Finite Circular Cylinder of Small Aspect Ratio. *Journal of Fluids and Structures*, 22, 919–928, 2006.

I. Afgan, C. Moulinec, R. Prosser and D. Laurence. Large Eddy Simulation of Turbulent Flow for Wall-Mounted Cantilever Cylinders of Aspect Ratio 6 and 10. *International Journal of Heat and Fluid Flow,* 28, 561-574, 2007.

E. Baban and R.M.C. So. Aspect Ratio Effect on Flow-Induced Forces on Circular Cylinders in a Cross-flow. *Experiments in Fluids*, 10, 313-321, 1991.

E. Baban, R.M.C. So and M.V. Ottigen. Unsteady Forces on Circular Cylinders in a Cross-flow. *Experiment in Fluids*, 7, 293-302, 1989.

G. Bosch and W. Rodi. Simulation of Vortex Shedding past a Square Cylinder with Different Turbulence Models. *International Journal for Numerical Methods in Fluids,* 28, 601-616, 1998.

J.A. Bourgeois, P. Sattari and R.J. Martinuzzi. Alternating Half-loop Shedding in the Turbulent Wake of a Finite Surface-Mounted Square Cylinder with a Thin Boundary Layer. *Physics of Fluids*, 23, 095101, 2011.

Y. Dubief and F. Delcayre. On Coherent-Vortex Identification in Turbulence. *Journal of Turbulence*, 1, 011, 2000.

J.H. Ferziger and M. Peric. *Computational Methods for Fluid Dynamics.* 2nd Edition, New York: Springer, 1999.

T.A. Fox and G.S. West. Fluid-Induced Loading of Cantilevered Circular Cylinders in a Low-Turbulence Uniform Flow. Part 1: Mean Loading with aspect ratios in the range 4 to 30. *Journal of Fluid and Structures,* 7, 1-14, 1993.

J. Frohlich and W. Rodi. LES of the Flow around a Circular Cylinder of Finite Height. *International Journal of Heat and Fluid Flow*, 25, 537-548, 2004.

O. Frederich, J. Scouten, D. M. Luchtenburg and F. Thiele. Large-Scale Dynamics in the Flow around a Finite Cylinder with Ground Plate. *Proceedings of the Sixth International Symposium on Turbulence and Shear Flow Phenomena,* Seoul, Korea, 1331-1336, 2009.

J. Frohlich, W. Rodi, Ph. Kessler, S. Parpais, J.P. Bertoglio, D. Laurence. Large Eddy Simulation of Flow around Circular Cylinders on Structured and Unstructured Grids. *Notes on Numerical Fluid Mechanics* 66, 319-338, 1998.

M. Germano, U. Piomelli, P. Moin and W.H. Cabot. A Dynamic Subgrid-Scale Eddy Viscosity Model. *Physics of Fluids A*, 3, 1760-1765, 1991.

D.G.E. Grigoriadis, J.G. Bartzis and A. Goulas. LES of the Flow past a Rectangular Cylinder Using the Immersed Boundary Concept. *International Journal for Numerical Methods in Fluids,* 41, 615-632, 2003.

F.E. Ham, F.S. Lien and A.B. Strong. A Fully Conservative Second-Order Finite Difference Scheme for Incompressible Flow on Nonuniform Grids. *Journal of Computational Physics,* 177, 117-133, 2002.

T. Kawamura, M. Hiwada, T. Hibino, I. Mabuchi and M. Kumada. Flow around a Finite Circular Cylinder on a Flat Plate (Cylinder Height Greater than Turbulent Boundary Layer Thickness). *Bulletin of JSME,* 27, 232, 2142-2151, 1984.

J. Kim and P. Moin. Application of a Fractional-Step Method to Incompressible Navier-Stokes Equations. *Journal of Computational Physics,* 59(2), 308-23, 1985.

S. Krajnovic. Flow around a Tall Finite Cylinder Explored by Large Eddy Simulation. *Journal of Fluid Mechanics,* 676, 294–317, 2011.

S. Lee. Numerical Study of Wake Structure behind a Square Cylinder at High Reynolds Number. *Wind and Structures*, 1, 2, 127-144, 1998.

T. Lee, C.L. Lin, C.A. Friehe. Large-Eddy Simulation of Air Flow around a Wall-Mounted Circular Cylinder and a Tripod Tower. *Journal of Turbulence,* 8, 29, 2007.

M. Lesieur and O. Metais. New Trends in Large-Eddy Simulations of Turbulence. *Annual Review of Fluid Mechanics,* 28, 45-82, 1996.

M. Lesieur, O. Métais and P. Comte. *Large-Eddy Simulations of Turbulence*. Cambridge University Press, USA, 2005.

C.W. Li and L.L. Wang. An Immersed Boundary Finite Difference Method for LES of Flow around Bluff Shapes. *International Journal for Numerical Methods in Fluids,* 46, 85-107, 2004.

D.K. Lilly, A Proposed Modification of the Germano Subgrid-Scale Closure Method. *Physics of Fluids A*, 4, 633-635, 1992.

C. Lin, T.C. Ho and S. Dey. Characteristics of Steady Horseshoe Vortex System near Junction of Square Cylinder and Base Plate. *ASCE Journal of Engineering Mechanics,* 134, 2, 2008.

T.M. Liou, S.H. Chen and P.W. Hwang. Large Eddy Simulation of Turbulent Wake behind a Square Cylinder with a Nearby Wall. *ASME Journal of Fluids Engineering,* 124, 81-90, 2002.

T.S. Lund and E.A. Novikov. Parameterization of Subgrid-Scale Stress by the Velocity Gradient Tensor. *Annual Research Briefs*, *Center for Turbulence Research, Stanford Univ.* 27-43, 1992.

D.A. Lyn, S. Einav, W. Rodi and J.H Park. A Laser-Doppler Velocimetry Study of Ensemble-Averaged Characteristics of the Turbulent near Wake of a Square Cylinder, *Journal of Fluid Mechanics,* 304, 285-319, 1995.

R. Mittal and G. Iaccarino. Immersed Boundary Methods. *Annual Review of Fluid Mechanics,* 37, 239-261, 2005.

Mohd-Yusof J. 1998. Development of immersed boundary methods for complex geometries. *Center for Turbulence Research Annual Research Briefs,* 325-336.

S. Murakami, S. Iizuka and R. Ooka. CFD Analysis of Turbulent Flow past Square Cylinder Using Dynamic LES. *Journal of Fluids and Structures,* 13, 1097-1112, 1999.

A. Okajima. Strouhal Numbers of Rectangular Cylinders. *Journal of Fluid Mechanics*, 123, 379-398, 1982.

S. Okamoto and Y. Sunabashiri. Vortex Shedding from a Circular Cylinder of Finite Length Placed on a Ground Plane. *ASME Journal of Fluids Engineering*, 114, 4, 512 -521, 1992.

S. Okamoto, K. Tsunoda and T. Takagi. Turbulent Near Wake behind Square Cylinder of Finite Length on Ground Plane. *Proceedings of the ASME/JSME Fluids Engineering and Laser Anemometry Conference and Exhibition, ASME Fluids Engineering Division,* 229:195-216, 1995.

C.W. Park and S.J. Lee. Free end Effects on the Near Wake Flow Structure behind a Finite Circular Cylinder. *Journal of Wind Engineering and Industrial Aerodynamics,* 88, 231-246, 2000.

C.W. Park and S.J. Lee. Flow Structure around a Finite Circular Cylinder Embedded in Various Atmospheric Boundary Layers. *Fluid Dynamics Research*, 30, 197-215, 2002.

S.B. Pope. A More General Effective-Viscosity Hypothesis. *Journal of Fluid Mechanics*, 72, 331-340, 1975.

S.B. Pope. *Turbulent Flows*. Cambridge University Press, UK, 2000.

P. Sagaut. *Large Eddy Simulation for Incompressible Flows: An Introduction*. Springer Verlag, Germany, 2005.

H. Sakamoto and M. Arie. Vortex Shedding from a Rectangular Prism and a Circular Cylinder Placed Vertically in a Turbulent Boundary Layer. *Journal of Fluid Mechanics*, 126, 147-165, 1983.

G.P. Salvador, T. Stoesser, J. Fröhlich, M. Kappler and W. Rodi. Large Eddy Simulations and Experiments of Flow around Finite-Height Cylinders. *Flow, Turbulence and Combustion,* 84, 2, 239-275, 2010.

M.V. Salvetti and S. Banerjee. A Priori Tests of a New Dynamic Subgridscale Model for Finite-difference Large-eddy Simulations. *Physics of Fluids*, 7, 2831-2847, 1995.

A. Sau, R.R. Hwang, T.W.H. Sheu and W.C. Yang. Interaction of Trailing Vortices in the Wake of a Wall-Mounted Rectangular Cylinder. *Physical Review E*, 68, 056303, 1-15, 2003.

A.J. Smits, T.T. Lim. *Flow Visualization: Techniques and Examples*, Imperial College Press, UK, 2000.

A. Sohankar, C. Norberg and L. Davidson. Simulation of Three-Dimensional Flow around a Square Cylinder at Moderate Reynolds Numbers. *Physics of Fluids*, 2, 288-306, 1999.

J.M.M. Sousa. Turbulent Flow around a Surface-Mounted Obstacle using 2D-3C DPIV. *Experiments in Fluids*, 33, 854-862, 2002.

D. Sumner, J.L. Heseltine and O.J.P. Dansereau. Wake Structure of a Finite Circular Cylinder of Small Aspect Ratio. *Experiments in Fluids*, 37, 720-730, 2004.

S. Tanaka and S. Murata. An Investigation of the Wake Structure and Aerodynamic Characteristics of a Finite Circular Cylinder. *JSME International Journal. Series B: Fluids and Thermal Engineering,* 42, 178-187, 1999.

M. Tutar, A.E. Hold. Computational Modelling of Flow around a Circular Cylinder in Sub-critical Flow Regime with various Turbulence Models. *International Journal for Numerical Methods in Fluids,* 35, 763-784, 2001.

B.C. Wang and D.J. Bergstrom. A Dynamic Nonlinear Subgrid-Scale Stress Model. *Physics of Fluids*, 17, 035109, 1-15, 2005.

H.F. Wang and Y. Zhou. The Finite-Length Square Cylinder near Wake. *Journal of Fluid Mechanics*, 638, 453-490, 2009.

H.F. Wang, Y. Zhou, C.K. Chan, W.O. Wong and K.S. Lam. Flow Structure Around A Finite-Length Square Prism. *15th Australasian Fluid Mechanics Conference, The University of Sydney, Sydney, Australia,* 2004.

H. Wang, Y. Zhou, C. Chan and T. Zhou. Momentum and Heat Transport in a Finite-Length Cylinder Wake. *Experiments in Fluids*, 46, 1173-1185, 2009.

H.F. Wang, Y. Zhou, C.K. Chan and K.S. Lam. Effect of Initial Conditions on Interaction between a Boundary Layer and a Wall-Mounted Finite-Length-Cylinder Wake. *Physics of Fluids,* 18, 065106, 1-12, 2006.

P. Wesseling and C.W. Oosterlee. Geometric Multigrid with Applications to Computational Fluid Dynamics. *Journal of Computational and Applied Mathematics,* 128, 311-334, 2001.

N. Wikstrom, U. Svennberg, N. Alin and C. Fureby. Large Eddy Simulation of the Flow around an Inclined Prolate Spheroid. *Journal of Turbulence,* 29, 1-18, 2004.

C.H.K. Williamson. Vortex Dynamics in the Cylinder Wake. *Annual Review of Fluid Mechanics,* 28, 477-539, 1996.

J.G. Wissink and W. Rodi. Numerical Study of the Near Wake of a Circular Cylinder. *International Journal of Heat and Fluid Flow*, 29, 1060–1070, 2008.

J. Wu, J. Sheridan, M.C. Welsh and K. Hourigan. Three-Dimensional Vortex Structures in a Cylinder Wake. *Journal of Fluid Mechanics,* 312, 201-222, 1996.

S.C. Yen, and C.W. Yang. Flow Patterns and Vortex Shedding Behavior behind a Square Cylinder. *Journal of Wind Engineering and Industrial Aerodynamics*. 99, 868-878, 2011.

Appendix A

Multi-Grid Approach

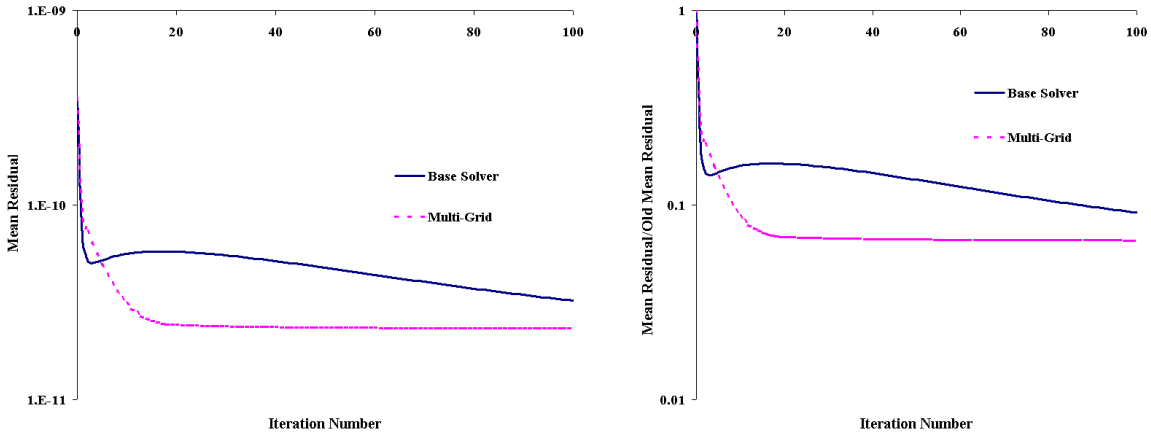

(a)

(b)

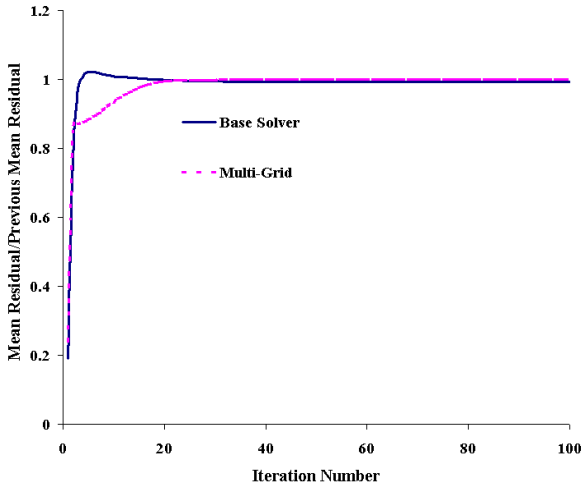

(c)

Figure A.1: Comparison between the base solver and the multi-grid's performance for a coarse grid based on the domain averaged values, a) maximum residual, b) maximum residual/maximum residual from the previous iteration, c) maximum residual/maximum residual from the previous iteration.

For a coarse grid of 64 × 72 × 48, the multi-grid and the base solver's performances are compared with each other for a flow around a wall-mounted square cylinder of AR = 3 and Re = 500. The comparison is made for a fully developed turbulent flow. The convergence criterion is deactivated temporarily for learning purposes. Results are presented based on the domain-averaged residuals in Figures A.1(a), A.1(b) and A.1(c) and the maximum residuals at Figures A.2(a), A.2(b) and A.2(c). Figure A.1(a) shows the domain-averaged residual for both schemes. After the first iteration the base solver and multi-grid lower the residual to 6.7×10^{-11} and 8.4×10^{-11}, respectively, where the initial residual is 3.5×10^{-10}. Although at the first few iterations the

residual is lower for the base solver, after the 3rd iteration the residual starts to grow. Unlike the base solver, the residual reduction curve is smooth and after about 15 iterations the domain-averaged residual reaches its minimum value. Figure A.1(b) shows the mean residual ratio over an initial domain-averaged residual. Since the data are non-dimensionalized, they give a better understanding of the solver's performance. Like Figure A.1(a), in the first three iterations the base solver presents a better performance, however in the long run, the multi-grid scheme converges much faster than the base solver. It should be noted that after the first iteration, the residual is lowered by about 75% for multi-grid and 80% for the base solver. After about fifteen iterations the multi-grid reaches the minimum level of 0.072 (i.e. 7.2% of an initial residual), while for the base solver even after one-hundred iterations the residual reduction curve has not reached its minimum value. Figure A.1(c) shows the domain-averaged residual ratio over the residual from the previous iteration. For the base solver after the first few iterations, this number is higher than one and then it descends to 0.99. For the multi-grid case, in the first three iterations the ratio jumps from 0.24 to 0.84 and then from iteration 4 to iteration 20, it moves slowly toward the 1-line. After iteration 20 there is not an obvious change in terms of the residual reduction rate.

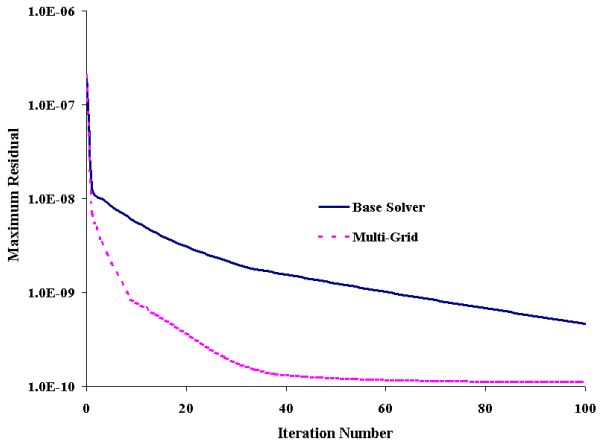

(a)

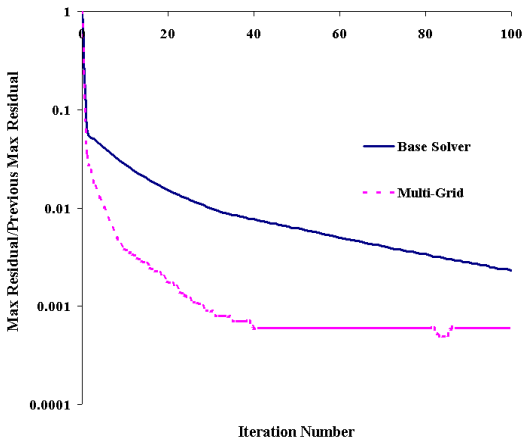

(b)

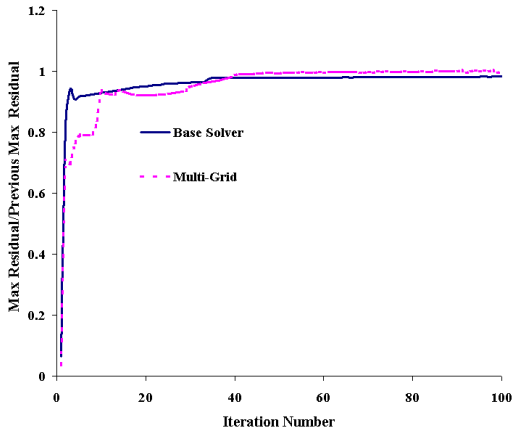

(c)

Figure A.2: Comparison between the base solver and the multi-grid's performance for a coarse grid based on the maximum residuals, a) maximum residual, b) maximum residual/maximum residual from the previous iteration, c) maximum residual/maximum residual from the previous iteration.

Figure A.2(a) shows that unlike the domain-averaged case even with the base solver there is a smooth curve of residual reduction at the maximum point. After the first iteration the base solver and the multi-grid lower the residual to 1.3×10^{-8} and 6.9×10^{-9}, respectively, where the initial residual is 2.0×10^{-7}. In case of multi-grid there is a sharp residual reduction until iteration 9 and from iteration 9 to iteration 20, the residual reduction rate slows down and after iteration 20 the change is not noticeable. Figure A.2(b) shows the maximum residual ratio over an initial maximum residual. At the first iteration the residual is lowered to 0.03 of an initial residual for the multi-grid and 0.065 for the base solver. After about 15 iterations the multi-grid reaches the minimum level of 0.007 (i.e. 0.7%) of an initial residual, where for the base solver even after 100 iterations the residual reduction curve has started to reach its minimum value. According to this figure, the residual remains unchanged after 40 iterations for the multi-grid while the residual is still descending to the lower value after 100 iterations for the base solver. Figure A.2(c) shows the domain-averaged residual ratio over the residual from the previous iteration. For the base solver in the first few iterations, this number is higher than 1 and then it descends to 0.99. For

the multi-grid case, unlike Figure A.1(c), the residual reduction curve is not smooth and apparently the residual reduction curve can be divided into three phases.

A.1. Convergence Criteria

Since the pressure equation (continuity) is of an elliptic nature, the main computational challenge in solving the Navier-Stokes equations relates to the pressure correction equation. Deciding when to stop an iterative process is important (setting an optimum number of iterations) which means spending the minimum computational effort while still meeting the required criteria.

A.2. Domain-averaged vs. Maximum Values

According to Figures A.1 and A.2 there are four possibilities to set the convergence criteria.

1- Domain-averaged residual ratio over an initial residual: Given the fact that locating an appropriate parameter where the residual or the residual ratio reaches its minimum value varies from one problem to another, makes this criterion unfavorable.

2- Domain-averaged residual ratio over the residual from the previous iteration: Although this method works properly for the multi-grid, it will stop the base solver from further advancement right from the beginning.

3- Maximum residual ratio over an initial residual: Like case 1 for the domain-averaged residual ratio over an initial residual, setting a proper parameter is difficult and varies from one problem to another.

4- Maximum residual ratio over the residual from the previous iteration: Based on this method the solution is converged where the residual ratio approaches one. In other words, further iterative process will not improve the solution. The only issue with this method is that it lowers the maximum residual by three orders of magnitude and requires at least forty iterations to complete.

A.3. Multi-Grid's Performance (Efficiency)

In a fully turbulent flow a four-level controlled W cycle functions in a similar way to a non-controlled V cycle, where, the solution uses the regular hierarchy of grids and each coarse grid is composed of eight adjacent control volumes. The solution starts from the finest grid then the solution is transferred to the next coarse grid where the spacing is $2h$. This procedure is called smoothing or restricting. After the equations are solved at the coarsest grid level, the solution proceeds upward by local subdivision of the coarse grids to the finer ones. This procedure is called prolongation (Figure A.3).

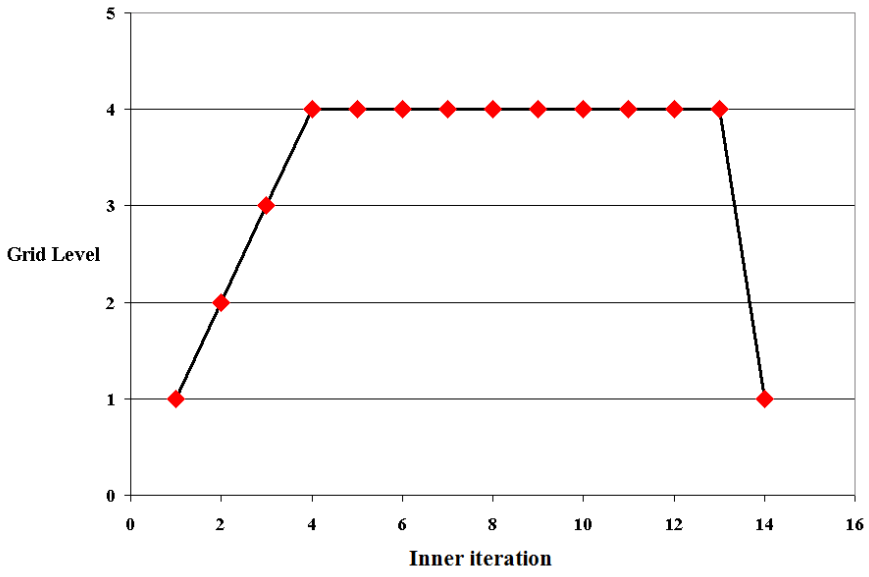

Figure A.3: An inner cycle of a multigrid scheme.

Since at the next coarse grid the spacing is $2h$, the computational effort is reduced to ½ in each direction and in a 3-D grid this number is $½^3$ therefore the computational effort required for one complete inner cycle for a multi-grid method is

$$2\times 1+1\times\left(\frac{1}{2}\right)^3+1\times\left(\frac{1}{4}\right)^3+10\times\left(\frac{1}{8}\right)^3\approx 2.16.$$

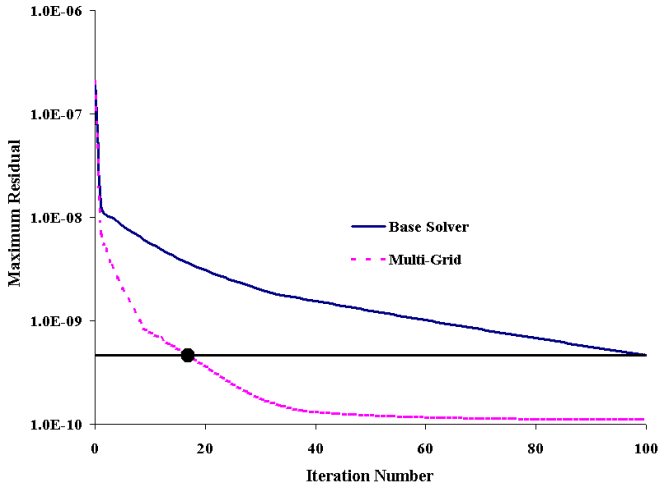

Figure A.4: Comparison between the base solver and the multi-grid's performance for a coarse grid based on the maximum residuals.

Figure A.4 compares the performance of the base solver vs. the multi-grid for a coarse grid based on the maximum residuals. Based on the maximum residual rates for a 64 × 72 × 48 grid, the multi-grid scheme is 100/(17×2.16) = 2.29 times more efficient than the base solver. Since in the TDMA scheme the information travels one grid per iteration, the number of iterations is linearly proportional to the number of nodes in one coordinate (Ferziger and Peric, 1999). However, all the iterative solvers converge more slowly on finer grids and this number should be higher for a finer grid.

A.4. Grid Size Effect

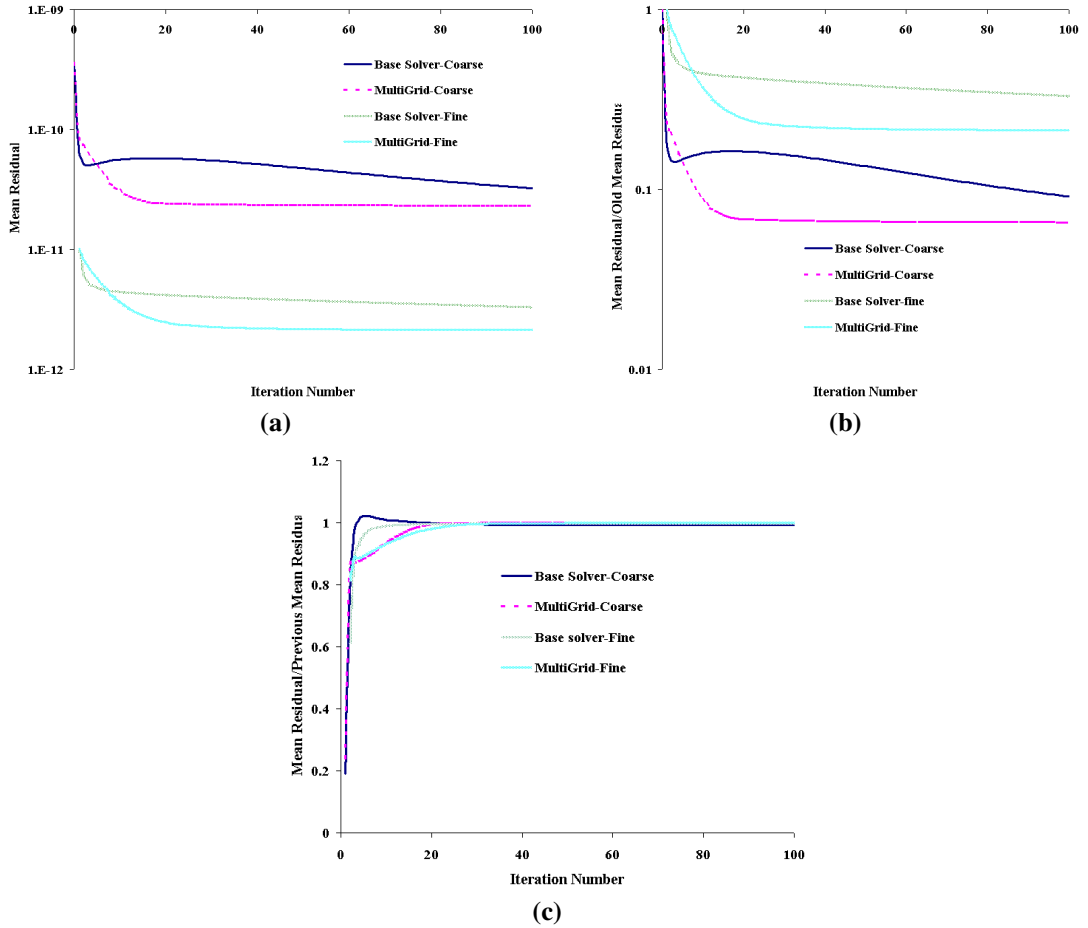

Figure A.5: Comparison between the base solver and the multi-grid's performance for both coarse and fine grids based on the domain averaged values, a) maximum residual, b) maximum residual/maximum residual from the previous iteration, c) maximum residual/maximum residual from the previous iteration.

For a finer grid of 128×144×96, the multi-grid and the base solver's performance are compared to that of 64 × 72 × 48 for a flow around a wall-mounted square cylinder of AR = 3 and Re = 500. As mentioned before, the comparison is made for a fully developed turbulent flow and the convergence criterion is deactivated temporarily. Results are presented based on the domain-averaged residuals in Figures A.5(a), A.5(b) and B.5(c) and the maximum residuals are presented in Figures A.6(a), A.6(b) and A.6(c). According to Figure A.5(a), although the domain-averaged residual is lower for the finer grid with both base solver and multi-grid approaches, the residual reduction rate is larger for the coarser grid. Figure A.5(b) also indicates that not only is the

residual reduction rate larger for the coarser grid, the base solver is much slower than the finer grid's case. Figure A.5(c) indicates, like the coarse grid case, this variable can not be set as the convergence criterion for the base solver.

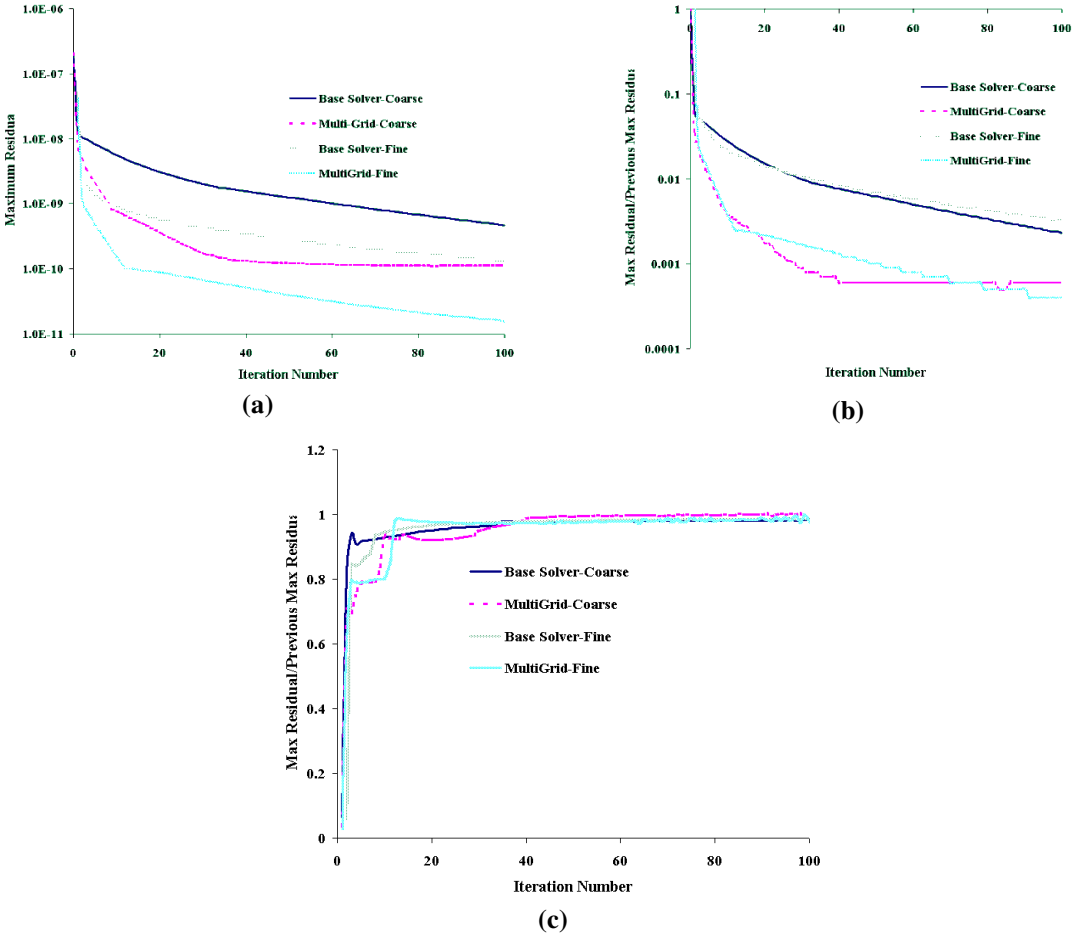

Figure A.6: Comparison between the base solver and the multi-grid's performance for both coarse and fine grids based on the maximum residual, a) maximum residual, b) maximum residual/maximum residual from the previous iteration, c) maximum residual/maximum residual from the previous iteration.

Figure A.6(a) shows that although the residual magnitudes are different for finer and coarse grids, both the base solver and multi-grid residuals follow the same pattern. Interestingly, even after 100 iterations with a multi-grid approach for a fine grid the residual reduction has not stopped and further calculations may improve the solution.

Based on the maximum residual rates for a 128 × 144 × 96 grid, the multi-grid scheme is 100/(10×2.16) = 4.63 times more efficient than the base solver. Since the pressure equation is of an elliptic nature, a change at one location influences the entire domain. As the grid becomes larger, this becomes problematic and slows down the solver. Therefore, for finer grids the multi-grid's existence (presence) is essential.

Appendix B

Dynamic Smagorinsky Model (DSM)

To correct the limitation of the Smagorinsky model, several models are proposed. Among them, the most popular one is the dynamic model which was first introduced by Germano et al. (1991) and then revised by Lilly (1992). In the dynamic Smagorinsky (DSM) model, C_s is determined as a variable of space and time, utilizing two filters with different characteristic scales: a grid filter and a test filter. This treatment of C_s is the first advantage of the DS model over the Smagorinsky model.

At the test grid level, the sub-grid scale tensor is as below;

$$T_{ij} = \widetilde{\overline{u_i}\overline{u_j}} - \widetilde{\overline{u}_i}\widetilde{\overline{u}_j}, \tag{C.1}$$

therefore:

$$T_{ij}^{*} = T_{ij} - \frac{\delta_{ij}}{3}T_{kk} = -2C_S\widetilde{\overline{\Delta^2}}\,\widetilde{\overline{|S|}}\,\widetilde{\overline{S_{ij}}} \tag{C.2}$$

The two SGS stresses, τ_{ij} and T_{ij}, are related by the Germano identity defined as

$$L_{ij} = T_{ij} - \tilde{\tau}_{ij}. \tag{C.3}$$

In the right hand side of the above equation, T_{ij} and $\tilde{\tau}_{ij}$ have to be modeled, while in the left hand side L_{ij} can be calculated explicitly from

$$L_{ij} = \widetilde{\overline{u_i}\,\overline{u_j}} - \widetilde{\overline{u}_i}\,\widetilde{\overline{u}_j}, \qquad \text{C.4}$$

Substituting the above equations lead to

$$\mathcal{L}_{ij}^{*} = -\alpha_{ij} C_S + \widetilde{\beta_{ij} C_S}, \qquad \text{C.5}$$

where

$$\alpha_{ij} = 2\tilde{\bar{\Delta}}^2 \left|\tilde{\bar{S}}\right| \tilde{\bar{S}}_{ij}, \text{ and} \qquad \text{C.6}$$

$$\beta_{ij} = 2\bar{\Delta}^2 \left|\bar{S}\right| \bar{S}_{ij}.$$

Assuming C_S as a constant, C_S can come out from the filtering and C_S may be evaluated from the following equation,

$$C_S = \frac{L_{ij}\bar{S}_{ij}}{M_{ij}\bar{S}_{ij}}, \qquad \text{C.7}$$

where M_{ij} is defined as: $M_{ij} = \alpha_{ij} - \tilde{\beta}_{ij}$.

The equation above is proposed by Germano et al. (1991), but testing on a channel flow, he showed that near the walls the denominator could become zero. Therefore, one year later Lilly (1992) introduced the least squares method,

$$C_S = \frac{M_{ij} L_{ij}}{M_{ij} M_{ij}}, \qquad \text{C.8}$$

and removed the indeterminacy of Germano's equation (Lesieur et al., 2005).

The second advantage of the DS model is the near wall treatment. In the Smagorinsky model, in the near wall area, an empirical model function f_μ is required for damping the SGS viscosity. However, in the DS model, since the value of C_s automatically goes to zero in the laminar region near the wall, f_μ is not necessary (Murakami et al., 1999).

Appendix C

Nonlinear Dynamic Model (DNM)

Although the DSM has considerable advantages over the Smagorinsky model, it still needs improvement in some areas. One of the main problems with DSM is the large fluctuations of the value of C_s.

The main drawback of the conventional methods like SM and DSM are that in these models a strict alignment between the τ_{ij} and S_{ij} tensors is required (Wang and Bergstrom, 2005).

Based on the Smagorinsky model, the generic SGS stress τ_{ij} can be written as a function of the resolved velocity gradient, the unit tensor δ_{ij}, and the cutoff filter size Δ:

$$\tau_{ij}^{*} = \tau_{ij} - \frac{\delta_{ij}}{3}\tau_{kk} = f\left(\bar{S}_{ij}, \bar{\Omega}_{ij}, \delta_{ij}, \bar{\Delta}\right). \qquad 1.\ \text{D.1}$$

S_{ij} and Ω_{ij} represent the symmetric and antisymmetric parts of the filtered velocity gradient, respectively. Therefore,

$$\bar{u}_{i,j} = \frac{1}{2}\left(\bar{u}_{i,j} + \bar{u}_{j,i}\right) + \frac{1}{2}\left(\bar{u}_{i,j} - \bar{u}_{j,i}\right) = \bar{S}_{ij} + \bar{\Omega}_{ij}. \qquad 2.\ \text{D.2}$$

Ideally, the general form of the SGS stress tensor τ_{ij}^{*} involves a polynomial tensors consisted of the S and Ω terms. According to the theory of invariants and the Cayley-Hamilton theorem, Pope (1975) proposed a generic relation for closure of the Reynolds stress in RANS, which involves a finite number of tensorial terms. Based on Pope's method, Lund and Novikov (1992) introduced a set of eleven independent symmetric tensorial elements related to the products of S and Ω.

3. D.3

$$T^{(1)} = S \qquad T^{(2)} = S^2$$

$$T^{(3)} = \Omega^2 \qquad T^{(4)} = S\Omega - \Omega S$$

$$T^{(5)} = I_d \qquad T^{(6)} = S^2\Omega - \Omega S^2$$

$$T^{(7)} = S\Omega^2 + \Omega^2 S \qquad T^{(8)} = \Omega S\Omega^2 - \Omega^2 S\Omega$$

$$T^{(9)} = S^2\Omega S - S^2\Omega S \qquad T^{(10)} = S^2\Omega^2 + \Omega^2 S^2$$

$$T^{(11)} = \Omega S^2\Omega^2 - \Omega^2 S^2\Omega$$

where the identity tensor, I_d is defined as:

4. D.4

$$I_1 = \mathrm{tr}\left(S^2\right) \qquad I_2 = \mathrm{tr}\left(\Omega^2\right)$$

$$I_3 = \mathrm{tr}\left(S^3\right) \qquad I_4 = \mathrm{tr}\left(S\Omega^2\right)$$

$$I_5 = \mathrm{tr}\left(S^2\Omega^2\right) \qquad I_6 = \mathrm{tr}\left(S^2\Omega^2 - S\Omega\right)$$

It should be noted that:

5. D.5

$$S\Omega = \overline{S}_{ik}\overline{\Omega}_{kj}$$

$$S^2 = \overline{S}_{ik}\overline{S}_{kj}$$

$$\mathrm{tr}(S\Omega) = \overline{S}_{ij}\overline{\Omega}_{jk}\overline{\Omega}_{ki}$$

Using the above tensors, the SGS stress tensor τ_{ij} is written as an explicit tensorial polynomial of S and Ω,

6. D.6

$$\tau_{ij} = \sum_{k=1}^{11} G^{(k)} T^{(k)},$$

where $G^{(k)}$ is the scalar coefficient function of the I_d.

Recalling the dynamic SGS modeling approach, the grid-level and test-grid level stress tensors are

7. D.7

$$\tau_{ij}^{*} = -C_S\beta_{ij} - C_W\gamma_{ij} - C_N\eta_{ij},$$

$$T_{ij}^{*} = -C_S\alpha_{ij} - C_W\lambda_{ij} - C_N\xi_{ij},$$

where,

8. D.8

$$\gamma_{ij} = 4\bar{\Delta}^2\left(\bar{S}_{ik}\bar{\Omega}_{kj} - \bar{\Omega}_{ik}\bar{S}_{kj}\right),$$

$$\lambda_{ij} = 4\tilde{\bar{\Delta}}^2\left(\tilde{\bar{S}}_{ik}\tilde{\bar{\Omega}}_{kj} - \tilde{\bar{\Omega}}_{ik}\tilde{\bar{S}}_{kj}\right),$$

$$\eta_{ij} = 4\bar{\Delta}^2\left(\bar{S}_{ik}\bar{S}_{kj} - \frac{1}{3}\bar{S}_{mn}\bar{S}_{nm}\delta_{ij}\right),$$

$$\xi_{ij} = 4\tilde{\bar{\Delta}}^2\left(\tilde{\bar{S}}_{ik}\tilde{\bar{S}}_{kj} - \frac{1}{3}\tilde{\bar{S}}_{mn}\tilde{\bar{S}}_{nm}\delta_{ij}\right),$$

and α_{ij} and β_{ij} were introduced beforehand in Appendix B.

Substituting τ_{ij}^{*} and T_{ij}^{*}, the Germano identity is written as

$$\mathcal{L}_{ij}^{*} = -C_S\alpha_{ij} - C_W\lambda_{ij} - C_N\xi_{ij} + \widetilde{C_S\beta_{ij}} + \widetilde{C_W\gamma_{ij}} + \widetilde{C_N\eta_{ij}}. \quad \text{D.9}$$

Using the least squares approach introduced by Lilly (1992), a quadratic optimal equation is obtained:

$$\begin{bmatrix} M_{ij}M_{ij} & M_{ij}W_{ij} & M_{ij}N_{ij} \\ W_{ij}M_{ij} & W_{ij}W_{ij} & W_{ij}N_{ij} \\ N_{ij}M_{ij} & N_{ij}W_{ij} & N_{ij}N_{ij} \end{bmatrix}\begin{bmatrix} C_S \\ C_W \\ C_N \end{bmatrix} = -\begin{bmatrix} L_{ij}^{*}M_{ij} \\ L_{ij}^{*}W_{ij} \\ L_{ij}^{*}N_{ij} \end{bmatrix}. \quad \text{D.10}$$

The above equation shows that the DSM is the first order approximation of the DNM (Wang and Bergstrom (2005)).

Appendix D

Instantaneous Velocity Vectors and Streamwise Vorticity Contours at x/D = 8 and 10

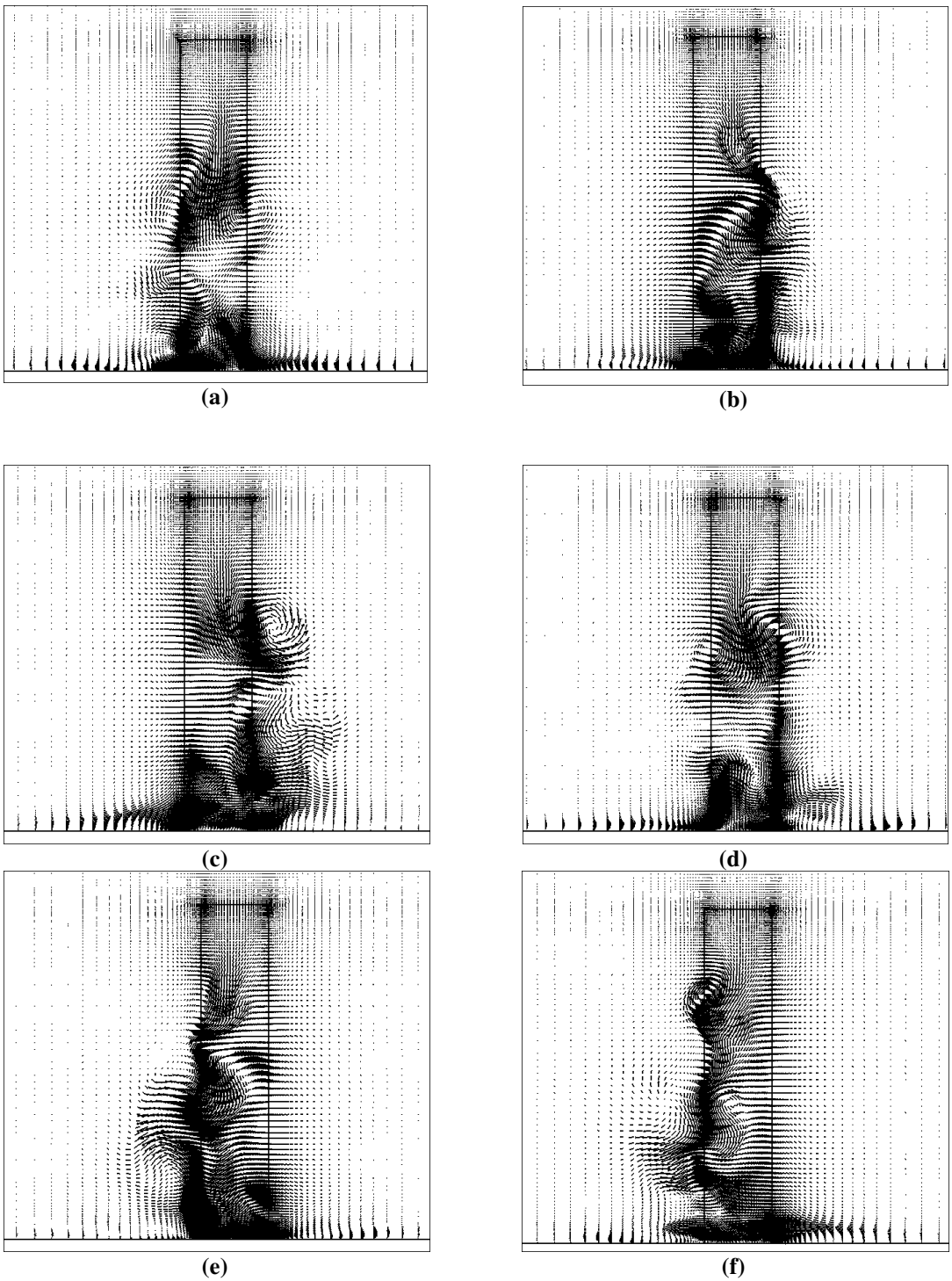

Figure D.1: Instantaneous velocity vectors located at x/D = 3 for six consecutive time-steps: a) 1/6T, b) 2/6T, c) 3/6T, d) 4/6T, e) 5/6T, and f) T.

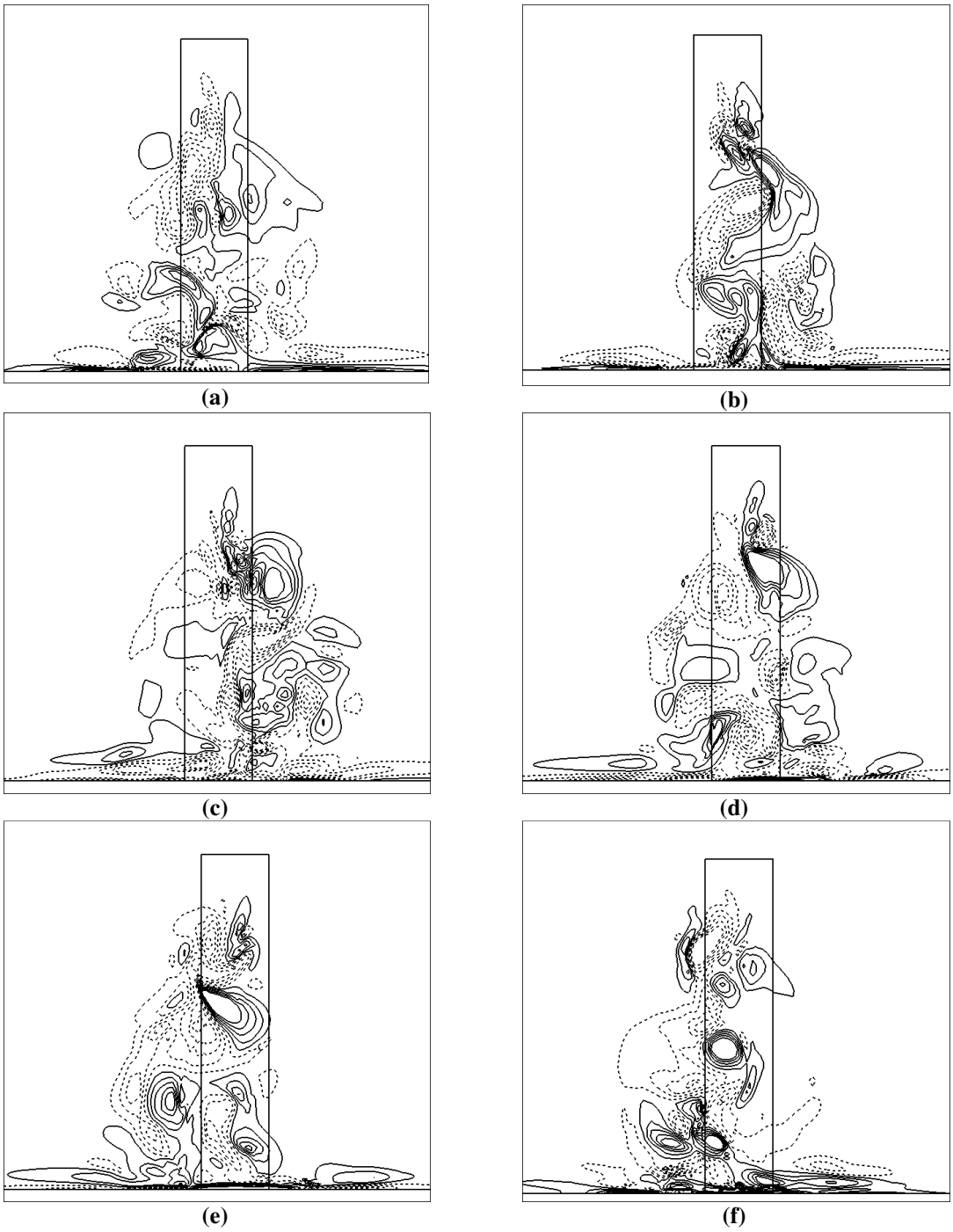

Figure D.2: Instantaneous streamwise vorticity contours located at x/D = 3 for six consecutive time-steps: a) 1/6T, b) 2/6T, c) 3/6T, d) 4/6T, e) 5/6T, and f) T.

Figures D.1 and D.2 show the instantaneous velocity vectors and the streamwise vortices contours in a normal plane located at x/D = 3 at six different time frames. The pair of tip vortices formed near the free has moved even further towards the ground plane. Although in

Figures D.2 (a) the vortices are formed in a more symmetric way the vortices observed in Figures D.2(c) and D.2(f) are entirely antisymmetric and are concentrated on one side of the cylinder. Also, the vortices have expanded in the spanwise direction compared to the previous cases. The pair of base vortices has become weaker compared to $x/D = 2$.

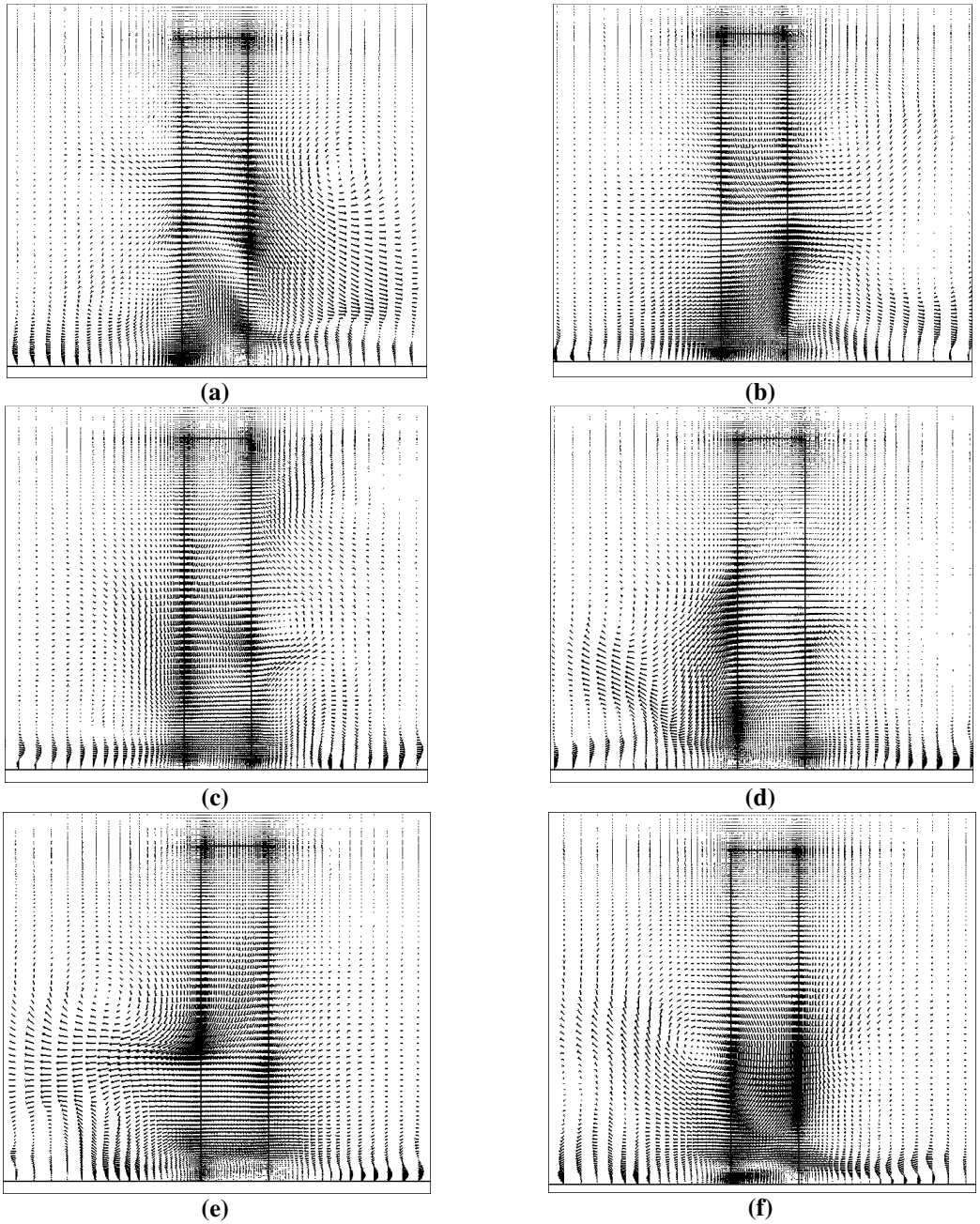

Figure D.3: Instantaneous velocity vectors located at $x/D = 8$ for six consecutive time-steps: a) $1/6T$, b) $2/6T$, c) $3/6T$, d) $4/6T$, e) $5/6T$, and f) T.

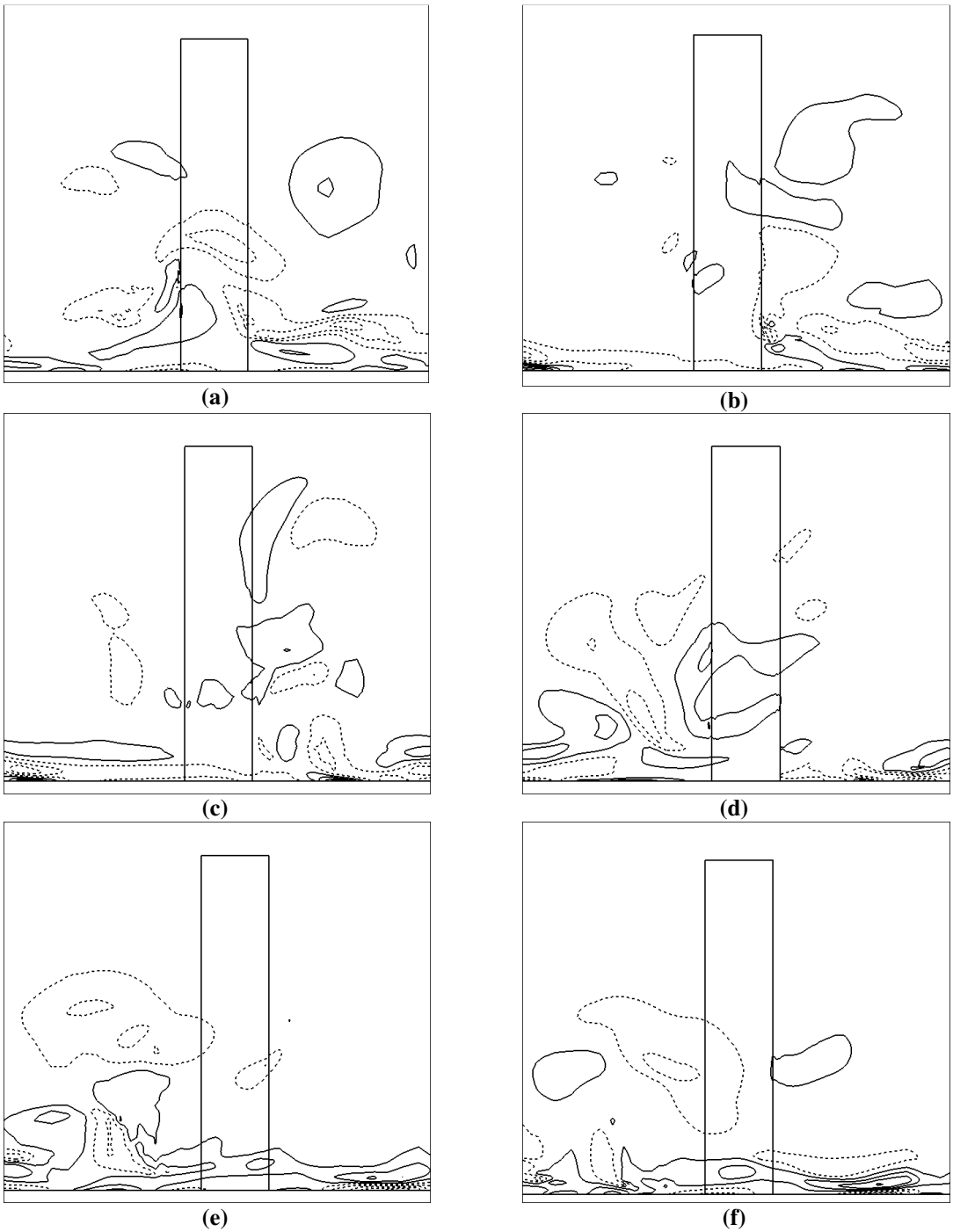

Figure D.4: Instantaneous streamwise vorticity contours located at x/D = 8 for six consecutive time-steps: a) 1/6T, b) 2/6T, c) 3/6T, d) 4/6T, e) 5/6T, and f) T.

The streamwise vorticity contours in Figure D.4 suggested a highly three-dimensional flow structure along the wake region of finite-height wall-mounted square cylinder at all six time frames.

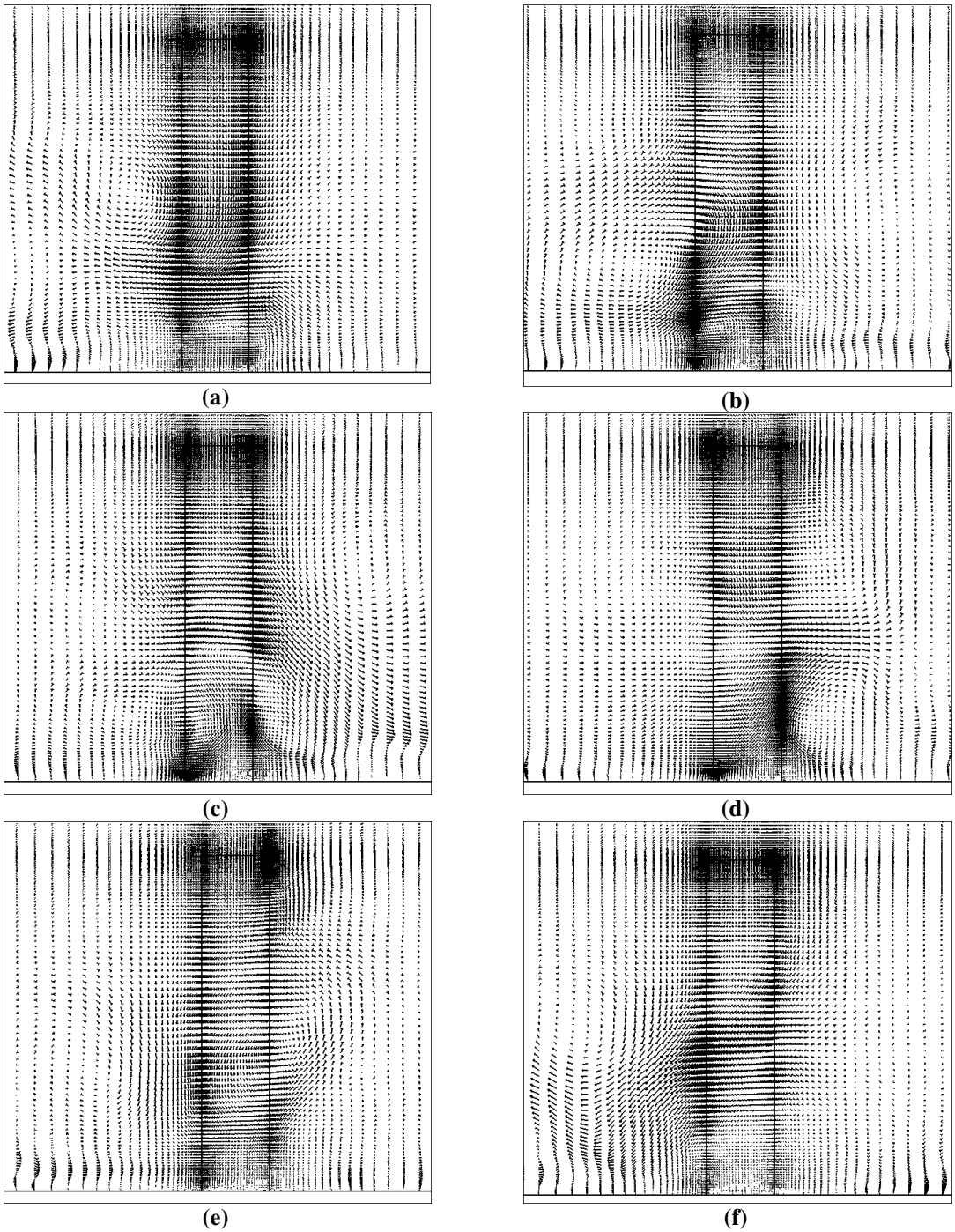

Figure D.5: Instantaneous velocity vectors located at x/D = 10 for six consecutive time intervals: a) 1/6T, b) 2/6T, c) 3/6T, d) 4/6T, e) 5/6T, and f) T.

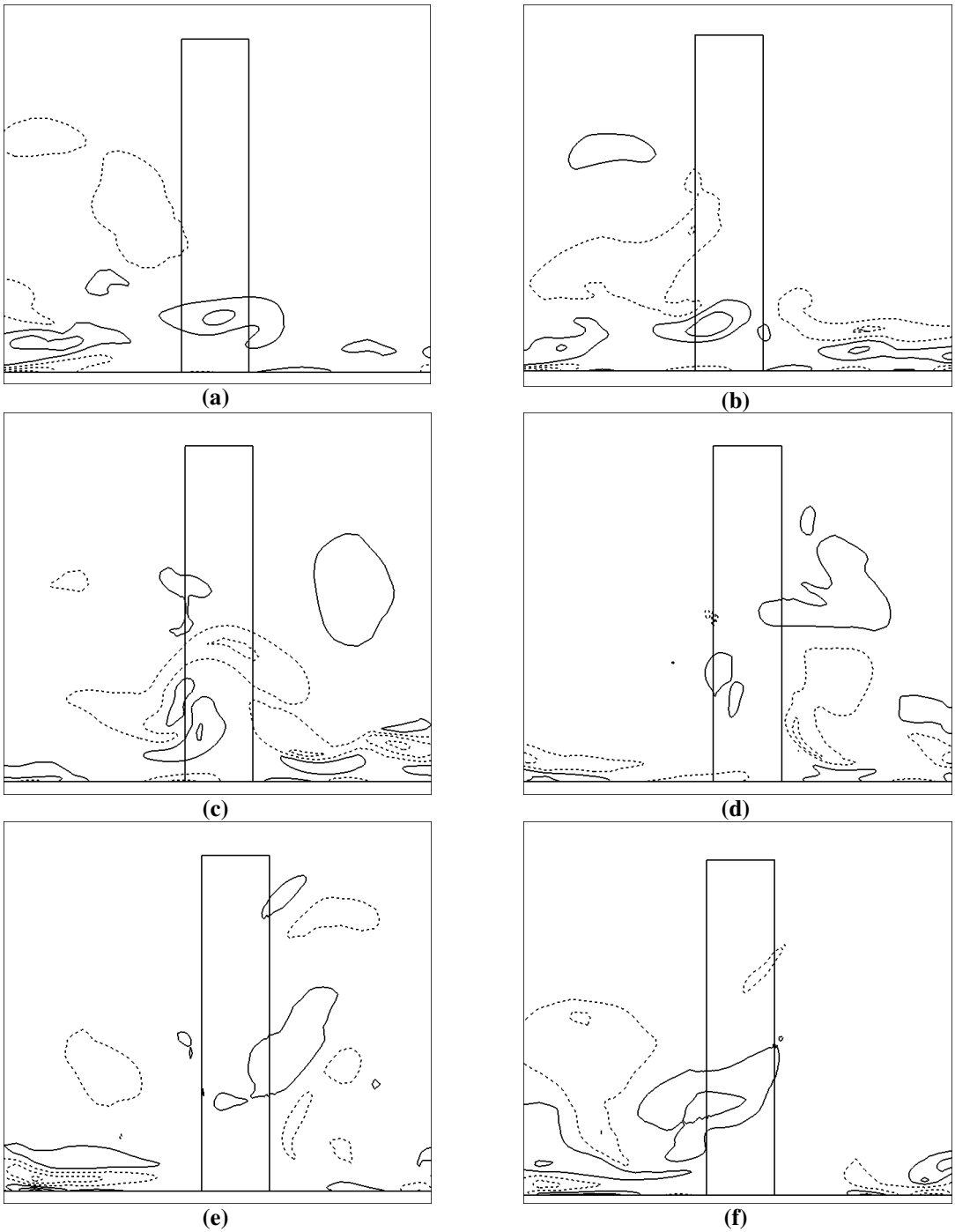

Figure D.6: Instantaneous streamwise vorticity contours located at x/D = 10 for six consecutive time intervals: a) 1/6T, b) 2/6T, c) 3/6T, d) 4/6T, e) 5/6T, and f) T.

Figures D.5 and D.6 show the instantaneous velocity vectors and the streamwise vorticity contours, ω_x, in a vertical plane located at x/D = 10. This section is well downstream of the cylinder and the flow structures in both Figures D.5 and D.6 are much weaker. The velocity

vectors in Figure D.5, show large regions of weak flow into and out of the wake. Curiously, the vectors still show some persistent motions near the top corners of the cylinder, although this may be partly the effect of grid refinement. The streamwise vorticity contours in Figure D.6 suggest a weak and highly irregular vortex pattern that has lost the definite structure of the time mean average field.